THE UNIVERSITY *of* EDINBURGH

Numerical Study of Floating Wind Turbines: Hydro- and Aero-mechanics

Raffaello Antonutti

Engineering Doctorate

The University of Edinburgh

2015

A thesis submitted in partial fulfilment of the requirements for the award of an Engineering Doctorate

"No! I tell you! The way is to the destructive element submit yourself, and with the exertions of your hands and feet in the water make the deep, deep sea keep you up."

— Joseph Conrad, *Lord Jim*

IDCORE

This thesis is submitted in partial fulfilment of the requirements for the award of an Engineering Doctorate, jointly awarded by the University of Edinburgh (lead), the University of Exeter and the University of Strathclyde. The work presented has been conducted under the industrial supervision of EDF R&D (Electricité de France Research and Development, Chatou, France) as a project within the Industrial Doctoral Centre for Offshore Renewable Energy.

THE UNIVERSITY
of EDINBURGH

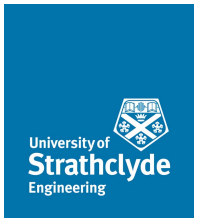

Lay Summary

The maritime environment is full of energy in the form of waves, currents, and wind. Humans have been harvesting a fraction of this energy for their own use for millennia. Without the predictable energy flow associated to trade winds, for example, large-scale global trade would not have occurred before the exploitation of combustion for ship propulsion.

Today wind energy can be converted into electricity using wind turbines. Large offshore wind turbines, which can be twice as tall as the Big Ben tower and power thousands of households, already populate the shallows of the North Sea. Since they are typically fixed to the seabed, the extent to which they can be built is severely limited by water depth.

Beyond about fifty metres depth, turbines can no longer be made to sit on the seabed economically and floating solutions are preferable. Although only a few floating prototypes have been tried thus far, this technology is rapidly improving and the wind industry is ramping up investment to prepare the installation of the first floating wind farms.

A fundamental challenge for design engineers is the prediction of the mechanical behaviour of a floating wind turbine under the action of wind, waves, and currents. For example, they must prove that their turbine will stay afloat without capsizing during a storm. Fail in doing this and you might experience a power interruption from the turbine. Further, it may be found washed up on the nearby beach the following day!

Anticipating the mechanical behaviour of a floating wind turbine system and its main parts – rotor, platform, and moorings – is the focus of this thesis. This is done using a range of different software, to highlight critical features which are vital for a correct design. The outcomes of this work are expected to help the safe and effective development of future floating wind turbines.

Abstract

Floating wind technology has the potential to produce low-carbon electricity on a large scale: it allows the expansion of offshore wind harvesting to deep water, indicatively from 50–60 to a few hundred metres depth, where most of the worldwide technical resource is found. New design specifications are being developed for floating wind in order to meet diverse criteria such as conversion efficiency, maintainability, buoyancy stability, and structural reliability. The last is the focus of this work.
The mechanics of floating wind turbines in wind and waves are investigated with an array of numerical means. They demand the simulation of multiple processes such as aerodynamics, hydrodynamics, rotor and structural dynamics; understanding their interaction is essential for engineering design, verification, and concept evaluation. The project is organised in three main parts, presented below.

Aero-hydro-mechanical simulation, characterising the rigid-body motions of a floating wind turbine. An investigation of multi-physical couplings is carried out, mainly through EDF R&D's time-domain simulator CALHYPSO. Wave forces are represented with the potential-flow panel method and the Morison equation. Aerodynamic forces are represented by a thrust model or with the blade element momentum theory.
Main findings: Exposure of finite-angle coupling for semi-submersible turbines with focus on heave plate excursion; characterisation of the aerodynamic damping of pitch motion provided by an operating vertical-axis turbine.

Dynamic mooring simulation, focussed on highly compliant mooring systems, where the fluid-structure interaction and mechanical inertial forces can govern line tension. EDF R&D's general-purpose, finite-element solver *Code_Aster* is configured for this use exploiting its nonlinear large-displacement and contact mechanics functionalities.
Main findings: Demonstration of a *Code_Aster*-based workflow for the analysis of catenary mooring systems; explanation of the dynamic mooring effects previously observed in the DeepCwind basin test campaign.

Aeroelastic analysis of vertical-axis rotors, aimed at verifying novel large-scale floating wind turbine concepts in operation, when aeroelastic-rotordynamic instabilities may occur. The finite-element modal approach is used to qualify rotor vibrations and to estimate the associated damping, based on the spinning beam formulation and a linearised aerodynamic operator.
Main findings: Characterisation of the vibration modes of two novel vertical-axis rotor concepts using the Campbell diagram; estimation of the related aerodynamic damping, providing information on the aeroelastic stability of these designs.

Acknowledgements

Funding from the Energy Technologies Institute (ETI) and the RCUK Energy Programme for the Industrial Doctoral Centre for Offshore Renewable Energy (Grant number EP/J500847/1) is gratefully acknowledged. I would like to express my gratitude to EDF R&D for hosting and supervising the industrial doctorate, and to the IDCORE teaching and administrative teams for their commitment.

I am most grateful to my main industrial supervisor and Jedi mentor Christophe Peyrard, who has deeply inspired me with his wizardly union of scientific rigour, engineering dexterity, and human understanding. My gratitude extends to the many formal and informal supervisors I have had from industry and academia alike: Atilla Incecik, David Ingram, Lars Johanning, and Nicolas Relun. This project would never have been such an extraordinary experience without their patience, precision, dedication, warmth, and humour.

My regards also go to the teams at EDF R&D and at the Saint-Venant Laboratory that have made this experience so enriching day by day. Special thanks to Alex, Alexis, Amélie, Ampea, Becky, Berto, Cécile, Gabe, Jérôme, Joe, Kaswar, Nacho, Siraj, and Steve for having shared the limited space of an office – above or beneath the ground, by the Seine stream or the Caledonian hills – and a snippet of their lives with me. Friends next door and remote, from the distant past or first met on the last Saturday, thank you all for your support.

I am grateful to my family who has become used to sending its love thousands of kilometres away. Off-scale gratitude and unconditional love go to Anna.

Declaration

I declare that this thesis was composed by myself and that the material presented, except where explicitly stated otherwise, is my own work. I declare that this work has not been submitted for consideration as part of any other degree or professional qualification. The materials included which have been published are my own work.

Signed: **Raffaello Antonutti**

Contents

List of Figures

List of Tables

Part 1

Introduction

Over the last few decades, the globalisation of the economy has radically changed the functioning principles of society. The geographical redistribution of industrial activities, previously concentrated in the OECD countries, has provided access to skilled labour and increasing wealth to other regions of the World, among which the most spectacular example is probably south-eastern Asia [1]. As a consequence, whilst the primary energy demand in the most developed countries tended to stabilise, the aggregate worldwide demand kept growing at a fast pace[1]. This has placed significant stress onto the global energy system which has been reflected in recent years by energy commodity price hikes and volatility [2, 3]. Secure and affordable sources of energy must be made available and integrated in future mixes to support global prosperity.

In the same timeframe a different form of pressure has been impacting the development of energy systems, which is related to climate policy. Having recognised the need for climate risk mitigation as a fundamental challenge of our times (see Rockström et al. [4] for a high-level perspective), politics have engaged in a set of plans of increasing ambition for the decarbonisation of the economy. These include support to the development of new renewable energy technologies, as a contribution to the transformation of the energy system. This, in fact, is responsible for a large share of the anthropogenic CO_2 emissions; in particular the electricity/heat sector is under the spotlight, accounting for an estimated 42% of the man-made CO_2 in 2012 [5].

The combined policy push and market pull mechanisms outlined above have been the main drivers behind the development of electrical wind power since the 1970s, which – even when intermittency is factored in – appears today as one of the most cost-effective forms of low-carbon electricity generation, at least up to a certain level of grid penetration [6, 7]. Toward the end of the 1990s the wind industry began expanding to the maritime continental shelf, mostly in the North Sea shallows, to harness the superior wind resources found offshore and mitigate the societal impact of windfarm installations. Despite its higher cost, recent years witnessed a rapid expansion of offshore wind centred in northern Europe, where the installed capacity nears the 10 GW mark

[1] In excess of 2% per year in the last two decades [2].

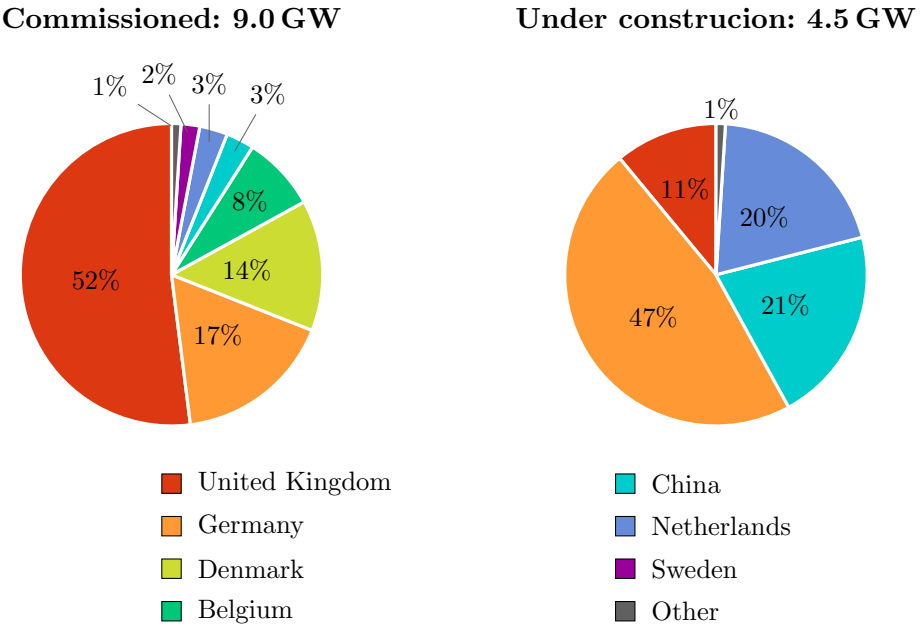

Figure 1.1: Repartition of operating and under construction offshore wind capacity in mid 2015. Data from NREL [11].

at the time of writing with over 70 windfarms operating across eleven countries [8]. The UK detains at present over half of the worldwide capacity (Figure 1.1, left) and is reportedly the most attractive market for offshore wind business development [9], largely as an outcome of its proactive policy [10].

A new player, France, has recently launched two GW-scale offshore windfarm consenting rounds in 2012 and 2014 for a total capacity of nearly 3 GW, scheduled for commissioning around 2020, and a third one is expected at the turn of this year. Other regions are entering the offshore wind market, including North America and the Pacific with the United States [11], as well as eastern Asia, where China has already begun large-scale deployment [10]. Other developed countries such as Japan and South Korea prepare ambitious plans in this respect [12]. The attainable scale of the industry in countries with limited shallow maritime space, Japan above all [11, 13, 14], will depend on the availability of deep-water technology; this leads to discussing the object of this work, floating offshore wind.

1.1 Floating wind power

In recent years floating wind power has been increasingly regarded as an attractive option for the production of low-carbon electricity, thanks to the potential to unlock vast resources which are inaccessible using fixed substructures; these are expected to become gradually unviable for depths beyond 50 m–60 m according to most observers including the European Wind Energy Association [15] and leading technology developers [16]. Being able to deploy wind turbines in deep water will be crucial to determine the scale of the industry within regions where the maritime continental shelf is steep. In spite of the presence of vast shallow areas especially in the North Sea, an estimate of the technical resource potential in Europe by the HiPRWind consortium indicates a deep-water share of about 70% [17]. Preliminary estimates for France lie in the range between 60% [18] and 80% [17], although a rigorous assessment is yet to be published. In Japan, now a prominent country in floating wind development, 80% of the offshore wind resources are located in deep water according to a landscape study by Main(e) International Consulting [19]. Musial and Ram [20] maintain that the deep-water share of the offshore wind resource potential for the United States amounts to about 2/3. Part of this abundance is related to the higher mean wind speeds typically found far offshore, where water depth is tendentially larger; nevertheless, it is expected that early commercial floating wind developments – presenting the highest economic value – will tend to occur in sweet spots where deep water is found relatively close to shore [21] and to existing grid nodes such as large cities.

Numerous countries hold most of their offshore wind potential in deep water, but only a handful have hosted utility-scale machine deployment so far. Statoil of Norway has commissioned the first operating MW-class floating demonstrator, Hywind, in 2009 [22]. Portugal has followed by hosting Principle Power's WindFloat prototype (Figure 1.2, left), deployed in 2011, and more recently two Japanese consortia have successfully installed floating test units off Goto city (Figure 1.2, right) and the coast of the Fukushima prefecture (see [19, 23, 24]). All but one commissioned, large-scale prototypes adopt turbines of about 2 MW capacity, mounted either on spars or semi-submersible platforms. As suggested by the installation of a 7 MW[2] unit at the Fukushima testing site in summer 2015, the industry is looking to exploit the economies associated to further wind turbine upscaling[3]. The ongoing industrialisation initiatives are also seeking to extend the operational floating wind turbine (FWT) design envelope with the use of tension-leg platforms, with the first utility-scale prototype currently under construction

[2] A rating which is close to the upper boundary of current wind power technology per se.

[3] Upscaling helps to reduce installation and maintenance costs and is reported as one of the major drivers of the cost reduction trend observed in UK offshore wind projects [25]. As pointed out by Henderson and Witcher [26], another expected benefit of upscaling in the floating realm comes from the relaxation of design space constraints for certain platform types.

Figure 1.2: WindFloat assembly in the Mitrena Shipyard near Lisbon (left), photo courtesy of Principle Power. Haen-kaze demonstrator sited off Goto in Japan (right), courtesy of David Ingram.

[27], barge-type platforms [28], and vertical-axis aerogenerator technology [29]. The combined energy supply, industrial development, and innovation potential of offshore wind in France has fostered the birth of a dedicated industrial ecosystem starting from the late 2000s. Large firms such as EDF, Engie, Alstom and Areva teamed up with national SMEs and international partners in order to provide the country with a fully operating offshore wind supply chain by around 2020. The overarching policy set by the French state to coordinate sustainable energy development is enshrined in the 2007 and 2010 *Grenelle de l'Environnement* laws and since more recently in the energy transition law approved by the parliament in 2015. In application of the European directives, the 2009 national plan for renewable energy assigns a capacity target of 6 GW for offshore wind by end-2020 [30].

Concerning floating wind, the French policy is encouraging a fast-track course to industrialisation, with the likely intention to leverage on the country's engineering and maritime expertise to achieve a leading position in a few-year timeframe. After funding the Vertiwind project [29] – looking at vertical-axis technology for floating applications – and the consenting of a first pilot farm in the Mediterranean labelled *Provence Grand Large*, French authorities have launched a pilot floating windfarm round in summer 2015. This should enable to identify up to four 20-50 MW projects by spring 2016 that

Figure 1.3: Bottom-fixed and floating offshore wind turbines, after Smith et al. [11].

will be co-financed by the funding body ADEME [31].
Benefitting from its participation to the pioneering Vertiwind/INFLOW programme, the EDF Group is readying to take part in the national pre-commercial deployments outlined above, first and foremost as the owner of the *Provence Grand Large* project. The longer-term aims of the utility hinge on the industrialisation and standardisation of FWT technology in order to establish itself as a leading project developer on the international scene. A permanent R&D programme accompanies EDF's business units in the process of evaluating alternative engineering solutions, verifying proposed design and modelling approaches, and de-risking the prototyping and deployment projects.
A brief presentation of floating wind technology is provided next, which has also been reproduced in a technology watch report of EDF [32].

1.2 Technology

The present work focusses on utility-scale, single-turbine floating units. Setting an offshore wind turbine afloat corresponds to choosing water as the reactive rotational (and vertical) support instead of the seabed[4]. The fundamental advantage comes along

[4]Excluding tension-leg arrangements.

with increasing depth: the water remains close to the point of application of rotor thrust and wave forces, assuring a short load path; if these are transmitted to the seabed, an increasingly longer load path is obtained instead, causing the associated moment to grow with depth. This in turn governs the dimensioning and hence the cost of a bottom-fixed turbine's substructure [26]. The significantly lower steepness of the projected cost curves as a function of depth for floating wind (see e.g. Myhr et al. [33]) is explained by this simple consideration.

1.2.1 Floating platform

In order to transfer its weight to the water a FWT must dispose of adequate buoyancy, which is proportional to the displaced volume of its hull. Moreover, due to the sensitivity to skewed flow of conventional aerogenerators and to structural integrity requirements, the allowable inclination under the action of the met-ocean loads is subjected to limitations. The vital function of guaranteeing sufficient buoyancy is fulfilled by the floating platform, whilst stability is provided jointly by the platform and the mooring system. The principle used to provide a FWT with adequate rotational stability defines three technological options currently considered in platform design, shown in Figure 1.3: ① semi-submersible/barge, ② tension-leg and ③ spar. Let $\triangle$ denote the structure's displacement, and considering the vertical distances at equilibrium between the keel point K, the buoyancy centre B, and the metacentre M, its stability with respect to small inclinations is quantified by the linearised restoring coefficient,

$$k = \triangle(\overline{\mathrm{KB}} + \overline{\mathrm{BM}} - \overline{\mathrm{KG}}) + k^{\mathrm{m}}\,, \tag{1.1}$$

where the first term of the second member is associated to hydrostatic stability and the second to the added stability provided by the mooring system. No active stabilisation devices such as pumped ballast are considered here. This enables to distinguish the platform families introduced above: owing to their large waterplane area, barges and semi-submersibles rely on a large metacentric height $\overline{\mathrm{BM}}$. Deep spar substructures, conversely, adopt bottom-mounted ballast to achieve large values of $\overline{\mathrm{KB}} - \overline{\mathrm{KG}}$. Equation 1.1 also shows that a reduction in platform displacement, sought by the optimisation of fabrication cost, tends to deteriorate the stability of any hydrostatically stabilised FWT regardless of its type.

The design constraints identified by Henderson et al. [34] by stretching an idealised cylindrical platform, reproduced in Figure 1.4, indicatively show the conflict among the key design parameters of a hydrostatically stabilised FWT with simple geometry. No limitation on the available water depth is assumed in the following interpretation of the diagram. Stability may become insufficient when the hull is too short and/or its waterplane area too small (top-left part of the figure), which roughly translates into

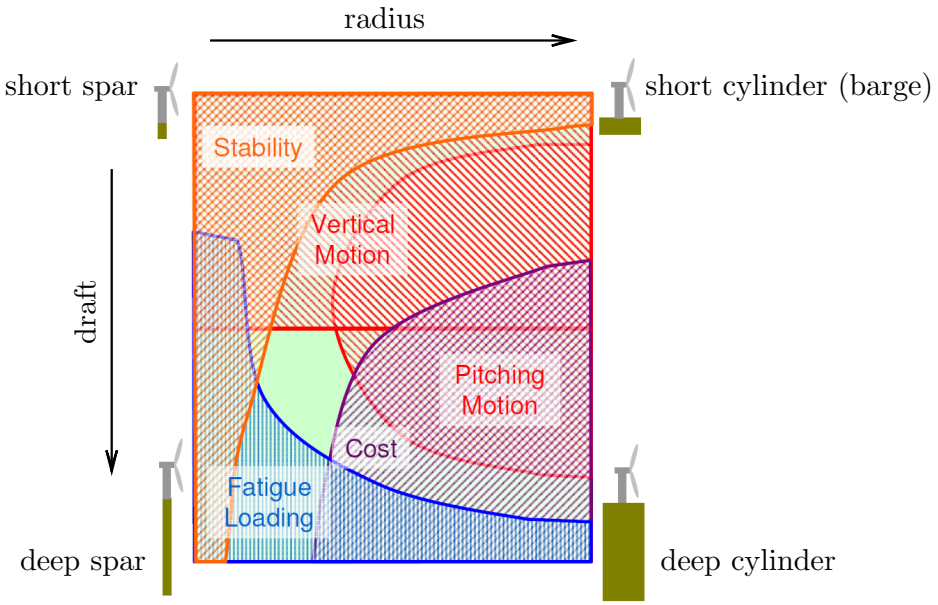

Figure 1.4: Identification of viable design space of an idealised floating wind turbine platform (green area) using five exclusion criteria. After Henderson et al. [34].

a lower boundary for floater size, depending on the expected overturning moments. Conversely, large and highly stable platforms (bottom-right) tend to entail unacceptable fabrication costs. Intertwined with these considerations is the problem of avoiding excessive motions in waves (top and centre-right), which can hinder the operability and integrity of the aerogenerator. Finally, deep and/or slender floater structures (bottom-left) may become too prone to fatigue, mainly related to bending.

The conflict between stability and cost is put in evidence by their diametrical opposition. Coupled with the large restoring demand associated to wind overturning, this observation poses one of the fundamental dilemmas of floating wind system optimisation: should the designer allow for reduced stability or introduce complementary stabilising mechanisms? TLPs resolve this dilemma by sacrificing hydrostatic stability in favour of the complementary mooring system stiffness k^{m} of Equation 1.1, allowing to adopt smaller platforms. In this case hull size is no longer governed by stability but by the buoyancy needed to counter the weight of the FWT and the tendon pre-tension forces. Discussed in 1.2.2 is the vertical-axis wind turbine option which may be used to reduce the stability demand instead, thanks to its better compatibility with tilted operation.

No clear winner is emerging as yet from the competition among different technologies, since trade-offs across construction, installation, and maintenance costs as well as project risk tend to level the playing field. Rather, it is expected that different solutions will prevail on a project-by-project basis due to the variance of site-dependent design conditions, bathymetry above all.

1.2.2 Aerogenerator

The horizontal-axis wind turbine (HAWT), seen in Figure 1.3, which presently monopolises the utility-scale wind industry has been transferred to the offshore and floating sectors with relatively minor adaptations; this however does not necessarily apply to future, optimised floating HAWTs. So far, then, floating wind prototypes simply tended to adopt high turbine design classes (see e.g. [35]) to withstand the loads associated to the enhanced dynamics, with particular concern for the tower whose flexural loading is aggravated. Floating-specific arrangements also concern the rotor control software: this requires at least a modification for the avoidance of negative aerodynamic damping [36], whereas proposed solutions also envisage more advanced control laws for the active mitigation of FWT motion response [37] and fatigue [38].

As anticipated above, a more radical re-designing of the aerogenerator may prove beneficial in floating applications. The vertical-axis wind turbine (VAWT) arrangement, practically abandoned since the 1990s at the utility scale, has reconquered significant interest due to potential benefits related to integrated FWT design [39]. Firstly, the aerodynamic performance of a VAWT tends to improve in skewed flow as pointed out among others by Wang et al. [40] – whilst that of a HAWT [41] is expected to deteriorate[5] – permitting efficient operation at large trim (Figure 1.5). A drastic relaxation of the stability constraint is the related design benefit[6]. Secondly, despite the greater mass per unit power characteristic of VAWT rotors, the turbine's centre of gravity may be significantly lowered by siting the power train at the bottom of the shaft (cf. [43, 44]), thereby reducing the negative contribution to stability represented by $\overline{\mathrm{KG}}$. The same architecture should also allow for easier access to the power take-off equipment compared to a HAWT [45]. Lastly, some analysts underline the benefits of reduced system complexity [43, 45] and upscaling potential [44] of floating VAWTs.

Whether the beneficial features introduced above will suffice to revive large-scale vertical-axis technology will ultimately depend on their combined ability to offset its well-known aerodynamic efficiency limitations, the limited industrial track record available, and potentially adverse characteristics such as the reduced ability to feather the blades in high wind conditions.

[5] Although this effect is better characterised in the literature for yaw misalignment than for vertical skew, see e.g. Boorsma [42].

[6] Provided that the blade airgap remains acceptable and, most crucially, that the turbine structure can accommodate the increased gravitational loading.

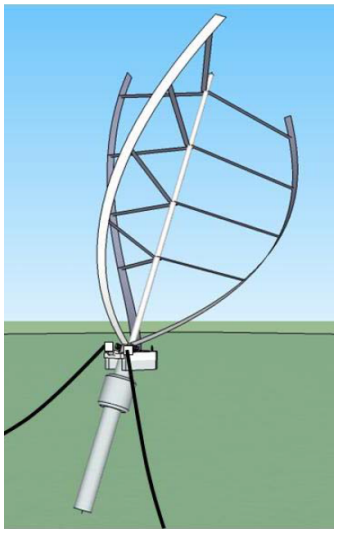

Figure 1.5: Japanese floating vertical-axis wind turbine concept allowing for large inclinations. Reproduced from Akimoto et al. [46].

1.3 Coupled dynamic simulation

According to DNV GL, the first certification body to issue a design standard dedicated to FWT structures [47], "*A key technical barrier to making* [global floating wind industry] *a reality is the ability to carry out a sufficiently accurate fully dynamic analysis, which requires integration of several engineering disciplines.*" [48]. The interfacing of profoundly diverse areas of knowledge such as aerodynamics, offshore hydrodynamics, structural dynamics, rotordynamics, electro-mechanics, control, etc. demanded by this application is challenging the existing engineering practices and calls for an in-depth review of the related design and verification principles. Understanding the interactions between the above areas requires the development of multi-physical simulation tools. Over the last years, the scientific and industrial communities have been developing a range of such tools based on the combination of offshore hydromechanical and wind turbine simulation modules in the time domain.

Platform hydrodynamics are often treated using the linear potential-flow approach combined with the Morison equation. The panel method is a well established way to resolve the potential-flow wave-structure interaction problem, producing a linear diffraction and radiation database in the frequency domain. MIT's WAMIT [49], ANSYS Aqwa [50], and the presently used NEMOH of the Ecole Centrale de Nantes [51] all employ this approach. Their output, a frequency-domain hydrodynamic database, underpins in turn the computation of the wave forces on the structure in the time domain. Loads on small members and around sharp appendices may be added using the Morison approach, which requires calibration. This workflow, typical of present state-of-the-art coupled FWT simulators such as NREL's FAST [52], Principia's DeepLines [53], and the

presently used CALHYPSO of EDF R&D, may also provide a partial reconstruction of nonlinear potential hydrodynamics based on quadratic transfer functions (see for example Philippe et al. [54]). Weakly or fully nonlinear potential-flow models in the time domain, such as that proposed by Dombre [55], may be used to compute the hydrodynamic forces with higher accuracy, albeit still neglecting viscosity. At the high end of physical fidelity, more computationally and labour-intensive Eulerian Navier-Stokes models are being used to predict the hydrodynamic loads on the floating platform [56]. Finally, in order to allow the physically consistent treatment of highly dynamic events such as breaking wave impacts, the adoption of meshless Lagrangian hydrodynamic approaches may be envisioned (see Tomasicchio et al. [57]).

The mechanical behaviour of the moorings is another major component of the system's dynamic response. Mooring lines are slender bodies offering significant compliance, which demands the use of a large-displacement resolution of their kinematics. The inexpensive quasi-static approach based on the catenary equation (see for instance Masciola [58]), neglecting inertia and the hydrodynamic interactions on the lines, is adopted by coupled simulation codes such as FAST and CALHYPSO. This method is known to become inaccurate when highly dynamic simulations and/or deep-water settings are concerned. A more reliable prediction of the mooring loads and also of the feedbacks on the floating system's motions can be obtained including the dynamics of the mooring lines in a time-domain model. This generally implies longitudinal discretisation via a lump-mass, multi-body, or finite-element formulation [59]; in this work the latter option is adopted by exploiting the functionalities of *Code_Aster*, EDF R&D's thermo-mechanical solver [60]. Said methodologies are currently in use in commercial dynamic mooring simulators such as Orcina's OrcaFlex [61], MARIN's aNySIM [62], and Principia's DeepLines [53].

The mechanics of a wind turbine generator, to be coupled to the above described systems, are dominated by aerodynamic excitation. In their simplest form, the aerodynamic forces and moments acting on the rotor may be reduced to a punctual tensor based on the turbine's thrust and torque coefficients, following the approach utilised for instance by Utsunomiya [63]. An exciter routine of this kind is also used in CALHYPSO for the representation of HAWT aerodynamics. Wind turbine aerodynamics have been largely studied with higher fidelity using derivations of Glauert's Blade Element Momentum theory [64], which enables to represent the airflow in a time and space-averaged form; FAST and Simo-Riflex [65], for example, feature libraries of this type. Programs such as FloVAWT [66] and Simo-Riflex-DMS [67] implement the vertical-axis variant of this method, originally developed by Paraschivoiu [68]. This is also the case for CALHYPSO, where the priority on VAWT simulation prompted the development of specific higher-grade aerodynamics. By simultaneously increasing numerical complexity and physical fidelity one may then find the cascade, vortex, and panel methods, all

based on potential-flow, incompressible aerodynamics. Finally, the viscous airflow past the turbine may also be modelled with Navier-Stokes solvers as done for example by Liu et al. [69] using the incompressible hypothesis. The simultaneous, multi-phase representation of the aero and hydrodynamic flows interacting with the FWT system has also been proposed in recent times [70].

Given the multiple physical processes described above and the related loads exerted on a FWT, platform and especially rotor flexibility may need to be included in the analysis depending on the outputs and fidelity demanded by each specific application. The cited engineering-level simulators can often handle aeroelasticity, whilst hydroelasticity is sometimes disregarded due to the relatively high rigidity of conventional floater structures; at the current state of development, this is the case for EDF R&D's CALHYPSO, which can handle a flexible VAWT structure whilst treating the platform as a rigid body.

For a comprehensive review of the current state of the art of coupled FWT simulation, covering different levels of model complexity, the reader may refer to the work of Borg and Collu [71]. The stochastic nature of met-ocean loads and the variety of normal and abnormal operating conditions multiply the load cases to be taken into account for a full analysis, even when a single design is considered. Thus, the mastery of computationally efficient, engineering-level models – and of their limitations – is of paramount importance in the concept evaluation and basic design stages. This type of simulation is at the heart of the research project documented in this manuscript, whose scope is articulated next.

1.4 Scope of work

A compact account of the main focus and physical processes treated in the technical parts of the manuscript is provided in Table 1.1. This allows one to distinguish the main areas of investigation which shape the structure of the EngD: global coupled dynamics, mooring hydromechanics, and rotor aeroelasticity. A detail literature review is organised contextually for each of these areas. Further, the diagram of Figure 1.6 provides a visual account of the relationships across these disciplines in the broader frame of floating wind turbine mechanics.

A top priority in the mechanical analysis of FWTs is the ability to predict the global dynamics (rigid-body motion) of the system in order to understand the structural demand on its components [47, 72]. Wind and wave-induced accelerations are of particular concern, as they tend to dominate the loading of critical system parts such as the tower-top machinery (see the work of Sethuraman et al. [73–76]), providing an important design criterion (cf. Figure 1.4). The combined action of aerodynamic, hydrodynamic, and operating loads determines the complex dynamic response patterns which are the

Table 1.1: Focus of manuscript parts and physical processes represented.

Part	Focus	Hydrodyn.	Aerodyn.	Deformability	Domain	
					frequency	time
2	Global	•	•		•	•
3	Moorings	•		•		•
4	Rotor		•	•	•	

focus of Part 2. In which, both the open-source frequency-domain diffraction and radiation solver NEMOH and EDF R&D's own time-domain offshore dynamics simulator CALHYPSO are used to single out and characterise, for the first time, multi-physical coupling mechanisms inherent in semi-submersible FWTs. As shown in Figure 1.6, both the platform and the turbine are considered as rigid bodies in Part 2 in order to simplify the analysis and focus on specific processes of interest; the wind turbine generator's drive train dynamics and control are also left out of the model.

Detailed FWT subsystem design and qualification cannot rely on global dynamic analysis alone because of the high elasticity and/or compliance of certain components of the floating system. Hence, Part 3 treats the highly nonlinear dynamics of compliant FWT moorings, which can strongly interact with the floater hydromechanics. The large-displacement compliance of catenary mooring lines, the local fluid interaction dominated by viscous effects, and the seabed contact constraint are brought together in *Code_Aster*, EDF R&D's finite-element mechanical analysis software, for the first time. The platform is once again treated as a rigid body, whilst the interaction between the mooring lines and the seabed is simplified as an unilateral contact condition, removing the need to represent soil mechanics (see Figure 1.6). In the presented case study, both coupled and motion-driven time-domain simulations in regular and irregular waves are carried out to benchmark the numerical outputs against published experimental results, with particular focus on the prediction of mooring line tension.

Another highly deformable FWT component requiring close inspection is the rotor, whose vibrations are at the centre of Part 4. The verification of the structural reliability of this subsystem for a range of operating regimes includes the characterisation of its aeroelastic behaviour: modal analysis, using finite structural elements equipped with an internalised representation of the aerodynamic and rotordynamic forces, is used to screen two VAWT prototypes of interest. This type of analysis is decoupled from the floating platform and is carried out in the frequency domain assuming a steady rotational speed. The outputs notably consist in the aeroelastic Campbell diagrams and the associated aerodynamic damping plots, which permit to rule out the onset of aeroelastic instability for a designated operating envelope.

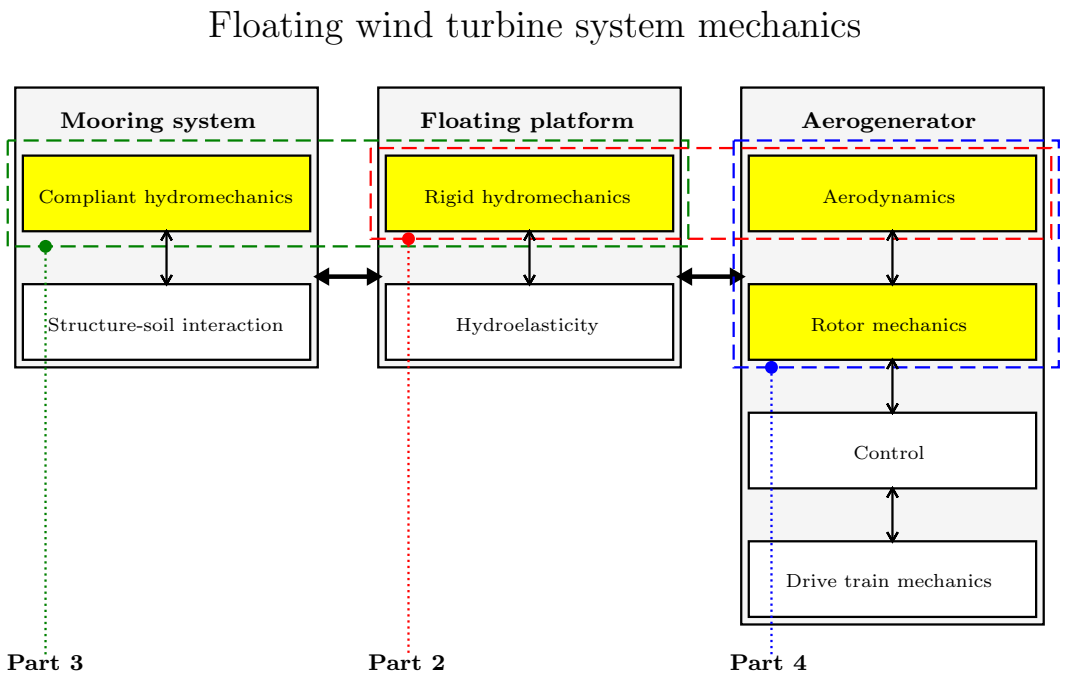

Figure 1.6: Disciplines involved in system-level floating wind turbine mechanics and presently covered areas.

Part 2

Aero-hydromechanical Simulation of Floating Wind Turbine Dynamics

The work carried out in the field of offshore aero-hydromechanical simulation of FWT dynamics is included in this Part. Section 2.1 begins by providing the generalities of the coupled multi-physical behaviour of floating wind turbines, along with an introduction to the key features which spurred the investigations presented. The methods employed by the aero-hydromechanical simulator CALHYPSO to combine and resolve the system dynamics are outlined in Section 2.2. A range of applications is then presented in Section 2.3, which is mainly aimed at characterising a number of aero-hydrodynamic interaction processes. A validation of the coupled model is also included in this Section, which uses existing experimental data as a benchmark. The outcomes of the studies presented are brought together in Section 2.4.
Much of this work has been described in the publications listed in Appendix H; parts of it are also included in the VALEF2 project[1] reports and in EDF R&D's technical documentation [78].

2.1 Introduction

Different from most conventional offshore floating structures, floating wind turbines (FWTs) are relatively small bodies which can exhibit stronger nonlinearities in their dynamic behaviour. They are also designed with the purpose of maximising the aerodynamic interaction related to wind energy extraction, which gives raise to unusually large aerodynamic load to displacement ratios. This may constitute an important source of dynamic coupling, especially as FWT platforms tend to evolve toward more optimised, lightweight solutions.

[1] A collaborative R&D project by *France Energies Marines* for the development, verification, and validation of floating wind turbine design methodologies [77].

Figure 2.1: Artist impression of the GustoMSC tri-floater supporting a 5 MW-class turbine (left), and of an older concept variant superposed to the DSS-21 drilling vessel of the same designer (right). After [81, 82].

The pioneering activities of the EDF Group in the field of floating wind power require active R&D support for the de-risking of current prototyping and industrialisation projects such as the pre-commercial farm development *Provence Grand Large* in the Mediterranean. The proposed technical solutions must be thoroughly analysed to de-risk and to steer these projects and to capitalise on the ongoing experience. More specifically, the mechanical behaviour of FWT concepts is a fundamental subject of investigation, due to the paramount role of the prediction and verification of the system's displacements and accelerations which govern the structural demand and the efficiency of the aerogenerator.
Characterising the mechanical behaviour of a floating wind turbine for design and verification purposes requires the coupling of wind turbine aerodynamics and control with offshore hydromechanics. The understanding of such coupled dynamics under complex met-ocean loading has recently been the driver of a novel generation of coupled offshore dynamic models designed for the requirements of FWT mechanical simulation, such as FAST [52, 65, 79], HAWC2 [65, 80], FloVAWT [66], Simo-Riflex [65, 67], and CALHYPSO of EDF R&D, the software used for a large part of the work presented in this Part.

2.1.1 Semi-submersible floating wind turbines

Semi-submersible, column-stabilised platforms are currently investigated as a FWT substructure solution owing to their low draft and ease of handling. As anticipated in Part 1, they count on widely spaced columns of large waterplane area to insure

the stability necessary to counter wind-induced overturning moment. These columns are generally interconnected by space frame structures or girder pontoons as in the examples of Figure 2.1.
The present study focusses on two semi-submersible FWT designs: the Dutch Tri-floater introduced by [83], which represents an industrially interesting case for its ability to support aerogenerators of relatively large rating compared to its size (see Figure 2.20), and the well-documented DeepCwind-OC4 platform used in combination with a Darreius-troposkein turbine (Figure 2.29), a concept suitable for the study of the aerodynamic damping of FWT motions provided by a vertical-axis aerogenerator.

2.1.2 Small offshore structure hydrodynamics

As of today, the semi-submersible structures considered for wind turbine support are generally of smaller size compared to their conventional offshore counterparts. The displacement of a material-efficient FWT with a capacity of around 5 MW, for example, is around an order of magnitude less than that of a typical drilling semi-submersible [82]. This is visually displayed in Figure 2.1 (right). Whilst future turbine upscaling may change the picture, this consideration prompts to look more closely into small offshore structure dynamics when present technology is concerned.
Compact floating platforms can exhibit increased hydrodynamic complexity when subjected to ocean waves compared to larger bodies; for example it is more likely to come across regimes where hydrodynamic drag plays an important part in excitation, as was observed experimentally on the DeepCwind-OC4 platform by Coulling et al. [84], and explained numerically in Masciola et al. [85]. These phenomena typically affect structures featuring sharp-edged motion control devices, tanks, and pontoons, which accentuate flow separation. Surface proximity effects can also manifest on these appendices when their submergence is limited, such as increased vertical wave loading (conjectured in Philippe et al. [86]) and run-up according to Cermelli and Roddier [87]. As shown by the experimental campaign carried out by Cozijnet al. [88] on a CALM buoy equipped with a skirt, a semi-empirical numerical model implementing linear potential diffraction/radiation and a Reynolds number-independent drag force formulation can satisfactorily (but not comprehensively, as explained in 2.1.3) represent the hydrodynamic forces acting on this type of structure for the calculation of dynamic response. Similar conclusions have been drawn by Aubault et al. [89] whilst comparing numerical and experimental motion results for a compact water-injection platform concept, the predecessor of the WindFloat platform design. An analogous numerical-experimental comparison carried out by Roddier et al. for the engineering design of WindFloat itself broadly confirmed the accuracy of this type of numerical model [16].

2.1.3 Water entrapment plates

Most proposed semi-submersible designs feature water entrapment devices located at the column foot which provide extra added mass, wave damping, and drag, as well as buoyancy far removed from wave excitation. The resulting heave added mass and hydrodynamic inertia in roll and pitch can be very significant, and often reach the same order of magnitude of the FWT's own structural inertias. This effect is fundamental in order to shift natural periods beyond the wave range while preserving sufficient stability and simultaneously limiting floater size.
A brief introduction to water entrapment plate hydrodynamics and the main related modelling challenges is presented next. These are investigated in detail in 2.3.1, leading to the characterisation of their influence on a highly compliant FWT in 2.3.2. Pioneered by Principle Power with the WindFloat prototype, the FWT heave plate appendix consists in a thin reinforced structure installed coaxially below the platform's columns, as visible in Figure 2.2. The dynamic stability provided by the use of heave plates, coupled with the extra static stability insured by a closed-loop active ballasting system, reportedly allowed the WindFloat prototype to adopt conventional aerogenerator technology [90].

Figure 2.2: Detail of a WindFloat prototype column. Photo courtesy of Principle Power.

Modelling water entrapment appendices[2] close to the free surface via linear diffraction and radiation plus a drag model should come with a caveat. As pointed out by Cozijn et al. [88], the radiation-dependent vertical added mass of these structures is suspected to suffer from the irrotational flow hypothesis (i.e. the model fails to take into account the momentum transfer needed to impel fluid rotation around the edges, causing underestimation of the added mass). Another issue consists in the sensitivity of the separation pattern to flow regimes, and in particular to the Keulegan-Carpenter

[2]Here the term 'appendix' refers to a protruding hull component of limited size compared to the platform.

number KC as shown by Tao and Cai [91]. The resulting drag forces which dominate the hydrodynamic damping for this type of platform may be affected by such regime changes, thus requiring appropriate adjustments of the drag coefficient. Lopez-Pavon and Souto-Iglesias have also recently observed that detail features which may seem of secondary importance in the fluid-structure interaction of heave plates, such as stiffeners and edge flaps, may play a significant role in their behaviour [92]. Finally, nonlinearities caused by complex phenomena such as wave decomposition, described by Kojima et al. [93], and breaking over the plates (see Yu et al. [94]) may perturb loading in ways that are not captured by the most common wave-structure interaction models. A more in-depth review of submerged plate hydrodynamics is included in 2.3.1.

2.1.4 Large inclinations

One of the routes to FWT CAPEX reduction is to save on the platform fabrication costs. An immediate consequence is the push for the minimisation of platform mass and hence size, that in turn entails the availability of smaller displacements and waterplane areas which affect the hydrostatic stability. Subsequently, low hydrostatic stability platform solutions are currently being proposed. One option is constituted by the tension-leg platform (TLP) – see for example Zhao et al. [95] – whose restoring capacity to oppose the aerodynamic overturning forces is built into the mooring system. An alternative approach is simply the acceptance of large-angle operation caused by limited stability, leading to the concept of highly compliant FWT technology proposed by NREL [96] and others [97]. This, combined with other technological considerations, has caused a range of tilt-tolerant floating VAWT designs to be spawned (see Borg et al. [44] for a technical discussion and Cahay et al. [43] for an industrial application), which may in turn foster radical innovation feedbacks at the system level, as it happened for the innovative floating axis solution proposed by Akimoto et al. [46, 98, 99]. Although conventional HAWT rotors are known to be tilt-adverse, especially with respect to their aerodynamic efficiency, angles up to $10\,^{\circ}$ are beginning to be considered acceptable as the operational limit for this type of turbine. An example is provided by the materials co-published by the FWT semi-submersible designer GustoMSC [100, 101].

Several widespread assumptions in the simulation of offshore structure dynamics are challenged due to the relatively large angular displacements. First of all, the ubiquitous hydrostatic linearisation may undermine the correct representation of these forces, especially when the geometry around the waterline is complex and/or hull sides are inclined (see for example the WINFLO concept [102]). The classic static representation of the mass matrix in the inertial frame can also cause errors in the computation of inertial reaction forces as large angles make the small displacement assumption invalid. Also, the widespread linear superposition of small rotations may prove inaccurate, an observation that has led to the development of FWT motion solvers by Wang and

Sweetman applying sequential Euler angle changes to represent correctly the nonlinear coupling between motions for a rigid-body [103, 104] and a multi-body system [105, 106]. Finally, in the present study the combination of limited draft, significant inclination, and the presence of hydrodynamically sensitive appendices – typical of semi-submersible FWTs unequipped with active wind load compensation – is shown to cause significant potential for geometric nonlinearity[3] in the diffraction/radiation behaviour of the hull, as detailed in 2.3.1, in addition to the loading regime changes associated with viscous effects (2.3.2).

2.1.5 Dutch Tri-floater experimental campaign

The dynamics of a semi-submersible FWT undergoing large inclinations are experimentally documented in a campaign by Courbois [107], where the Dutch Tri-floater is subjected to coupled wind-and-wave tests. The tests have been carried out within the fresh-water ocean basin of the Ecole Centrale de Nantes at the $1/50^{\text{th}}$ scale, for an equivalent water depth of 250 m. A picture of the experimental equipment used is given in Figure 2.3. The motion outputs of this campaign will be later used for the validation of the present numerical model.

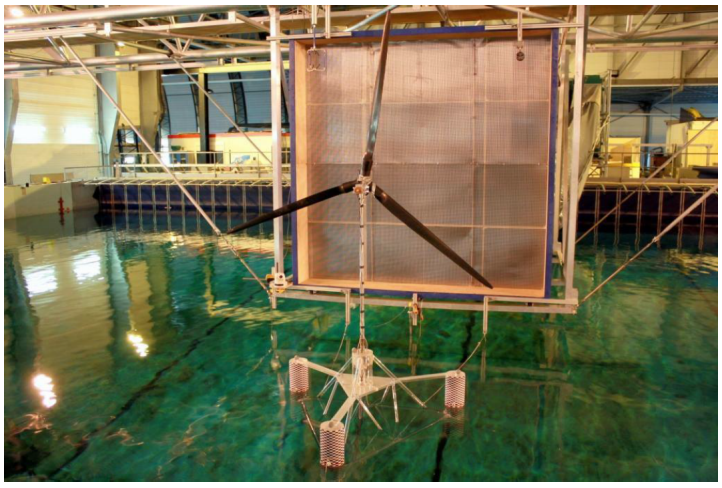

Figure 2.3: Experimental set-up of the Dutch Tri-floater tests. The nozzle of the wind generation apparatus is visible behind the turbine rotor, whilst the wavemakers are seen in the background. Reproduced from Courbois [107].

[3] A manifestation of the breaking of the small-displacement assumption of the linear sea-keeping method.

2.1.5.1 Scaling criteria

Coupled basin testing of FWTs challenges the conventional approaches of offshore engineering, in that the notorious mismatch of the model- and full-scale Reynolds numbers severely affects the ability to represent the full-scale aerodynamic processes in the laboratory whilst preserving the vital geometric similarity and Froude similitude. The approach utilised in Courbois's campaign consists in an heuristic matching of the rotor thrust force at the rated point (reportedly 830 kN at full scale and about 6.6 N at reduced scale), measured at the model shaft, by simultaneous increase of the blade sectional twist and incident wind speed. Active blade pitching is not used during the tests, and the rotor speed is maintained constant by a controlled break and equal to the nominal downscaled value, that is 85 rpm. The resulting mean thrust is hence made to satisfy both the geometric and Froude scaling laws, whilst its dynamic component does not obey any similitude. The incident wind speed used to obtain the nominal thrust is much larger than what would be prescribed by plain geometrical/Froude scaling, specifically around 4.6 m/s in lieu of 1.6 m/s. In these conditions, aerodynamic damping is likely overrepresented in the basin.

2.1.5.2 Model definition

Brought at full scale, the Dutch Tri-floater platform geometry used in the experiments is in almost all aspects identical to the variant here presented into detail in 2.3.1.3. The only discrepancies are the thickness of the water entrapment plates[4], which is down to 0.15 m from 1.00 m, and the operating draft, which is reduced to 10.9 m from the nominal value of 12.0 m. Both differences contribute to a reduction of the platform volume, which is now equal to $\bigtriangledown = 2440\,\mathrm{m}^3$. Motion outputs are provided as displacements of the system's CoM (see Table 2.1) with respect to the fixed orthonormal frame, using optical motion capture equipment. The potential-flow hydrodynamic modelling of thin plates required to represent this platform model prompted the development of the extrapolation approach described in 2.3.4.3.

Intended to represent the NREL 5 MW reference design [108], the experimental turbine consists in a three-bladed rotor using the same profile distribution as in the reference (profiles in geometrical similarity), modified with a radius-dependent increase of twist between 15 ° and 30 °. A thin rigid mast connects the instrumented nacelle to the platform, respecting the nominal hub height over the still-water level (SWL) of 90 m. This height is slightly increased by the operating draft reduction reported above. The full-scale rotor axial inertia is $3.88 \cdot 10^4\,\mathrm{t\,m}^2$.

Table 2.1 provides the aggregate platform and parked turbine mass properties. The small discrepancy between the computed mass and the target onboard mass required

[4] With a constant vertical position of the lower plate surface in the floater frame.

Table 2.1: Full-scale experimental Dutch Tri-floater mass/inertia properties including the turbine. Quantities are expressed with respect to the origin O at the still-water level.

Mass [t]	2428
Vertical position of CoM ($\equiv$ CoG) [m]	22.2
Roll moment of inertia [t m^2]	$5.409 \cdot 10^6$
Pitch moment of inertia [t m^2]	$5.421 \cdot 10^6$
Yaw moment of inertia [t m^2]	$1.753 \cdot 10^6$

to meet the system's operating displacement in fresh water (12 t) is tolerated.
The mooring kit consists of two elastic aerial lines with negligible mass connecting the FWT frontal bracings to the nozzle structure as visible from Figure 2.3. These are slack when the platform sits in the undisturbed equilibrium position, as there are no compensating aft lines. In the presence of a positive transitory (1$^{\text{st}}$ order wave) or constant (wind thrust, wave drift) surge force, these lines become tensioned and are expected to alter the restoring behaviour of the system. Due to lack of data, the likely nonlinearities related to this arrangement cannot be easily replicated in a numerical simulation.

2.1.6 Aerodynamic damping of global motion

One of the investigations included in this Part regards the aerodynamic damping of global motions provided by an operating VAWT (2.3.3). Numerous existing studies address the effects of rotor forces on the coupled dynamic response of horizontal-axis FWTs, where the rotor control strategy is a key variable determining aerodynamic damping of frontal rotor motion (see for instance Jonkman [109]). Unlike horizontal-axis turbines, floating VAWTs have been seldom investigated with respect to global aerodynamic damping in an explicit manner. Remarks on this phenomenon are found for instance in the model-to-model comparison of Borg et al. [110]. The presence of aerodynamic dissipation is observable from the results of the floating VAWT simulations carried out by Wang et al. [111], and further commented in comparison with the aerodynamic damping from a HAWT in [67]. Discussions on the effects of taking into account the relative flow speed in double-multiple streamtube (DMST) modelling, altering the aerodynamics of a Darreius rotor on a moving floating platform, are available in Collu et al. [66] and Borg and Collu [112]. Past work by Merz [113] points out the role of dynamic inflow in relaxing the turbine-flow interaction when a DMST model is used, thereby potentially increasing the strength of aerodynamic damping for pure horizontal motion.

2.2 Methodology

Next the building blocks of the methodology underpinning the simulations of 2.3 are presented. The terms entering the coupled dynamic equations of motion (EoM) are punctually described, along with the theories enabling their calculation. Close-ups are also provided on the unconventional (2.3.2.1 and 2.3.4.3) or relatively complex (2.2.3) hydrodynamic and aerodynamic modelling strategies adopted.

2.2.1 Coupled rigid-body dynamics

The program CALHYPSO (*CALcul HYdrodynamique Pour les Structures Offshore*) developed at EDF R&D incorporates the aerodynamic, hydrostatic, hydrodynamic, structural inertial, and mooring forces exerted on a FWT to determine its dynamic behaviour in the time domain. Whilst HAWT aerodynamics are here represented via a reactive thrust module (2.2.2), CALHYPSO features a fully-fledged double-multiple streamtube representation of VAWT aerodynamics (2.2.3). The offshore hydromechanical part uses the common time-domain sea-keeping approach and a linearised or quasi-static moorings model. This simulation tool has been both verified and validated in the past in the context of EDF's joint industrial projects, whilst a more recent experimental validation of both the solver and the methodologies proposed here is included in 2.3.4. FWT dynamics are implemented using a six degree of freedom (DoF), rigid body assumption with the reference point O generally placed at the centre of the undisplaced structure's waterplane area. Although the choice of this point is entirely arbitrary for the representation of rigid-body dynamics, when floating structures are concerned the above choice of O allows to adopt the widespread metacentric representation of hydrostatic stiffness without incurring in transportation errors. Based on Newton's second law of motion, the EoM of the system are written in the inertial system of reference centred in O in the form:

$$\begin{aligned}(\mathbf{M}+\mathbf{A}^{\infty})\ddot{\mathbf{x}}(t) = \mathbf{f}^{\mathrm{h}}(t)+\mathbf{f}^{\mathrm{e}}(t)+\mathbf{f}^{\mathrm{r}}(t)+\mathbf{f}^{\mathrm{v}}(t)+\\ \mathbf{f}^{\mathrm{i}}(t)+\mathbf{f}^{\mathrm{a}}(t)+\mathbf{f}^{\mathrm{g}}(t)+\mathbf{f}^{\mathrm{m}}(t)\,,\end{aligned} \tag{2.1}$$

where $\mathbf{M}$ denotes the rigid body's generalised inertia matrix, $\mathbf{A}^{\infty}$ the infinite-frequency added inertia matrix, and $\ddot{\mathbf{x}}$ the acceleration vector. The right-hand side member consists of the summation of the instantaneous hydrostatic forces $\mathbf{f}^{\mathrm{h}}$, the hydrodynamic excitation forces $\mathbf{f}^{\mathrm{e}}$, the wave radiation forces $\mathbf{f}^{\mathrm{r}}$, the viscous hydrodynamic forces $\mathbf{f}^{\mathrm{v}}$, the slender-member inertial hydrodynamic forces $\mathbf{f}^{\mathrm{i}}$, the aerodynamic forces $\mathbf{f}^{\mathrm{a}}$, the rotor gyroscopic forces $\mathbf{f}^{\mathrm{g}}$, and the mooring restoring forces $\mathbf{f}^{\mathrm{m}}$. These terms will be described in the next paragraphs, starting from the modelling of the forces on the aerogenerator and then moving on to the hydromechanical parts. This equation allows to calculate $\ddot{\mathbf{x}}$ at each time step, then the time domain motion is obtained by numerical integration of

the acceleration vector. The preferred integration scheme is here the Newmark implicit method, which is applied in acceleration-form (known as A-form, see Appendix B).
It should be noted that writing the rigid-body EoM of Equation 2.1 based on the linearisation of rotations in the inertial system of reference, denoted R in the scheme of Figure 2.4, is conditional to the small-displacement assumption. As shown in this study, floating wind turbines may make this assumption invalid when wind forces induce large rotations. This limitation is treated in 2.3.2.1 by redefining the linear tensors describing the system's mechanics about the inclined state. An alternative modelling option consists in the choice of the frame bound to the rigid body (R' in the figure) for the resolution of Newton's second law of motion, provided that the external forces be re-expressed in its own coordinates at each time step.

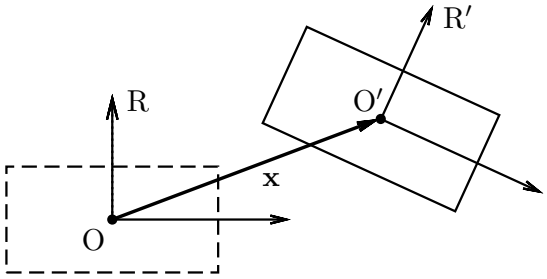

Figure 2.4: Inertial and bound systems of reference R and R'. The solid form represents the rigid body in its instantaneous position while the dashed form its initial undisturbed configuration.

2.2.2 Reduced aerodynamic model for horizontal-axis wind turbines

The routine used for the computation of HAWT aerodynamics is a simple coupled exciter module based on aggregated force coefficients. The aerodynamic forces acting on the rotor and the tower are both assimilated to a thrust-type force, applied punctually at the rotor's and tower's respective centres of thrust. The aerodynamic torque exerted on the rotor is also computed. Given a steady operating condition characterised by a thrust coefficient c_T and a torque coefficient c_Q, the thrust and torque on the rotor are computed using a modified version of the coupled formulation used by Utsunomiya et al. [63]:

$$T_\mathrm{r} = \frac{1}{2} c_T \rho_\mathrm{a} A |U-u|(U-u)\cos\vartheta\,, \tag{2.2}$$

$$Q_\mathrm{r} = \frac{1}{2} c_Q \rho_\mathrm{a} A R |U-u|(U-u)\cos\vartheta\,, \tag{2.3}$$

where ρ_a denotes the air density, A the rotor swept area, R the rotor radius, U the incident wind speed at hub height, u the component of the hub velocity in line with

the incident wind speed, and ϑ the instantaneous leeward inclination of the rotor due to platform motions. This coefficient-based reactive model assumes that blade pitch does not adjust to the aerodynamic fluctuations due to the motions of the FWT. Such set-up loosely corresponds to an idealised implementation of a known control option for floating HAWTs where the frequency of the controller is deliberately moved below that of FWT motions, in order to avoid the appearance of negative damping (see Larsen and Hanson [36]). The thrust T_r is applied horizontally in the direction of the incident wind and its moments are calculated with respect to the EoM reference point using the updated position of the hub. Q_r is also applied as a horizontal torque vector in the wind direction (it is assumed that the rotor is perfectly yawed into the wind at all times).
The use of a coefficient-based model ensures that the rotor's aerodynamic excitation tensor matches a prescribed (equilibrium) operating point, based on the specifications supplied by the turbine designer. Apart from the averaging of rotor forces and the absence of the effects of turbine control, an important limitation of such models consists in the combination of motion-induced speed with the free-stream wind speed before induction, which is larger than the real-world inflow velocity in the vicinity of the rotor. This, along with the absence of a feedback mechanism relating the inflow speed to the fluctuations of T_r and Q_r, causes an overestimation of the aerodynamic forces' variance in presence of windward/leeward motion which is particularly significant at low frequency, when in reality the inflow has sufficient time to react[5]. An example is given in Figure 2.5, where the thrust component in the x direction for a rigid NREL 5 MW rotor oscillating in the direction of the incident wind is shown as predicted by the FAST software by NREL[6] and by the present simplified model.
The incident wind speed and operating parameters of the turbine are set at the rated point and a constant wind profile is used. The Figure shows how the coefficient-based model provides the correct average thrust and a good approximation of the shape and phasing of its evolution over time, but produces a significantly larger variance than the more sophisticated Blade Element Momentum theory.
Finally, the thrust exerted on the tower is also computed with Equation 2.2, using $c_T = c_D$, the drag coefficient for a cylindrical section. In this case A denotes the tower's projected area and u the component of the motion-induced velocity of the centre of thrust in the direction of the incident wind. The set of generalised aerodynamic forces resulting from the above model are summed and included in the term denoted $\mathbf{f}^\mathrm{a}$.

[5] A useful discussion of inflow reactive features when using the BEMT for floating VAWT modelling is available in a study by Merz [113].

[6] FAST v.8.08, using dynamic inflow. The rotor speed and blade pitch are fixed. Surge motion is obtained with the application of a harmonic horizontal force as proposed in the NREL forum [114].

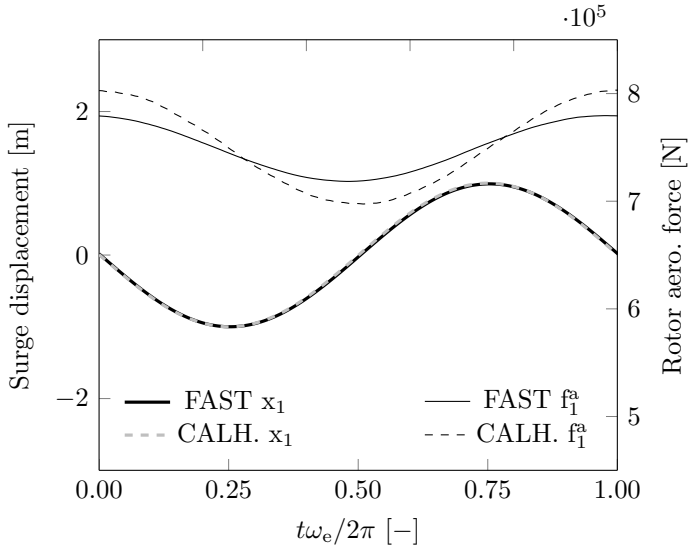

Figure 2.5: Forced oscillation in the direction of wind (surge) of an operating NREL 5 MW rotor, for an excitation frequency of $\omega_e = 0.40\,\mathrm{rad/s}$.

2.2.3 Double-multiple streamtube model for vertical-axis wind turbines

CALHYPSO includes an option enabling the dynamic linkage to a VAWT aerodynamics resolution routine, which is documented in an internal EDF note [115]. The representation of the aerodynamic forces is based on Paraschivoiu's double-multiple streamtube (DMST) method [68], which utilises Blade Element theory in combination with a two-stage momentum loss formulation[7]. The inflow and wake aerodynamics considered by this model are highly simplified in that velocity is considered in space- and time-averaged form. The airflow is described by discretising the in and outflow over the swept area of the rotor with an array of independent control volumes called streamtubes (see Figure 2.6). By definition, the flow rate is constant along each streamtube, and the flow speed is assumed homogeneous at any cross section.

Let ρ_a be the incompressible fluid's density, $\tilde{s}$ the longitudinal streamtube coordinate with the origin located at the turbine's axis, negative upstream and positive downstream, $A = A(\tilde{s})$ the streamtube's sectional area, and $U = U(\tilde{s})$ the flow speed, the conservation of mass may be written as

$$\rho_a A(-\infty)U(-\infty) = \rho_a A(\tilde{s})U(\tilde{s}) = \rho_a A(+\infty)U(+\infty) \tag{2.4}$$

for the classic single tube. It appears clear for the above Equation that the (gradual) flow speed decrease in the downstream direction associated to energy extraction must be

[7] This is the VAWT declination of the classic blade element momentum theory, which was originally proposed by Glauert [64] for propeller modelling.

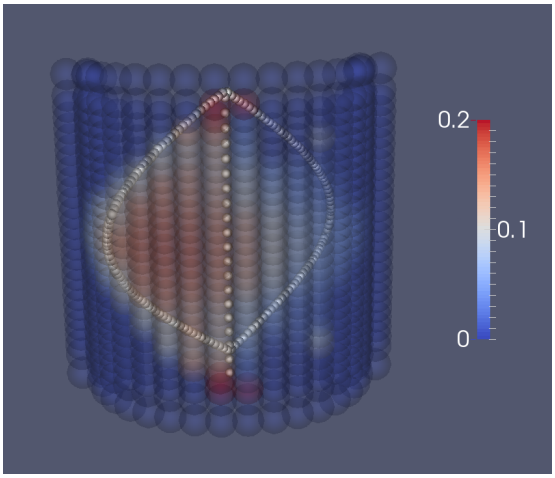

Figure 2.6: Streamtube distribution over a Darreius rotor operating at rated conditions in homogeneous wind. The colour of the point sprites provides the steady-state induction factor at the upwind actuator surface.

accompanied by streamtube expansion, i.e. an increase in sectional area. The pressure in the streamtube is related to flow speed through Bernoulli's steady equation, plus a pressure drop concentrated on the actuator surface.

When the DMST method is used, the tandem configuration required to model the upwind and downwind blade sweeps is implemented by placing two streamtubes in series, communicating through an intermediate flow speed U_{int} which roughly represents the mean axial speed found centrally inside the rotor, as shown in Figure 2.7. Neglecting turbine-scale flow expansion allows to equate the global momentum flux to the forces related to the pressure drops Δp using

$$\begin{cases} \rho_{\text{a}} S V_1 \left[U_{\text{up}} - U_{\text{int}} \right] = \Delta p_1 S \\ \rho_{\text{a}} S V_2 \left[U_{\text{int}} - U_{\text{down}} \right] = \Delta p_2 S \end{cases} , \tag{2.5}$$

where S is any streamtube's constant cross-sectional area at the rotor, which is imposed by the user's discretisation of the frontal area. The far upstream wind speed U_{up} is imposed, whilst the far upstream flow speed U_{down} is unknown.

The local axial speed at the actuator surfaces V is defined by the unknown axial induction factors a and a', such as $V_1 = U_{\text{up}} (1 - a)$, $V_2 = U_{\text{int}} (1 - a')$. These also determine the remaining elements in the left member of Equations 2.5: from the application of the actuator surface theory on the upwind surface we derive $U_{\text{int}} = U_{\text{up}} (1 - 2a)$; the same theory applied to the downstream tube yields $U_{\text{down}} = U_{\text{int}} (1 - 2a')$. Substituting

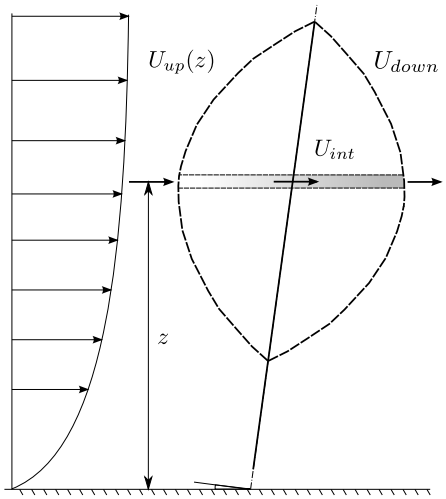

Figure 2.7: Sketch of streamtube with tilted operation.

these terms in Equations 2.5 provides

$$\begin{cases} 2\rho_a S U_{up}^2 a(1-a) = \Delta p_1 S = \overline{F_1} \\ 2\rho_a S U_{up}^2 a'(1-a')(1-2a)^2 = \Delta p_2 S = \overline{F_2} \end{cases} . \tag{2.6}$$

As shown in the above Equations, for each of the two streamtubes in the tandem the pressure drop force is equal to $\overline{F}$, the axial force associated to the blade passages, averaged over one rotor revolution. This is computed via the Blade Element theory using the relative airspeed of the blade sections in their own sectional plane (the spanwise component is disregarded), which in turn depends from the induction factors. An iterative procedure is therefore required to resolve Equation 2.6 at each time step. Within the Blade Element portion of the model, the instantaneous angle of attack and Reynolds number are used to derive the instantaneous lift and drag coefficients, and hence the corresponding forces. For this sake, this library relies on empirical lift and drag coefficient curves stored in look-up tables.

2.2.3.1 Dynamic stall

The blade sections of a MW-scale VAWT operating at mid to low tip-speed ratio (below a value of about 3) undergo relatively rapid and large changes in the local angles of attack, which may cyclically exceed the stall limit of the concerned profiles. Flow separation and reattachment on an airfoil are dynamic processes which require a finite time for their establishment and cause the quasi-steady blade element method to produce inaccurate forces in the stall region when this is crossed rapidly. This is the reason why BEMT software usually employ the steady lift and drag coefficient curves in combination with a dynamic stall model, which uses both the angle of attack and its

derivatives to estimate the instantaneous aerodynamic coefficients.
Dynamic stall is here implemented using the Gormont model [116], originally developed for the representation of unsteady aerodynamics on helicopter rotors, which empirically reproduces the hysteresis cycle characteristic of dynamic stall. Due to the low tip-speed ratio (TSR) regimes characteristic of VAWT operation and the associated large maximal angles of attack the Gormont theory requires correction. The EDF model implements Berg's method [117] with respect to this need, which operates by interpolation between the quasi-steady and unsteady aerodynamic formulations. The interpolation is governed by a calibrating coefficient, which was fixed on the basis of an experimental campaign carried out by a Vertiwind project partner.

2.2.3.2 Adaptation to the floating context

The application of DMST theory to floating turbines is an active subject of research. In principle, it requires at least the inclusion of the local wind direction and velocity perturbations caused by six-DoF motion in the numerical model. Wind skew, the first phenomenon, has been the object of past studies in the context of rooftop [118–120] and floating [40] wind power. In the present model, this is treated by anchoring the streamtubes to the mean free-stream speed frame, while the instantaneous position of the blade elements is continuously updated according to the combination of rotor revolution and platform motion, as displayed in Figure 2.7. This set-up is essential to preserve a correct physical representation of the flow when the rotor undergoes a finite inclination. The second effect, the relative velocity perturbation induced by the platform motions, is taken into account by updating the blade elements' speed at all time steps following the system's 6-DoF motion and combining such speed with the tangential (revolution) speed and the flow speed vectors. The orientation of the blade elements in the fixed frame, required for the calculation of the sectional component of the relative airflow, is constantly updated.
The modular nature of the DMST routine permits to couple it to the global dynamic solver in the form shown in Figure 2.8. It has been verified that the large difference between the timescale of the aerodynamic processes involved and the typical time steps δt required by the global dynamic simulation (in the order of 10^{-1} s at the most) allows to avoid iterating the process of Figure 2.8 at the single time steps without compromising accuracy.
An operating FWT rotor undergoing large motions with respect to its own developed streamtube set may also experience unsteady effects such as exposure to spatially varying induction (frontal motion) and momentary interactions with the shear zone at the peripheral streamtube boundaries (lateral motion). Accounting for these processes should be object of further research.

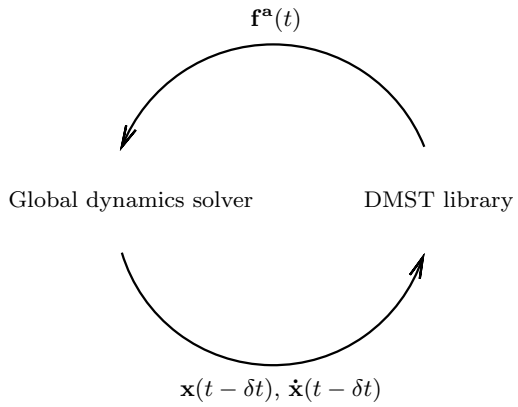

Figure 2.8: Information exchange between the global motion and double-multiple streamtube routines at the time step taken from $t - \delta t$ to t.

2.2.3.3 Other corrections and limitations

The tower wake is modelled via a downstream speed deficit formulation. A tip loss formulation is available in the library, albeit not used in the Darreius turbine case study considered in this manuscript. Not represented here are rotor deformability and dynamic inflow (see Hansen et al. [121] for a comprehensive review of the aerodynamic processes involved in wind turbine operation and their modelling). Dynamic inflow is a process of particular importance when trying to assess global aerodynamic damping, as it dictates the reactive behaviour of the flow as a whole in presence of a perturbation, increasing the damping by a latency in flow adjustment [113]. Streamtube expansion at the rotor scale [68] along with the associated 3D effects [115] and local flow curvature [122] are also not considered, although the influence of these effects on floating VAWT mechanics has been found to be limited by Borg et al. [123].

The DMST theory is known for its reliability in the mid TSR region for low-solidity rotors [44, 68], but its accuracy in representing the rotor aerodynamic interaction is generally constrained there by different limitations. The momentum Equation 2.6 gradually loses significance at very high (> 6) TSR, as stressed by Paraschivoiu [68] and Islam et al. [124]. Due to the presented modelling hypotheses, complex flow features such as 3D structures and wake vorticity cannot be represented with this model. This is expected to become problematic for high-solidity rotors and/or at low TSR. The results of 2D RANS (Reynolds-averaged Navier–Stokes) modelling carried out at EDF R&D suggests that the effects of the eddies shed with the upwind blade passage become significant in the momentum balance of the downwind sweep below TSR ≈ 2 for the type of turbine studied, translating into decreasing accuracy of the DMST theory at lower TSR (cf. [125]). This limitation should be kept in mind with special attention when evaluating the aeromechanical loading outputs at the cut-out point, which typically lies around or below this TSR for multi MW-scale VAWTs.

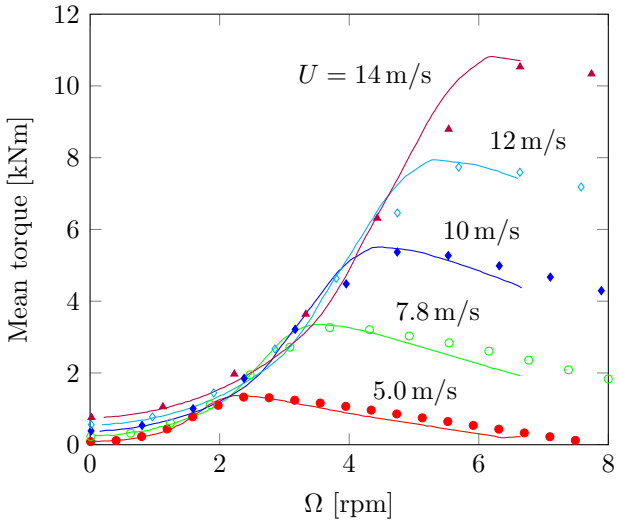

Figure 2.9: Verification of the output torque of the 5 MW Darreius turbine. Dots represent the outputs of CALHYPSO and lines those of the comparable model Simo-Riflex-DMS, digitised from Wang et al. [111].

2.2.3.4 Verification

The model has been successfully verified by EDF for a 2 MW-class helical VAWT (the same shown in Figure 4.15) against the outputs of independently developed, comparable software in the course of the Vertiwind R&D programme. Both the power output (hence the integral torque) and the blade forces showed satisfactory agreement with the alternative simulations [115]. In the present context, a code-to-code verification was carried out using the Darreius rotor concept object of the case study of 2.3.3 in bottom-fixed configuration. Figure 2.9 shows a comparison with published results obtained with a comparable, validated model exhibiting good agreement.

2.2.4 Rotor gyroscopic forces

Past studies by Philippe et al., Blusseau and Patel, and Akimoto et al. revealed the importance of gyroscopic coupling in floating wind turbine dynamics [99, 126, 127]. An oscillating structure bearing a rotor revolving at constant speed receives a gyroscopic reaction moment $\mathbf{q}^{\mathrm{g}}$ that can be written using the d'Alembert principle [128],

$$\mathbf{q}^{\mathrm{g}}(t) = -I_{\mathrm{r}}\Omega\boldsymbol{\Gamma}(t) \times \mathbf{i}^{\mathrm{r}}(t)\,. \tag{2.7}$$

In the above equation I_{r} represents the axial inertia of the rotor, Ω its rotational speed and $\mathbf{i}^{\mathrm{r}}$ the associated unit vector, whilst $\boldsymbol{\Gamma} = (\dot{\mathrm{x}}_4, \dot{\mathrm{x}}_5, \dot{\mathrm{x}}_6)$ denotes the structure's rotational speed vector. The gyroscopic term included in Equation 2.1 is then written

as

$$\mathbf{f}^{\mathrm{g}} = (0, 0, 0, \mathrm{q}_1^{\mathrm{g}}, \mathrm{q}_2^{\mathrm{g}}, \mathrm{q}_3^{\mathrm{g}})\,. \tag{2.8}$$

This type of reactive force becomes prevalent when the studied turbine disposes of high operating momentum, that is when rotor inertia (e.g. in Blusseau and Patel's study [127]) and/or rotational speed is large.

2.2.5 Hydrostatic forces

The hydrostatic force is computed using the conventional sea-keeping linearisation:

$$\mathbf{f}^{\mathrm{h}}(t) = -\mathbf{K}^{\mathrm{h}}\,\mathbf{x}(t)\,. \tag{2.9}$$

By assigning a seawater density ρ_{w} and calculating the waterplane area A_{w}, the third diagonal hydrostatic stiffness coefficient is obtained as $\mathrm{K}_{33}^{\mathrm{h}} = \rho_{\mathrm{w}} g A_{\mathrm{w}}$. By denoting the displacement $\Delta = \rho_{\mathrm{w}} g \bigtriangledown$, where $\bigtriangledown$ is the hull volume, and the transverse and longitudinal metacentric heights over the CoG respectively $\overline{\mathrm{GM}}_{\mathrm{T}}$ and $\overline{\mathrm{GM}}_{\mathrm{L}}$, the roll and pitch hydrostatic stiffness coefficients are written as $\mathrm{K}_{44}^{\mathrm{h}} = \Delta\,\overline{\mathrm{GM}}_{\mathrm{T}}$ and $\mathrm{K}_{55}^{\mathrm{h}} = \Delta\,\overline{\mathrm{GM}}_{\mathrm{L}}$. For each of these, $\overline{\mathrm{GM}} = \overline{\mathrm{KB}} + \overline{\mathrm{BM}} - \overline{\mathrm{KG}}$ (cf. Equation 1.1), using the transverse metacentric height $\overline{\mathrm{BM}} = \overline{\mathrm{BM}}_{\mathrm{T}}$ for roll and the longitudinal metacentric height $\overline{\mathrm{BM}} = \overline{\mathrm{BM}}_{\mathrm{L}}$ for pitch. The remaining entries of the $\mathbf{K}^{\mathrm{h}}$ matrix are nil for the types of structure studied.

2.2.6 Hydrodynamic forces

As is frequently done in floating structure dynamic modelling, hydrodynamic wave forces are calculated via a superposition of inertial and viscous components. The conventional classification used for the evaluation of wave forces over a structure decomposes the hull into small and large substructures (see for example Sarpkaya and Isaacson [129]). For a FWT semi-submersible platform, this typically distinguishes a set of large columns from the slender interconnecting bracings (see for instance Figure 2.16). The former are dominated by inertial wave forces – with significant diffraction at low wave periods and additional drag around sharp edges – whilst the latter are generally drag-dominated. The two corresponding hydrodynamic regimes for a cylindrically shaped structure are marked in Figure 2.10, where the governing parameters are the cylinder diameter-to-wavelength ratio D/λ and the Keulegan-Carpenter number defined by $\mathrm{KC} = U_{\mathrm{m}} T/D$. Here U_{m} represents the maximum flow velocity and T the period characterising the unsteady flow. By assuming that this flow is associated to a deep-water harmonic wave propagating across the cylinder, and that fluid-structure interaction happens in the vicinity of the free surface, $\mathrm{KC} \approx 2\pi\tilde{a}/D$ with $\tilde{a}$ denoting the wave amplitude.

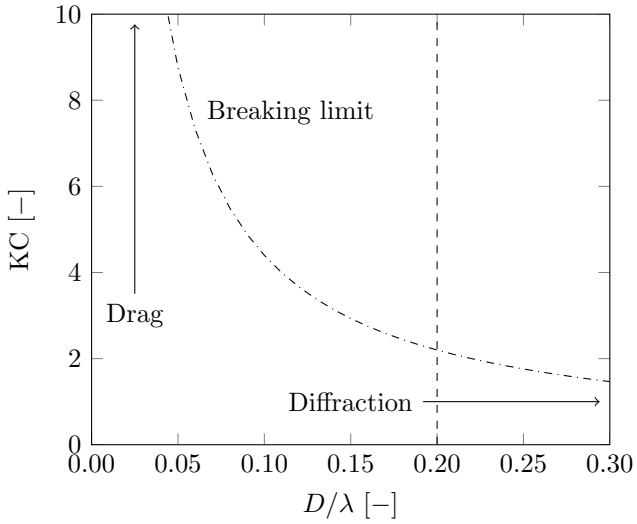

Figure 2.10: Wave loading regimes characterised by the dominance of drag and that of inertia/diffraction. Water depth = 100 m.

The inertial wave forces on the large members are computed by NEMOH, a potential-flow, open-source linear diffraction and radiation solver developed by the Ecole Centrale de Nantes [51], and imported within CALHYPSO in the form of a frequency-domain hydrodynamic data base[8]. This is used in turn to recreate, in the time domain, the incident wave excitation vector $\mathbf{f}^{\mathrm{e}}$ and the reactive force associated to wave radiation $\mathbf{f}^{\mathrm{r}}$ in the form reported next.
The j^{th} element of the wave excitation vector is defined for an N-component, bi-dimensional wave train of incidence θ as

$$\begin{aligned} \mathrm{f}_j^{\mathrm{e}}(t) = \sum_{n=1}^{N} \Psi_{jn} \tilde{a}_n \cos(-\omega_n t + k_n \bar{x}(t) \cos\theta + \\ + k_n \bar{y}(t) \sin\theta + \Phi_{jn} + \phi_n) \,, \end{aligned} \tag{2.10}$$

where Ψ_{jn} and Φ_{jn} are the amplitude and phase of the n^{th} excitation harmonic in the j^{th} DoF, $\tilde{a}_n$ the amplitude of the corresponding spectral component (or simply the incident wave amplitude if $N = 1$), ω_n and k_n the wave component's frequency and number which are bound by the linear wave dispersion relation, $(\bar{x}, \bar{y})$ the structure's mean horizontal offset, and ϕ_n a randomly generated phase ($\phi_n = 0$ if $N = 1$).

[8] NEMOH uses the widespread boundary-element formulation to obtain appropriate harmonic solutions of the unsteady potential-flow problem associated to progressive gravity waves. A set of 3D panels discretises the body's wetted surface, whilst the remaining boundary conditions are imposed analytically. This popular methodology has been documented in numerous past works, for example in [130–132] in relation to the analogous software Aquaplus.

The radiation force vector $\mathbf{f}^{\mathrm{r}}$ is included using the linear impulsive model by Cummins [133] via the convolution integral

$$\mathbf{f}^{\mathrm{r}}(t) = -\int_{t-T_{\mathrm{c}}}^{t} \tilde{\mathbf{K}}(t-\tau)\dot{\mathbf{x}}(\tau)\mathrm{d}\tau\,, \tag{2.11}$$

where T_{c} is the convolution window length and $\tilde{\mathbf{K}}$ the convolution kernel, which is derived from the frequency-dependent radiation damping matrix with Ogilvie's procedure [134].

The viscous forces are computed by discretising the hull into segments and evaluating the quadratic drag forces acting on each with the Morison formulation [135]. If deemed necessary, this also allows to model the forces acting on slender elements based on the Froude-Krylov pressure field and the relative flow-structure acceleration. Equation 2.12 provides the transverse (or normal) force F^{n} per unit length l on a slender cylinder with diameter D according to Morison:

$$\frac{dF^{\mathrm{n}}}{dl} = \frac{1}{2}\rho_{\mathrm{w}} c_{\mathrm{d}}^{\mathrm{n}} D(v^{\mathrm{n}} - \dot{x}^{\mathrm{n}})|v^{\mathrm{n}} - \dot{x}^{\mathrm{n}}| + \rho_{\mathrm{w}}(1 + c_{\mathrm{a}}^{\mathrm{n}})\frac{\pi}{4}D^2\frac{\partial v^{\mathrm{n}}}{\partial t} - \rho_{\mathrm{w}} c_{\mathrm{a}}^{\mathrm{n}}\frac{\pi}{4}D^2\ddot{x}^{\mathrm{n}}\,, \tag{2.12}$$

denoting the component of the undisturbed flow velocity normal to the cylinder's axis with v^{n} and the normal component of the structure's local speed and acceleration with $\dot{x}^{\mathrm{n}}$ and $\ddot{x}^{\mathrm{n}}$. The parameters $c_{\mathrm{d}}^{\mathrm{n}}$ and $c_{\mathrm{a}}^{\mathrm{n}}$ represent the normal-flow drag and added mass coefficients respectively.

The axial and transverse components of the local relative flow are hence derived from both the incident wave kinematics and the structure's motion. Adopting axial and normal-flow coefficients, dependent on element geometry, allows to calculate the corresponding components of the hydrodynamic force. In the studies presented, the transverse Morison coefficients of all cylindrical sections are assigned based on a (KC, β)[9] pairing for each member, representative of an average wave regime, using the experimental data provided by Molin [136]. This procedure is adaptable to both full and reduced-scale FWT simulations. The hull subcomponents which are already represented in the potential hydrodynamic part of the model are loaded with drag only.

Using Equation 2.13, axial drag is applied exclusively on the heave plates and tanks in integral form and proportionally to A, the transverse area of the appendix:

$$F^{\mathrm{a}} = \frac{1}{2}\rho_{\mathrm{w}} c_{\mathrm{d}}^{\mathrm{a}} A(v^{\mathrm{a}} - \dot{x}^{\mathrm{a}})|v^{\mathrm{a}} - \dot{a}^{\mathrm{a}}|\,. \tag{2.13}$$

The axial component of the incident wave velocity field and of the local structure motion are used here, denoted by a superscript 'a'. The axial drag coefficient $c_{\mathrm{d}}^{\mathrm{a}}$ is

[9] For this type of problem, the Stokes parameter is defined by $\beta = D^2/\nu T = \mathrm{Re}/\mathrm{KC}$, where Re denotes the Reynolds number, and ν the kinematic viscosity of the fluid.

assigned based on Robertson et al. [137] and Philippe et al. [86], where appropriate values are derived by calibration of numerical simulations against basin test results. Scale effects are disregarded for this particular coefficient: in a first approximation, this approach may be justified by the presence of sharp edges governing flow separation, thereby reducing the drag forces' dependence from the Reynolds number.
The local drag forces are integrated over the hull to form the viscous force vector $\mathbf{f}^{\mathrm{v}}$ at every time step, whilst the inertial fluid-structure interaction forces over the slender members are integrated and included in the term $\mathbf{f}^{\mathrm{i}}$.
This description of floating body hydrodynamics is subjected to the small-displacement assumption. A phenomenon known as geometric nonlinearity may occur when motions become sufficiently large, which makes the linearisation of hyrdodynamics inaccurate using the classic sea-keeping procedure. FWT concepts which are sufficiently prone to inclination may incur in this problem, which will be later addressed with a specific methodological adjustment (2.3.1.3, 2.3.2.1).

2.2.7 Mooring forces

CALHYPSO includes the capability for a multi-segment, quasi-static representation of catenary moorings and their forces (a similar model is described by Masciola [58]. However, mooring restoring forces are represented in this Part with a linearised model employing the stiffness matrix $\mathbf{K}^{\mathrm{m}}$,

$$\mathbf{f}^{\mathrm{m}}(t) = -\mathbf{K}^{\mathrm{m}}\,\mathbf{x}(t)\,, \tag{2.14}$$

in order not to incur offset-dependent mooring stiffness nonlinearity and response bifurcation.
Equation 2.14 does not account for the undisturbed mooring (weight) force, which is implicitly included in the model set-up by introducing a lump weight at the fairleads in the weight count, which determines the system's aggregate gravitational properties: displacement and centre of gravity (CoG) location. These are equal in turn to the overall weight force and the weighted integral of the position of the elementary gravity forces over the body. The presence of the mooring system is disregarded when computing the mechanical inertia of the FWT. This requires to distinguish the CoG from the inertial centre of mass of the system, CoM, which is obtained as the weighted integral of the position of the elementary masses, hence excluding the moorings.

2.3 Applications

This Section presents four applications of the model described herein, related to the investigation of aero-hydrodynamic coupling effects and the validation of the proposed methodology. The potential flow method is used in 2.3.1 in a set of sensitivity studies to provide a grounding for the interpretation of the heave plate excursion effect, which is related to large wind-induced inclination of highly compliant semi-submersible platforms. The following study of 2.3.2 employs the coupled aero-hydromechanical model to identify the large-inclination effects on the dynamic response of a HAWT-type FWT. The focus is moved upon vertical-axis turbine technology in 2.3.3, where the coupled model is used for the characterisation of the aerodynamic damping of pitch motion for different operating conditions of the aerogenerator. Finally, an experimental validation of the model is included in 2.3.4.

2.3.1 Heave plate excursion and platform hydrodynamics

The focus of this study is the effect of varying heave plate submergence on the diffraction and radiation loading of a semi-submersible FWT platform. A review of the submerged plate problem is first presented in 2.3.1.1, followed by two applied cases.
Fluid-structure interaction is represented under the linear potential-flow hypothesis, hence neglecting all viscous effects and holding only for small wave amplitude and slope. Frequency-domain wave forces and hydrodynamic coefficients are obtained numerically via NEMOH (see 2.2.6). In 2.3.1.2 a surface-piercing column equipped with a bottom plate is analysed at different drafts. It follows the analysis of a Dutch Tri-floater variant (2.3.1.3) at multiple trim angles, with rotations occurring about the upright centre of waterplane. This is a floating platform's static pivoting centre, assumed that it behaves like a perfect vertical-walled (Scribanti) buoyant (see for example Journée and Massie [138]).

2.3.1.1 Review of submerged horizontal plate problem

Offshore oil & gas structure researchers have in the past investigated water entrapment device behaviour for motion control of deep draft floating facilities. Studies have been made available by Lake, Thiagarajan, et al. which look at bottom plate forces [139, 140]; local flow separation in the same context is at the focus of works by Tao et al. [91, 141]. None of these addresses the alteration of the diffraction/radiation problem of a plate of varying submergence. Underwater horizontal plates have also been extensively studied in the domain of coastal engineering; a general account of the material published up to 2002 is given by Yu [142]. Large flat structures are regarded as a potential breakwater solution exploiting fluid-fluid interaction [142], but also as wave focussing

devices for wave energy extraction purposes according to McIver [143]; the issue of variable submergence is largely covered in this field. Next follows a scrutiny of the relevant coastal engineering and fluid mechanics research, noting that a heave plate, although small compared to a breakwater, will be exposed to similar surface proximity effects if brought close enough to the still water level.

The wave diffraction problem of a thick plate has been addressed by Zheng et al. [144] under linear approximation and by Kojima et al. [145] up to the II order, while that of a thin plate is discussed by Porter [146]. Its formulation for an arbitrarily shaped, submerged cylinder is also proposed by Vada [147]. Martin and Farina and Porter studied the linear wave radiation problem of a heaving horizontal disc [146, 148]. The latter study treats an infinitely long flat plate as well, while Zheng et al. analyse the wave radiation resulting from the oscillation of a thick rectangular pontoon [144]; this work also shows that the wave forces and coefficients obtained with the BEM approach fit well the results of the popular approach based on eigenfunction expansion matching.

The recapitulative messages for our use deriving from the above review are:

- The submergence of a plate- or pontoon-shaped structure can strongly influence first and higher order wave forces and hydrodynamic coefficients (see for example Figure 2.11).
- The behaviour of the first order quantities above consists in increased response as submergence is reduced, with the partial exception of added mass.
- First order forces prevail if submergence is sufficiently large compared to the horizontal size of the structure. At very small submergence (one order of magnitude below the structure's size or less), non-linear effects dominate and numerical resolution becomes increasingly difficult.
- Most modelling efforts are based on potential flow. The majority of these subdivide the fluid domain and match the resulting eigensolutions of the Laplace equation to deduce the potential.
- This method yields good agreement with the experimental results obtained in terms of wave forces, given that viscous effects be superposed using calibrated drag coefficients.
- At first order, the results of the above models are virtually equivalent to those found with the BEM approach.

The wave-plate interaction problem is rendered complex by effects of more difficult treatment such as wave trapping, treated by Parsons and Martin [149] and Linton and Evans [150], and other non-linear phenomena including wave decomposition (see Kojima et al. [93]) and breaking (Yu et al. [94]) over the plate's topside, occurring when wavelength and plate extension are large enough compared to submergence. The aforementioned studies neglect or superpose the viscous hydrodynamic effects. The complete representation of viscous wave flow over a submerged plate has been attempted

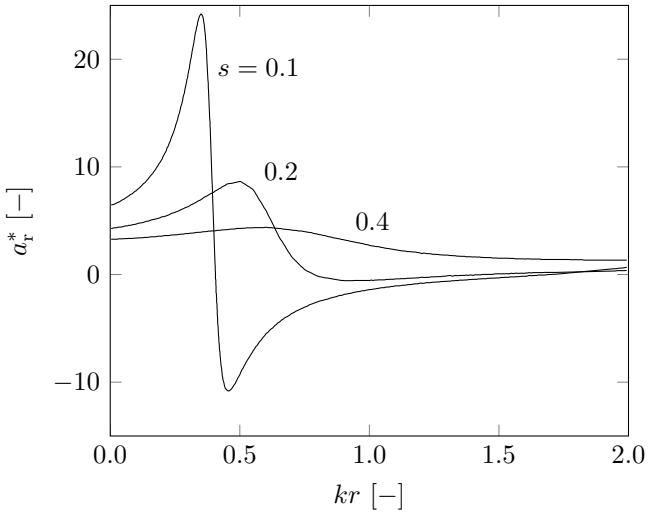

Figure 2.11: Variation of the non-dimensional heave added mass $a_r^* = a_r/(\rho_w r^3)$ of a thin horizontal disc in infinitely deep water, depending on its submergence $s = d/r$. Disc radius and draft are denoted r and d respectively, a_r is the dimensional added mass and ρ_w the fluid's density. $k = \omega^2/g$ denotes the wave number. Digitised from Martin and Farina [148].

by Yu and Dong [151] using the finite volume method.
This knowledge can now be reconducted into FWT hydrodynamics, to better characterise the wave forces acting on a low-draft structure fit with bottom plates.

2.3.1.2 Submergence sensitivity of a platform column

The considerations of 2.3.1.1 apply to water entrapment devices in that their vertical excursion impacts the forces arising from incident, diffracted, and radiated waves. An isolated axisymmetric column with attached bottom plate is extracted from the modified Dutch Tri-floater concept, detailed in 2.3.1.3. A parametric study is here organised by varying the column's relative submergence s and regenerating the wetted surface mesh at each draft. Relative submergence is defined as $s = d/r$, where d denotes upper plate surface depth and r (constant) plate radius (see Figure 2.12). The remaining geometric proportions are fixed with $q/r = 4/9$ and $t_p/r = 1/9$. Solving the diffraction problem yields the wave excitation exerted on the structure: Figure 2.13 shows the variation of the heave force response amplitude operator (RAO) obtained when submergence is perturbed, given an infinite water depth and a unit incident wave amplitude. It is possible to observe that smaller draft leads to increased excitation as anticipated in 2.3.1.1, conversely the vertical force RAO tends to zero for an infinite draft for any wave harmonic of finite period. This well-known effect is mostly observable at values of kr larger than the heave excitation suppression point, a range where the rapid exponential decay of wave potential affects the plate's depth range and diffraction

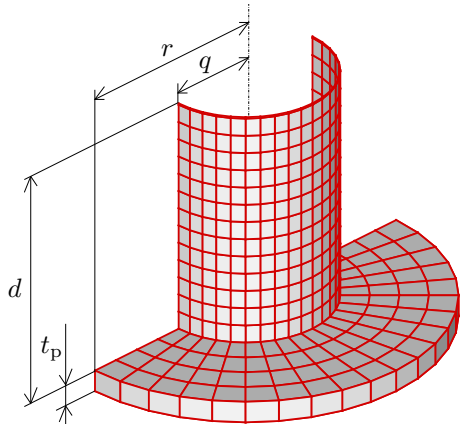

Figure 2.12: Mesh of modified Dutch Tri-floater column at baseline draft. Only half the structure is represented since the solver can exploit planar symmetry to reduce the size of the discrete problem. Quote q denotes the column's radius, r the heave plate's radius, t_p its thickness, and d the depth of plate topside below the free surface.

is strongly affected by plate submergence.

Figure 2.14 reports the frequency-domain vertical added mass and wave damping coefficients found as a function of the wave scattering parameter kr. As expected, the column's heave radiation characteristics are also found to be affected by submergence: added mass (Figure 2.14, left) shows little alteration for $s > 1$; for $s \leq 1$ it is observed a pattern similar to what seen in Figure 2.11; the wave damping coefficient's behaviour (Figure 2.14, right), analogous to that of heave excitation, consists in exponential increase in a definite band as relative draft is reduced. The outputs of the radiation calculation suffer from a certain amount of numerical noise that could neither be attributed to insufficient mesh resolution nor to incomplete convergence of the matrix inversion. This especially affects the radiation damping coefficient for certain values of kr, where the size of the anomaly reaches a magnitude comparable to the signal for $s > 1.5$. In this region of high submergence, however, wave damping forces become small and hence the impact of said anomaly on FWT motion can be deemed negligible.

One can look at the surface proximity effect from a different standpoint: identifying the combined scattering parameter and submergence envelope where perturbing draft causes a significant change in wave forces. Figure 2.15 exemplifies this idea for the heave load: by defining the quantity $f_h^* = f_h/(\rho_w g r^2)$, where f_h is the heave force per unit amplitude incident wave, its derivative with respect to submergence $-df_h^*/ds$ may be used as a proxy for sensitivity to vertical excursion. This quantity, mapped against kr and s, exhibits a monotonic decrease as submergence is increased, and a maximum at $kr \approx 1.3$ for any constant submergence. The blue region on the right represents the range for which waves are so small that their vertical penetration is not sufficient to reach the depth of the heave plate; the low-valued areas to the left and towards the top

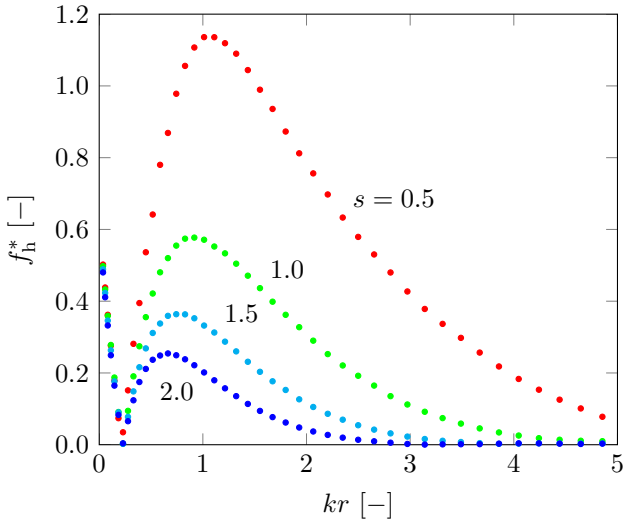

Figure 2.13: Variation of non-dimensional heave force $f_h^* = f_h/\rho_w g r^2$ (with f_h heave force response amplitude operator) when the column with water entrapment plate is displaced vertically in infinite water depth.

of the plot are associated in turn to large-scale wave kinematics compared to structure size, and to large plate submergence: the former requires large vertical excursions to determine a change of loading regime (hence sensitivity is small), whilst the second is associated with vertical extinction of wave potential. The region of highest sensitivity sits where pronounced decay of the diffraction potential occurs just around the plate's depth.

From these simple numerical experiments one can anticipate a low-draft semi-sub platform's behaviour: when its columns lose submergence, the plates interact more strongly with surface waves, causing wave-structure interaction alterations which are most significant in a specific band. In the case of the FWT concept analysed next, this region largely coincides with the dominant wave energy band. Finally, it should be remarked that the presence of multiple columns in the wave field will cause more complex diffraction and radiation patterns to appear next, where the interference between the columns grows with their size and declines with their mutual distance. This is taken into account but not discussed in the following study. More complex wave phenomena found in a multi-column setting such as trapped modes cannot be treated using the present model and should be studied in the future.

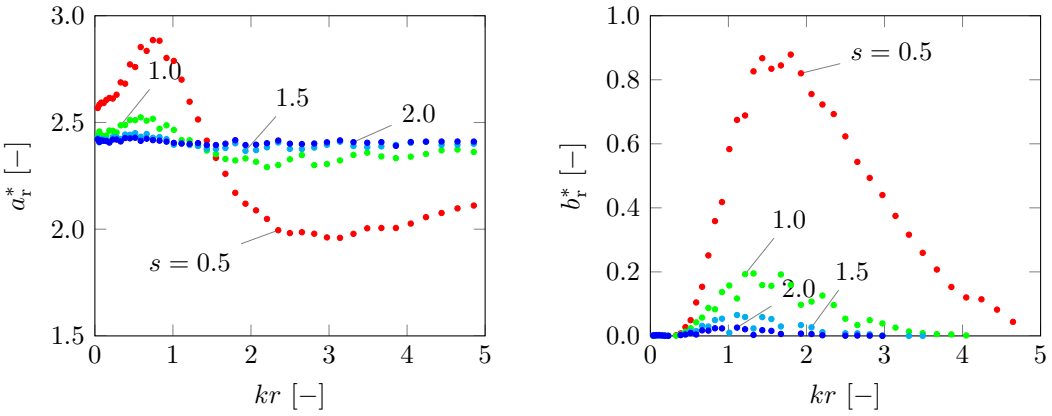

Figure 2.14: Non-dimensional heave added mass and wave damping $b_r^* = b_r/\rho_w\sqrt{gr^5}$ of column with water entrapment plate for varying submergence. For reference, the classic potential solution for the added mass of a disc of infinite submergence, available in Lamb [152], is $a_r^* = 8/3$.

2.3.1.3 Inclination sensitivity of a semi-submersible platform

The column studied above is derived from a MW-scale FWT platform design, the Dutch Tri-floater, documented by Philippe et al. in [86, 153] and by Courbois [107]. This has been slightly modified as explained below. A perturbation analysis is conducted on platform potential hydrodynamics similar to what has been done in 2.3.1.2, only with variation of inclination in lieu of draft. Only the large members are treated, implying that all the slender cross-members are disregarded in the linear potential flow solution consistently with the approach presented in 2.2.6. The distance of the columns from the FWT's static pivoting point determines both plate excursion and rotation, causing a change in the resulting wave force patterns.

The Dutch Tri-floater is a three-column semi-sub platform concept designed to support HAWTs with a rating of around 5 MW. Its stabilising system is passive, unlike in other designs where slow-varying wind overturning moments are compensated with active ballast shifts (see [154]). Since the original concept features thin water entrapment plates, which cause numerical problems when treated with the panel method (an issue which was later overcome with the method outlined in 2.3.4.3), it was decided to modify the floater by thickening its plates to an acceptable level; the introduction of extra submerged volume at platform bottom required contextual re-distribution of its mass in order to restore the originally intended degree of hydrostatic stability. The modified floater geometry is shown in Figure 2.16, while its main defining parameters are given in Table 2.2.

The structure is next subjected to incremental isocarenic trimmings of $\pm 5\,^\circ$ about the

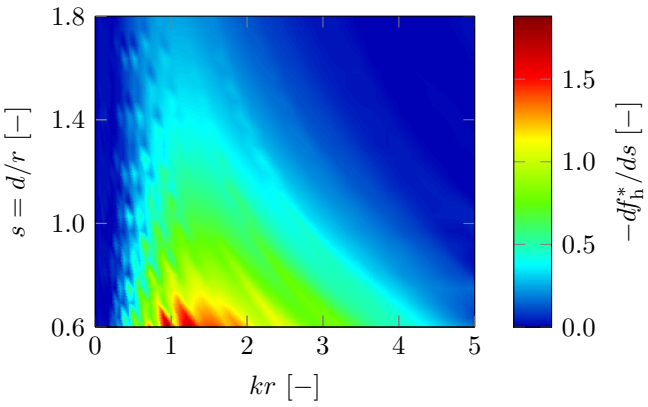

Figure 2.15: Vertical wave load sensitivity to submergence for a column with heave plate.

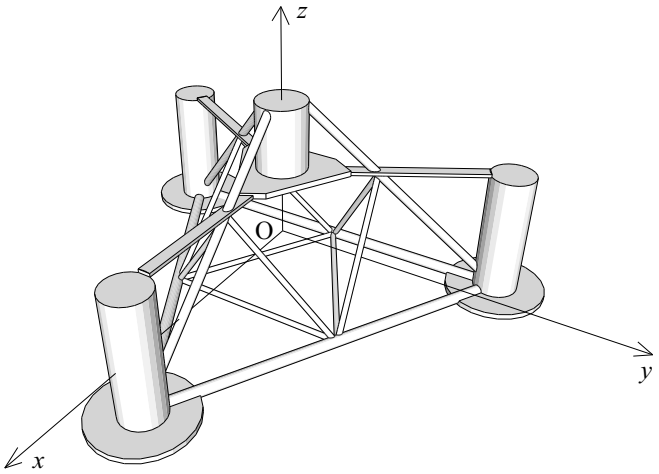

Figure 2.16: Modified Dutch Tri-floater geometry and system of reference.

pitch axis y. Heave plates rigidly follow, undergoing the same rotations plus a vertical excursion of about ±1.7 m (aft columns) and ±3.4 m (fore column). These in turn cause plate mean submergence s to vary in the range between 0.84 and 1.60 at ±5 °, while in the upright configuration all columns are are characterised by $s = 11/9 \approx 1.22$ (cfr. Figure 2.15). Actualising the mean wetted surface enables to evaluate the wave load variations. Water depth is assumed to equate 50 m, allowing to relate these results to the case study of 2.3.2, and the chosen direction of propagation of the incident waves is along the x axis.

The graphs included next show the platform's vertical and vertical-rotational excitation features. Figure 2.17 displays the heave and pitch force response for the upright and trimmed configurations. It is possible to observe that the imposed inclinations significantly modify wave excitation in the central portion of the studied range, which largely overlaps with the ocean wave band. For instance around $kr = 1.5$ (where the incident wave period is $T \approx 5$ s), an inclination of +5 ° practically doubles heave excitation and

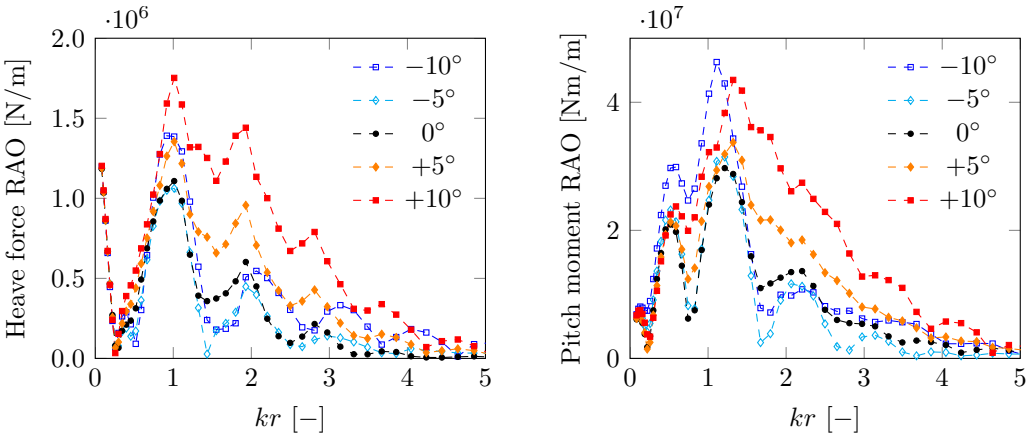

Figure 2.17: Inclination effects on the modified Dutch Tri-floater's heave force and pitch moment response in regular waves.

increases that of pitch by 30%–50% compared to the upright platform forces. Trimming also alters the radiation problem: while diagonal added masses are little impacted (cf. 2.3.1.2), radiation damping is magnified by plate proximity to the surface as visible in Figure 2.18.

Moreover, radiation-induced coupling appears in the trimmed configurations, due to the loss of hull axisymmetry. This is observable in Figure 2.19, where the introduction of heave-pitch hydrodynamic coupling is evidenced by the appearance of significant extra-diagonal terms. It is straightforward to relate the results of the current section to what presented in 2.3.1.2: reading the values of Figure 2.15 at the initial submergence of the platform plates, $s \approx 1.22$, helps to explain the divergence of the load response curves, which is most marked in the scattering parameter interval $kr \in [0.5, 4.0]$.

This investigation has shown that significant changes of linear wave-structure interaction can occur when a semi-sub FWT platform equipped with water entrapment plates undergoes mean inclinations in the order of 5 ° or more, undermining the validity of the classic small displacement assumption used for the computation of wave loads.

Table 2.2: Modified Dutch Tri-floater geometric parameters.

Design draft [m]	12.0
Hull volume at design draft [m^3]	3048
Column centre-to-centre spacing [m]	68.0
Column diameter [m]	8.0
Column depth incl. plate [m]	24.0
Plate diameter [m]	18.0
Plate thickness [m]	1.0
Bracing diameter [m]	1.0 to 2.0

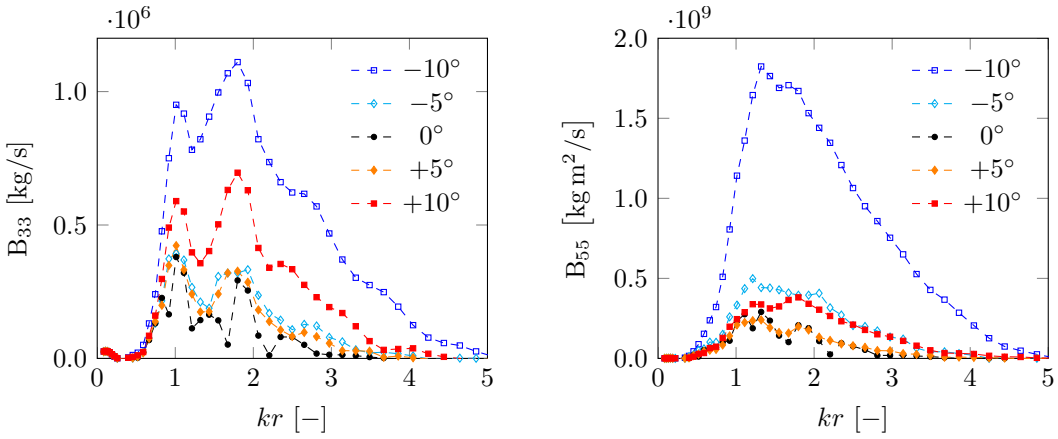

Figure 2.18: Inclination effects on the modified Dutch Tri-floater's heave and pitch radiation damping.

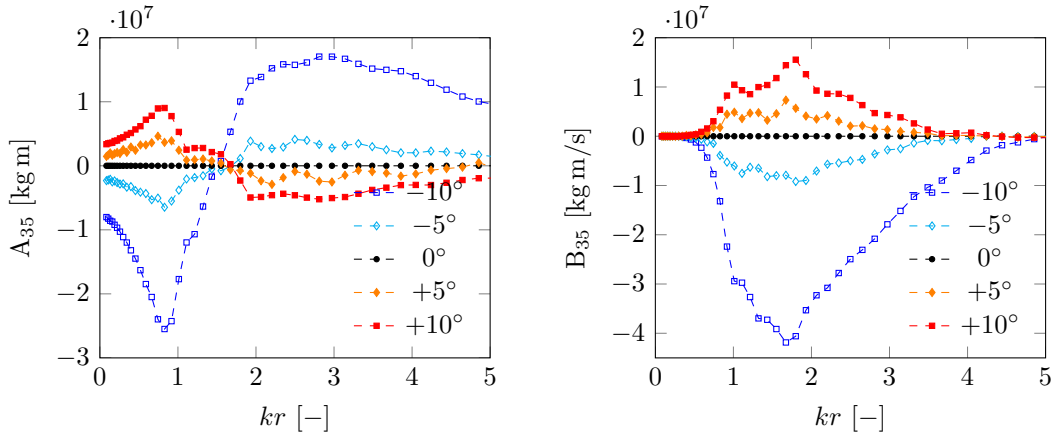

Figure 2.19: Inclination effects on the modified Dutch Tri-floater's heave-pitch coupling added mass and wave damping.

The study presented in 2.3.2 further builds on these considerations by evaluating the dynamic response of the fully assembled system subject to wind and wave loading, where the geometric non-linearity concurs to altering global motion response in presence of large mean inclinations.

2.3.2 Large-inclination coupling study

Following from 2.3.1, the modifed Dutch Tri-floater will be the subject of a fully fledged large-inclination dynamic response study. The structure is subjected to inline and cross wind and wave regimes using a homogeneous wind profile and regular or irregular waves as inputs. In the irregular wave cases, the standard JONSWAP formulation is used to calculate the input spectrum, employing $\gamma = 3.3$. All wavetrains propagate in the positive x direction, exciting the structure in presence of zero, inline, and cross wind at rated speed, constant over time. The wind turbine's operating conditions are parked for zero wind speed and rated for the cases including wind. A compact definition of the loading cases considered is given in Table 2.3.

The floating platform is coupled to a NREL 5 MW reference offshore wind turbine [108], using the structural adaptation by Philippe [153], totalling 3124 t of displacement (Figure 2.20). Station keeping is assured by the chain-wire hybrid, 6-point mooring system defined by the same author [153] with two lines departing from the outer bottom of each column, at a radial distance of 4.0 m from the centre of the column. The line properties are given in Table 2.4. A water depth of 50 m is assumed. The parameters defining the platform's mass features are given in Table 2.5, whilst the wind turbine generator's mechanical parameters required to model it in rigid form are given in Table 2.6. The operating parameters in rated conditions are also provided. As said the mooring forces are included with a simple restoring term; the undisturbed downwards mooring force, equal to 183.5 t, is accounted as a single weight lumped at fairlead height in the gravitational set-up of the system. Equation 2.15 defines the values

Table 2.3: Definition of loading cases. Angles are measured in the horizontal plane counter-clockwise starting from the x axis (90° is aligned with y).

Regular waves $\omega \in [0.1, 1.5]$ rad/s			
Loading case name	LC0	LCX	LCY
Wind speed [m/s]	0.0	11.4	11.4
Wind direction [deg]	-	0.0	90.0
Turbine operation	parked	rated	rated
Wave height [m]	4.0	4.0	4.0
Wave direction [deg]	0.0	0.0	0.0
Irregular waves			
Loading case name	LC0i	LCXi	LCYi
Wind speed [m/s]	0.0	11.4	11.4
Wind direction [deg]	-	0.0	90.0
Turbine operation	parked	rated	rated
Sig. wave height [m]	4.0	4.0	4.0
Peak period [s]	10.0	10.0	10.0
Wave direction [deg]	0.0	0.0	0.0

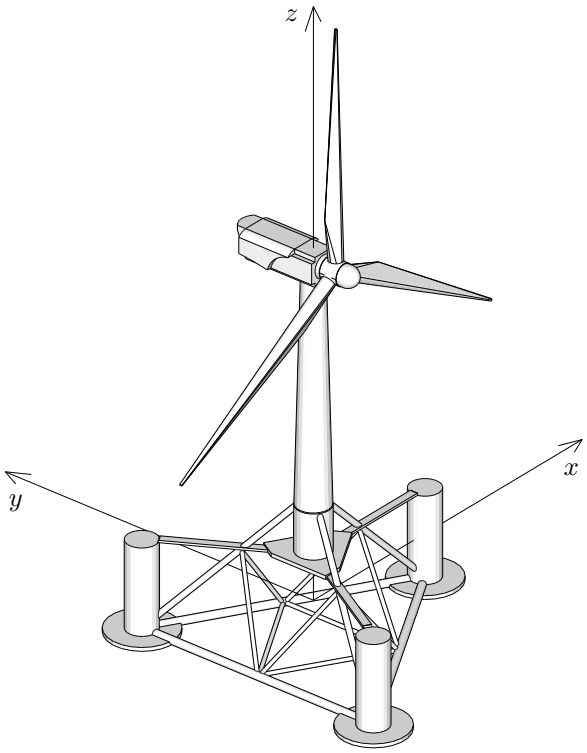

Figure 2.20: Modified Dutch Tri-floater with 5 MW class horizontal axis wind turbine. The latter is adapted from a graphical model made available by Somerville [155].

Table 2.4: Properties of a Dutch Tri-floater mooring line.

Component	studless chain	wire
Material	steel	steel
Nominal diameter [m]	0.15	0.16
Unstretched length [m]	190	225

assigned to the mooring stiffness tensor, as calculated by Philippe [153]. The units used are [m, rad] for displacements and [N, Nm] for the generalised forces:

$$\mathbf{K}^{\mathrm{m}} = \begin{pmatrix} 1.6{\cdot}10^5 & 0 & 0 & 0 & 1.9{\cdot}10^6 & 0 \\ & 1.6{\cdot}10^5 & 0 & -1.9{\cdot}10^6 & 0 & 0 \\ & & 1.5{\cdot}10^5 & 0 & 0 & 0 \\ & & & 1.1{\cdot}10^8 & 0 & 0 \\ & \text{sym.} & & & 1.1{\cdot}10^8 & 0 \\ & & & & & 1.7{\cdot}10^8 \end{pmatrix} . \tag{2.15}$$

Table 2.5: Modified Dutch Tri-floater mass/inertia properties. Quantities are expressed with respect to the origin O at the still-water level.

Mass [t]	2263
Vertical position of CoM [m]	-0.1
Roll/pitch moment of inertia [t m^2]	$1.535 \cdot 10^6$
Yaw moment of inertia [t m^2]	$2.522 \cdot 10^6$

Table 2.6: Adapted 3-blade upwind 5 MW NREL offshore wind turbine data. Mechanical quantities are expressed with respect to the origin O at still-water level with the exception of the rotor's inertia.

Mechanical parameters	
Overall mass [t]	678
Overall vertical position of CoM [m]	83.0
Overall roll/pitch moment of inertia [t m^2]	$3.779 \cdot 10^6$
Overall yaw moment of inertia [t m^2]	$5.220 \cdot 10^3$
Rotor axial inertia [t m^2]	$3.876 \cdot 10^4$
Elevation of tower/platform interface [m]	25.0
Rotor diameter [m]	126
Hub height [m]	90.0
Rated operating parameters	
Incident wind speed [m/s]	11.4
Rotor speed [rpm]	12.1
Rotor thrust coefficient c_T [-]	0.82
Rotor torque coefficient c_Q [-]	0.066
Tower drag coefficient c_D [-]	1.0

2.3.2.1 Treatment of mean inclination

The approach adopted here to treat the FWT's relatively large wind-induced inclinations is based on re-linearising the dynamic system about the tilted and offset configuration attained by the FWT under pure wind loading. It is assumed that further dynamic oscillations of small amplitude will occur around this position.

A preliminary computation is required to obtain the offset configuration referred to: in this study this consists in applying the rotor forces obtained with the desired operational regime and running the dynamic simulation in the absence of incident waves until the steady-state, static offset is reached. When this method is applied to the Dutch Tri-floater, small static rotations are found about the z axis (up to around 0.2 °) and about the horizontal axis aligned with the wind (up to around 0.4 °). These are respectively due to the eccentricity of the thrust force with respect to the z axis and the stator's reaction to the rotor torque. Such secondary rotational components are neglected whilst the larger leeward equilibrium angle due to wind overturning is used to rewrite the EoM terms with the methods explained next.

As it will be pointed out in 2.3.2.2, because of the nonlinearities present in the model

the effective mean inclinations in the wind-and-wave dynamic simulations do slightly depart from the static values obtained as described above. Although this problem may be solved iteratively, in the present simulations this relatively small discrepancy between input and output mean inclination is tolerated.

Rigid-body inertia. The generalised inertia matrix is actualised to the mean rotated position using

$$\mathbf{M} = \begin{pmatrix} m & 0 & 0 & 0 & mz_\mathrm{C} & -my_\mathrm{C} \\ & m & 0 & -mz_\mathrm{C} & 0 & mx_\mathrm{C} \\ & & m & my_\mathrm{C} & -mx_\mathrm{C} & 0 \\ & & & J_{11} & I_{12}-mx_\mathrm{C}y_\mathrm{C} & I_{13}-mx_\mathrm{C}z_\mathrm{C} \\ & \text{sym.} & & & J_{22} & I_{23}-my_\mathrm{C}z_\mathrm{C} \\ & & & & & J_{33} \end{pmatrix}, \tag{2.16}$$

$$\begin{aligned} J_{11} &= I_{11}+m(y_\mathrm{C}^2+z_\mathrm{C}^2)\,, \\ J_{22} &= I_{22}+m(x_\mathrm{C}^2+z_\mathrm{C}^2)\,, \\ J_{33} &= I_{33}+m(x_\mathrm{C}^2+y_\mathrm{C}^2)\,, \end{aligned} \tag{2.17}$$

where the terms denoted by the variable I are the elements of the central inertia tensor. Vector $(x_\mathrm{C}, y_\mathrm{C}, z_\mathrm{C})$ represents the position of the CoM in the inertial frame after applying the rotation.

Hydrostatics. A set of preliminary calculations has determined that the changes in hydrostatic stiffness never exceed 1% for the treated hulls and their mean inclinations. Regarding vertical hydrostatic stiffness they consist in computing the updated water-plane area, whilst for the rotational terms the positions of G (centre of gravity), B (centre of hull volume), and M (longitudinal/transversal metacentre) are recalculated after applying an isocarenic inclination. Thus their heights over the reference keel point K concur to determining the updated hydrostatic restoring moment arm $\overline{\mathrm{GM}} = \overline{\mathrm{KB}} + \overline{\mathrm{BM}} - \overline{\mathrm{KG}}$ and finally the stiffness terms $\mathrm{K}_{44}^\mathrm{h}$ and $\mathrm{K}_{55}^\mathrm{h}$ as described in 2.2.5. Following these considerations, it was decided to neglect the nonlinear hydrostatic effects due to the mean inclination, (which is in the order of 6 ° to 8 ° in the present studies). Concerning the rotational terms, the above finding is consistent with the well-known behaviour of wall-sided floating bodies, which exhibit linear hydrostatic restoring up to trim/heel angles of about 10 ° (see for instance Journée and Massie [138]). Thanks to the choice of point O at the SWL, no extra-diagonal terms appear within the $\mathbf{K}^\mathrm{h}$ matrix following a static inclination.

Potential-flow hydrodynamics. The geometric nonlinearity affecting the hull's wave diffraction and radiation in the presence of a significant inclination can be treated as in 2.3.1 by updating the hydrodynamic mesh to the new mean position, effectively re-linearising the inertial hydrodynamic forces about a new equilibrium point. To date, a few published studies implement this approach. In particular, Philippe et al. actualise the mesh of a circular barge supporting a FWT to characterise its motion under simultaneous wind and wave loading [126], as well as that of a semi-submersible FWT hull for similar purposes [86, 153, 156], although the water entrapment plates are removed from the potential flow problem. The same approach is presently employed

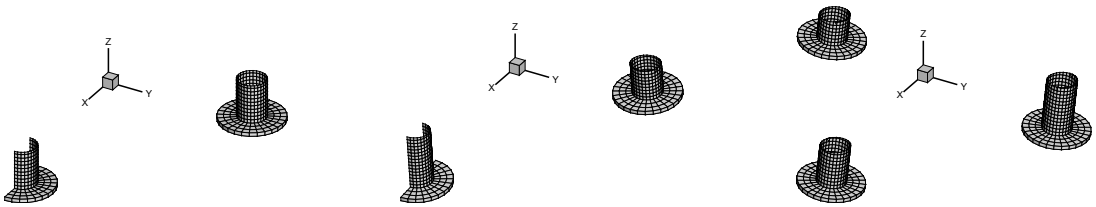

Figure 2.21: Wetted surface discretisations used for the wave diffraction and radiation calculations. (a) upright, (b) with rotation about y, and (c) with rotation about x.

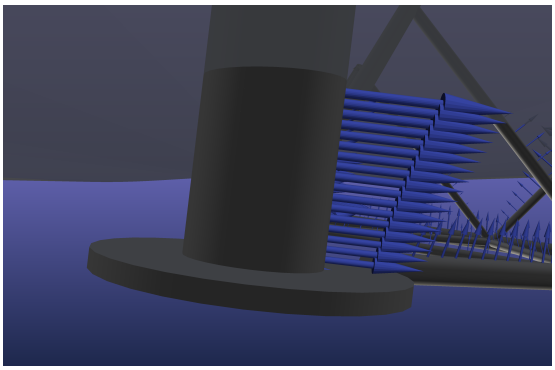

Figure 2.22: Snapshot of transverse drag forces exerted on a platform column by a 12 s wave of 4 m height. The arrow size is proportional to the computed magnitude of the local force.

with a full incorporation of the large platform appendices: Figure 2.21 shows the upright potential hydrodynamic mesh of the modified Dutch Tri-floater (see 2.3.1) and the actualised meshes following application of wind overturning in the x and y direction. It can be noticed that in the presence of a rotation about the x axis the xz planar symmetry is lost, leading to the need to discretise the entire wetted surface. An important remark based on this figure is that the water entrapment plates undergo significant vertical excursion in (b) and (c), causing the potential flow hydrodynamic regime perturbations scrutinised in 2.3.1.

Viscous hydrodynamics. The process of calculating the hydrodynamic drag forces includes updating the position of the discrete hull elements at every time step as a consequence of the motion of the structure. Thus the preliminary computation of the mean inclination described above needs not be an input, since the correct Morison element displacements are continuously applied in the time domain. This implies that the elements are exposed to wave particle kinematics of varying intensity depending on their vertical excursion and of varying phasing, the latter depending on their horizontal excursion. Figure 2.22 provides a visual example of the lateral drag force exerted on a platform column undergoing excursion.

Mooring forces. All nonlinearities related to the catenary mooring system are here neglected to keep the focus on platform hydrodynamics, hence the initial linearised stiffness matrix $\mathbf{K}^{\mathrm{m}}$ is employed unchanged.

2.3.2.2 Results

This section presents the results of the above defined simulations. The preliminary offset calculation yields the generalised position vectors

$$\begin{array}{r} \text{LCX \& LCXi: } \mathbf{x}=(3.96 \;\; 0.08 \; 0.00 \;\; 0.41 \;\; 6.37 \; 0.18)^{\mathrm{T}}\,, \\ \text{LCY \& LCYi: } \mathbf{x}=(-0.08 \; 3.96 \; 0.00 \; -6.37 \; 0.41 \; 0.18)^{\mathrm{T}}\,, \end{array} \tag{2.18}$$

with displacements given in [m] and rotations in [deg]. As one may expect, the most significant static offsets are displacements in the wind direction, which are resisted by the mooring system, and a leeward rotation mainly countered by hydrostatic restoring. The symmetric stiffness features of the system also emerge from Equations 2.18. The FWT's dynamic response in regular waves exhibits nearly harmonic form at steady state. Obtaining the pseudo-transfer function of motion in any DoF i requires post-treating the time-domain signal, which in this case is done by

$$r_i(\omega) = \frac{\max[x_i(t,\omega)] - \min[x_i(t,\omega)]}{H}\,, \tag{2.19}$$

where $H = 2\tilde{a}$ is the incident wave height. It must be pointed out that because of the nonlinearities present in the model, the pseudo-transfer function magnitude is dependent on the excitation magnitude within certain bands. When the wind force is applied, the response characteristics r_i are to be interpreted as the normalised amplitude of the dynamic response to wave excitation about the mean wind-induced offset.

Figure 2.23 displays the ensemble of the pseudo-transfer functions calculated for the loading cases defined in Table 2.3. For each DoF the corresponding uncoupled, undamped natural frequency ω_{n} is reported to facilitate interpretation. It can be seen that the most important response features lie in the xz plane (surge, heave, pitch), which is expected for a 2D wavetrain propagating in the x direction over a roughly symmetric structure. Most resonances are confined at the far left of the studied band, a desirable hydromechanic feature in the light of the distribution of wave energy and the subsequent first-order excitation. An in-depth screening of these results is given in 2.3.2.3.

Figure 2.25 provides a snapshot of a dynamic simulation in regular waves after the steady state is reached. The quasi-harmonic motion time histories of surge and pitch are shown with their respective aerodynamic excitation signals, for an incident wave frequency of 0.40 rad/s and two different loading cases. The mean forces and by consequence the offsets obtained when wind is applied are immediately evident. This case

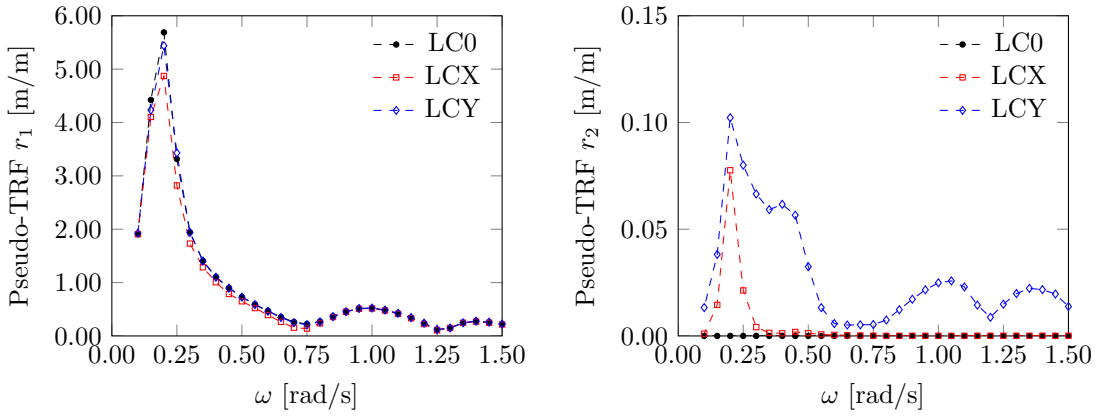

(a) Surge. $\omega_n \approx 0.18\,\text{rad/s}$.

(b) Sway. $\omega_n \approx 0.18\,\text{rad/s}$.

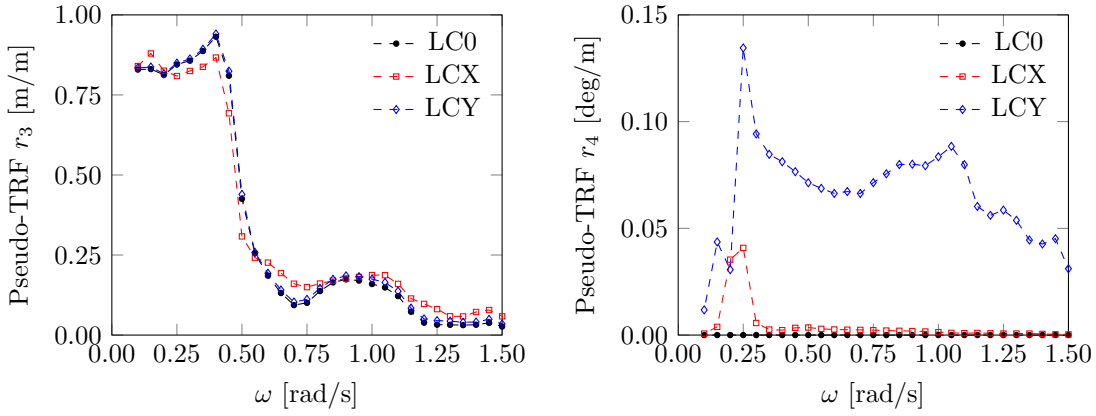

(c) Heave. $\omega_n \approx 0.46\,\text{rad/s}$.

(d) Roll. $\omega_n \approx 0.25\,\text{rad/s}$.

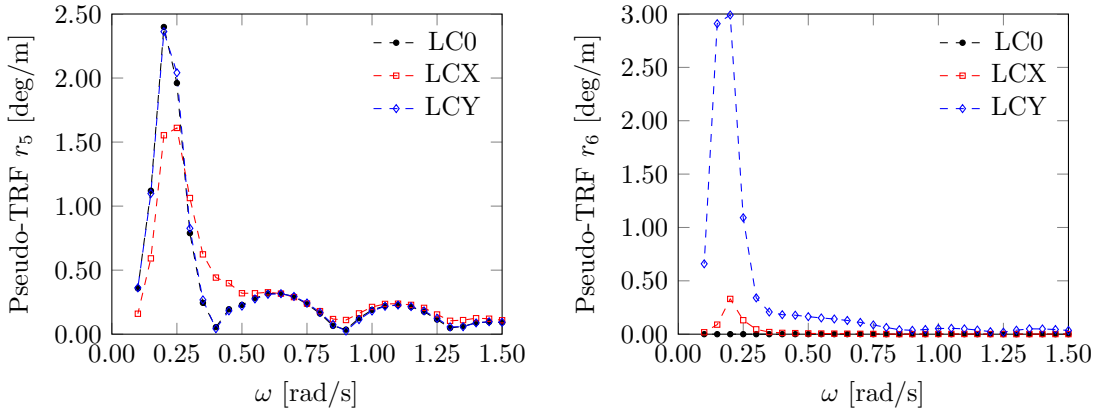

(e) Pitch. $\omega_n \approx 0.25\,\text{rad/s}$.

(f) Yaw. $\omega_n \approx 0.18\,\text{rad/s}$.

Figure 2.23: Pseudo-transfer functions of the modified Dutch Tri-floater subjected to wind and regular wave excitation.

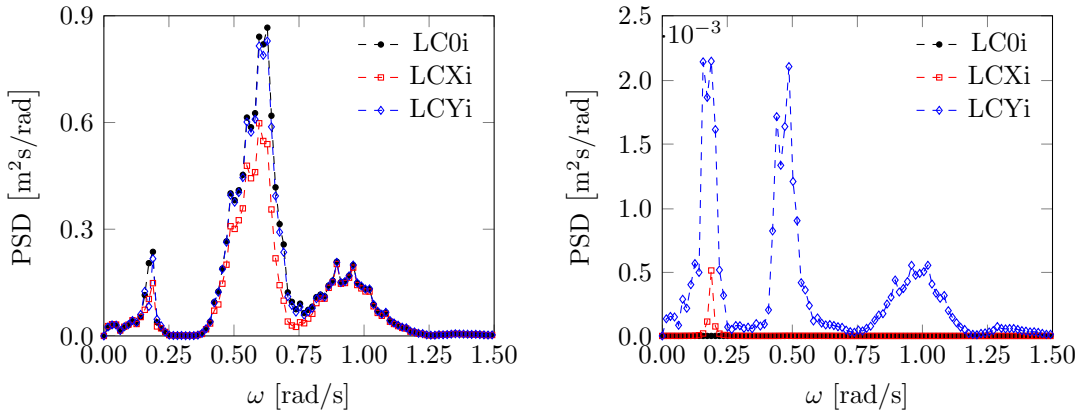

(a) Surge.

(b) Sway.

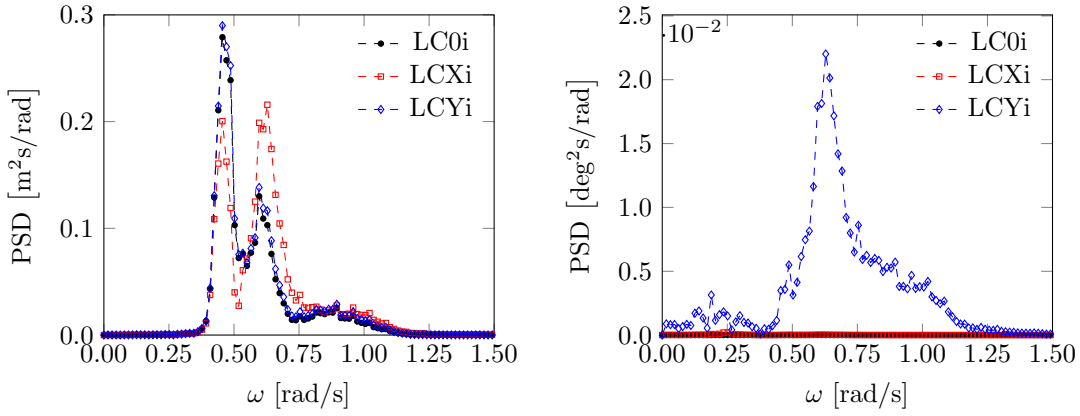

(c) Heave.

(d) Roll.

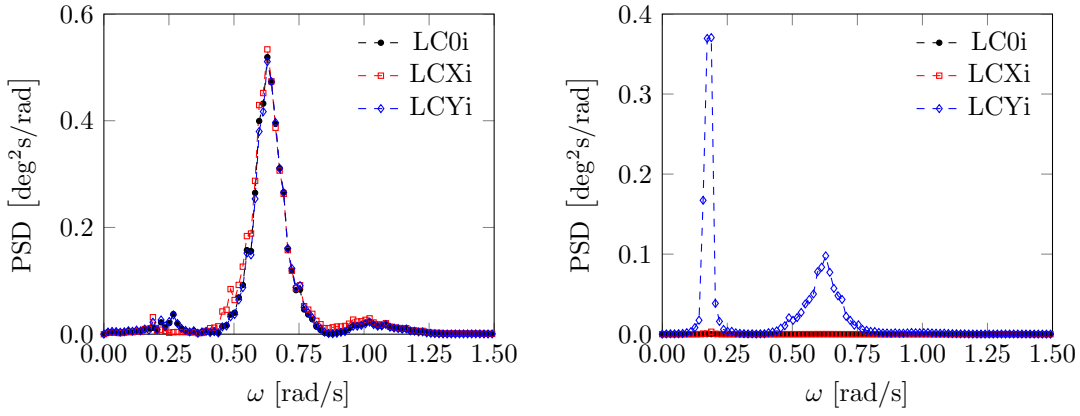

(e) Pitch.

(f) Yaw.

Figure 2.24: Power spectral density of the motions of a modified Dutch Tri-floater subjected to wind and irregular wave excitation.

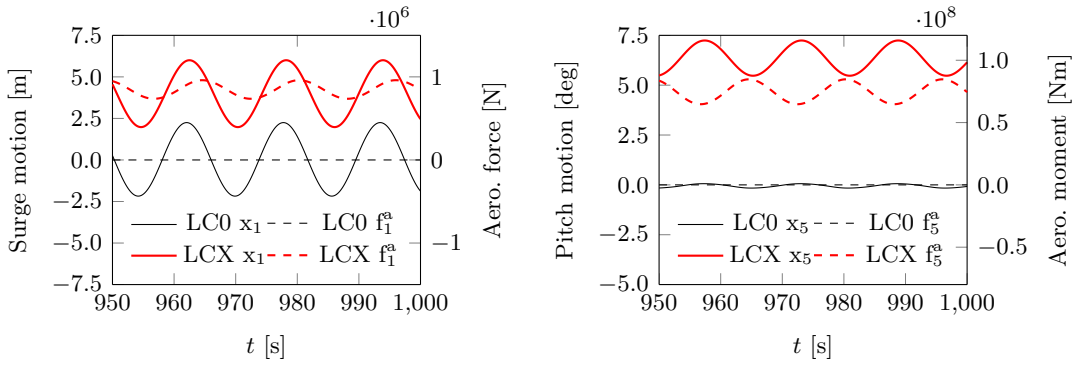

Figure 2.25: Time-domain output motion and aerodynamic forcing in surge (left) and pitch (right), for an incident wave of 0.40 rad/s.

will be used later to clarify the inter-DoF aerodynamic coupling observed around said frequency.

The motion outputs of the irregular wave simulations are shown in Figure 2.24 in spectral form. The underpinning time series have a duration of 2 hours and represent the fully developed dynamic response of the structure in a stationary sea state. The input spectral realisation, defined by a particular choice of component phases, is the same for all loading cases. These results will be used in 2.3.2.3 to contextualise the dynamic response features of the system for a specified, realistic met-ocean condition: the fact that most of the input wave energy lies between 0.5 rad/s and 0.9 rad/s brings out the response features of the studied FWT in this central band.

Finally, the mean leeward inclination angles attained in the steady-state phase of all dynamic simulations are plotted (in absolute value) in Figure 2.26. It appears that although limited in magnitude, discrepancies exist between the assumed mean inclination and that effectively produced by the dynamic simulations in regular waves. This is especially pronounced for load case LCX, where nonlinear forces with non-zero mean are present (i.e. hydrodynamic drag) which have a large component in the same plane of the leeward inclination. The subsequent deviations from the statically calculated inclination do not exceed 4% and are deemed tolerable.

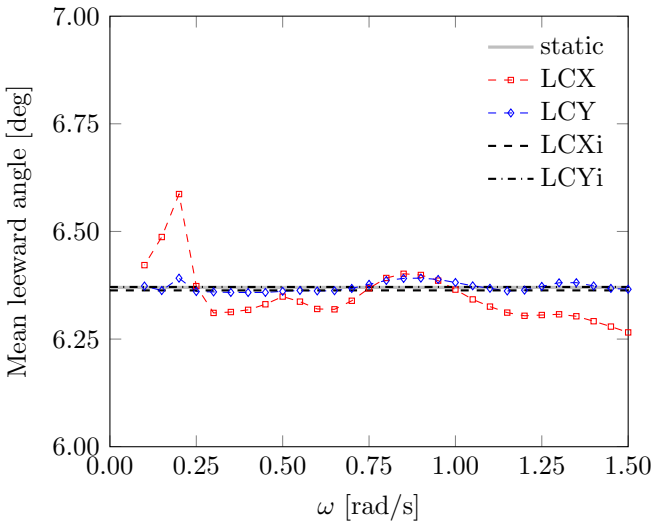

Figure 2.26: Mean leeward angles obtained from wind-and-wave dynamic simulations.

2.3.2.3 Discussion

Numerous elements of interest can be derived from the results shown in 2.3.2.2. They will be discussed in the following by considering each motion degree of freedom in turn, then the key findings will be related to existing experimental results.

Dynamic response analysis. Response in **surge** (Figure 2.23a) is not particularly affected by the presence of rotor forces and platform inclinations. Only when the rotor is aligned with the surge motion (LCX) a minor dampening effect occurs due to aerodynamic damping thereby reducing the amplitude of the oscillation at the peak, located at 0.18 rad/s. The reduction in off-peak response is instead related to the alteration of inertial hydrodynamic excitation of the surge-pitch coupled mode. Observing Figure 2.24a reveals the significance of these features in irregular waves.
As expected, and visible from Figures 2.23b and 2.24b, **sway** response is identically zero when the structure receives wave excitation only (directed along the x axis). Resonant inter-DoF coupling and loss of hydrodynamic $x\mathrm{O}z$ symmetry respectively cause small sway response for collinear and cross-wind loading cases.
Heave motion (Figure 2.23c) exhibits a marked dependence on rotor forces and inclinations in the case of collinear wind and waves: excitation suppression around $\omega \approx 0.7$ rad/s becomes less pronounced mainly because of the simultaneous vertical excursion of two heave plates toward the free surface (see Figure 2.21, centre). This in turn triggers (1) an increase (and a phase shift) of the inertial wave excitation, an effect already discussed in 2.3.1, and secondly (2) an increase in hydrodynamic drag under the action of stronger wave kinematics. Whilst effect (2) significantly contributes to altering response in said central band, effect (1) is solely at the root of the increased response observed at higher frequencies. The slight reduction of motion amplitude observable

around the resonance peak is also an effect of the large inclination due to heave-pitch coupling deriving from imbalance in wave radiation forces (in the model: significant extra-diagonal terms appear in the added mass tensor, see 2.3.1). The prevalence of these effects in the central band makes them significant in the studied irregular wave scenario, as observable from Figure 2.24c. In the low-frequency band, the heave response operator is less than unit; this is primarily due to vertical mooring restoring and, secondarily, to a numerical excitation deficit related to the representation of the bracing forces with the Morison equation. In fact, this method does not account for the small inertial force imbalance at the intersections with the free surface.

Roll (Figure 2.23d) is another DoF whose response is nil in the upright position and in the absence of rotor forces. Whilst the results are practically unchanged for LCX apart from a small resonance effect, a broad, albeit limited motion response is present in cross-wind conditions because of the loss of symmetry in port-starboard column excitation (see Figure 2.21, below), which is also detectable in Figure 2.24d.

Figure 2.23e reveals that **pitch** response at low frequency is particularly affected by the action of wind forces and the subsequent inclination in the collinear case. As expected, the resonance peak around $\omega_n = 0.25\,\mathrm{rad/s}$ is attenuated by the aerodynamic damping, whose impact is otherwise insignificant in the cross-wind case. The increased response manifested by LCX at the far right of the peak is exclusively due to the plate excursion effect (1) described above. A most prominent feature of pitch motion for the collinear loading case is the appearance of significant response in the immediate vicinity of the resonance peak, where wave excitation is suppressed for LC0 and LCY. This is caused by two concurring factors: heave plate excursion and the aerodynamic excitation of pitch caused by surge motion. This aerodynamically sourced, inter-DoF coupling will be further clarified next. In the irregular wave case studied, these pitch response features lose significance due to the low energy available below $0.5\,\mathrm{rad/s}$ (Figure 2.24e).

Figures 2.23f and 2.24f display the response in **yaw**, which rests unexcited by the waves in the absence of wind. The combination of gyroscopic coupling and resonance produces a limited response peak for LCX. It is the cross wind-and-wave cases LCY and LCYi that display the largest motions: the immersion of the port column and the emersion of the starboard column (Figure 2.21, below) cause an imbalance creating the potential for broad yaw forcing across the studied frequency band, that combines with the aerodynamic excitation due to the lateral motion of the hub. Where this excites resonant motion, in the band around $0.18\,\mathrm{rad/s}$, the dynamic response becomes very significant. It should be noted that since the present model omits the damping contributions of mooring line drag and rotor yawing, peak yaw response is likely overestimated.

Aerodynamic inter-DoF coupling. In the present case, the band between $0.25\,\mathrm{rad/s}$ and $0.55\,\mathrm{rad/s}$ is rich in inter-DoF coupling, which intertwines with the effects of wind-induced inclination in a complex fashion. As pointed out above, aerodynami-

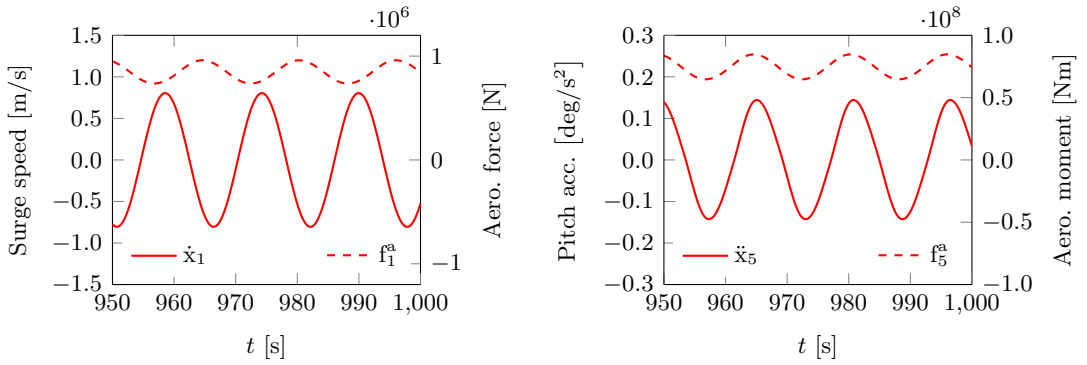

Figure 2.27: Time-domain surge speed (left) and pitch acceleration (right) of loading case LCX, for an incident wave of 0.40 rad/s. The respective aerodynamic force and moment signals are also shown.

cally sourced surge-pitch coupling explains in part the observed difference in response between LCX and the other regular wave loading cases (cf. Figure 2.23e). LCX is the sole case where the rotor operates in line with the hub speeds induced by pitch motion. Reactive aerodynamic damping is a well-known consequence of this set-up. Within the frequency band centred on 0.4 rad/s, however, wave-induced pitch response is relatively small and the aerodynamic force oscillations due to the motion-induced hub velocity tend to be more associated with surge response. This is made evident by rearranging the LCX results of Figure 2.25 (left) in terms of surge speed and aerodynamic force, as displayed in Figure 2.27 (left). Hence it emerges the relationship between surge and the aerodynamic force in the x direction: such force appears to react to surge motion, being in near phase opposition with surge velocity. At the same time, its fluctuations cause variations in the external pitch moment. The phasing between aerodynamic excitation and pitch acceleration visible in Figure 2.27 (right) for case LCX reflects this inter-DoF coupling effect, as the aerodynamic reactions are driving, not dampening, pitch motion. Of course, the retroactions present in the dynamic system close the loop and ultimately render the one-way cause-and-effect dynamic explained less clear-cut. The effect of the rotor control strategy – conventional, low-frequency [36], or with active motion damping [37] – on the intensity of this coupling is likely significant, although not treated here. It should also be pointed out that since the present thrust-based model tends to overestimate the aerodynamic reactive force (see 2.2.2), the strength of this coupling mechanism is likely overestimated as well, at least in the absence of active motion damping by control.

Experimental evidence of heave plate excursion effect. The observed interaction between heave plates and wave forces in the presence of large vertical excursions is only accounted for by nonlinear fluid dynamic models or, to a certain extent, by

re-linearising a linear model about the offset position as done here, thereby limiting the errors caused by geometric nonlinearity. A past publication by Philippe et al. [86] shows that the experimentally observed dynamics of a similar FWT subjected to collinear wind and waves are not entirely captured using the conventional modelling method based on linearising the fluid-structure interaction about the initial equilibrium. Virtually equivalent results are also available in [107, 153]. The predictions of pitch – a key DoF for FWTs – shown by these authors are particularly inaccurate in the 0.25 rad/s to 0.50 rad/s band, that is around the excitation suppression point next to the resonance peak: said numerical models underestimate the relatively large pitch motion obtained experimentally. On the contrary, the modelling strategy presented in this study may enable a more accurate representation of FWT dynamics in this range, as suggested by the sustained pitch response of LCX to the right of the main peak in Figure 2.23e. The validation cases presented in 2.3.4, which concern a very similar floating system, verify this capability against experimental data. The pitch response deficit caused by neglecting the geometric nonlinearity and hence the excursion effect is shown in Figure 2.28, which also permits to quantify the remaining effects in the vicinity of 0.4 rad/s, dominated by aerodynamic surge-pitch coupling.

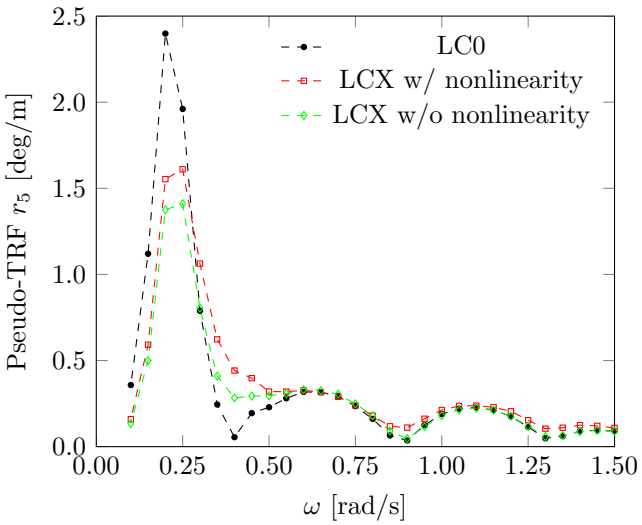

Figure 2.28: Pitch response characteristic predicted with and without treatment of the geometric nonlinearity.

2.3.3 The pitch aerodynamic damping of a floating vertical-axis turbine

This study concentrates on the aerodynamic damping impacting the pitch motion of an operating, floating VAWT concept, depicted in Figure 2.29. The time-domain coupling tool CALHYPSO introduced in 2.2 is used in conjunction with the EDF R&D's DMST aerodynamics library (outlined in 2.2.3), to extract pitch damping information from the simulation outputs. Given the large hydrostatic stability of this FWT, limiting the mean roll and pitch inclinations to 1 ° to 3 ° during operation, the large-angle treatment method of 2.3.2.1 is not adopted. The steady-state mean yaw angle is limited below 5 ° by the restoring power of the mooring system.
The following sections briefly describe the FWT concept employed as a case study and the post-treatment strategies. A range of numerical decay test results is then presented, followed by simulations in regular waves. The observed aerodynamic damping effects are contextually discussed.

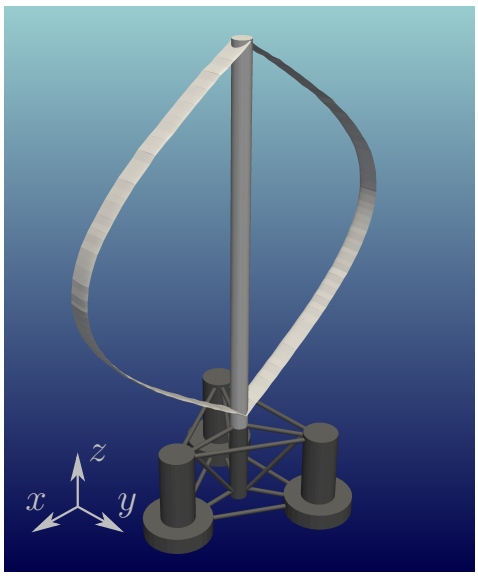

Figure 2.29: Floating vertical-axis wind turbine concept proposed by Wang et al. [111].

2.3.3.1 Floating wind turbine concept

The floating VAWT concept used for this study has been proposed by Wang et al. [111] and further characterised in published work by Borg et al. [110]. It consists of a combination of a 5 MW Darreius-troposkein turbine developed by Vita [157] for floating applications and the OC4-DeepCwind semi-submersible support structure detailed in a report by NREL [137]. As previously said, this concept uses catenary mooring lines for station-keeping: its particulars are available in [137], as well as the values of the corresponding linearised restoring coefficients. Incidentally, these are also the object of a moorings model verification carried out in Part 3 (see 3.4.3). The principal turbine properties, floater geometric parameters, and aggregated mass/inertia characteristics are given in Table 2.7. The fundamental parameter requiring calibration in the hydrodynamic model is the vertical drag coefficient on the lower columns, which is fixed at 4.80 based on past work by Masciola et al. [85].

Table 2.7: Properties of floating vertical-axis wind turbine concept. The mooring weight is included in equivalent lump form. Inertias are expressed with respect to the origin O at the still-water level.

Turbine geometry		**Floater geometry**	
Rotor radius [m]	63.74	Design draft [m]	20.0
Rotor height [m]	129.56	Hull volume at design draft [m^3]	13919
Airfoil type	NACA 0018	Column centre-to-centre spacing [m]	50.0
Blade chord [m]	7.45	Diameter of central column [m]	6.5
Turbine operation		Diameter of upper offset column	12.0
Rated power [MW]	5.0	Diameter of lower offset column [m]	24.0
Rated rotor speed [rpm]	5.26	Height of lower offset column [m]	6.0
Rated wind speed [m/s]	14.0	Bracing diameter [m]	1.6
Aggregate mass and inertia			
Displacement [t]	14267	Roll/pitch moment of inertia [$kg\,m^2$]	$1.500 \cdot 10^{10}$
Height of CoG from keel [m]	11.27	Yaw moment of inertia [$kg\,m^2$]	$1.262 \cdot 10^{10}$

2.3.3.2 Post-processing

When a symmetric, two-bladed turbine is operating, the motion outputs of any dynamic simulation contain a periodic fluctuation of period T_{2P}, that equals a half of the rotor's revolution period. This effect is particularly marked for a Darreius VAWT because of its large force swings, and implies that output data must be post-processed in order to retrieve certain sets of information. In this study FWT motion is characterised *after* having filtered out the aforementioned fluctuation. In the case of decay tests, a moving average approach is employed to smoothen the signal and retrieve the appropriate oscillation peak amplitudes for computation of the damping ratio. Concerning motion under regular waves, pseudo-RAOs are retrieved from steady-state motion using the amplitude of the Fourier component which corresponds to wave forcing. These two

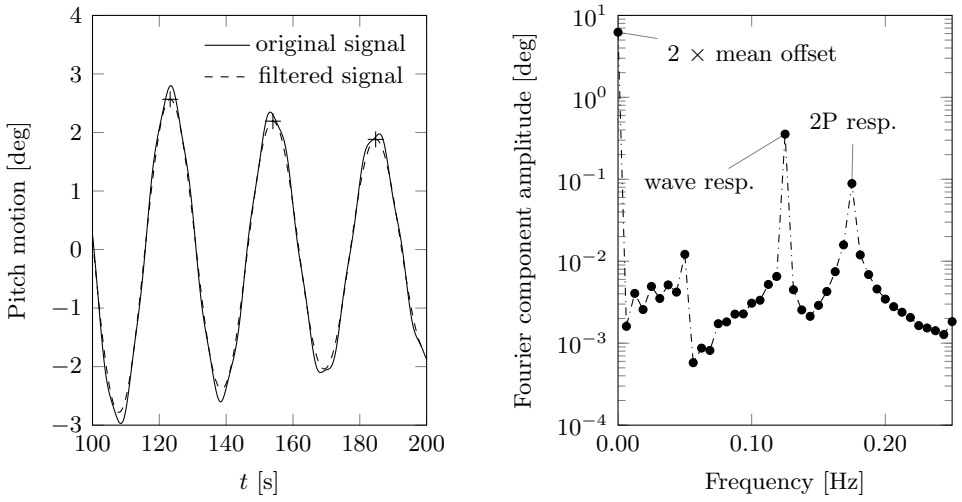

Figure 2.30: Filtering of 2P component from the pitch decay signal (left) and Fourier transform of the steady-state pitch response in waves (right).

processes are depicted in Figure 2.30.

In case numerical decay tests are carried out, filtering the 2P motion component leaves a decaying, oscillating signal whose peaks are denoted $\hat{x}_i$. Positive linear damping in underdamped dynamic systems results in exponentially decaying, sinusoidal free oscillations. Although the system in question contains significant nonlinearities and hence motion extinction does not exactly assume this form, it is nevertheless possible to evaluate the equivalent linear damping ratio ζ for any number of oscillation cycles N with

$$2\pi N\zeta = \log\left(\frac{\hat{x}_i}{\hat{x}_{i+N}}\right) . \tag{2.20}$$

By imposing $N = 1$ in Equation 2.20, the equivalent damping ratio for each oscillation cycle is obtained. This is the quantity ultimately used to characterise the aerodynamic damping affecting the free pitch oscillations of a floating VAWT.

2.3.3.3 Decay tests

This section reports the key outcomes of the time-domain simulations. Motion decay is presented in terms of evolution of the single-cycle damping ratio over time. Pitch response in waves is supplied in the form of pseudo-transfer functions. In all cases a baseline operating condition is defined where rotor and wind speed are constant and respectively equate $\Omega = 5.217\,\text{rpm}$ and $U = 14.00\,\text{m/s}$. A set of operating points is also generated around the above pairing by perturbing in turn Ω and U. The imposed incident wind is stationary, with a homogeneous vertical profile.

Pitch motion decay about the mean equilibrium position is obtained for a range of

operating conditions. Due to significant inter-DoF coupling, it is chosen to allow the structure to oscillate in pitch only, otherwise the observed dissipation would be associated to concurring multi-DoF mechanisms rather than pitch alone. In order to isolate the damping originating from rotor forces, all sources of hydrodynamic damping are zeroed; the only exception is the hydrodynamically damped case, reported for comparison, where the aerodynamic forces are suppressed instead.

All tests are set up by applying an initial pitch displacement of $+5\,^\circ$ at $t = 0\,\mathrm{s}$ from the mean offset attained with the rotor in operation (see Table 2.8), before releasing the structure into a free oscillation regime. The incident wind propagates along the x axis. Applying Equation 2.20, with $N = 1$, to the first ten motion cycles leads to the results of Figure 2.31. The first cycle does not appear where a moving average is used (i.e. for $\Omega \neq 0\,\mathrm{rpm}$). In the 'hydrodynamics only' case, damping decays over time:

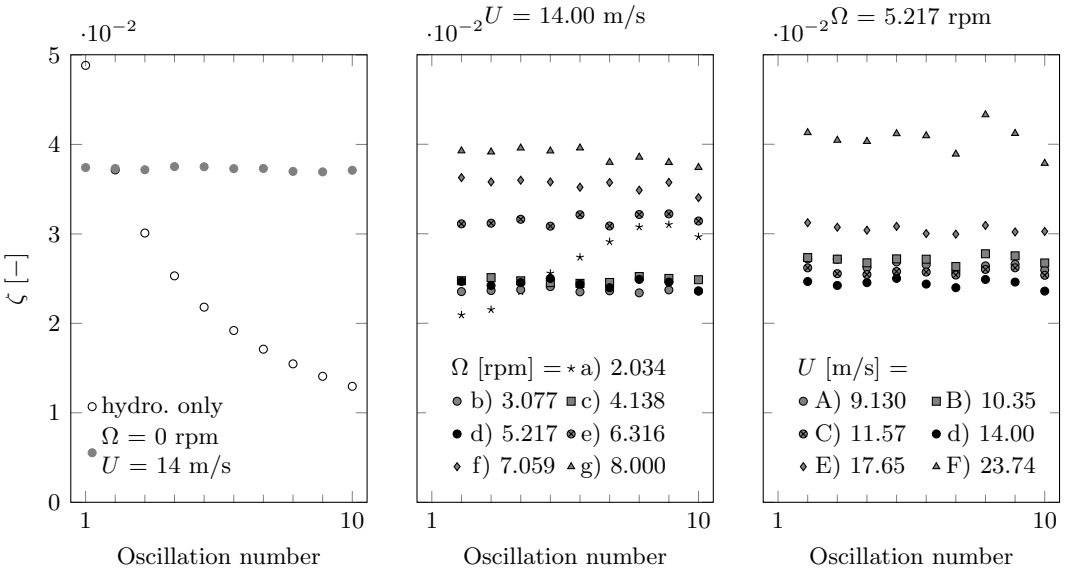

Figure 2.31: Damping ratio ζ of pitch oscillations with hydrodynamics only and parked rotor (left), varying rotor speed (centre), and varying incident wind speed (right).

this reflects its quadratic nature, caused by the dominance of drag-type forces: at the natural period of pitch, $T_\mathrm{p} \approx 31\,\mathrm{s}$, linear radiation damping is close to nil. The observed aerodynamic damping ratios vary between 2% and 4%, and keep nearly constant over time. This reveals that the system is almost linearly damped, a feature that will be further discussed in 2.3.3.5. It can be noted that in the 'parked rotor' configuration of Figure 2.31 (left) all damping descends from the action of aerodynamic drag forces: the rotor's azimuth is constant and corresponds to that shown in Figure 2.29, implying that the flow is perpendicular to the chord of all blade elements. As it will be discussed, the resulting damping ratio is also constant over time in virtue of the presence of a

relatively large incident wind speed U.

There is one exception to the above statement on nearly-constant aerodynamic damping, which is case a): the oscillation of ζ observed in Figure 2.31 (centre) is explained by the excitation of pitch resonant motion by the 2P aerodynamic load, with $T_\mathrm{p}/T_\mathrm{2P} \approx 2.09$. In this particular case, inferring damping from peak amplitude decay is incorrect. The mean trim angles found for the different operating points examined are provided with Table 2.8. These are limited below 5.3 °, providing a reduction of the projected swept area of less than 0.5%. On this basis, and considering the skewed-flow tolerance of Darreius turbines, it may be argued that the aerodynamic damping of the studied FWT is unlikely to be significantly influenced by the variations of the mean trim angle in the considered range of operating conditions.

2.3.3.4 Regular wave simulations

Incident regular waves propagating along positive x (hence collinear with the wind) are used here to excite the system, which is free to move in the six DoF. Only pitch motion is analysed, which is presented in the frequency domain through pseudo-transfer functions. These are obtained by normalising the amplitude of the motion's Fourier component of choice over the incident wave amplitude, $H/2$, where $H = 2\,\mathrm{m}$ is the wave height. The frequency of this component is equal to the wave frequency.

Figure 2.32 displays pitch response for a subset of the operating conditions considered in 2.3.3.3. When the turbine is operating, significant aerodynamic damping of pitch around the resonance peak is observed. In the case of the studied FWT concept, this is far removed from the prevalent 1$^\mathrm{st}$ order wave force band, hence variations in resonant motion amplitude due to varying damping bear a minor impact on the turbine's motion in waves. Nevertheless this may not be the case for response characteristics in different degrees of freedom (e. g. horizontal, where higher-order loads can cause large resonant motions), and in general for floating systems whose natural periods are closer to the wave band.

With respect to the hydrodynamics-only case, the peak amplitude of pitch is reduced

Table 2.8: Calculated mean trim angle for an aerodynamically excited Darreius floating wind turbine in operation.

Case	Mean angle [deg]	Case	Mean angle [deg]
a)	1.4	g)	4.7
b)	1.8	A)	2.0
c)	2.4	B)	2.3
d)	3.1	C)	2.6
e)	3.8	E)	3.8
f)	4.2	F)	5.3

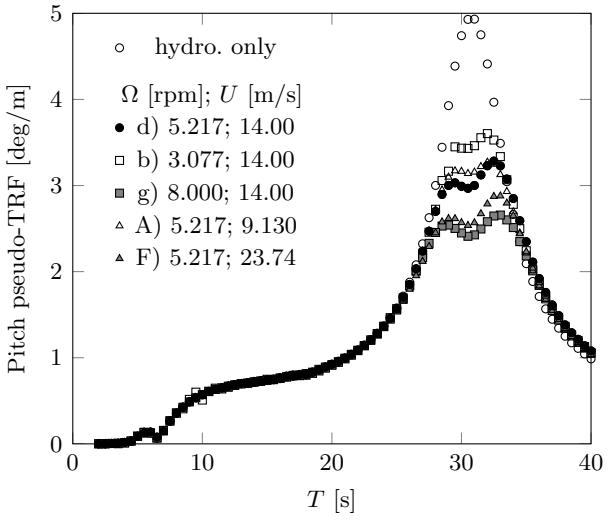

Figure 2.32: Pseudo-transfer function of pitch for different operating conditions.

by 25% to 50% thanks to the presence of rotor forces; it should be pointed out that this reduction potential is dependent on the incident wave amplitude due to the role of viscous hydrodynamic dissipation, which gains importance when response is larger. The differences in peak height across the operating cases reflect the amounts of aerodynamic damping at play and are in general agreement with the values of ζ shown in Figure 2.31. However, minor apparent inconsistencies manifest, such as the larger resonant motion damping of case g) compared to case F). These, along with the undulating shape of the peaks, are due to a significant roll-pitch coupling arising from the rotor gyroscopic effect, that causes an increasing participation of roll in the system's dynamic response when rotor speed and/or motions are large.

2.3.3.5 Aerodynamic damping dependencies

The results presented in 2.3.3.3 and 2.3.3.4 suggest that the aerodynamic damping of pitch motion significantly depends on the turbine's operating parameters, namely rotor speed and incident wind speed (relative direction also matters, which is not treated here). Rearranging the results in terms of tip-speed ratio can help in understanding the underlying patterns. This is accomplished by extracting the values of ζ corresponding to the 2^{nd} pitch oscillation from the curves shown in Figure 2.31. These values are displayed as a function of TSR in Figure 2.33. The most striking feature of this graph is that for TSR < 2.5 the main parameter influencing ζ is wind speed, with ζ positive function of U, whilst damping is relatively insensitive to changes of rotational speed. Conversely, for TSR > 2.5 it is the rotational speed that mostly influences the damping ratio.

In the light of the blade profile-scale analysis of Appendix C, the dependence of damping

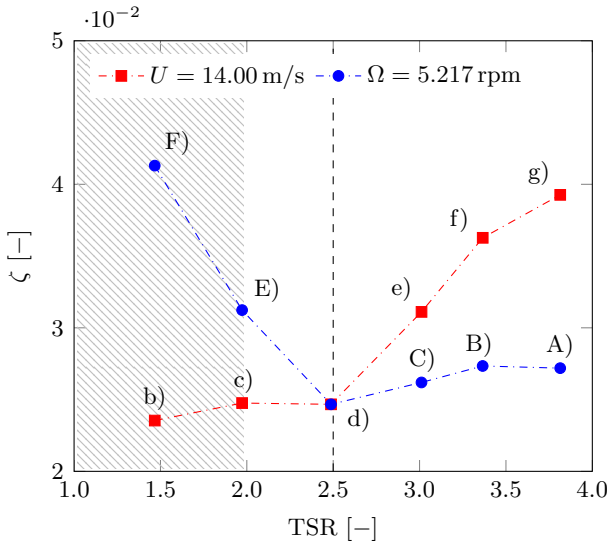

Figure 2.33: Damping ratio of second pitch oscillation for varying tip-speed ratios.

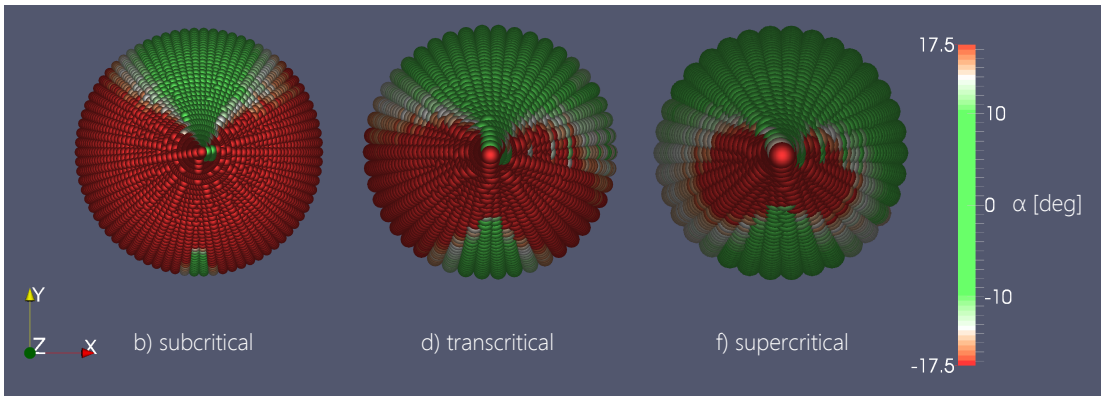

Figure 2.34: Top-down view of airfoil angles of attack for all blade azimuths on a Darreius wind turbine.

from U can be associated to the drag mechanism, whilst where damping is most affected by Ω the variations can be mainly attributed to lift forces. This identifies a critical TSR ≈ 2.5 where a shift occurs between a drag-dominated and a lift-dominated regime. The shaded area in the figure represents the region where the fidelity of the DMST model is challenged by increasing flow complexity (see 2.2.3), which prompts for a more careful interpretation of the model outputs. This range is nonetheless retained in the analysis for its significance with respect to typical cut-out conditions, i.e. point F). Within this region, the qualification of aerodynamic damping bears on the numerical model itself than on the real-life VAWT system.

In support of the above interpretation, Figure 2.34 shows the distribution of the angles of attack over a 360 ° blade sweep for three selected operating conditions, using a bottom-fixed turbine. Any datum with $|\alpha| \leq 10\,°$ is coloured in green denoting attached

flow in the linear region of $C_L(\alpha)$ (cf. Figure C.2). The green-white-red transition defines local angles of attack with $|\alpha| \in]10, 17.5[^\circ$, where the flow is attached and the slope of the $C_L(\alpha)$ function is generally declining. $|\alpha| = 17.5^\circ$ is the critical angle of attack for which C_L reaches its maximum. Beyond this point – the red areas in the figure – stall occurs and the airfoil is no longer capable of reacting to an increase in the angle of attack with an increase in lift force. The lift-induced damping mechanism breaks.

The azimuth regions generating most aerodynamic damping in pitch are upwind and downwind, respectively to the left and to the right of the sweep plots of Figure 2.34. In the subcritical operating condition b) the blades are stalled over most of the upwind and downwind sweeps. This in turn implies that the lift-based damping mechanism is marginal, and that aerodynamic damping in pitch mainly arises from U-dependent drag (affecting both blades and tower). In the transcritical case d) part of the upwind/downwind sweep occurs in attached flow regime and part is stalled. Finally, the supercritical operating condition f) is characterised by mostly attached flow over a blade sweep: here the Ω-dependent lift mechanism becomes most important in determining aerodynamic damping.

2.3.4 Experimental validation

The validation of the coupled dynamic simulations carried out with CALHYPSO has been made possible by EDF's participation to the VALEF2 initiative, which unites a consortium of French firms around the subject of coupled FWT modelling. The subset of cases reported in this section regards the analysis of the motions of the 'experimental' variant of the Dutch Tri-floater, mounting a downscaled NREL 5 MW turbine. The experimental campaign and physical mode set-up are described in 2.1.5.

2.3.4.1 Loading cases

Regular long-crested wavetrains directed in the positive x direction (using the same convention of Figure 2.16) are used to hydrodynamically excite the structure in the loading cases selected for the validation. When wind excitation is introduced in the experiments, a homogeneous, low-turbulence ($\sigma_x < 4\%$ over the rotor-swept section located about 2 m downstream of the nozzle outlet) wind profile is generated in line with the waves, while the rotor operates at the thrust-matched nominal condition. This level of turbulence is ignored in the numerical model, where the incident wind speed is assumed constant. Table 2.9 specifies the incident wave and wind combinations used in the numerical model. It should be noted that the wind speed is corresponds to the

Table 2.9: Regular wave and constant wind loading cases considered.

Wave height [m]	Wave period [s]	Wind speed [m/s]
0.69	7.01	0.0
0.92	7.87	0.0
2.32	12.57	0.0
2.78	13.92	0.0
3.68	15.60	0.0
4.23	16.75	0.0
5.51	18.85	0.0
6.53	21.04	0.0
0.66	7.01	11.2
0.91	7.84	11.2
2.32	12.57	11.2
2.79	13.92	11.2
3.68	15.60	11.2
4.37	16.91	11.2
5.52	19.25	11.2
6.54	21.04	11.2

selected full-scale operating point rather than the thrust-matching laboratory value[10].

2.3.4.2 Numerical model inputs

The comparison of numerical and experimental outputs is carried out at the full scale, which is also the scale of choice in dimensioning the numerical model excluding the choice of the Morison hydrodynamic coefficients. As done in 2.3.2, a plate axial drag coefficient of 5.7 is adopted from Philippe et al. [86]. As explained next in 2.3.4.3, a numerical limitation of the diffraction and radiation solver used prompted the conception of a special methodology for the treatment of the particularly thin heave plates mounted on this platform. This combines with the large-angle inclination method when wind overturning is present (2.3.2.1). Table 2.10 reports the imposed full-scale operating parameters of the turbine, which reflect the neglection of stator torque and tower drag. Moorings are modelled with the diagonal stiffness coefficients provided by the parameter identification carried out by Philippe [153], which correspond to $\mathrm{K}_{11}^{\mathrm{m}} = 6.5 \cdot 10^4\,\mathrm{N/m}$, $\mathrm{K}_{22}^{\mathrm{m}} = 6.5 \cdot 10^3\,\mathrm{N/m}$, and $\mathrm{K}_{66}^{\mathrm{m}} = 6.3 \cdot 10^7\,\mathrm{Nm/rad}$.

[10] See 2.1.5 for the description of the aerodynamic thrust matching procedure employed in this campaign.

Table 2.10: Numerical model input parameters chosen to represent the experimental turbine at the full scale.

Rotor speed [rpm]	12.1
Rotor thrust coefficient c_T [-]	0.866
Rotor torque coefficient c_Q [-]	0.0
Tower drag coefficient c_D [-]	0.0

2.3.4.3 Thin heave plate modelling

A hydrodynamic modelling challenge related to semi-submersible FWT platforms is the representation of the hydrodynamic behaviour of thin heave plates, as these may be difficult to handle with certain numerical diffraction and radiation solvers. In the report where the Dutch Tri-floater structure is first detailed [83], for instance, numerical instabilities are said to be encountered when the plates are included in the input geometry. Hence, the authors choose to increase the thickness to 1.0 m as a workaround for the generation of the hydrodynamic data base (HDB).
As an alternative, a Morison term may be used to estimate the loads on the plates as done for example by Philippe [153]. However, in the light of the size of these appendices and their proximity to the free surface, it can be expected that they may originate significant diffraction, as already discussed in (2.3.1). Thus, it is presently decided to include the thin plates in the diffraction/radiation problem; on the wake of Bulder et al. [83] it is observed that their presence causes numerical issues using NEMOH (v2.02) below a thickness of about 0.5 m. This problem is linked to the limited resolution available for the discretisation of the Green function in space [11].
As it will be shown in the following, the thickness increase workaround leads to significant errors while computing the hydrodynamic forces. As a consequence, a different strategy has been devised and verified for the representation of the thin plates. The present strategy uses linear extrapolation to derive the HDB terms at the target thickness based only on the reliable NEMOH outputs obtained for larger thicknesses.

Extrapolation of the hydrodynamic data base. Four wetted surface geometries are considered in the diffraction and radiation calculation. An example of the related meshes is reproduced in Figure 2.35 where a single floater column is shown. Hull mesh (A) represents the target geometry, brought at the full scale. The geometries characterising cases (B), (C), and (D) have been obtained by moving the upper and lower plate surfaces to $z = d_\mathrm{p} \pm t_\mathrm{p}/2$, where d_p is the original plate (mean) draft and t_p the modified plate thickness. A two-point linear extrapolation is used to recreate a new HDB (E) at the target thickness using the (B) and (C) values as inputs, as shown in Figure 2.36. The HDB values obtained for case (D) are only used for control purposes.

[11] The issue described is reportedly due to be resolved with the next version of the software.

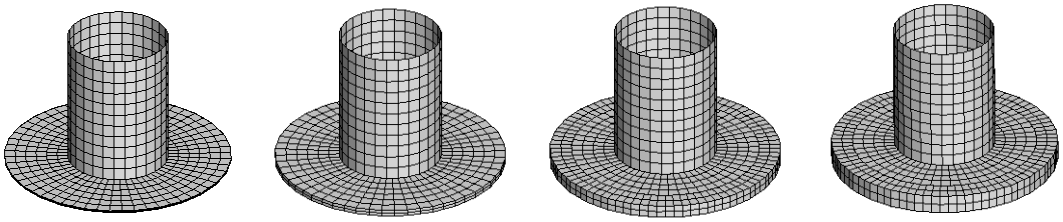

Figure 2.35: Mesh of column and heave plate with increasing plate thicknesses.

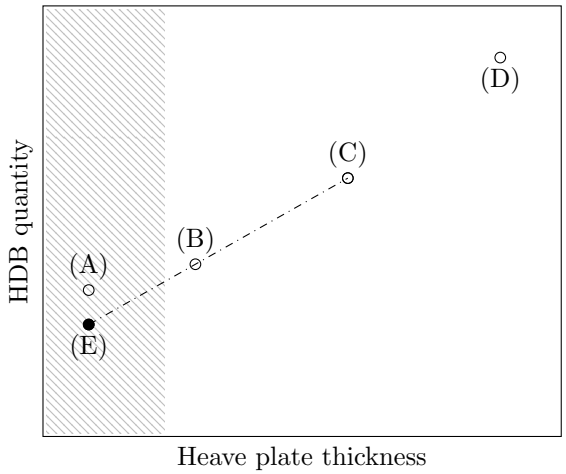

Figure 2.36: Sketch of linear extrapolation method. The extrapolated quantities are the real and imaginary part of the excitation force response amplitude operator, and all of the added mass and wave damping coefficients.

Application to the experimental Dutch Tri-floater The extrapolation strategy described is used to derive a reliable HDB for the thin-plated 'experimental' Dutch Tri-floater object of the case study detailed in 2.3.4. Table 2.11 specifies the thickness values used in this application. Figure 2.37 displays the in-plane force response amplitude characteristics (surge, heave, pitch) of the above defined cases as well as a few benchmarking points, denoted NWT, which have been obtained using EDF R&D's potential-flow, fully nonlinear numerical wave tank developed by Dombre [55], using $t_\mathrm{p} = 0.15\,\mathrm{m}$. In this case the first-order harmonic of the time-domain force signal was extracted using the Fourier transform.

Table 2.11: Heave plate thicknesses used while applying the extrapolation method to the 'experimental' Dutch Tri-floater.

Geometry	(A),(E)	(B)	(C)	(D)
t_p [m]	0.15	0.50	1.00	1.50

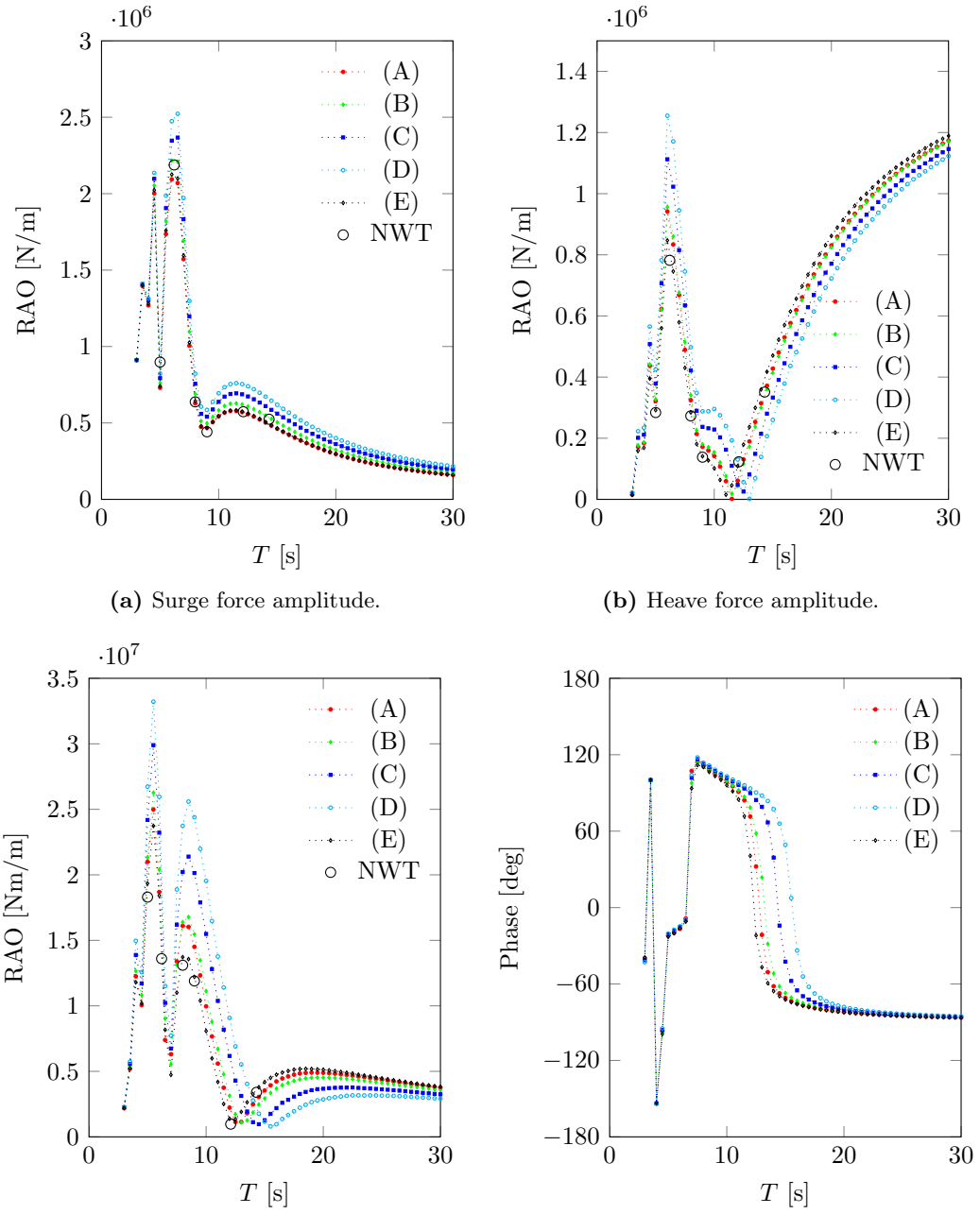

(a) Surge force amplitude.

(b) Heave force amplitude.

(c) Pitch moment amplitude.

(d) Pitch moment phase.

Figure 2.37: In-plane generalised force transfer functions of the experimental Dutch Tri-floater with wave propagation along the x axis (cf. 2.3.4).

Firstly, the tendencies found by increasing heave plate thickness can be said to be consistent and close to linear for cases (B), (C), and (D). The surge force tends to increase with thickness over all the studied range (Figure 2.37a), whilst heave and pitch excitation forces increase at low periods and decrease beyond the phase-shift regime found between 11 s and 15 s (Figures 2.37b and 2.37c). Secondly, it can be noted

that the results of the extrapolation procedure (E) are the ones in best agreement with the NWT. Compared to this, the direct resolution of linear fluid-structure interaction with NEMOH at $t_p = 0.15\,\mathrm{m}$ (A) exhibits a systematic error which manifests itself in the behaviour of the vertical quantities (heave, pitch). Another important remark is that the adoption of artificially thicker plates with a thickness of 1.00 m (C) induces very significant errors in the computation of all force RAOs across the studied range. An interesting feature is the observed behaviour of the pitch moment phase (2.37d): the phase is most sensitive to plate thickness between about 12 s and 16 s. The phase shifting range moves to increasingly higher periods when the plate thickness is increased.
The above comparison is repeated in Figure 2.38 for the diagonal hydrodynamic coefficients deriving from the solution of the wave radiation problem. On the added mass side, the coefficients steadily increase with plate thickness although with changes which are less dramatic than those characterising wave excitation, and suffer only a modest overestimation if the 1.00 m thickness approximation (C) is used. Figures 2.38a, 2.38b, 2.38g, and 2.38h also confirm the equivalence between (A) and (E) for horizontal quantities (surge, yaw). In the vertical motion domain, HDB (A) shows a rebound in the value of the heave and pitch added mass coefficients compared to (B) which is likely a numerical artefact (Figures 2.38c, 2.38e). The wave damping coefficients are also varying less than the excitation forces; here we limit our remarks to a warning: both (A) and (E) produce slightly negative, unphysical results in the central band when vertical motion coefficients are concerned (Figures 2.38d, 2.38f).

Based on the above evidence, the extrapolation method denoted by (E) is retained in the calculation chain.

2.3.4.4 Results and discussion

As usual the point of resolution of rigid-body motion in the fixed frame is chosen at the centre of the undisturbed system's waterplane area at the operating draft, whilst the output motions are computed at the CoM and treated with Equation 2.19 to obtain the response amplitude transfer functions.

Waves only. A comparison of the simulated and experimental in-plane motions in regular waves with no incident wind is provided in Figure 2.39, which exhibits a satisfactory agreement between the two. The estimated uncoupled natural frequencies ω_n are indicated for each DoF. In Figure 2.39a the surge motion amplitudes obtained numerically closely follow the experiments, with no apparent over/underestimation patterns. Figure 2.39b reveals two moderate mismatches in the low-frequency band for heave. Firstly, the apparent convergence of the numerical RAO slightly below unit reflects a limited lack of low-frequency excitation which may be due to the model's inability to accurately represent the inertial wave forces at the intersection of the nu-

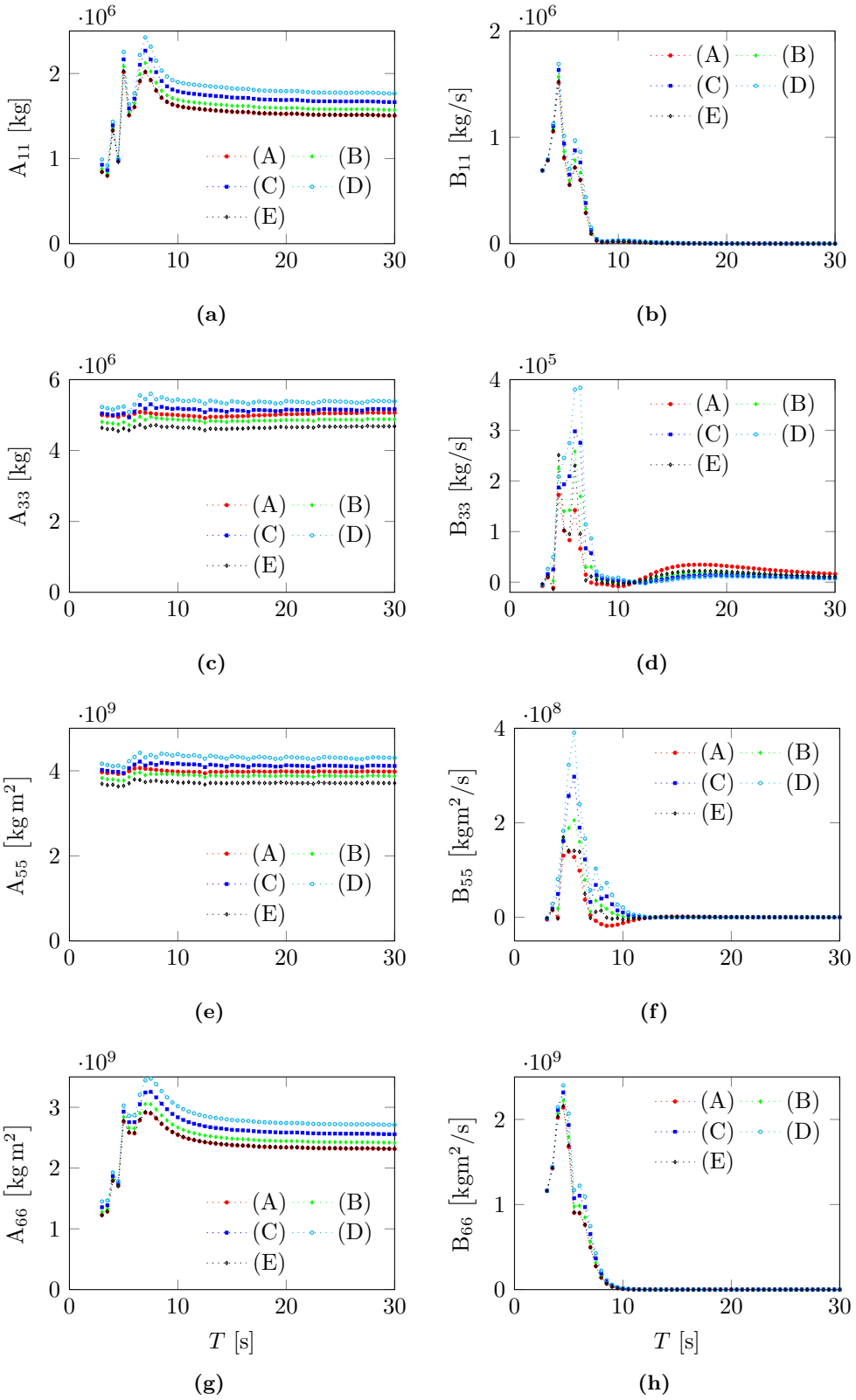

Figure 2.38: Diagonal hydrodynamic coefficients of the experimental Dutch Trifloater.

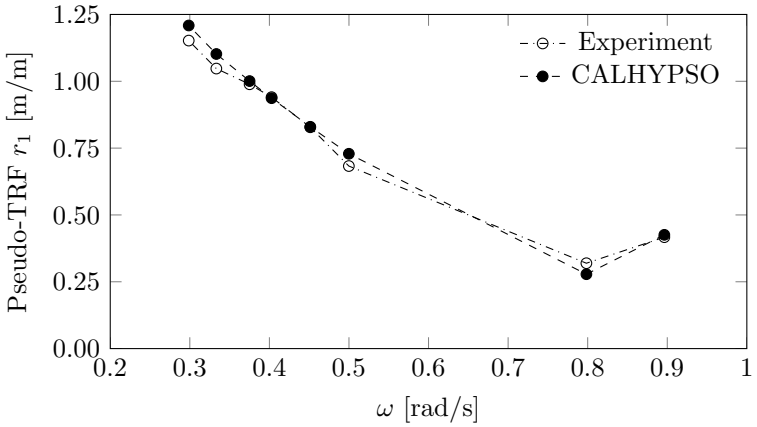

(a) Surge. $\omega_n \approx 0.13\,\text{rad/s}$.

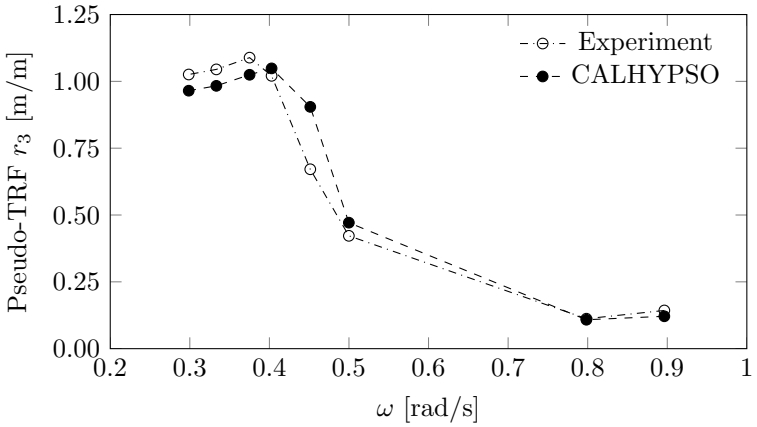

(b) Heave. $\omega_n \approx 0.45\,\text{rad/s}$.

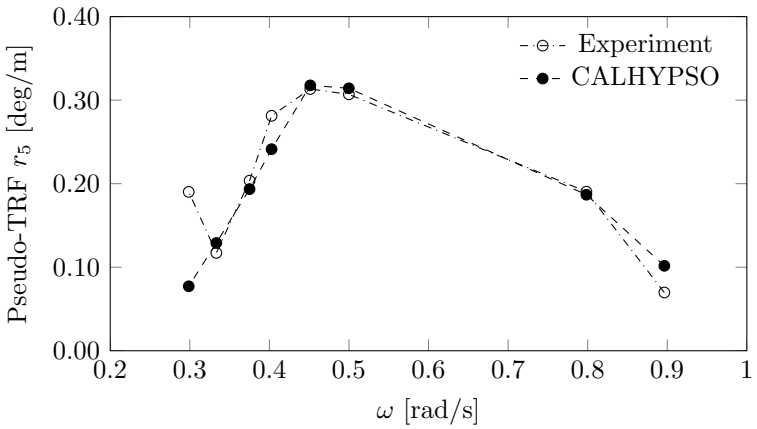

(c) Pitch. $\omega_n \approx 0.23\,\text{rad/s}$.

Figure 2.39: Measured and computed motion transfer functions of the Dutch Tri-floater under regular waves. The experimental response amplitude operators are a courtesy of the VALEF2 project consortium using data from Courbois [107].

merous hull bracings with the free surface. Secondly, the heave response characteristics suggest that the numerical natural frequency may be higher than the physical model's; this may be explained by the (uncalibrated) vertical added mass computation on the heave plates, which neglects the effect of flow rotation (cf. 2.1.3). Pitch response, plotted in Figure 2.39c, shows a good agreement with the exception of the extremity data points. Whilst both the numerical and physical models present a motion suppression region at low frequency, there appears to be a shift between the two. The delicate, markedly coupled[12] pitch dynamic equilibrium of the Dutch Tri-floater in this band (cf. 2.3.2.3) makes it difficult to pinpoint the possible causes.

Wind and waves. The plots of Figure 2.40 display the transfer function outputs of the coupled wind and wave cases for the same three DoF. It is important to remark that the mean leeward inclination predicted by CALHYPSO is significantly larger than the physical model's, more specifically 8.6 ° versus 6.4 °. This issue has been encountered by other partners engaged in the software benchmark and could be caused by the appearance of rotational mooring stiffness in the presence of thrust-induced line tension[13], which is not represented numerically.
Regarding the dynamic component of motions, the simulations predict the RAOs produced from the experiments relatively well, apart from the discrepancies discussed next. Surge response is well matched excluding the moderate numerical overestimation observable at low frequency in Figure 2.40a. This may be caused by a larger aerodynamic damping in the experiment (see 2.1.5.1). Similar to what is observed in regular waves only, Figure 2.40b reveals a possible natural frequency overestimation for heave, whereas dynamic response is well predicted for the rest of the spectrum. Figure 2.40c shows that the modelled and measured pitch response curves are in good agreement with errors mostly limited below 10%. Only in the vicinity of the resonance peak the physical model's response shows signs of larger dampening, which can be related to an experimental overrepresentation of the dynamic part of the thrust force (2.1.5.1).
Finally, comparing the pitch characteristics of Figures 2.40c and 2.39c one can recognise the pattern already observed in purely numerical form in the large-inclination coupling study presented in 2.3.2. The motion suppression region found in the waves-only case between 0.3 rad/s and 0.5 rad/s is characterised by sustained pitch response in presence of wind, when the thrust force causes a significant platform inclination and alters the coupled dynamic behaviour of the system. The multi-DoF aerodynamic coupling process detailed in 2.3.2 also concurs to determine the simulated pitch response, which is in agreement with the physical observations.

[12] Large surge motion produces a significant knock-on on the excitation-suppressed pitch motion.
[13] Both diagonal and off-diagonal pitch stiffness components may manifest since the fairleads are located above the free surface, and depart even farther from it when the structure is inclined by wind.

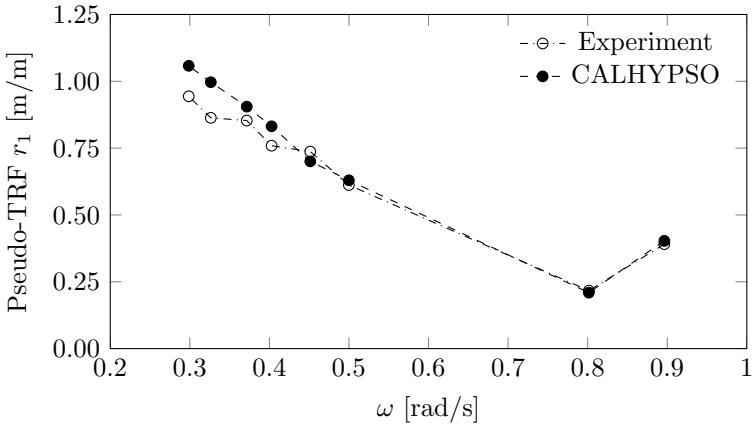

(a) Surge. $\omega_n \approx 0.13\,\text{rad/s}$.

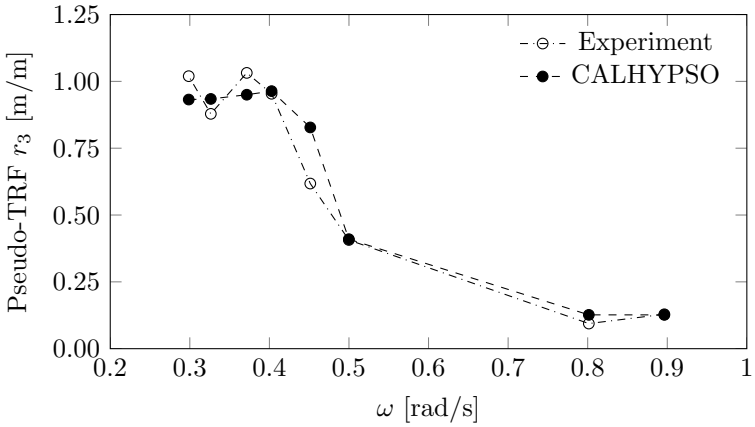

(b) Heave. $\omega_n \approx 0.45\,\text{rad/s}$.

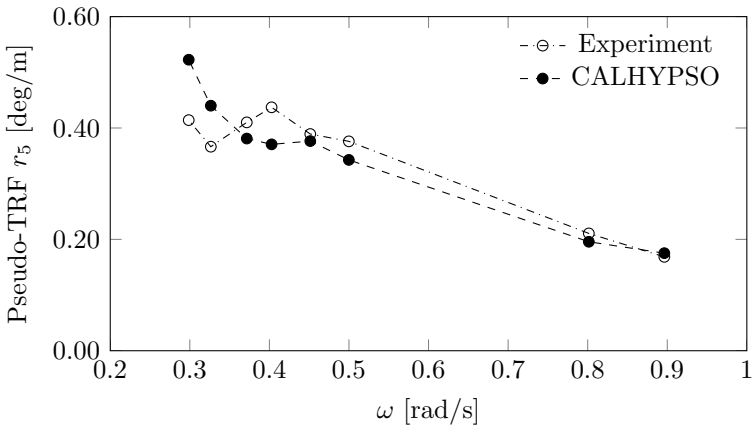

(c) Pitch. $\omega_n \approx 0.23\,\text{rad/s}$.

Figure 2.40: Measured and computed motion transfer functions of the Dutch Tri-floater under regular waves and wind. The experimental response amplitude operators are a courtesy of the VALEF2 project consortium using data from Courbois [107].

2.4 Conclusion

The use of CALHYPSO, EDF R&D's coupled aero-hydromechanical solver in conjunction with original methodologies has permitted to study a range of interactions between the aerodynamic and hydrodynamic processes with respect to their impact on global FWT motion. The numerical representation of part of these effects has been validated against scaled experiments. Among the forms of aero-hydrodynamic interaction which have been detected and characterised are the hydrodynamic regime alteration by the geometric nonlinearity associated to wind-induced platform inclinations, a form of inter-DoF aerodynamic coupling, and the aerodynamic damping of global motions of a floating VAWT. These findings have been the object of a set of publications [158–160]. The main conclusions follow next.

Large wind-induced inclinations. The hydrodynamically focussed frequency-domain study provided in 2.3.1 has shown for the first time that, in presence of large enough wind thrust, low-draft water entrapment plates undergoing vertical excursion alter the inertial wave loads on a FWT tri-floater. This phenomenon is significant when the semi-submersible platform studied reaches mean angles in the order of 5 ° or more, which can easily be attained by currently proposed concepts. It is shown that the small motion assumption customary in sea-keeping may no longer be valid, demanding a different modelling approach. The identification of the plate excursion effect has prompted further investigation by EDF using CFD methods to include viscosity and separation in the analysis, while other actors in the French ocean engineering community are planning bespoke basin tests for a better appraisal of this issue.

The use of a time-domain model with an inclination-dependent, yet linear implementation of potential-flow hydrodynamics complemented by position-updated Morison forces has enabled in 2.3.2 to evaluate the influence of wind inclination on the motions of the Dutch Tri-floater, a floating semi-submersible HAWT. Both in-line and cross wind-and-wave cases have been treated, showing that the geometric nonlinearity which descends from the leeward inclination of the FWT significantly affects dynamic response through the vertical excursion of the columns and water entrapment plates. With respect to the direction of wave propagation, in-plane response (surge, heave, pitch) is mostly affected for collinear wind and waves, whilst out-of-plane response (sway, roll, yaw) is shown to be altered by the application of cross wind. The present methodology has been successfully validated against existing experiments in 2.3.4. It should be noted that in normal operation the aerodynamic thrust acting on a HAWT reaches its maximum in the presently studied rated condition, which by consequence is the most sensitive to finite inclination couplings. For higher wind speeds thrust decreases again, likely causing the geometric linearity to become less important in highly energetic states.

An original classification of the wind-induced inclination couplings is provided in Ta-

Table 2.12: Summary of the observed wind-induced inclination effects on floating wind turbine dynamics.

Incl. effect	Nature of force	Location	Affected DoF	Bandwidth	LC type
plate excursion	hydro. inertial	plates	heave, pitch	wide	collinear
	hydro. viscous	plates	heave	narrow	collinear
	hydro. inertial	plates	roll	wide	cross
column excursion	hydro. inertial	columns	yaw	wide	cross

ble 2.12 in the light of the above described investigation. Further work will be required to broaden the characterisation of the inclination effects to cover more operating conditions, different highly compliant designs (e.g. a soft spar), and possibly the interaction of these phenomena with wind turbulence and rotor control. A high-level classification of FWT concepts may also be performed, for instance by evaluating their motion sensitivity to the inclination effects as a function of governing parameters such as the wind load to displacement ratio.

Given that the cost optimisation of FWT systems may keep pushing the allowable wind-induced inclinations further, the nonlinearities inherent to the coupled dynamic system are likely to increasingly manifest, especially in the highly dynamic, dimensioning loading cases. The dynamic modeller must then apply careful judgement: methodologies of increasing complexity will be required, likely departing from conventional offshore structure analysis. Although the present method can represent a computationally efficient alternative to treating geometric nonlinearity, higher-order resolution of fluid-structure interaction is likely required to accurately compute the hydrodynamic loads in the presence of larger inclinations. Nonlinear angular resolution of the EoM also becomes appropriate where angles exceed magnitudes of 10° to 15° and the linear superposition of rotations is no longer accurate.

Aerodynamic damping of pitch motion. The study presented in 2.3.3 has characterised the aerodynamic damping of a floating VAWT affecting its pitch motion in waves, exploiting the results of a set of dynamic simulations carried out with CAL-HYPSO. Special attention has been paid to post-treating the motion outputs because of the presence of a significant 2P (blade passage) response component. Decay simulations in particular have been handled with caution since one deals with 'excited' motion extinction: spurious phenomena can occur, such as resonance, which invalidate the common procedure for the calculation of the damping ratio.

The aerodynamic damping in pitch supplied by the operating rotor has been found to depend on both incident wind speed and rotor speed. It amounts to about 2%–4% of the critical damping and provides a reduction in peak pitch response of 25% to 50% for the studied wave conditions. The damping ratios emerging from the decay simulations are consistent with the results of the simulations in regular waves, and their dependencies

reveal the contribution of both lift- and drag-induced damping mechanisms. These have been shown to function in an essentially linear fashion, a finding that is in agreement with the experimentally observed behaviour of a floating HAWT (see Le Boulluec [102]) and with the analytic considerations given in Appendix C.

To the Author's knowledge, the aerodynamic damping affecting the pitch motion of a floating VAWT has been scrutinised for different operating conditions for the first time. Analysing the dependencies of the damping ratio indicates that it exists a critical tip-speed ratio below which drag dominates the variations in damping, while lift forces explain the variations above the critical TSR. A thorough understanding of the knock-ons of varying aerogenerator operating regimes on platform motion may provide an extra tool to achieve motion mitigation by integrated floating system design.

It is important to notice that these results and interpretations do not necessarily represent the physics of a real FWT system, but rather the behaviour of a numerical model (Paraschivoiu's DMST) that is widely used across the industry. The represented aerodynamics do not give account of the rotor wake structures, which are expected to affect the loads especially in the low TSR region. The computational model used is also known to lose validity at very high tip-speed ratios because of the inadequacy of the momentum equations beyond a certain threshold, although these are located outside the studied operating envelope. Moreover, the non-stationarity due to platform motion is treated under the quasi-steady hypothesis; a model upgrade to account for dynamic inflow should be considered for an improvement in accuracy. Further numerical, and possibly experimental investigation on the aerodynamic damping of floating VAWTs will be required to verify and validate the phenomena shown.

Part 3

Finite-element Analysis of Floating Wind Turbine Moorings

This Part presents the work carried out in the field of mooring system modelling, which consists in the development of a workflow based on EDF R&D's finite-element (FE) tool *Code_Aster*, enabling the static and dynamic analysis of mooring systems for floating wind turbines. After the introductory Section 3.1, the numerical methodology underpinning this study is explained in Section 3.2. Insights are there provided with respect to the main *Code_Aster* functions used to build the model and the related assumptions. Section 3.3 moves on to describing the procedures developed to unlock the mechanical representation of a mooring system in the given computing environment. A range of applications is then provided with Section 3.4, demonstrating the model's capability to represent the main static features of catenary FWT mooring systems. The focus moves onto dynamics in Section 3.5 where an articulate case study is presented, corroborated by experimental data, ultimately attesting the dynamic performance of the model. The conclusive remarks for this Part are drawn in Section 3.6.
The work described in this Part is included in a technical report of EDF R&D by Peyrard and Antonutti [161].

3.1 Introduction

The station keeping of a floating wind turbine is achieved by transferring the mean horizontal loads, which are dominated by wind thrust, to the seabed. The mooring system, defined as the ensemble of components involved in the load path from the fairleads to the soil, must be designed to resist cyclical and extreme loads with adequate safety and, if required, a redundancy margin. For a general and relatively up-to-date introduction to offshore mooring systems and their functions, design, and certification, the reader may refer to Chakrabarti [162].
The most common type of mooring system found in permanent offshore applications uses the catenary principle (Figure 3.1, left) to produce horizontal restoring, exploiting

the gravitational potential of a heavy suspended line. On the contrary, the restoring power of taut mooring arrangements (Figure 3.1, right) primarily relies on the elasticity of the mooring lines. In this case, significant rotational restoring power may become available, combining with the floating structure's hydrostatic stiffness. Whilst the MW-scale FWT prototypes installed to date (Hywind, WindFloat, and the units installed at Goto and Fukushima) employ slack chain moorings, semi-taut, taut or tensioned arrangements are also considered for floating wind applications. Examples of such station-keeping solutions are found for instance within the DCNS Sea Reed design, or in the Glosten PelaStar concept.

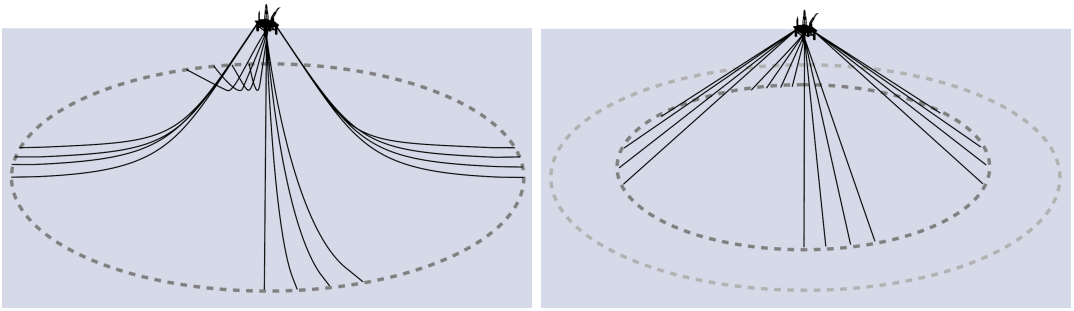

Figure 3.1: Catenary (left) and taut (right) mooring arrangement a classic offshore platform, after Vryhof Anchors [163].

Although offshore renewable energy inherits considerable know-how from classic offshore engineering, which has developed around the oil & gas business, important distinctions must be made which clearly bear an impact on mooring design. In classic offshore, loss of station during operation is often a high-impact catastrophic event, potentially endangering human lives and entailing severe environmental consequences especially if the structure is used to handle dangerous fluids. A broken oil riser caused by excessive horizontal displacement or a faulty wellhead disconnection are elementary examples of environmentally critical events.
In the case of floating wind, the mooring system risk assessment may lead to different outcomes. A partial mooring failure threatens the integrity of the umbilical cable first; its loss certainly represents an economic damage for the stakeholder, but may not come with a critical risk for human safety or the environment since FWTs are unmanned and do not contain significant amounts of hazardous fluids. A full loss of the station-keeping system poses a threat to the remaining units in the windfarm as well as to maritime traffic, other than being likely catastrophic for the concerned turbine. All in all, the safety requirements of this novel application need to be reassessed, suggesting a potential reconsideration of current engineering practices: already envisaged in the current standards is the proposition of unconventional arrangements, provided that a sufficient level of safety be demonstrated by the applicant (cf. for example [47]) – a

task which demands accurate simulation tools; a possible outcome could also be the acceptance of less conservative design approaches, although the added cost of insurance may become a significant obstacle. At the same time, offshore renewable installations are subjected to a higher pressure for project cost reduction compared to their counterparts. Moorings are a significant cost driver: recent studies estimate that the mooring system cost (including its installation) may represent 5%–15% of a floating windfarm's CAPEX [33]. Once again, the optimisation of a FWT mooring system relies among other factors on the accuracy of the front-end simulations for engineering design.

The design of a permanent floating windfarm mooring system that is low-maintenance, sufficiently reliable, and optimised for cost hence challenges the existing practices and holds large potential for improvement by R&D. Given the above context, a thorough understanding of its mechanical behaviour in the highly dynamic conditions found offshore becomes fundamental. The current state-of-the-art software for the design and analysis of offshore mooring systems (e.g. OrcaFlex, aNySIM, Flexcom, FASTlink[1], etc.) typically include dynamic simulation capabilities; the marked nonlinearity characterising mooring line mechanics imposes the use of time-domain methodologies for the resolution of the system's motion in dynamic form.

As it will be confirmed once more by the results of this study, the historical quasi-static approach to mooring modelling (documented for instance by Faltinsen [164]) cannot guarantee a reasonably accurate prediction of the line tensions in conditions relevant to line dimensioning, in other words dynamic effects dominate the tension variance. This is especially true in domains where high energy and high deformability coexist, such as floating systems for wave energy conversion (see for example Johanning et al. [165]) and deep-water offshore applications, as remarked by Mavrakos et al. [166] and Lin [59]. Also, since floating renewable energy structures tend to be subjected to higher and more dynamic environmental loads (relative to their displacement) compared to conventional offshore platforms, the role of mooring system dynamics in determining the global dynamic response may become increasingly important, requiring accurate simulation of inertial and damping retroactions on the floater. For example, the excitation of the platform modes by unsteady aerodynamic loading or difference-frequency wave loads may cause low-frequency resonant motion, whose amplitude can be governed by mooring system dissipation for lightly damped platform DoF (see for instance [136], [162]).

The *Code_Aster*-based dynamic mooring simulator presented in this Part joins the modelling toolbox currently developed by EDF to enable comprehensive R&D support to the *Provence Grand Large* project and the subsequent floating wind deployments of the Group.

[1] A simulator coupling NREL's code FAST and OrcaFlex.

3.1.1 Finite-element modelling of floating wind mooring systems

After about half a century of offshore engineering experience, the role of dynamics in the mechanical behaviour of mooring systems is vastly documented. It is commonly accepted that the quasi-static representation of mooring lines becomes too inaccurate for the sake of engineering design when the motions of the structure are highly dynamic, when drag-intensive components are used (for instance, a mooring chain), when water depth exceeds about 150 m, or with any combination of the above [167]. In such cases, the dynamic effects due to inertial, hydrodynamic, and seabed contact loads are known to magnify the dimensioning extreme and cyclical tensions of offshore mooring lines.
These guidelines apply directly in the floating wind context and dictate the use of dynamic simulation tools, especially when mooring system mechanics are included in the focus of the analysis. Past research (see for example Karimirad [65]) has shown that the dynamic mooring effects tend to bear a limited impact on FWT motion, due to the economical limitations to the practicable water depth – presently a few hundred metres at the most. Yet even in these conditions the impact on platform motion may become observable for extreme sea states, as pointed out by Masciola et al. [85] through a numerical and physical modelling campaign assessing the dynamics of the DeepCwind-OC4 concept. Increasing the water depth beyond this range rapidly augments the sensitivity of platform motion to the mooring system dynamics, as reported by Matha et al. [167]: for instance, a lumped-mass model is used by Lin [59] to reproduce the coupled mooring-platform response of a spar FWT, using slack chains, for increasing water depths (320, 600, and 900 m) confirming the growing importance of dynamic line tension in determining the global response. A different picture can be drawn for the dynamic effects on mooring line tension: among others, Coulling et al. [84] and Masciola et al. [85] demonstrate that the quasi-static tensions severely underestimate experimental measurements even at the limited depth of 200 m and for operational met-ocean conditions.
A recent review of the dynamic mooring line theories developed so far is provided by more recent work by Masciola et al. [168], distinguishing three main categories: lumped-mass, finite-difference, and finite-element. Literature shows that both the popular finite-element and lumped-mass theories provide accurate tension predictions when FWT simulation is concerned, although with more stringent resolution requirements by the latter approach [59, 168].
The finite-element method has been chosen by numerous authors in the FWT dynamic mooring modelling field. A study by Jeon et al. [169] evaluates the response of a spar-type FWT using a catenary system, evidencing the extensional vibrations of the mooring lines. The dynamics of large multi-turbine platforms are analysed by Kallesoe et al. [170] and by Kim et al. [171] incorporating a FE moorings model. Finite bar-type elements are used in the coupled simulations of Cheng et al. [172]

to assess different VAWT arrangements, and by Bachynski et al. [173] to determine the severity of transient, wind turbine fault-related events on mooring tension. Coupled motion response and dynamic mooring tensions are obtained by Zhang et al. [174] for a MW-sized HAWT on a small semi-submersible platform, also using the FE method to represent mooring dynamics. The global effect of the hydrodynamic damping forces exerted on the mooring lines is characterised in the work of Hall et al. [175] for a spar-type FWT using a nonlinear cable model. A tension-leg system has also been studied with the FE approach by Bae and Kim [176], allowing to bring out the effects of 2^{nd} order sum-frequency wave excitation on structural response. The outputs of coupled simulation software using a range of different mooring theories are benchmarked in a report by Jonkman et al. [177].

A promising alternative for the representation of mooring dynamics is the multi-body formulation, as maintained by Borg et al. [44] and Muskulus [178], which may enable a reduction of computational effort compared to FE resolutions. For example, Matha et al. [167] use this representation to demonstrate the onset of hydrodynamic non-linearities in the behaviour of a FWT due to dynamic mooring effects.

3.1.2 Code_Aster

Code_Aster is EDF R&D's all-purpose open-source FE solver for the thermo-mechanical study of structures [60]. After over 20 years of development, this software offers in the order of 400 finite element typologies for the discretisation of solids and a broad range of solvers, all features which are thoroughly tested and validated. It most notably enables the static, dynamic, and vibrational analysis of mechanically loaded structures as well as modal analysis.

The current study looks to employ the nonlinear capabilities of this software to represent the static and dynamic behaviour of floating wind turbine mooring lines, which are intrinsically characterised by nonlinear kinematics due to the presence of large displacements and intermittent seabed contact. The features peculiar of mooring system modelling which are not readily available in the classic *Code_Aster* workflow have been implemented by manually augmenting the command file with the necessary scripts, and by developing practical methodologies based on appropriate sequences of simulations.

Although *Code_Aster* is written in French language, the interested anglophone reader can acquire a grip on this software by consulting specialised wiki pages which provide examples and tutorials, such as [179]. Two related manuscripts have also been recently published which are rich in hands-on examples [180, 181].

The version of the software employed for this study is 12.2.10 (development release). Part of the ongoing developments, which will be integrated in the next versions of *Code_Aster*, consists in the implementation of drag forces over 1D elements whose underlying formulation is outlined in 3.2.4.

3.1.3 DeepCwind-OC4 experimental campaign

An experimental campaign was conducted at MARIN's wind and wave basin with the aim of calibrating and validating a coupled offshore hydromechanics model implemented in NREL's FAST. Its outcomes are documented by published work by Masciola et al. [85] and Coulling et al. [84], where the outputs of different numerical implementations are compared to the measurements. Other authors have recently utilised this campaign for the sake of numerical model validation, using both the finite-element [182] and lumped-mass [183] approaches to dynamic mooring modelling.
Object of this campaign is a $1/50^{\text{th}}$-scale model of the DeepCwind-OC4 FWT (Figure 3.2), which consists in a NREL 5 MW aerogenerator mounted on a three-column semi-submersible platform, operating at an equivalent water depth of 200 m[2].

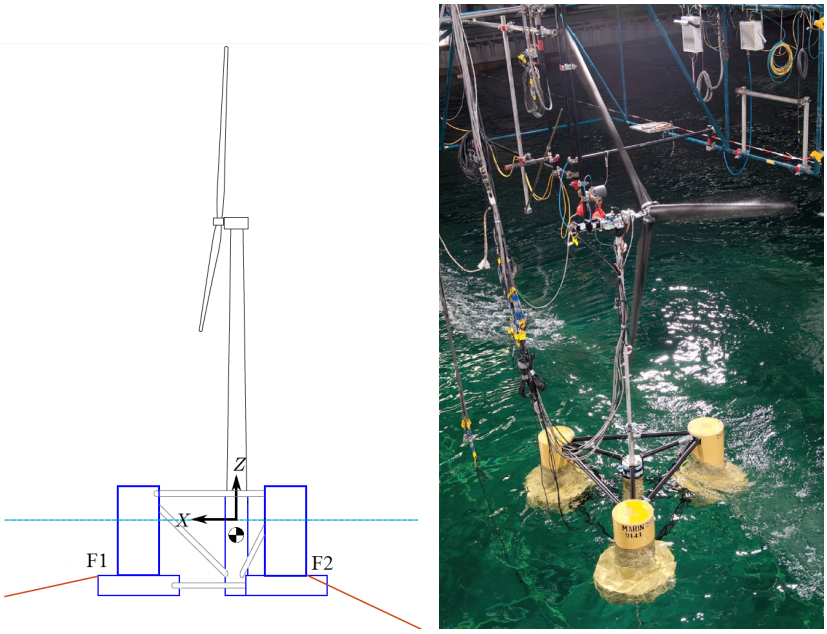

Figure 3.2: Sketch of the DeepCwind-OC4 floating wind turbine (left) and a picture of the scaled model under the action of wind and waves (right). Reproduced from Masciola et al. [85] and Coulling et al. [84].

Included in the physical model is a downscaled mooring system, realised with a brass chain, which closely resembles the full-scale three-leg arrangement specified in [137]. Load cells mounted at the fairleads provide the mooring tension signal. The series of experiments carried out includes free-decay, pull-out, wind-only, wave-only, and coupled wind-wave tests; the numerical model benchmarks clearly exhibit the limitations of the quasi-static mooring modelling when it comes to assessing the dynamic tension ranges. A subset of these experiments is used in Section 3.5 to validate the presented dynamic simulation model and the underlying methods.

[2]The same platform geometry is employed in Part 2 in conjunction with a vertical-axis wind turbine.

3.2 Methodology

The finite-element method enables the spatial discretisation of a continuum, reducing the DoF of a solid to a finite set which can be treated numerically. A corresponding set of equations written with respect to the system's nodal DoF is then used to seek the static or dynamic equilibrium configuration of the structure, under any given combination of external loads and constraints.

3.2.1 One-dimensional discretisation

The centrepiece of the proposed methodology is the homogeneous, 1D finite element denoted 'CABLE' available in *Code_Aster*, which was originally developed to simulate the mechanical behaviour of overhead electrical lines [184]. This two-node element is a version of the classic 'bar' element, adapted to the large displacement context; as it is explained in the following, this makes it suitable for representing highly compliant mooring lines.

As discussed above, cables represent only one of many modelling possibilities: a simpler and widespread option for dynamic mooring modelling is the lumped mass with spring and damper connections, which requires higher mesh resolution than a cable. Whether this approach can be successfully implemented in *Code_Aster* remains to be investigated. On the other side, the next FE type in terms of complexity is the beam. Large-displacement beams are available in *Code_Aster* – which may be used to model mooring lines characterised by significant bending, torsional, or shear stiffness – but have been shown to be prone to error accumulation when undergoing repeated large rotations. They also prove overcomplex when the mooring line's dominant mechanical resistance is axial: a beneficial feature of cables with respect to beams is in fact the halving of the global DoF at the nodes (rotational DoF are unassigned) which preserves computational efficiency.

It should be finally noted that the absence of rotational reactions which characterises the CABLE is a reasonable modelling hypothesis only for mooring line types which oppose negligible resistance to bending and torsion. Whilst this is generally accepted for chains [61], the behaviour of less flexible lines operating at low tension such as short and stiff rope segments may not be accurately represented under this assumption, especially in the vicinity of rotational constraints. Focussing on bending and assuming a linear isotropic material and a constant line section, the classic beam theory provides the governing parameter which if large enough causes elastic behaviour, the segment's relative bending stiffness EI/L. This is defined by the material's Young's modulus E, the sectional bending inertia I, and the characteristic length of the segment L. In presence of a low (homogeneous) tension T, this term may no longer be marginal with respect to the contribution of geometric bending stiffness, which is proportional

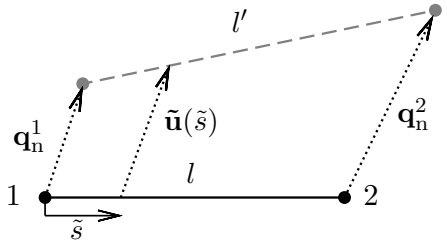

Figure 3.3: CABLE element before and after application of nodal displacements.

to TL and usually dominant in the reactive balance of a tensioned mooring line. The underlying assumption of bending-soft segments may be then written as $EI/L \ll TL$.

3.2.1.1 Finite element constitution

A CABLE finite element is defined as a straight, two-node segment of length l with a constant cross section of surface area A. The element's sections are supposed to be undeformable and to maintain a constant orientation in the local frame. Used in 3D space, a CABLE disposes of six nodal DoF in the global inertial system of reference, which correspond to the nodal translations $\mathbf{q}_\mathrm{e} = [\mathbf{q}_\mathrm{n}^1; \mathbf{q}_\mathrm{n}^2]$ (Figure 3.3). Linear shape functions $\mathbf{L}$ are used to express the internal displacement vector $\tilde{\mathbf{u}}$ in the global frame as a function of the normalised axial position on the element, $\xi = \tilde{s}/l$, as

$$\tilde{\mathbf{u}}(\xi) = \mathbf{L}\mathbf{q}_\mathrm{e}\,, \tag{3.1}$$

using

$$\mathbf{L} = \begin{bmatrix} 1-\xi & 0 & 0 & \xi & 0 & 0 \\ 0 & 1-\xi & 0 & 0 & \xi & 0 \\ 0 & 0 & 1-\xi & 0 & 0 & \xi \end{bmatrix}. \tag{3.2}$$

The mechanical reaction tensors characterising the system of interconnected cables can be obtained by applying the Lagrange equations and hence assembling the DoF-matched individual element contributions with the same procedure illustrated in 4.2.1. In this case, however, no basis change is necessary thanks to the purely translational constitution of this element type, which allows to write the kinematics directly in the common global frame.

CABLE elements react to axial deformation only. Statically, the relationship between tension T and strain ϵ is simply given by

$$T = E\epsilon A = \frac{\Delta l}{l_0} EA\,, \tag{3.3}$$

where l_0 is the length of the element when the axial load is nil and $\Delta l = l' - l_0$. Both T and ϵ are constant over the element length. The *Code_Aster* implementation of CABLE incorporates an option enabling to assign different Young's moduli for tension and compression. When chains and flexible ropes are modelled, it is appropriate to set the compression modulus to zero [61]. This permits to incorporate the nil compression stiffness associated to chain link separation or to the buckling of a soft rope segment.

3.2.1.2 Discretisation by cables

In this study the geometry of any mooring line segment is discretised along its length with an arbitrary number of cable elements, as shown in Figure 3.4, where the extremity nodes A and F represent the anchoring point and the fairlead respectively. As the

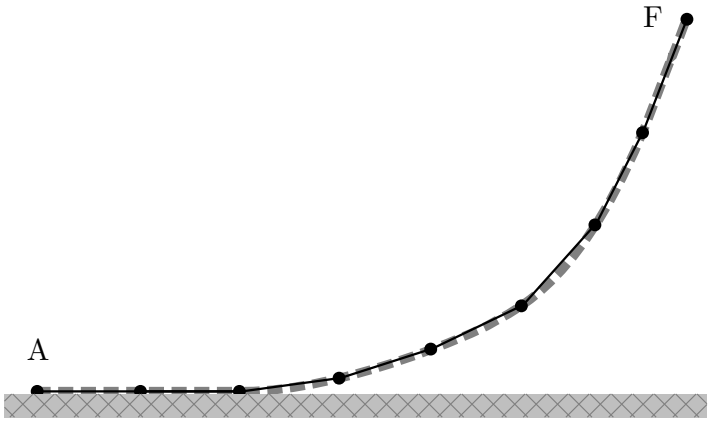

Figure 3.4: Mooring line (grey dashes) and its discrete representation (black).

elements have a first-order deformed shape, both the undisturbed and deformed states of a cable are straight lines connecting two nodes. In principle, this implies that the mesh resolution required to represent any curved topology must be larger where the expected radii of curvature are smaller. Other criteria dictating the minimum mesh resolution are the accurate representation of longitudinal changes in the properties of the line and the combination of mesh resolution with the wave kinematic field differentials.
Finally, it should be remarked that in the present model it also exists an upper limit to mesh resolution, caused by the increasing numerical instability affecting the dynamics of small-length cable elements, particularly in presence of seabed contact. In practice, beyond a certain mesh resolution the numerical instability arising from contact shocks becomes so strong that the amount of algorithmic damping required to stabilise the simulation starts to be significant with respect to the physical damping in the system, which is essentially provided by drag.

3.2.2 Large displacements

The presence of large displacements, whether due to deformation or rigid-body kinematics, introduces a nonlinearity in solid mechanics, causing the classic linearised methods to lose their ability to accurately describe the displaced configuration of the structure. When the finite-element method is used, writing the rotation kinematics is also more complex because large rotations in 3D space cannot be represented with a vector. They become in fact non-commutative and must be treated with more complex methods such Euler angles or quaternions [185]. In the present model this only affects the support beam elements (3.3.4), since the rotations of the CABLE elements take place implicitly, following the nodal displacements (3.2.1.1).

Code_Aster treats the large displacements with the updated Lagrangian method (UL) originally introduced by Bathe and Bolourchi [186], which operates a reactualisation of the structure's geometry at every Newton-Raphson iteration. Contrary to the classic static representation of matrices in linear solid mechanics, the assembled system matrices are continuously recalculated. An example application of the updated Lagrangian method to a 1D element is next given with reference to Figure 3.5. The structure's

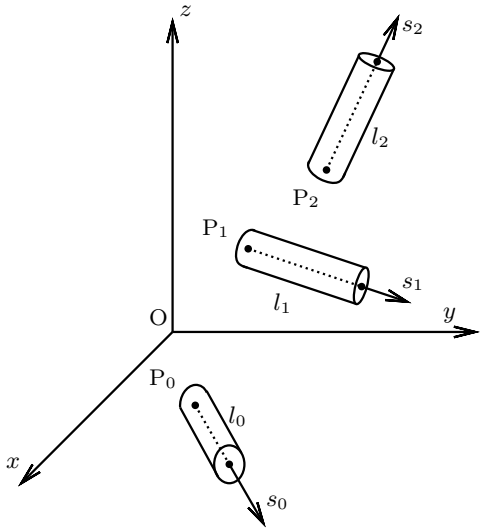

Figure 3.5: Large displacements of 1D element in 3D space. Adapted from Yang and McGuire [187].

response is represented in the global inertial system of reference, Oxyz, whilst the CABLE axial deformation takes place along s in the local frame Ps. We may define the initial, undeformed state of the element with the numeral 0, identifying an initial frame P_0s_0 and an element length l_0. It is then assumed that a new equilibrium must be found for the next instant in time, which is characterised by a different loading state. Let the configuration denoted with '1' be reached after a first Newton-Raphson iteration takes place (see Appendix D). The new coordinate s_1 will then be associated to the internal

strain of the element in the next iteration, whilst the local deformation is reset to zero as the new configuration with length l_1 becomes the reference geometry. The new reference stress state must naturally be nonzero to account for past strain in the definition of the element's geometric stiffness [185]. The following Newton-Raphson iteration is carried out by recalculating the system tangent matrix in the new configuration, leading to the next displacement guess at 2. The procedure is repeated until convergence is achieved within the time step.

3.2.3 Seabed contact

The interaction of a mooring line with the seabed is a complex subject which interfaces structural and geotechnical engineering. The state-of-the-art seabed theory proposes a combination of two non-linear dissipative phenomena for the representation of the reactive soil forces: lateral friction and uplift-repenetration resistance [61]. A model of this type is expected to provide a representation of seabed interaction which is accurate enough for the accurate assessment of the fatigue life of mooring segments located at the touchdown point, according to Randolph and Quiggin [188].
In the present study a smooth and rigid seabed model is used instead, which reduces contact to a reversible conservative phenomenon. Among the contact modelling options available in *Code_Aster*, this is the simplest and most robust. The introduction of dissipative contact is possible in *Code_Aster* and may be sought by further work; this will likely require the creation of shell elements to represent the seabed, and the assignment of a master-slave hierarchy between the mooring line elements and said shells (see the relevant documentation [189]).
Under the current hypotheses, the two variables governing surface contact are d, the clearance between the structure (e.g. a node) and the contact surface, and σ, the normal contact stress. The Hertz-Signorini-Moreau contact conditions are introduced (see for example [190]):

- Impenetrability (kinematic condition): $d \geq 0$.
- Non-negative contact stress (dynamic condition): $\sigma \geq 0$.
- Complementarity (energetic condition): $d\sigma = 0$.

Figure 3.6 represents these three conditions in graphical form. The resulting unilateral contact law is then expressed as

$$\begin{cases} d \geq 0 \\ \sigma \geq 0 \\ d\sigma = 0 \end{cases} , \tag{3.4}$$

which is satisfied in the domain visualised in Figure 3.7. The positive, semi-definite d-σ

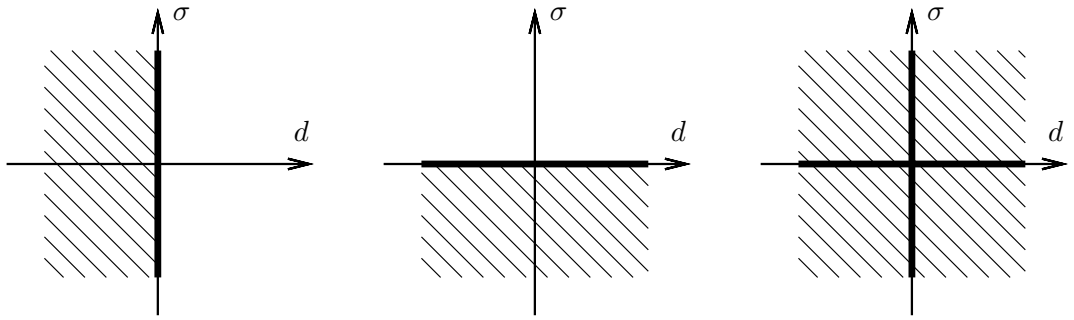

Impenetrability. Non-neg. contact stress. Complementarity.

Figure 3.6: Hertz-Signorini-Moreau contact conditions. White areas and thick black lines indicate where these conditions are verified.

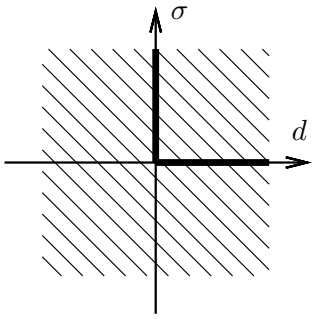

Figure 3.7: Unilateral contact law. Thick black lines indicate where this is satisfied.

relationship found is non-univocal and is not differentiable in $d = \sigma = 0$: these features make it a non-trivial numerical implementation. As it is further detailed in Appendix D, unilateral contact is introduced in the model as a constrained optimisation problem using Karush-Kuhn-Tucker (KKT) conditions [191], which are in practice applied to an arbitrary set of nodal DoF [192].

On the user side, the unilateral boundary condition is imposed by applying an analytically defined inequality to the nodal displacements. When touch-down contact over a flat seabed located at $z = -H$ is considered, this assumes the form

$$\Delta z \geq -\left(H + z_0\right) . \tag{3.5}$$

In the above expression Δz denotes the cumulated vertical displacement of a node over the simulation and z_0 its initial vertical coordinate.

As shown in Appendix D, contact is physically introduced into the mechanical problem by a modification of the equilibrium equation to take into account the related reaction forces, depending on the verification of the contact condition.

3.2.4 Mooring line hydrodynamics

The Morison approach is employed in the form detailed next to compute the hydrodynamic forces on the lines by taking into account both the structure's motion and the wave particle kinematics. First, a simplification is made by disregarding the inertial wave forces, i.e. the second term of the right member of Equation 2.12: due to the small diameter of the mooring lines compared to the length of ocean waves, these are negligible with respect to viscous forces (see 2.2.6). This modelling hypothesis is also used by commercial mooring simulation software such as MARIN's aNySIM [62]. The last term appearing in Equation 2.12, associated to the fluid's added mass force, is accounted for in reactive form with the procedure outlined in 3.2.4.2 and removed from the external loads. This leaves only the drag part of Equation 2.12, which is computed as follows.

The mooring line is assimilated to a circular cylinder of equivalent volume whose diameter is D, the mooring line's volumetric diameter. An arbitrarily oriented orthonormal frame P$\tilde{x}\tilde{y}\tilde{z}$ with $\tilde{x} \equiv s$, is assigned for the decomposition of velocity. Unit vectors $\mathbf{i}$, $\mathbf{j}$, and $\mathbf{k}$ define the directions of axes $\tilde{x}$, $\tilde{y}$, and $\tilde{z}$ in the global frame respectively; following from 3.2.1.1, let $\mathbf{u}$ denote the instantaneous position of a section and $\mathbf{v}$ the absolute flow velocity at the section's location in the fluid, the relative flow velocity is defined by $\mathbf{w} = \mathbf{v} - \dot{\mathbf{u}}$. Subsequently the axial and normal components of vector $\mathbf{w}$ are, with respect to the element's frame,

$$w_{\tilde{x}} = \mathbf{w} \cdot \mathbf{i}\,,\; w_{\tilde{y}} = \mathbf{w} \cdot \mathbf{j}\,,\; w_{\tilde{z}} = \mathbf{w} \cdot \mathbf{k}\,. \tag{3.6}$$

This forms the basis enabling the decomposition of the drag problem of a porous 1D body in 3D space such as a mooring chain. The axial drag force per unit length is written as

$$\frac{dF_{\tilde{x}}}{dl} = \frac{1}{2}\rho_{\mathrm{w}} c_{\mathrm{d}}^{\mathrm{a}} D |w_{\tilde{x}}| w_{\tilde{x}}\,. \tag{3.7}$$

The transverse component of the relative velocity defined with

$$\mathbf{w}^{\mathrm{n}} = \mathbf{w} - w_{\tilde{x}}\mathbf{i} \tag{3.8}$$

enters the computation of the normal drag force:

$$\frac{dF_{\tilde{y}}}{dl} = \frac{1}{2}\rho_{\mathrm{w}} c_{\mathrm{d}}^{\mathrm{n}} D |\mathbf{w}^{\mathrm{n}}| w_{\tilde{y}}\,,\;\; \frac{dF_{\tilde{z}}}{dl} = \frac{1}{2}\rho_{\mathrm{w}} c_{\mathrm{d}}^{\mathrm{n}} D |\mathbf{w}^{\mathrm{n}}| w_{\tilde{z}}\,. \tag{3.9}$$

Note that the axial declination of this formula uses the same reference diameter as the normal one: this is customary in mooring analysis and requires a consistent choice of $c_{\mathrm{d}}^{\mathrm{a}}$ and $c_{\mathrm{d}}^{\mathrm{n}}$. Equations 3.7 and 3.9 can also be written equivalently with reference to the nominal line diameter, which corresponds to the bar diameter for a mooring chain.

3.2.4.1 Viscous forces

Equations 3.7 and 3.9 represent the viscous drag forces, which dominate wave-structure interaction for slender bodies such as mooring lines, and enter the global EoM as a time- and displacement-dependent excitation term (see D.2). The normal and axial drag force components are treated as distributed loads and their integral over the length of each element is approximated using the Gauss method. Using n Gauss points enables to compute force distributions up to the $(2n-1)^{\text{th}}$ order; in the present application, $n = 3$ is used which should suffice to capture correctly the drag force variability over mooring segments of limited length. In order to do this, the local speed $\dot{\mathbf{u}}$ is calculated at each of the Gauss points by interpolation between the extremity nodes, whilst $\mathbf{v}$ is obtained using the incident wave particle kinematics, providing the local drag force per unit length. The integration of the approximating polynomial times the element shape function finally yields the equivalent nodal forces, which enter the dynamic equilibrium equation after being reexpressed in the global system of reference.

3.2.4.2 Inertial forces

The inertial fluid reactions may play a significant role in determining a line's dynamic response since they contribute to the effective modal mass. For a conventional steel chain segment, for example, added mass represents about a tenth of the normal modal mass. This is why the reactive part of the inertial hydrodynamic force is considered here by means of a left-hand side (LHS) added mass force. Based on the methods commonly employed by the present industrial software [62],[61], the axial-flow and normal-flow added masses of a slender mooring segment are respectively expressed with

$$m_{\text{a}}^{\text{a}} = c_{\text{a}}^{\text{a}} \rho_{\text{w}} \bigtriangledown, \; m_{\text{a}}^{\text{n}} = c_{\text{a}}^{\text{n}} \rho_{\text{w}} \bigtriangledown \, . \tag{3.10}$$

This formula employs the volumetric acception of the added mass coefficient c_{a}. The other defining parameters are water density, ρ_{w}, and the segment volume $\bigtriangledown$.
As it will be shown in 3.3.2, the hydrodynamic added mass is here summed to the mechanical mass of the cables by an increase of material density; while on one hand this benefits from the FE representation, allowing to include the added inertia moment natively, on the other it assumes $m_{\text{a}}^{\text{a}} = m_{\text{a}}^{\text{n}} = m_{\text{a}}$, which in most cases is incorrect. For example, for mooring chains a reasonable normal to tangential added mass ratio is in the order of 3 (see [62]). Fortunately, far from the fairlead excitation the dynamic displacements of pre-tensioned mooring chain segments take place mostly in the transverse direction, reflecting the low modes of a slender and axially stiff structure. It is therefore reasonable to calibrate c_{a} on the normal added mass at the expense of the representation of axial fluid reaction. Although not being severe, this is a limitation which should be addressed by further work.

3.3 Model set-up

The present Section provides the user-side procedures which enable to carry out mooring simulations with *Code_Aster*. First, it describes the selection of an appropriate combination of physical parameters for the simultaneous representation of gravitational, buoyancy, structural inertial, and hydrodynamic added mass forces on the lines. Then the catenary laying procedure is explained, which was developed to initialise the mooring simulation. The representation of the FWT platform with its rigid-body dynamics is also briefly outlined. Finally, an account is made of the selection of the time integration scheme along with the choice of its characterising parameters.

3.3.1 Buoyancy force correction

In the present study it is assumed that the entirety of the mooring system is submerged, and hence that all of its parts are subjected to a constant hydrostatic buoyancy force. The buoyancy force exerted on a submerged mooring component is directed upwards and can be expressed with

$$f_{\mathrm{A}} = \rho_{\mathrm{w}} \bigtriangledown g \,. \tag{3.11}$$

In the above equation ρ_{w} is the water density and $\bigtriangledown$ the component's displaced volume. The component is simultaneously subjected to a downward weight force,

$$f_{\mathrm{W}} = \rho_{\mathrm{m}} \bigtriangledown g \,, \tag{3.12}$$

assuming it has homogeneous density ρ_{m}. In order to account for the presence of the buoyancy force, it is possible to impose a corrected downwards gravitational acceleration of magnitude g' such that

$$\rho_{\mathrm{m}} \bigtriangledown g' = \rho_{\mathrm{m}} \bigtriangledown g - \rho_{\mathrm{w}} \bigtriangledown g \,, \tag{3.13}$$

which yields

$$g' = g \left(1 - \frac{\rho_{\mathrm{w}}}{\rho_{\mathrm{m}}} \right) . \tag{3.14}$$

For a given water density, the corrected gravity acceleration found with Equation 3.14 depends only on the component's material density. By introducing a third arbitrary material density ρ_{c}, which is used in the computational model to represent a chain by a mechanically equivalent CABLE element with hydrodynamic added mass (see 3.3.2), one may reformulate Equation 3.13 as

$$\rho_{\mathrm{c}} \bigtriangledown g'' = \rho_{\mathrm{m}} \bigtriangledown g - \rho_{\mathrm{w}} \bigtriangledown g \,. \tag{3.15}$$

Expliciting the corrected gravitational acceleration from Equation 3.15 finally gives

$$g'' = g\left(\frac{\rho_\mathrm{m} - \rho_\mathrm{w}}{\rho_\mathrm{c}}\right). \tag{3.16}$$

3.3.2 Chain-equivalent element

Mooring chains need to be treated with caution when assimilated to homogeneous 1D elements in a mathematical model. Their complex geometry and the presence of articulated joints (Figure 3.8) translate in large longitudinal variations of the mechanical properties at the link scale. In order to correctly represent a mooring chain segment with a bar-type finite element, these attributes must be expressed in longitudinally averaged form.

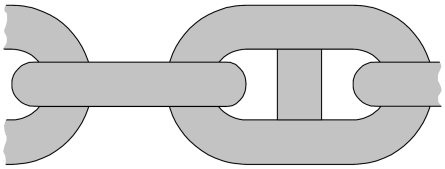

Figure 3.8: Studlink chain geometry.

A homogeneous CABLE element is defined by the material-specific quantities: E_c and E_c^-, the Young's moduli associated to tension and compression, and the volumetric mass ρ_c. The following geometrical quantities also concur in defining the element: A_c, the cable's sectional area, and l_c, the element span. Among these parameters, E_c^- is set to zero for a chain, and l_c is dictated by the input mesh for each element. To determine the remaining parameters, the modeller must pay attention to the following aspects:

- **Axial stiffness.** The nominal axial stiffness found in the chain specifications, κ, must be respected by the equivalent cable element, that is $\kappa_\mathrm{c} = E_\mathrm{c}A_\mathrm{c} = \kappa$.
- **Inertial mass per unit length.** Another catalogue parameter is ϱ, the chain's average mass per unit length. In order to assign the correct mass to the equivalent cable element for the computation of inertial forces[3], one must satisfy $\rho_\mathrm{m}A_\mathrm{c} = \varrho$, with ρ_m denoting the chain material's density.

The above relations combined identify the equivalent cable's sectional area and Young's modulus as

$$A_\mathrm{c} = \frac{\varrho}{\rho_\mathrm{m}},\ E_\mathrm{c} = \frac{\kappa}{A_\mathrm{c}} = \frac{\kappa\rho_\mathrm{m}}{\varrho}. \tag{3.17}$$

[3]Quasi-static mooring simulations frequently employ an 'in-water' equivalent mass value which corrects the weight force to include buoyancy. This shortcut cannot be adopted in a dynamic simulation because of the dependency of inertial forces from mass.

Note that the quantities found with Equations 3.17 must be distinguished from the physical chain's geometric and material properties.
Since in the present implementation it is chosen to approximate the reactive added mass force by an isotropic increase of inertial mass (see 3.2.4), an according correction on material density must be introduced. Let ρ_w be the water density and c_a the volumetric added mass coefficient, the input equivalent cable density becomes

$$\rho_\mathrm{c} = \rho_\mathrm{m} + c_\mathrm{a}\rho_\mathrm{w}\,. \tag{3.18}$$

The corrected gravitational acceleration provided by injecting ρ_c in Equation 3.16 is hence

$$g'' = g\left(1 - \frac{c_\mathrm{a}+1}{c_\mathrm{a}+\rho_\mathrm{m}/\rho_\mathrm{w}}\right)\,, \tag{3.19}$$

which insures that the correct weight per unit length, inclusive of the buoyancy force, is applied in the simulation.

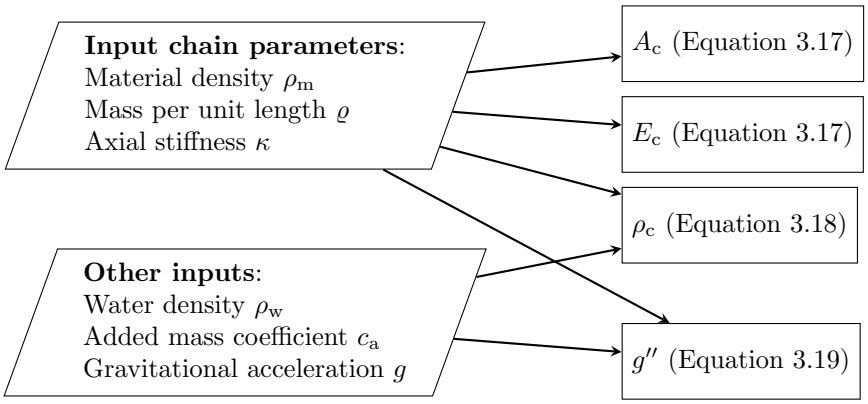

Figure 3.9: Definition of the simulation parameters from the input physical quantities, for a chain-equivalent CABLE.

3.3.3 Catenary laying

Finding the static equilibrium configuration of highly flexible structures such as offshore moorings is a known numerical challenge in finite element analysis (see for instance Webster [193]). If one excludes the pre-generation of the equilibrium mooring geometry using catenary formulae, the above challenge translates into finding a gravitationally loaded static equilibrium configuration which is far removed from an arbitrarily chosen initial geometry. The calculation strategy proposed here to solve this problem and initialise the mooring simulation is described next for a single mooring line.
Let F and A be the fairlead and anchor point, whose location in space is known. Assuming L, the unstretched mooring line length, as an input, a convenient starting

geometry is obtained by breaking the mooring line into two straight segments[4] $\overline{\mathrm{AK}}$ and $\overline{\mathrm{KF}}$ lying in the vertical plane which contains A and F, with

$$\overline{\mathrm{AK}} + \overline{\mathrm{KF}} = L\,. \tag{3.20}$$

This defines the initial configuration Ω_I shown in Figure 3.10. The target static equilibrium configuration Ω_S also appears in the Figure. From the starting state Ω_I, the

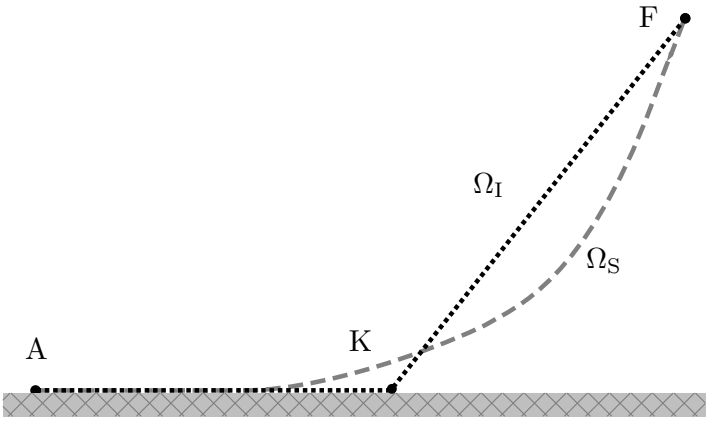

Figure 3.10: Initial controlled geometry before catenary laying (black dots) and target equilibrium geometry (grey dashes).

quasi-static FE solver available in *Code_Aster* (see Appendix D) cannot approach Ω_S through a sequence of quasi-static solutions by gradually increasing the load, since the equilibrium geometry – neglecting elastic deformation – is the same for any magnitude of the gravitational forcing. In the case of catenary laying the system must find the equilibrium state mostly by undergoing rigid-body displacements, as opposed to elastic deformations. Unfortunately, quasi-free rigid-body motion is characterised by a singular tangent stiffness matrix (see D.1)

$$\frac{\partial \mathbf{g}_i^{n-1}}{\partial \mathbf{u}}\,, \tag{3.21}$$

which makes the problem untractable with the quasi-static solver. In such cases, using the dynamic solver (detailed in D.2) permits to reestablish the equilibrium between internal and external forces thanks to the contribution of inertia (and damping) to the tangent matrix.

Introducing inertia alone stabilises the calculation, but cannot provide the motion decay required to attain Ω_S. In other words, a source of dissipation is needed to remove the potential energy differential between Ω_I and Ω_S from the system. This is achieved with the introduction of a controlled amount of Rayleigh damping, which expresses the

[4]Defining the initial mooring line geometry as a set of straight lines in space is functional to both mesh generation and the imposition of the unilateral contact laws of 3.2.3 in analytical form.

damping matrix as a linear combination of the mass and stiffness matrices[5]:

$$\check{\mathbf{C}} = \check{\alpha}\check{\mathbf{K}}^{\mathrm{T}} + \check{\beta}\check{\mathbf{M}}\,. \tag{3.22}$$

Only the mass-proportional Rayleigh damping component is used in this case, which corresponds to choosing $\check{\alpha} = 0$ and $\check{\beta} > 0$. After imposing the gravitational load, clump boundary conditions in F and A, and the seabed contact conditions, a decaying dynamic simulation with near-critical damping may be obtained by selecting an appropriate value of $\check{\beta}$. Such a simulation generally leads to a satisfactory approximation of Ω_{S} in a few tens of seconds simulation time. At the end, a one-step static simulation is run using Ω_{S} as input, in order to eliminate any spurious dynamic effect; its output, $\Omega_0 = \Omega(t_0)$, is used to initialise the subsequent simulations of physical interest.
The above procedure applied to a mooring line provides a result of the type shown in Figure 3.11, where the arrows indicate the local displacements. Since the only solution of interest is the final static configuration, the transient states between Ω_{I} and Ω_{S} are simply discarded after the catenary laying stage.

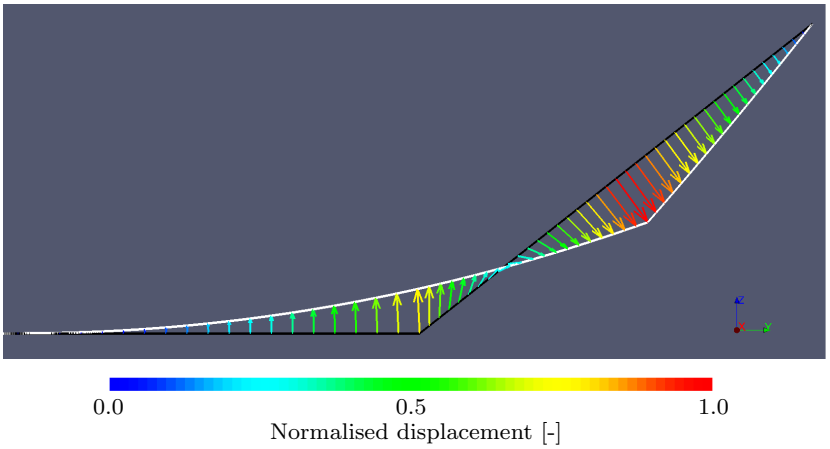

Figure 3.11: Catenary laying of a mooring line with clump weight, output from *Code_Aster*.

[5]The check symbol is here used to distinguish the aggregate system's mechanical tensors from the rigid platform tensors of 3.3.4.

3.3.4 Floating platform geometry and dynamics

Studying the mechanics of a complete FWT mooring system requires to link the fairlead points to simulate the presence of the floater. A rigid platform model is presently utilised for this sake, which consists in a set of massless, undeformable beam elements (see Fléjou [194] for a description of beam elements in *Code_Aster*) each connecting a fairlead to the platform pivoting point. Figure 3.16 provides a visual example of this arrangement in the context of a practical application. This representation underpins all the static and motion-driven dynamic simulations presented in this Part.

It must be specified that adopting the motion-driven, i.e. uncoupled, approach in dynamic mooring simulation does not permit to close the feedback loop between platform dynamics and the dynamic component of the mooring system's response (see for instance Ormberg and Larsen [195]). In qualitative terms, the severity of this limitation is proportional to the relative size of the mooring system with respect to the floater, which is governed by water depth [59, 196]. Catenary lines of increasing length react with larger dynamic forces, which may increasingly affect the platform motion. At the same time, the frequency of the principal modes of the mooring system also diminishes with line length, typically approaching the platform modes and increasing the interaction. The dynamically uncoupled approach used in this study seeks to contain the retroaction inaccuracy through the use of a quasi-static, nonlinear mooring model in the preliminary calculation of platform motion, but does not include any representation of dynamic mooring effects such as additional damping.

If the platform dynamics are not imposed and need instead to be resolved by the model in a coupled simulation, that is the methodology labelled '*Code_Aster*(1)' in 3.5.3, a rigid hydromechanical floating structure model (of the type included in CALHYPSO, see 2.2.1) is to be introduced. This is presently done by lumping the aggregate structure mass and stiffness tensors defined at the floating structure's equilibrium, $\mathbf{M}$ and $\mathbf{K}^{\mathrm{h}}$ (see Equations 2.1 and 2.9), onto a 6-DoF punctual (0D) element [197] located at the pivoting point, where the incident wave excitation is also applied. Only harmonic (regular wave) simulations can be organised with this method, since the convolution treatment of aharmonic wave radiation forces (Equation 2.11) is unavailable in this model. By assuming that motion is monochromatic and that its frequency equals that of the incident wave, ω, these forces may be represented in the LHS by assigning frequency-independent, linear added mass and damping tensors to the above defined 0D element, $\mathbf{A}(\omega)$ and $\mathbf{B}(\omega)$, based on the outputs of the frequency-domain radiation calculation. Finally, the hull drag forces are imposed on the structure using an extra set of rigidly connected massless beams and the method of 3.2.4.1.

3.3.5 Numerical damping

Dynamic mooring analyses aim to precisely represent low frequencies (wave excitation and mooring system modes) and tend to be affected by parasitic high-frequency oscillations caused by the system non-linearities. This is a common problem in structural mechanics, often addressed by suppressing high-frequency instability with controlled numerical damping. In particular, Hilber et al. [198] proposed a dissipative time integration scheme of the Newmark family (see Appendix B), commonly referred to as HHT, which introduces low numerical damping in the low-frequency band and high damping at high frequency, thereby allowing to stabilise the simulation.
The HHT integration scheme is recommended for the dynamic treatment of cable elements in *Code_Aster* for the above reasons, especially in the presence of the shocks caused by contact [184, 199]. The Newmark parameters β and γ are in this case expressed as functions of a third parameter, α, such as

$$\beta = \frac{(1-\alpha)^2}{4}\,,\ \gamma = \frac{1}{2} - \alpha\,,\ \alpha \leq 0\,. \tag{3.23}$$

The amount of damping introduced numerically is governed by α, which is used to manage the compromise between high-frequency and low-frequency dissipation. Imposing $\alpha = 0$ leads to the classic, nondissipative average acceleration scheme, whilst increasing dissipation is obtained with increasingly negative values. In its full application, the HHT scheme also introduces a weighing of the internal and external forces, always governed by parameter α, which is described in the original article [198].
In the applications presented in Section 3.5, a viable value of α has been chosen by gradually increasing its magnitude until the fairlead tension, used as reference output signal, becomes free of high-frequency noise. An example of the results obtained by imposing low and high-end values of α is provided in Figure 3.12, which draws from the results of a regular wave loading case treated in the following.

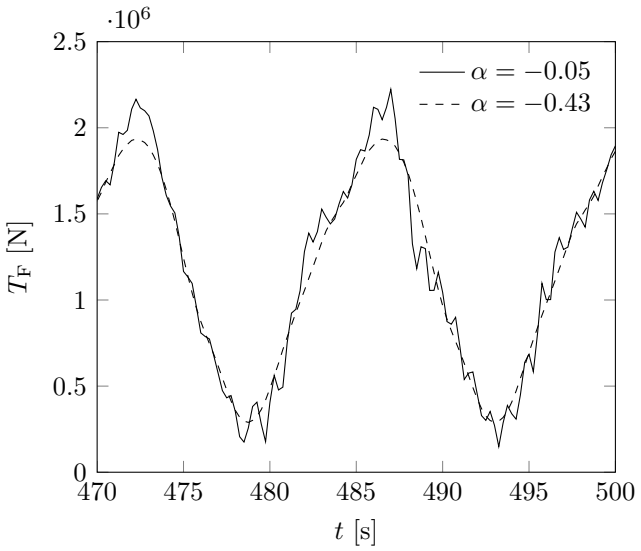

Figure 3.12: Upwave fairlead tension of the DeepCwind-OC4 floating wind turbine under regular waves, with low and high numerical dissipation of high-frequency components. Loading case = F, as defined in Table 3.5.

3.4 Static applications

A set of verifications of the presented mechanical moorings model is provided in this Section. All of them make use of the above described methods to predict the static behaviour of FWT mooring systems, which by definition excludes all inertial forces and hydrodynamic interactions. The restoring characteristics of a generic mooring line and of a realistic mooring arrangement are compared herein with appropriate reference results. It is also shown how the linearised mooring system stiffness matrix for a well-documented FWT concept can be successfully reconstructed.

3.4.1 Restoring characteristic of a catenary mooring line

A single, homogeneous mooring line with the properties of a typical offshore chain in relatively shallow water is here used as a basis for the verification of the static performance of the *Code_Aster*-based model. The horizontal restoring problem of a single mooring line (Figure 3.13) is planar, and the parameters provided in Table 3.1 in nondimensional form are sufficient to define an univocal catenary configuration of the mooring line which satisfies the static equilibrium. The normalising quantities used are h, the fairlead height over the (flat) seabed, ϱ, the mass per unit length, and g. By

Table 3.1: Single mooring line parameters.

Unstretched line length L/h [-]	6.140
Material density $\rho_{\mathrm{m}} h^2/\varrho$ [-]	$1.280{\cdot}10^5$
Water density $\rho_{\mathrm{w}} h^2/\varrho$ [-]	$1.682{\cdot}10^4$
Axial stiffness $\kappa/\varrho g h$ [-]	$8.233{\cdot}10^3$
Horizontal force at equilibrium $F_0^{\mathrm{h}}/\varrho g h$ [-]	9.033
Volumetric added mass coefficient c_{a} [-]	0

imposing an initial horizontal pull force F_0^{h} in F and by assuming that the fairlead is free to move horizontally and constrained vertically, the continuous quasi-static approach (see for example [164] for theory and [58] for an implementation example) provides an analytical solution for the horizontal distance between anchor and fairlead at equilibrium, in the following terms:

$$r = r(F^{\mathrm{h}}) = s(F^{\mathrm{h}}) + \overline{\mathrm{AT}},\ F^{\mathrm{h}} > 0\,, \tag{3.24}$$

where s denotes the scope, the projection of the suspended line on the seabed. By posing $r_0 = r(F_0^{\mathrm{h}})$ as the reference horizontal fairlead distance from A, the horizontal displacement from this position is defined as $\delta = r - r_0$. The mooring line's force-displacement characteristic consists in the $F^{\mathrm{h}}(\delta)$ relationship, which is nonlinear and convex.

Two mechanical modelling options are used for verification, which are inelastic and

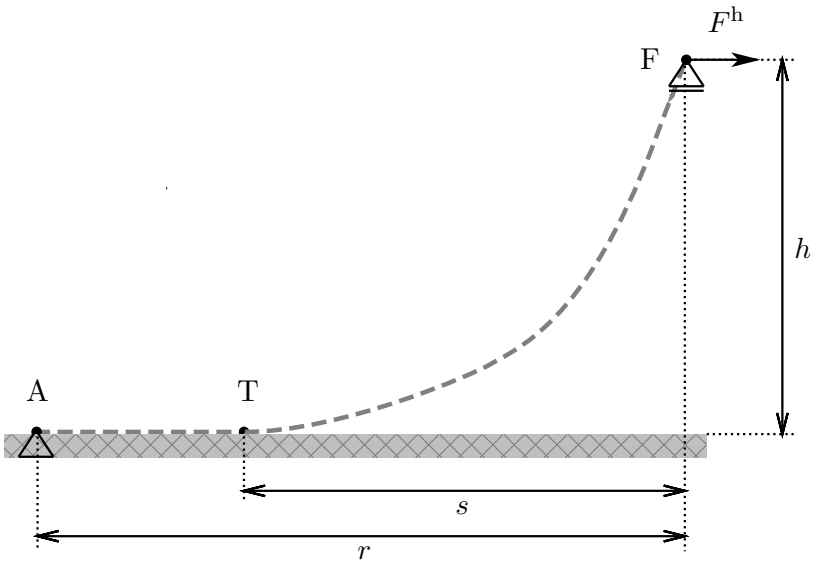

Figure 3.13: Quasi-static problem of a single mooring line.

elastic behaviour. In order to obtain a numerical result representative of the inelastic behaviour, the axial stiffness κ is increased by two orders of magnitude in the numerical model. In the analytical model the inelastic catenary simply translates into a special case of the general elastic formulation. On the contrary, the elastic line adopts the axial stiffness indicated in Table 3.1. In this case, comparing the analytical and numerical model outputs requires to take into account the elongation of the line segment between the anchor point A and the touchdown point T in the analytical model. After the deformation, the length of this segment becomes

$$\overline{\mathrm{AT}} = \overline{\mathrm{AT}}^{\mathrm{u}} \left(1 + \frac{F^{\mathrm{h}}}{\kappa}\right) \approx \left[L - \overset{\frown}{\mathrm{TF}}^{0}(F^{\mathrm{h}})\right] \left(1 + \frac{F^{\mathrm{h}}}{\kappa}\right) , \tag{3.25}$$

where $\overline{\mathrm{AT}}^{\mathrm{u}}$ is the unstretched length of the seabed segment and $\overset{\frown}{\mathrm{TF}}^{0}$ represents the suspended length calculated analytically in the inelastic case.

The convergence of the numerical solver for increasing mesh resolution is shown for the elastic case in Figure 3.14 (left). In terms of force-displacement relationship about the given equilibrium configuration, the results of the continuous (analytical) and finite-element (numerical) quasi-static models are found to be practically equivalent for both the elastic and the inelastic case, as shown in Figure 3.14 (right).

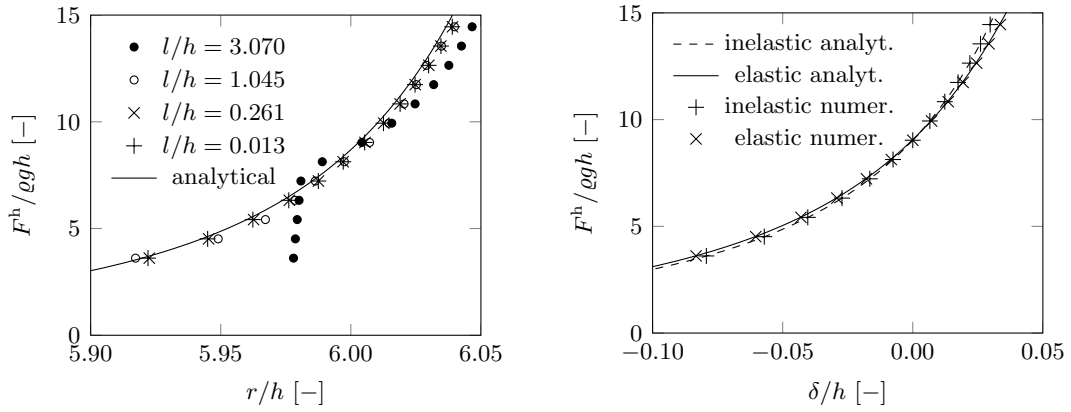

Figure 3.14: Relationship between horizontal fairlead force and position of an elastic line using increasing mesh resolution (left). Restoring characteristic of a mooring line with inelastic and elastic behaviour (right), where the numerical results use $l/h = 0.013$.

3.4.2 Restoring characteristic of a mooring system

A three-leg mooring system designed by an industrial partner of EDF for the Vertiwind floating wind turbine is documented in [200][6]. In the reference document, a static analysis conducted with state-of-the-art mooring simulation software OrcaFlex is carried out, including the evaluation of the aggregated force-displacement characteristic of the mooring system for three different line lengths. Next is presented the equivalent analysis based on the presented methodology with *Code_Aster*. All reported quantities are made nondimensional for confidentiality reasons using h, the fairlead height over the seabed, ϱ, the chain mass per unit length, and g as normalising parameters, as done in 3.4.1.

3.4.2.1 Definition of the mooring system

Three equally spaced steel chains moor the floating wind turbine to the flat seabed. Each of these is equipped with a clump weight (which is here modelled with a concentrated downward force) producing the undisturbed equilibrium geometry with discontinuous slope already shown in Figure 3.11 for a single line. A sketch of this mooring arrangement is provided in Figure 3.15. All the input data which are used in the present study are available in the reference report [200] with the exception of the chain mass per unit length, not explicitly indicated, which is presently derived from the chain's nominal diameter with the relationships found in [61], assuming a standard studlink chain construction.
Three variants are considered, characterised by different values of the unstretched line

[6] Confidential.

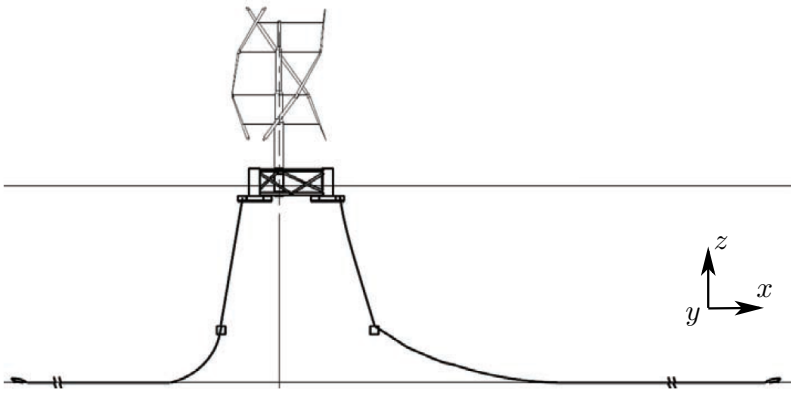

Figure 3.15: Mooring configuration of the Vertiwind floating system, after Cahay et al. [43].

length L. Table 3.2 provides these values as well as the corresponding normalised pre-tensions at the fairlead, $T_{\mathrm{F}}^{*} = T_{\mathrm{F}}/\varrho g h$. Both the reference and the calculated pre-tensions are supplied, along with the percent error of the presented model. The slight underestimation of the pre-tension by *Code_Aster* may be explained by the estimation of the chain mass per unit length based on practical formulae.

3.4.2.2 Force-displacement characteristic

The restoring characteristic of the mooring system defined above is therefore obtained by applying finite increments to the horizontal load on the rigid floater assembly, F_x, and allowing the platform to displace in the x direction, whilst restraining displacement in the remaining rigid-body DoF. Figure 3.16 provides an example of the equilibrium positions found for positive values of $F_x^{*} = F_x/\varrho g h$. The Figure shows how the fore line, to the right, is gradually unloaded as the structure is pushed forwards, whilst the aft mooring lines become more tensioned topping at more than three times the initial tension. The resulting normalised displacements δ_x/h are plotted versus the horizontal force in Figure 3.17, where they are compared with the reference results, showing that *Code_Aster* can successfully reproduce the nonlinear static behaviour of a complete catenary mooring system.

Table 3.2: Parameters of the studied mooring configurations.

Case #	L/h [-]	Reference T_{F}^{*} [-]	Calculated T_{F}^{*} [-]	Error [%]
1	12.75	15.57	15.28	-1.86
2	12.81	13.35	13.07	-2.08
3	12.93	10.43	10.15	-2.66

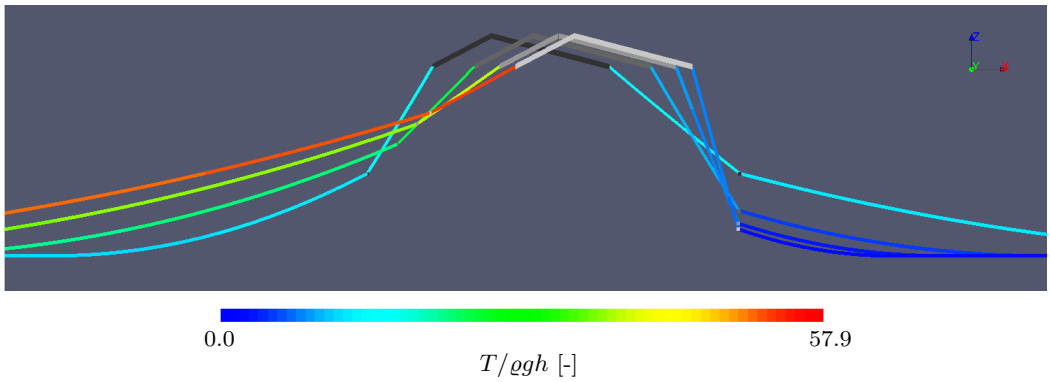

Figure 3.16: Undisturbed equilibrium configuration of Case 1 and configurations found with three incremental force increases of $\Delta F_x^* = 17.37$. The color map provides the nondimensional line tension.

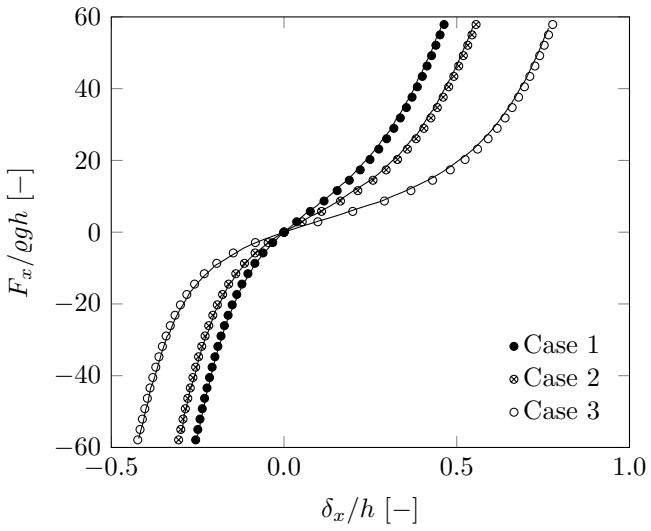

Figure 3.17: Comparison of three calculated (markers) and reference (lines) force-displacement characteristics. The reference results are digitised from the Vertiwind mooring design report [200].

3.4.3 Mooring system stiffness matrix

Computational mooring simulators are often used to linearise the behaviour of mooring systems about an arbitrary configuration, most commonly the undisturbed one. An equivalent 6×6 stiffness tensor is computed about said central position, allowing to approximate the mooring system's restoring force to the first order (see 2.2.7).
Next the mooring stiffness matrix of the DeepCwind-OC4 concept, defined in [137], is calculated with the static *Code_Aster* methodology. The mooring system, designed for a constant water depth of 200 m, is composed by three axisymmetric chain lines angled at 120 ° from one each other. The geometric parameters defining the mooring system and the chain characteristics are given in Tables 3.3 and 3.4 respectively.
A water density of 1025 kg/m^3 and a nil added mass coefficient are assumed. The first step is the usual calculation of the undisturbed equilibrium configuration, shown in Figure 3.18. The distribution of tension along the lines is given by the colour map. The nodal reaction vectors are also plotted, which indicate where the boundary conditions intervene mechanically in this particular state. The magnitude of these vectors is to scale, except for the seabed contact reactions (in white) which are magnified by a factor of 10^2.
Finite, positive perturbations[7] Δx_j^{P}, $j = 1 : 6$, are then applied in turn to each of the nodal DoF at the pivoting point P, located at the intersection of the platform centreline and the free surface, whilst the other five remain clamped. For each of the six loading cases the corresponding boundary reaction $\mathbf{q}^{\mathrm{P}}(j)$ is extracted from the solution after calculating the new static equilibrium. The perturbation in nodal reaction is then obtained with $\Delta\mathbf{q}^{\mathrm{P}}(j) = \mathbf{q}^{\mathrm{P}}(j) - \mathbf{q}_0^{\mathrm{P}}$ with reference to the undisturbed reaction force.

Table 3.3: DeepCwind-OC4 mooring system geometry.

Fairlead depth below the free surface [m]	14.00
Fairlead radius from platform centre [m]	40.87
Anchor radius from platform centre [m]	837.6
Unstretched line length L [m]	835.5

Table 3.4: DeepCwind-OC4 studless mooring chain parameters.

Nominal diameter [m]	0.0766
Material density ρ_{m} [kg/m^3]	7800
Mass per unit length ϱ [kg/m]	125.1
Axial stiffness κ [N]	$753.6 \cdot 10^6$

[7] Corresponding to a set of Dirichlet boundary conditions on displacement.

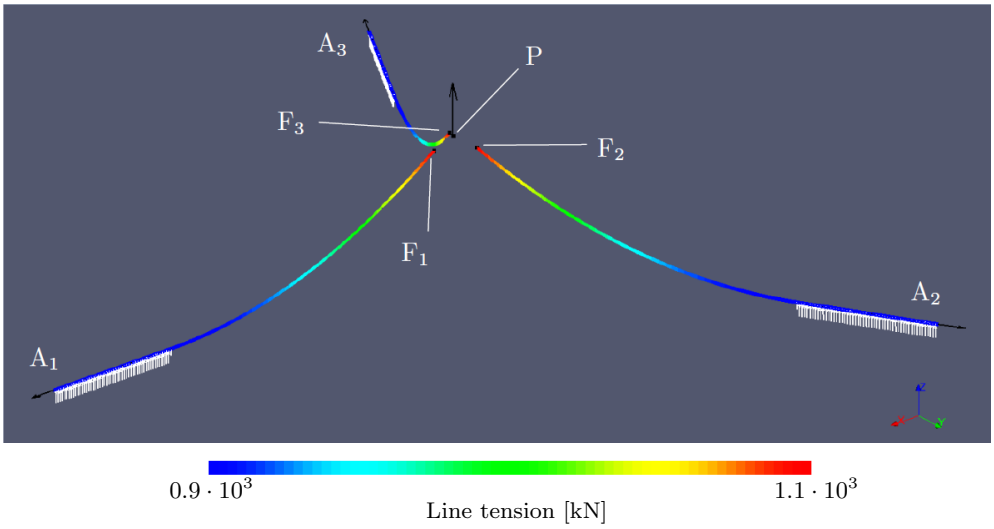

Figure 3.18: Undisturbed equilibrium configuration of the DeepCwind-OC4 mooring system showing the line tension (colour map) and the nodal reactions vectors (arrows).

The positive-displacement mooring stiffness is derived with

$$K_{ij}^{\mathrm{m}+} = \frac{\partial q_i^{\mathrm{P}}(j)}{\partial x_j^{\mathrm{P}}} \approx \frac{\Delta q_i^{\mathrm{P}}(j)}{\Delta x_j^{\mathrm{P}}} \,. \tag{3.26}$$

The same procedure is used to derive the negative-displacement stiffness terms, $K_{ij}^{\mathrm{m}-}$, by imposing negative perturbations $-\Delta x_j^{\mathrm{P}}$. Finally, the tangent mooring stiffness matrix is obtained with

$$K_{ij}^{\mathrm{m}} = \begin{cases} \frac{1}{2}\left(K_{ij}^{\mathrm{m}+} + K_{ij}^{\mathrm{m}-}\right) & \text{if } \operatorname{sgn}(K_{ij}^{\mathrm{m}+}) = \operatorname{sgn}(K_{ij}^{\mathrm{m}-}) \,, \\ 0 & \text{if } \operatorname{sgn}(K_{ij}^{\mathrm{m}+}) \neq \operatorname{sgn}(K_{ij}^{\mathrm{m}-}) \,. \end{cases} \tag{3.27}$$

Note that an equivalent approach would consist in perturbing the concentrated force in P and computing the equilibrium displacements. The linear mooring stiffness matrix obtained with Equation 3.27, $\mathbf{K}^{\mathrm{m}}$, is equal to (in SI units):

$$\mathbf{K}^{\mathrm{m}} = \begin{bmatrix} 7.02{\cdot}10^4 & & & -1.02{\cdot}10^5 & & \\ & 7.02{\cdot}10^4 & & & 1.03{\cdot}10^5 & \\ & & 1.91{\cdot}10^4 & & & \\ & 1.04{\cdot}10^5 & & 8.67{\cdot}10^7 & & \\ -1.04{\cdot}10^5 & & & & 8.67{\cdot}10^7 & \\ & & & & & 1.16{\cdot}10^8 \end{bmatrix} . \tag{3.28}$$

Let $\mathbf{E}^{\mathrm{m}}$ represent the percent errors with respect to the absolute values of the homologous coefficients published in [137],

$$\mathbf{E}^{\mathrm{m}} = \begin{bmatrix} -0.8 & & & -6.0 & & \\ & -0.9 & & & -4.4 & \\ & & -0.1 & & & \\ & -3.1 & & -0.7 & & \\ -3.2 & & & & -0.7 & \\ & & & & & -0.8 \end{bmatrix} . \tag{3.29}$$

With respect to the reference solution, the present model is capable of predicting diagonal mooring stiffness coefficients with errors below 1% – which is by the way in the order of the precision of the available results. Nevertheless, non-diagonal coefficients are significantly underestimated, exhibiting discrepancies in the 3%–6% range which remain unexplained. Error convergence was checked with respect to the spatial resolution of the mesh and the magnitude of the perturbations Δx_j^{P}.

3.5 Dynamic applications

The present Section describes the set of dynamic simulations of a floating wind turbine mooring system carried out with *Code_Aster* using the above methodology. It is next attempted to reproduce numerically a documented experimental campaign (3.1.3) where a scale model of the DeepCwind-OC4 FWT is subjected to wave excitation [84, 85]. The experimental setup incorporates the geometrically downscaled three-line mooring system, enabling to compare the measured fairlead tensions with the numerical predictions.

3.5.1 Experiment selection

Among the variety of loading cases presented in Masciola et al. [85], it is here chosen to model the subset for which the authors provide experimental fairlead tension data. This corresponds to six regular wave scenarios (here denoted with letters B to G) plus an irregular wave case. Another low-energy regular wave scenario (A) is reproduced from Coulling et al. [84]. In these tests wavetrains of varying properties are sent over the structure in the negative X direction (consistently with the usual orthonormal reference system shown in Figure 3.2); the main focus of the campaign is placed upon highly energetic sea states, representing extreme oceanic conditions, which should help to bring out the dynamic features of the mooring system. Tables 3.5 and 3.6 provide a definition of the loading cases considered, with full-scale dimensions.
It can be seen that the regular waves used to excite the structure are moderately steep, causing them to fall into the 2^{nd} order Stokes field of the classic wave theory classification (cf. Le Méhauté [201]). A relatively low peak enhancement factor, equalling 2.2, is used in the irregular wave case following the experiments carried out at MARIN.

3.5.2 Numerical model parameters

As it is frequently the case in offshore engineering, the reference study compares experimental and numerical outputs at the full scale; full-scale quantities are hence used here as inputs. The geometric parameters of the OC4 floater correspond to those previously given in Table 2.7. What varies here is the definition of the wind turbine and ballast on the platform, and by consequence the aggregated mass and inertia of the floating system, which are provided in Table 3.7. Since all the considered loading cases feature a parked turbine, which intervenes in the model as a rigid onboard mass, it is not necessary to reproduce the wind turbine particulars in greater detail.
The mooring system geometry is identical to that presented for the full-scale DeepCwind turbine in 3.4.3, designed for a full-scale water depth of 200 m and adopting the defining parameters of Table 3.3. However the model's full-scale mooring chain properties, provided with Table 3.8, depart slightly from nominal. The drag coefficients indicated in the Table are assigned based on the values proposed by MARIN [62] for standard (full-scale) chains, whilst the volumetric added mass coefficient is set to unit consistently with [85].
The gravitational equilibrium requirement is satisfied by countering the undisturbed mooring line weight with an equal vertical force applied at each fairlead. This reintroduces the need to represent the stabilising effect of the mooring system weight with a corresponding gravitational correction in the computation of $\mathbf{K}^{\mathrm{h}}$ (see 2.2.7), which determines a height of the CoG over the keel of 9.743 m.

Table 3.5: Regular wave loading cases considered. Wavelength is calculated using the Airy wave dispersion relationship in finite water depth.

Case	Wave height H_{w} [m]	Wave period T_{w} [s]	Wave steepness H_{w}/λ [%]
A	1.92	7.5	2.19
B	7.58	12.1	3.32
C	7.14	14.3	2.24
D	7.57	20.0	1.25
E	10.30	12.1	4.52
F	10.74	14.3	3.37
G	11.12	20.0	1.84

Table 3.6: Irregular wave loading cases considered.

Sig. wave height H_s [m]	Peak period T_p [s]	Spectrum
7.04	12.18	JONSWAP ($\hat{\gamma} = 2.2$)

3.5.3 Results and discussion

Next is presented a comparison of the outputs of the simulations carried out with *Code_Aster* and the MARIN experiments. The modelling strategies used are the following:

- CALHYPSO. The dynamic simulation uses the software described in Part 2, where the mooring forces are calculated with the quasi-static method.
- *Code_Aster*(1). The coupled system's dynamics are calculated with the dynamic moorings model.
- *Code_Aster*(2A). The platform motions are derived with CALHYPSO as above and hence imposed to the dynamic moorings model (motion-driven simulation).
- *Code_Aster*(2B). Equivalent to *Code_Aster*(2A), neglecting the incident wave kinematics in the calculation of mooring drag forces.

For regular waves, both the motion and the fairlead tension outputs are given in the RAO form using the definition of Equation 2.19, applied to the steady-state dynamic regime. Where irregular waves are concerned, the power spectral density of the quantities of interest is presented. This is calculated for a stationary regime of two-hour duration. Provided that the highest natural period of the structure, that of surge motion, is in the order of 100 s, more than 50 resonant surge cycles are allowed. Considering this feature, and that the input energy is located at smaller periods, two hours seem sufficient to capture the variability of the stochastic processes involved[8]. Samples of the underpinning time-domain tension signals are provided for visual complement.

Table 3.7: Global mass and inertia properties of the DeepCwind-OC4 model brought at full scale, moorings excluded.

Displacement [t]	14267
Height of CoM from keel [m]	9.792
Central roll/pitch moment of inertia [kg m^2]	$1.344{\cdot}10^{10}$
Central yaw moment of inertia [kg m^2]	$1.396{\cdot}10^{10}$

[8]Note that longer simulation times would be required to determine the extreme responses.

Table 3.8: Parameters of the studless chain used to moor the DeepCwind-OC4 model, brought at full scale. Drag coefficients are referred to the chain's nominal diameter.

Nominal diameter [m]	0.0766
Material density ρ_m [kg/m^3]	8500
Mass per unit length ϱ [kg/m]	123.5
Axial stiffness κ [N]	$753.6{\cdot}10^6$
Volumetric added mass coefficient c_a [-]	1.0
Axial drag coefficient c_d^a [-]	0.8
Normal drag coefficient c_d^n [-]	2.4

3.5.3.1 Response in regular waves

Figure 3.19 displays the platform dynamic response under regular wave excitation found by the MARIN campaign, and through the simulations carried out with CALHYPSO and the coupled dynamic moorings model. In-plane motions (surge, heave, pitch) are the only rigid-body DoF excited.

As commonly found in slack-moored offshore structures, surge amplitude increases with the oscillation period. Similar response operators are found for the two different wave heights. In this DoF, the outputs of CALHYPSO and *Code_Aster* are close to equivalent, showing the limited effect of mooring dynamics on platform motion in this particular case. With reference to the experiments, both models tend to underestimate response slightly, especially for $T_\mathrm{w} = 20\,\mathrm{s}$ where the error is in the order of 10%. A similar accuracy has been obtained in the reference study by modelling these cases with NREL's FAST [84].

The normalised dynamic response in heave is limited to a fraction of a unit at low periods, whilst at the near-resonant period of $T_\mathrm{w} = 20\,\mathrm{s}$ it exceeds unit. The heave DoF is also well predicted by both numerical models, which produce amplitude errors of a few percent points. It is once again at 20 s that the models err the most, showing however better performance than the FAST results reported by Coulling et al. [84]. This may be explained by the explicit inclusion of platform drag in the present models, which significantly contributes to exciting the structure vertically, where in the referenced FAST simulation the drag model is only reactive. Said thesis is reinforced by the model-to-model comparison provided by Masciola et al. [85].

Pitch appears to be a more problematic DoF to be simulated in this case. CALHYPSO mostly underestimates pitch response across the studied range, with an error pattern closely resembling that of the simulation outputs published by Coulling et al. [84]. In all cases but A and B, the explicit inclusion of mooring dynamics enabled by *Code_Aster* seems to positively affect the accuracy of the simulated platform response. Once again, the system dynamics at the wave period of $T_\mathrm{w} = 20\,\mathrm{s}$ appear to be particularly sensitive to the modelling approach. For pitch, this is likely to be an effect of the proximity of the semi-submersible platform's excitation suppression point (discussed in Part 2), which

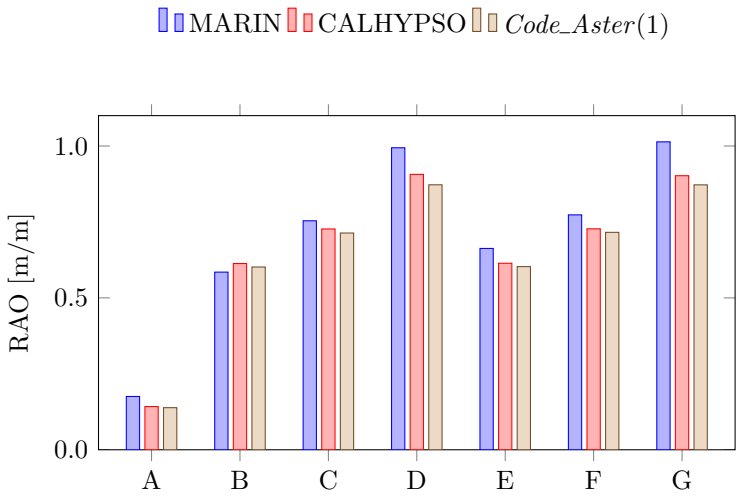

(a) Surge motion.

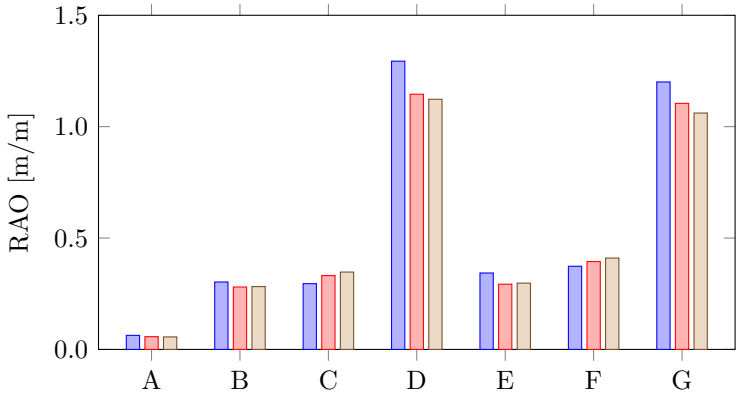

(b) Heave motion.

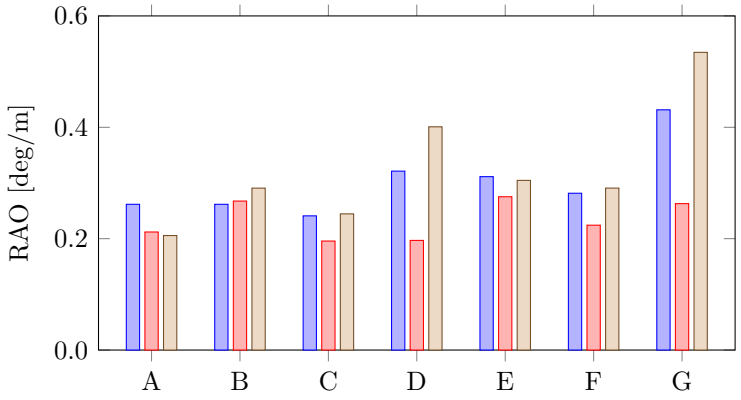

(c) Pitch motion.

Figure 3.19: Measured and computed motion response amplitude operator of the DeepCwind-OC4 floating system in regular waves. The experimental data are digitised from Coulling et al. [84].

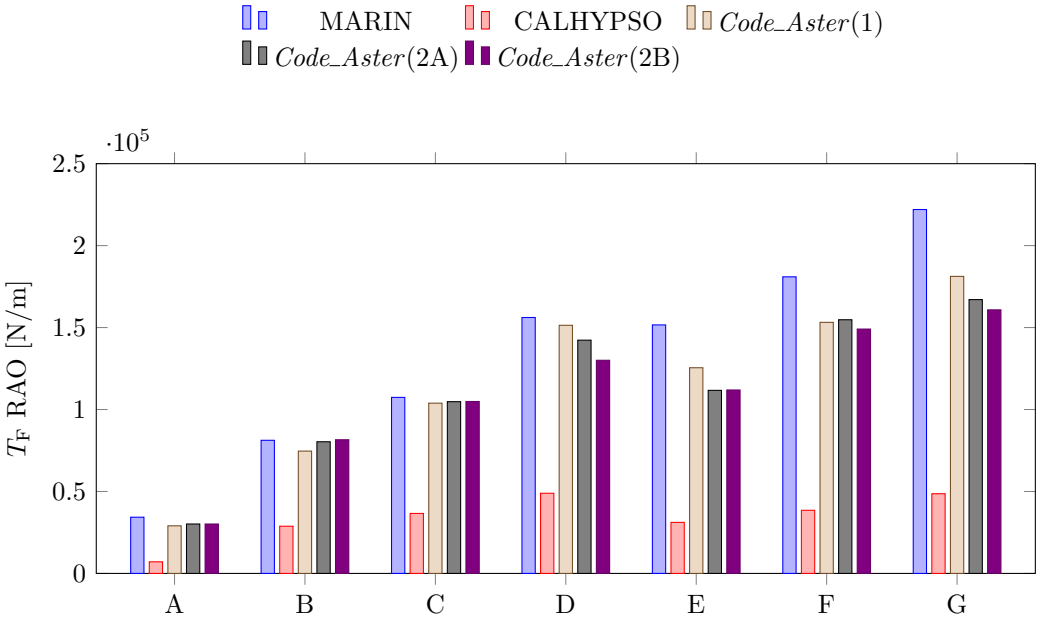

(a) Line tension at fairlead F1.

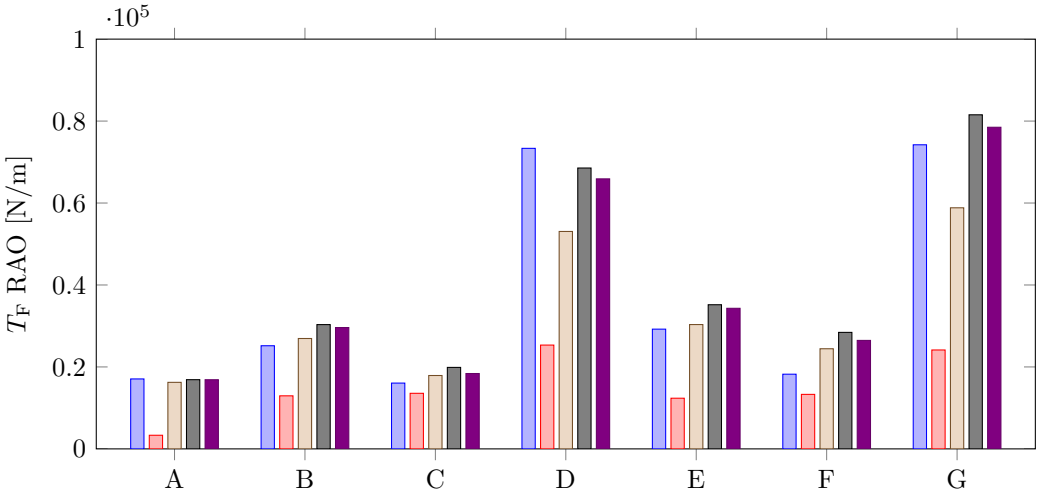

(b) Line tension at fairlead F2.

Figure 3.20: Measured and computed fairlead tension response amplitude operator in regular waves. The experimental data are digitised from Coulling et al. [84].

reduces the effect on response of the inertial wave excitation, dominant elsewhere, thereby exalting the importance of secondary force systems.

The measured and predicted fairlead tensions in regular waves are shown in Figure 3.20. A first and most striking, if unsurprising, observation is that the quasi-static representation of CALHYPSO severely underestimates the tension variance across the entire set of cases. All dynamic mooring model outputs provide a more accurate estimate of the tension RAOs, both for the upwave fairlead F1 and the downwave fairlead

F2, and exceed the performance of the dynamic mooring simulations presented in Masciola et al. [85], which underpredict the response amplitude. The best performance is provided by the coupled dynamic simulation, '*Code_Aster*(1)', with the exception of downwave tension at 20 s (D, G) which is better predicted by the motion-driven approach. Accuracy seems to deteriorate for larger wave heights, as observable from period-matched case pairs such as B, E. The root cause may be sought in the extra tuning required by the chain drag coefficients (governing the dynamic mooring effects at high energy), which are currently static and calibrated at the full scale. Another possible cause may be the absence of potential, 2$^{\text{nd}}$ order hydrodynamic excitation (wave drift forces) in the present numerical models.

The three dynamic modelling approaches presented here exhibit good mutual agreement with the exception of the downwave line tension for $T_{\text{w}} = 20\,\text{s}$. In this case the coupled simulation provides a tension RAO which is around 75%–80% of the motion-driven one, possibly due to the differing pitch responses obtained by CALHYPSO and *Code_Aster*(1), as already seen in Figure 3.19c. Further work will be required to clarify the system's dynamics at this particularly sensitive period.

Finally, the motion-driven output tensions obtained by neglecting the incident wave kinematics are shown to slightly undershoot the standard motion-driven results – by up to 8% in the worst case. This result is used to justify the use of approach '*Code_Aster*(2B)', neglecting the wave kinematics, in the following to simulate the mooring dynamics under irregular waves[9].

3.5.3.2 Response in irregular waves

CALHYPSO is used here to compute the DeepCwind FWT motion response under the irregular wave case defined in Table 3.6. Verifying the correct prediction of the dynamic response features of the platform is a required passage before moving on to analysing the dynamic fairlead tensions obtained with *Code_Aster*. In order to facilitate the interpretation of the output spectra, the uncoupled natural frequencies of the floater and of the undisturbed mooring lines are provided in Table 3.9. The latter are calculated with the method described in [202], based on the transverse-excitation modes of offshore mooring lines, and disregarding the hydrodynamic added mass.

The power spectral density (PSD) of motion in the three excited DoF is provided with Figure 3.21, where the experimental results are available only for the translational DoF. The surge motion spectrum is bimodal, with two distinct response peaks descending from the first-order and second-order (drag) hydrodynamic excitation on the platform; both peaks exhibit good agreement with the measurements. It is important to remark that satisfactory resonant response in surge is here obtained numerically without the

[9] Irregular wave kinematics are not implemented in *Code_Aster* yet.

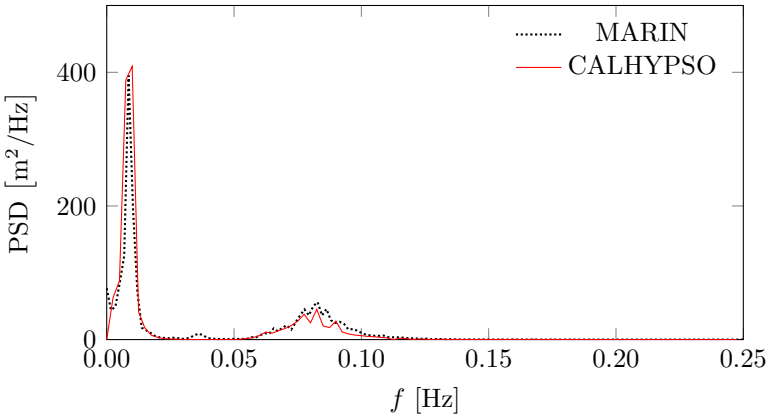

(a) Surge motion.

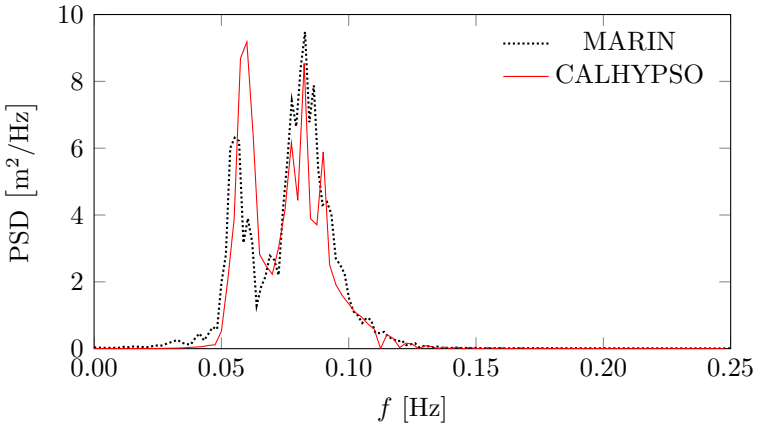

(b) Heave motion.

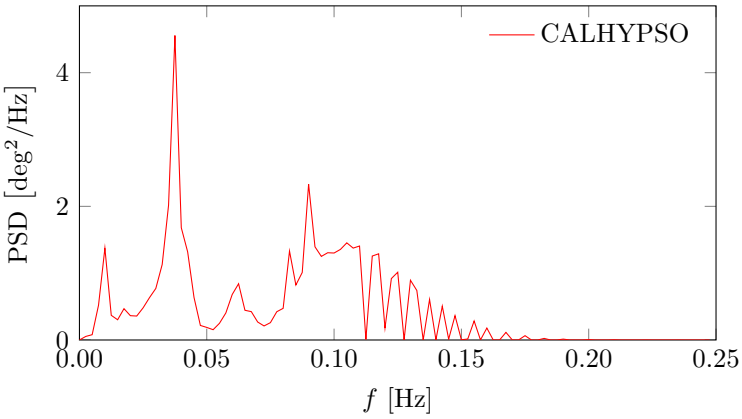

(c) Pitch motion.

Figure 3.21: Measured and computed power spectral density of the motions of the DeepCwind-OC4 floating system in irregular waves. The experimental curves are digitally imported from Masciola et al. [85].

inclusion of potential-flow, difference-frequency forces. As it was also observed during the VALEF2 project, the representation of hull drag forces on a position-updated basis introduces a low-frequency forcing which can dominate the excitation of the surge mode, depending on the type of structure studied. In light of this, the underprediction of resonant response in surge by the numerical model utilised in Masciola et al. [85] may be due to the missing actualisation of the Morison elements following the platform's displacements.

Heave response in the wave frequency band is also well represented by the numerical model, whilst the adjacent peak which identifies resonant motion – excited by both inertial and viscous wave forces – is slightly less well captured: whilst the excess motion amplitude may be due to insufficient vertical dissipation in the model, the slight natural frequency mismatch is likely due to the numerical added mass deficit on the Morison elements. For pitch motion, first-order wave excitation combines with the pitch response characteristic of the FWT providing the response energy visible in the central band. Secondary peaks appear to the left of this band suggesting the presence of weak inter-DoF couplings and pitch resonance.

Using the motion time histories above as input, the motion-driven dynamic simulation performed with the '*Code_Aster*(2B)' method provides the fairlead tension spectra displayed in Figure 3.22. Only the experimental spectrum of the upwave fairlead is available for comparison. Both spectra are trimodal, with a low-frequency peak governed by the resonant surge response of the platform, a broader wave frequency peak and a high-frequency tail. The dynamically simulated spectrum matches the experimental observations, net of the spectral noise caused at high frequency by the constant block averaging resolution chosen for the post-processing. Mainly due to the angled geometry of the downwave mooring lines with respect to the in-plane motion of the platform, the dynamic component of the simulated tension is much lower than in the upwave line.

An important limitation of the present comparison consists in the random phases chosen to translate the input wave spectrum into a time-domain signal. A more rigorous numerical representation of the experiments could be carried out by matching the basin test phases; unfortunately, these are unknown. Whilst the first-order dynamic

Table 3.9: Natural frequencies of the floating DeepCwind-OC4 system.

Subsystem	Mode	Frequency [Hz]
Platform	Surge/sway	0.009
Platform	Heave	0.059
Platform	Roll/pitch	0.039
Platform	Yaw	0.012
Mooring lines	1^{st} transverse	0.077
Mooring lines	2^{nd} transverse	0.153
Mooring lines	3^{rd} transverse	0.230

response is unaffected by phasing, response related to nonlinear processes combining different harmonics is linked to the specific phase set in the realisation[10]. Due to missing information regarding the spectral realisation of the basin tests (phases and duration of experiment), the phasing issue is not assessed in the present study.

Included in CALHYPSO is a quasi-static moorings model, whose performance in terms of tension prediction is satisfactory only at low frequency. In the wave frequency band and above this model severely underestimates the tension range, especially at the upwave fairlead. This is an expected outcome of the use of the quasi-static catenary representation of mooring forces in a highly dynamic offshore structure simulation. Although the first natural mode of the mooring lines sits in the vicinity of the first-order excitation peak, a sensitivity analysis (not included) permitted to determine that drag rather then inertia is the dominant process causing tension magnification in this band, which is not captured with the quasi-static approach. This is a known feature of catenary mooring systems in limited water depth.

Both numerical fairlead tension spectra obtained with *Code_Aster* contain significant high-frequency energy, due to the mechanical nonlinearities of the mooring system and a possible excitation of the second transverse mode of the lines (see Table 3.9). This prediction is confirmed by the available experimental spectrum. The broad frequency spreading of this response feature may be explained with the parametric behaviour related to the low-frequency variation of line tension and suspended length caused by platform motion. The high-frequency energy content is relatively more important for the downwave line, as it is also intuitively visible from Figure 3.23. A close inspection of the tension time histories confirms the trimodal nature of the dynamic tension signals and the absence of the high-frequency response from the quasi-static results.

[10] See for instance Roald et al. [203].

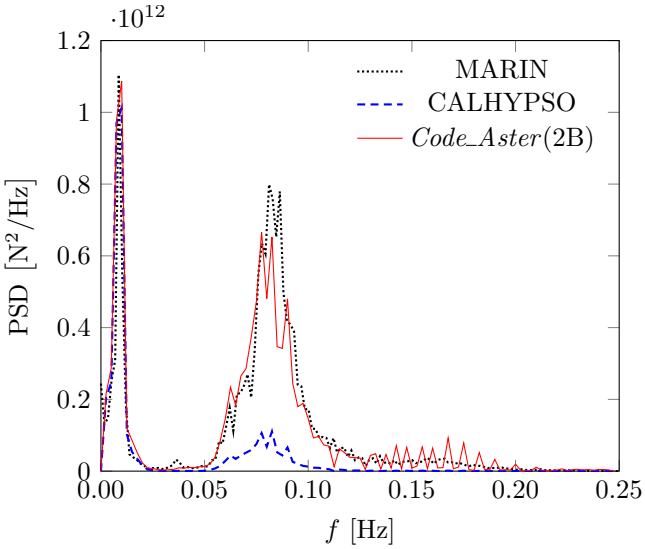

(a) Line tension at fairlead 1.

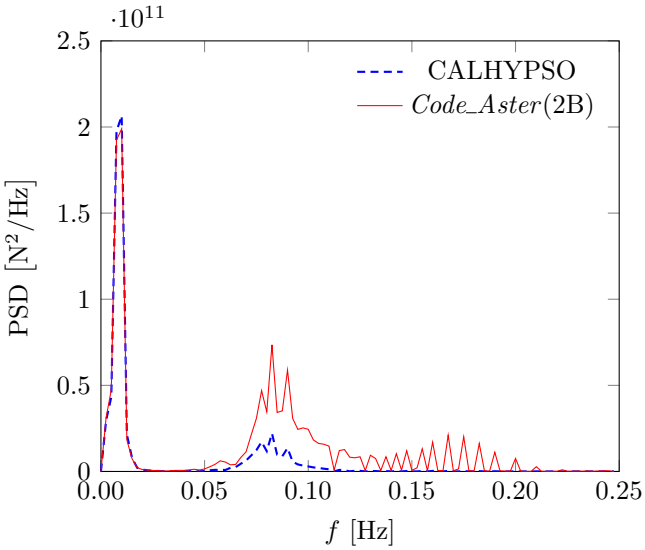

(b) Line tension at fairlead 2.

Figure 3.22: Measured and computed power spectral density of the fairlead tensions under irregular wave excitation. The experimental curve is digitally imported from Masciola et al. [85].

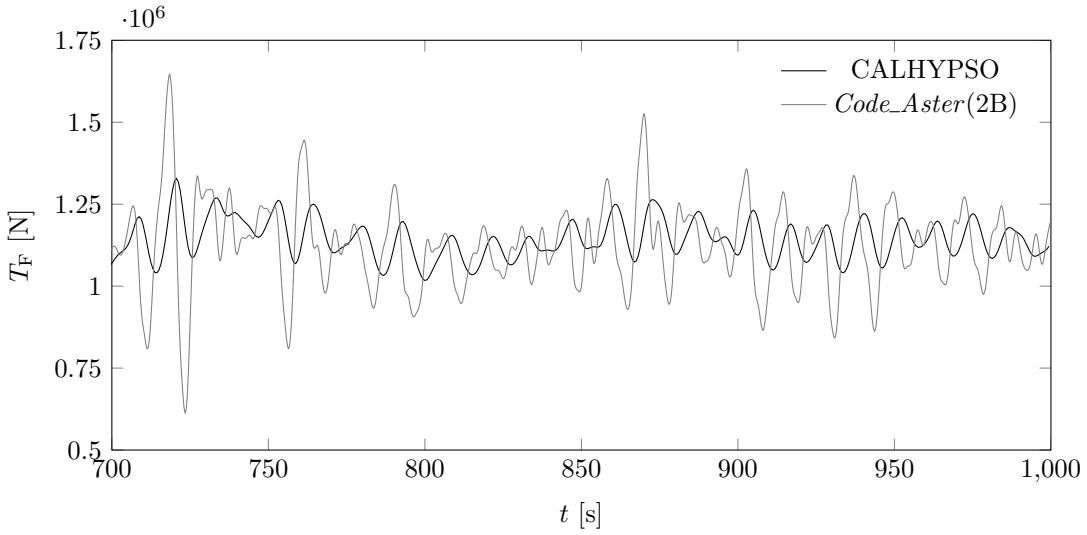

(a) Line tension at fairlead 1.

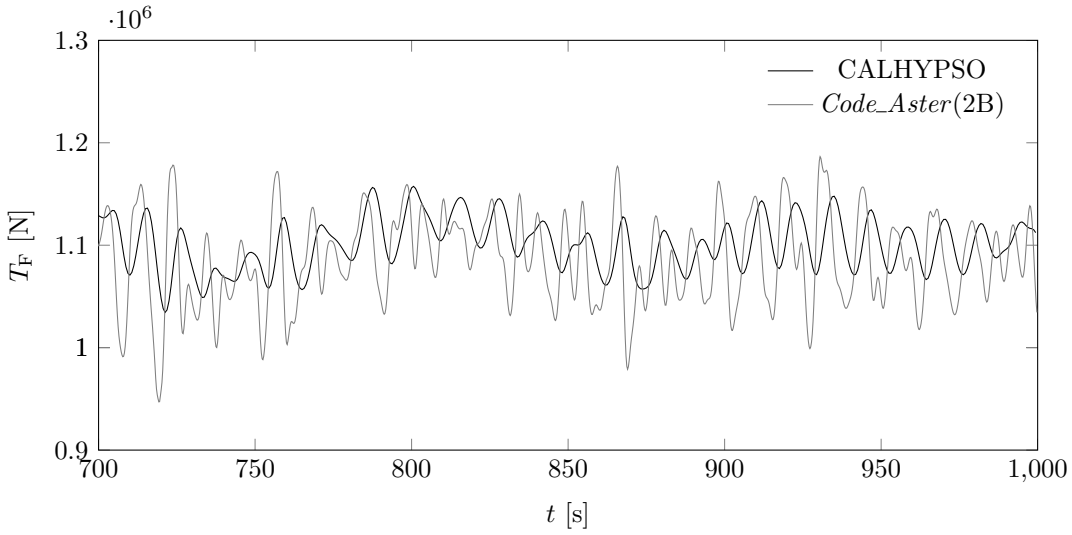

(b) Line tension at fairlead 2.

Figure 3.23: Excerpts of simulated line tension under irregular wave excitation using quasi-static and dynamic mooring analysis.

3.6 Conclusion

For the first time *Code_Aster*, the open-source mechanical analysis software developed by EDF R&D, has been used here to simulate offshore mooring dynamics. Successful applications to the floating wind technology have been included in this Part. After the presentation of the methodological choices, hinging on the 1D finite-element representation of slender and compliant structures and unilateral contact mechanics, it has been shown that appropriate model set-up and initialisation permit to handle the hydromechanics of catenary mooring systems with this general-purpose tool.

A series of static simulations has been used first to document the accuracy and capability of the model, enabling to reconstruct the nonlinear and linearised behaviour of slack mooring systems for FWTs. Subsequently, a range of dynamic simulations has been performed and compared with experimental results available from the literature. The model has been shown to satisfactorily predict the coupled platform-moorings dynamics of a FWT in regular waves. The dynamic fairlead tensions are in particular well represented, albeit with seemingly decreasing accuracy as the wave height is increased. A motion-driven simulation representing the system's dynamics under irregular waves has also been carried out and compared with experimental observations from the literature, once again validating the accuracy of the fairlead tensions predicted via *Code_Aster*. It has been shown that all the constituents of dynamic tension response (low-frequency, wave frequency, and high-frequency) are captured by the numerical solution, suggesting that the model correctly reproduces the main physical processes at play. Accuracy may be improved by further work: for instance, the choice of comparing the measured and simulated response at the full scale brings with it a degree of scaling uncertainty, which may affect in particular the viscous hydrodynamics of the mooring lines. Additional calibration efforts may be sought in the future, perhaps by complementing the modelling workflow with reduced-scale analyses.

A more thorough verification of the capabilities of this model will require the evaluation of the behaviour of different platform and mooring system combinations, especially considering that the presented validation case regards a large, academic-type floater concept using a conventional slack mooring system. Considering the current trends in FWT technology, priority may be placed on the implementation of fibre rope behaviour (especially with respect to nonlinear stiffness characteristics) and on the verification of taut/tensioned system simulation. The implementation of higher-order wave forcing on the platform in the calculation chain should also permit to ascertain their influence on the system's dynamic response, especially considering that the low-frequency motions and tensions obtained here seem to match well the experiments although no second-order potential hydrodynamics are represented.

The inclusion of aerodynamic forcing, either steady or turbulent, is already possible with the motion-driven approach, and should be investigated in the future for the

characterisation of the effects of aerodynamics on the mooring line tensions. A further step may consist in dynamically linking the finite-element solver to CALHYPSO to enable fully coupled mechanical simulations.

In its current form, the presented *Code_Aster*-based dynamic moorings model has become part of EDF R&D offshore mechanics calculation chain and has already been used for concept verification and classification (see Peyrard and Antonutti [161]); it has been employed by the utility to evaluate FWT mooring arrangements of different complexity, in the context of the Group's calls for tenders – where solutions by MODEC, Ideol, and other applicants were analysed – and of a joint industrial project (Vertiwind). Further development efforts may be directed toward coefficient calibration, a more detailed representation of the seabed interaction and of the fluid-structure interaction, and a generalisation of the types of mooring components tractable (ropes, buoys, etc.). In particular, finite elements of higher complexity (beams) may be used for the representation of less flexible 1D equipment such as umbilical cables, provided that a reliable large-displacement behaviour is implemented.

Part 4

Aeroelastic Analysis of Vertical-Axis Wind Turbines

This Part presents the doctoral work carried out in the field of vertical-axis wind turbine rotordynamics and aeroelasticity, with application on helical-type VAWT rotors of the Vertiwind class. An introduction to the domain of aeroelasticity and an outline of the aeroelastic stability problem are given in Section 4.1. The motivation of the present study and a review of past research in this area are also contextually supplied. Section 4.2 introduces the methodology used to establish the finite-element rotor-dynamic model representing the structure in the absence of aerodynamic interaction. The classic output of this type of model, the Campbell diagram, is also presented in Section 4.2 with application to two VAWT rotor architectures. The following Section 4.3 further builds on the rotor-dynamic model leading to a representation of the integral aeroelastic system. This serves to characterise and discuss the coupled vibrational-aerodynamic behaviour of the two VAWT rotors of interest. Finally, Section 4.4 summarises the conclusions of this Part, and points out its methodological limitations.
A subset of the materials contained in this Part has been used within an internal EDF R&D deliverable by Relun and Antonutti [204].

4.1 Introduction

Offshore wind turbine rotors are among the largest rotating structures ever constructed. Designing these machines to guarantee long-term structural integrity in a cost-effective way is one of the main challenges faced by the wind industry, and constitutes a rich research area. Due to the increasing size (especially offshore) and compliance of modern rotor designs, admissible blade deformations are increasing (Figure 4.1). Because of structure elasticity, the aerodynamic loads tend to become increasingly affected by the turbine's structural response, resulting in a coupling of two dynamic systems: the structural system and the aerodynamic system, which combined form a dynamic aeroelastic system (see Figure 4.2). As it will be later explained, such systems are

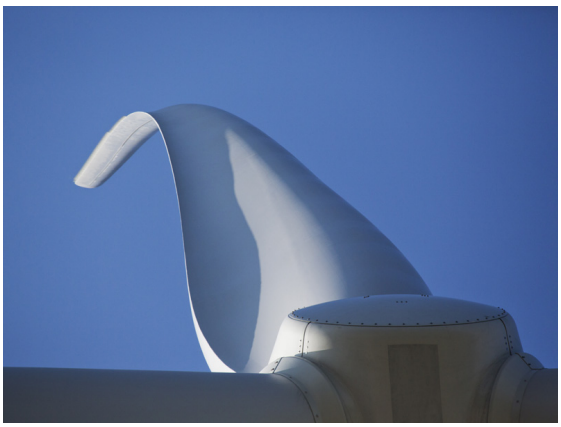

Figure 4.1: Aeroelastic deflection of a wind turbine blade. After Siemens [205].

susceptible of entering self-excited dynamic states which may hinder the capacity of the structure to resist normal operating loads, or even lead to rapid failure. This is why the structural reliability of a large wind turbine rotor must be studied with an aeroelastic approach: methodologies originally conceived for the study of subsonic aircraft wings are today broadly used in this context.

Classic examples of aeroelastic systems are large-span suspension bridges and airplane wings. These structures combine high aerodynamic loading with structural compliance in different manners. On one hand, modern suspension bridge design allows for large displacements to redistribute the internal stresses and achieve material efficiency. The parasitic aerodynamic forces arising from the action of wind interact with said displacements and may trigger adverse aeroelastic phenomena such as flutter, a self-excited state which caused the notorious collapse of the Tacoma Narrows bridge. On the other hand, aircraft wings are designed to produce large aerodynamic whereby minimising structural weight: once again the outcome is a system which simultaneously exhibits high aerodynamic loading and structural compliance, thus requiring aeroelastic analysis for its design and verification. The aerodynamic complexities specific to the above applications (chiefly vortex shedding for bluff civil engineering structures and compressible aerodynamics for aircraft wings) will be left out of the present study, enabling to concentrate on the aeroelastic features characteristic of a vertical-axis wind turbine rotor.

As seen in Part 1, the EDF Group is currently pioneering the use of large-scale vertical-axis rotors for use in floating wind projects. As it has been pointed out, verifying the structural integrity of the rotor configurations proposed by the technology developers requires to characterise their aeroelastic behaviour. The key question is whether the proposed designs risk to be affected by aeroelastic instability. Verifying a rotor configuration means, firstly, making sure that such instabilities are not triggered in the machine's operating envelope, and that sufficient margins lie between the operating

envelope and any detected unstable states. Secondly, the presented method allows to produce an estimate of the beneficial aerodynamic damping generated by the aeroelastic interaction. Its prediction and incorporation in the design phase allows to avoid over-designing the rotor, whose vibrations – especially in resonant conditions – can be significantly reduced in amplitude by this phenomenon. In fact, given the typically low structural damping of wind turbine rotors, the aerodynamic component tends to dominate their vibrational damping [206].
The numerical model presented in this Part was developed for the purposes described above. The upstream doctoral work exploits a pre-existing in-house finite element environment written in C++ and includes the implementation of rotating beam theory, linearised airfoil theory, as well as the separate resolution of the modal problem in the Scilab programming environment. The model is hence applied to two rotor configurations of interest. The first is related to an ongoing testing campaign for the qualification of a 600 kW rated sub-assembly of the Vertiwind turbine (see Figure 4.11), which is expected to provide full-scale experimental data enabling the validation of the numerical model. The second application concerns the prediction of the aeroelastic vibrational behaviour of the fully assembled 2 MW Vertiwind rotor for use in the EDF Group's pilot floating windfarm project *Provence Grand Large*.

4.1.1 Aeroelastic stability of wind turbines

As said above, the discipline of aeroelasticity combines in its classic formulation structural and aerodynamic analysis; grounding in this domain is available for instance in textbooks by Balakrishnan [207] and Clark et al. [208]. More specifically, structural forces can be broken down into elastic and inertial components, which allows to identify the field of dynamic aeroelasticity through the Collar diagram shown in Figure 4.2. It

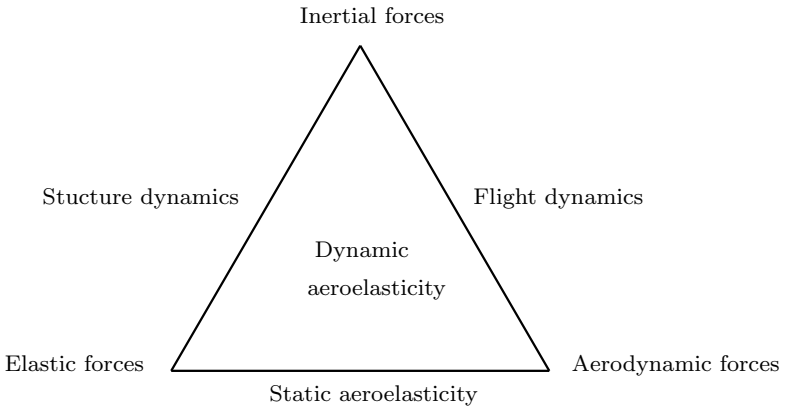

Figure 4.2: Relationship between structural and aerodynamic forces with respect to typical dynamic systems, also known as Collar's aeroelastic triangle.

is straightforward to acknowledge that the interaction of inertial and elastic forces in a solid defines the field of classic structural dynamics. When a free, unconstrained body is subjected to aerodynamic loading, its dynamics are in essence determined by the interaction of these loads with the body's own inertial forces. This defines the field of flight dynamics in Figure 4.2. When elastic forces interact with an aerodynamic system with little participation of the structure's inertial forces, the resulting motion is well described by means of static aeroelasticity considerations as shown in the Figure. This is for example the case of an idealised zero-mass airfoil which is compliant in pitch: the pitch angle determines the lift force and hence the moment exerted on the airfoil, while at the same time it is driven by these same external forces. In other words, a coupling is present which links the aerodynamic and structural elastic subsystems.

Most rotating machinery using air as a working fluid – in essence all sorts of air pumps and turbines – is comprehensively described by the dynamic aeroelastic scheme, where the aerodynamic and inertial forces must however include the effects of rotation. On the aerodynamic side, a homogeneous rotation of the structure around a fixed axis induces a tangential airspeed on its components which is combined with the incident airflow. The curved trajectory followed by any part of the structure located at a distance from the revolving axis also causes a perturbation of the relative airflow compared to the usual rectilinear flow considered in classic aeroelastic models. On the structural side the distributed gyroscopic/Coriolis and centrifugal forces affect the rotor's vibrations and cause its modes to depart from those experienced at standstill. All structural spinning effects are related to the principle of inertia and can hence be included in the upper vertex of the Collar triangle. However they all depend from the rotational speed: explicitating the distinction between them and the classic standstill inertial forces can help in understanding the elements at play into the rotor-dynamic system, as it will appear evident in Section 4.2. The corresponding picture may be provided visually by rearranging the Collar triangle into a tetrahedron as done in Figure 4.3.

As anticipated in the introduction, the concept of aeroelastic instability descends from the observation that in certain conditions aeroelastic systems can enter self-excited states leading to the loss of stability, which may be due to either static or dynamic effects. It is important to remark that these states are distinct from resonant vibration and may prove far more dangerous if left unchecked: a rapid and complete failure can easily occur after the onset of aeroelastic instability, or otherwise the structure may resist by locking into undesirable and typically damaging limit-cycle oscillations [1]. Hence such instabilities need to be recognised in advance and typically designed out of the operating envelope of the machine to prevent the incursion of catastrophic failure

[1] A limit-cycle oscillation is a high-amplitude vibrational state for which the system exhibits non-linear dynamics. Refer for instance to Dutta and Bhattacharjee [209]. The associated cyclical loads often exceed the elastic limits of the structure and/or produce a rapid escalation of structural damage.

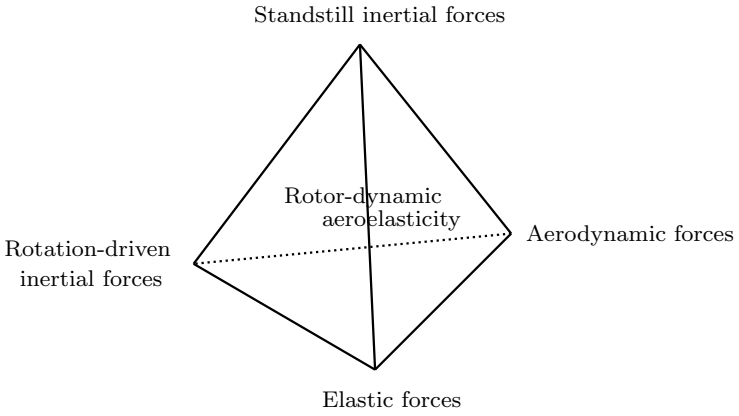

Figure 4.3: Extension of the Collar's aeroelastic triangle to allow for rotor-dynamic effects.

modes.

In the field of subsonic, attached-flow aeromechanics, a fundamental type of static instability is the the lift-induced divergence phenomenon: when a lift generating structure's marginal restoring force in the torsion mode becomes smaller than the marginal lift moment increase associated to the same rotation, runaway rotation is the consequence. Flutter, labelled as "*the most dramatic physical phenomenon in the field of aeroelasticity*" by Clark et al. [208], is instead the key dynamic instability mechanism. This takes place when coupled flapwise and torsional motion of a lift-generating structure causes lift force oscillations which are in-phase with its motion; if the mode is not damped enough, the net energy intake of each oscillation cycle is positive, leading to increasingly large displacements and a risk of structural failure. When rotating machinery is concerned, the flutter mechanism can interact with the effects of structure rotation and may be triggered by a reduction of effective structural stiffness due to spin-softening and/or centrifugal pre-loading. This form of instability commonly found on rotors is denoted whirl flutter, for example by Buhl et al. [210]. A common prediction found in the literature is that as wind turbines grow in scale and additional flexibility is designed in to improve large-blade load management, lift-induced flutter (also called classical flutter) may become increasingly important as a design constraint. Taken to the extreme consequences, this tendency may cause a shift from load-driven design to stability-driven design when very large and elastic rotors are concerned, as pointed out by Bir and Jonkman [211], as well as Ashuri [212].

The aeroelastic stability of large wind turbine rotors of the horizontal and vertical-axis kind remains today a relatively immature research area where a limited amount of reported work is available. In addition, no experimental data has been published in this field for utility-scale turbines to be used as a suitable validation basis. A comprehensive review of the research in both aerodynamic and aeroelastic analysis of wind turbines

by Hansen [121] concentrates on the horizontal-axis architecture. A close-up on the aeroelastic stability problem of large wind turbines is provided in Hansen et al. [213]. Concerning the HAWT arrangement, there is agreement on the fact that two potential instability types are prevalent: the lift-induced flutter mechanism described above and the stall-induced vibration mechanism. Lift-induced flutter is shown to potentially affect the stability of a pitch-controlled turbine, especially when in idling state under high wind, whilst blade operation in the stall region is pointed out as a concurring source of instability for stall-regulated HAWTs as remarked by Madsen et al. [214], Thomsen et al. [215], and Holierhoek [216]. The latter phenomenon, due to the decrease of reactive lift experienced during blade vibrations, becomes particularly important when the blade airfoils exhibit abrupt stall characteristics. A study by Zhang and Nielsen [217] shows that turbulent inflow can also provide a significant contribution to this type of instability.

The aeroelastic behaviour of vertical-axis wind turbines has been described in the time domain when rotor deformability is included in the model, for example in Wang et al. [111], where the blade element momentum Theory is used to apply the aerodynamic loads on a deformable Darreius VAWT. However, the characterisation of aeroelastic stability is often not well documented when such coupled simulation models are used, because the spinning effects, critical for the assessment of stability, are not explicitly treated. A relatively simpler frequency-domain set-up allows direct determination of the stable operating envelope and the estimation of the rotor's aerodynamic damping characteristics at limited computational cost, though generally accepting more stringent hypotheses. This is the approach used for instance by Lobitz [218] to evaluate the flutter propensity of an isolated HAWT blade, which is also studied using different modelling options in Owens et al. [219]. An evaluation of the sensitivity of flutter for a HAWT blade with respect to its construction parameters is provided by Lobitz [220] using the same approach, as well as by Resor et al. [221].

More dated works by Lobitz and Ashwill, and Popelka [206, 222] evaluate the aeroelastic features of a full VAWT assembly with an analogous method; vertical-axis rotors are also investigated in Owens and Griffith [223], where several MW-scale concepts are treated.

The aforementioned studies address the aeroelastic problem by simplifying aerodynamics through the use of blade element theory. More physical and computationally expensive approaches potentially enable much greater accuracy in the characterisation of the aeroelastic behaviour of a VAWT. For example a study combining the FE and RANS methods, proposed by Raciti Castelli et al. [224], organises the coupled aerodynamic-structural problem with full resolution of the aerodynamic flow.

4.2 Modal analysis of vertical-axis rotors

This section describes the methodology underpinning the model used to identify the vibrational modes of a VAWT rotor and the evolution of their characteristic frequency with respect to rotational speed (Campbell diagram). Two Vertiwind-type rotors of interest are then analysed, providing a direct industrial application example and a basis for discussion of rotordynamic effects.

4.2.1 Methodology

The VAWT rotor assembly is studied here as a solid, elastic continuum undergoing rotation about a fixed axis, with the position of the bearing assumed fixed in space. The interaction with the surrounding fluid is disregarded: this part will be later introduced in the form of a model augmentation in Section 4.3. The structure of the rotor is hence undergoing large rotational displacements, whereby its vibrations can be assumed to be small in amplitude. This enables to decouple the kinematic representation of revolution from that of vibration: if one assigns a prescribed rotational speed to the rotor, corresponding to a given operating condition, then the small deformations of the solid around the equilibrium geometry may be expressed in the corrotating system of reference, eliminating the need to re-actualise the structure's geometry following the variation of the azimuth angle. Thus by assuming linear material behaviour and small vibration amplitude the vibrational dynamic problem can be linearised and solved in the rotating, non-inertial frame attached to the structure. This treatment allows the use the classic finite-element modelling tools (see for example Abbas [225]). The methodological basis used to build the numerical model of a spinning rotor is next presented.

4.2.1.1 Kinematics

A point P in 3D space is shown in Figure 4.4. Given an inertial reference system XYZ, and assuming that the point is rotating at constant speed Ω around Y, one can assign a corrotating, non-inertial system of reference (SoR) $\bar{x}\bar{y}\bar{z}$ where $\bar{y} \equiv Y$ and $\bar{x} = X, \bar{z} = Z$ for $t = 0$. Vector $\mathbf{r}$ denotes the position of P in the corrotating system. A simplifying hypothesis adopted in this study descends from the assumption that the rotor bearing is fixed in the inertial system of reference – which in practice corresponds to disregarding the offshore platform motions and the deformations of the structure which supports the bearing. This permits to impose that the translations of the floating frame be identically zero, as well as the rotations other than that associated to rotor speed in operation, in our case $\tilde{\omega}_1 \equiv \tilde{\omega}_3 \equiv 0$. After imposing a generic constant rotational speed, $\tilde{\omega}_2 = \Omega = \text{const.}$, a spinning matrix $\mathbf{\Omega}$ is introduced to link the motion expressed in the

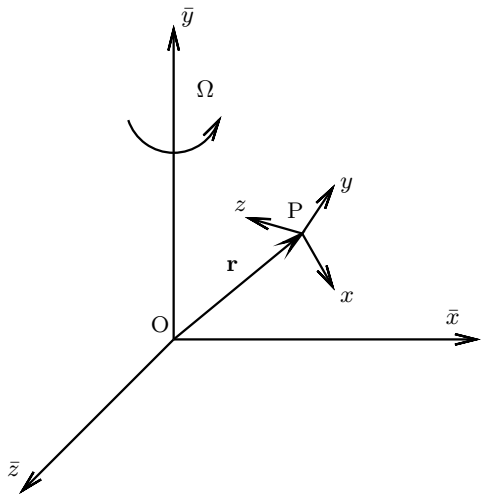

Figure 4.4: Location of point P in a rotating system of reference $\bar{x}\bar{y}\bar{z}$.

inertial and spinning systems of reference:

$$\mathbf{\Omega} = \begin{bmatrix} 0 & 0 & \Omega \\ 0 & 0 & 0 \\ -\Omega & 0 & 0 \end{bmatrix}. \tag{4.1}$$

Let $\mathbf{p}$, $\dot{\mathbf{p}}$, and $\ddot{\mathbf{p}}$ be the position, velocity, and acceleration vectors in the inertial frame, under the above hypotheses the kinematics of P in XYZ are given by

$$\mathbf{p} = \mathbf{r}\,, \tag{4.2}$$

$$\dot{\mathbf{p}} = \dot{\mathbf{r}} + \mathbf{\Omega}\mathbf{r}\,, \tag{4.3}$$

$$\ddot{\mathbf{p}} = \ddot{\mathbf{r}} + 2\mathbf{\Omega}\dot{\mathbf{r}} + \mathbf{\Omega}^2\mathbf{r}\,. \tag{4.4}$$

For clarity, $\dot{\mathbf{r}}$ and $\ddot{\mathbf{r}}$ represent the point's speed and acceleration in the rotating frame, $\mathbf{\Omega}\mathbf{r}$ the tangential spinning velocity, $2\mathbf{\Omega}\dot{\mathbf{r}}$ the Coriolis acceleration and $\mathbf{\Omega}^2\mathbf{r}$ the centripetal acceleration. As visible in Figure 4.4, a third (corrotating) local frame xyz is associated to point P, which will later come in handy to express the beam deformations on a convenient local basis. One may then define $\mathbf{u} = (u, v, w)^{\mathrm{T}}$ as the displacement of P in xyz and

$$\bar{\mathbf{u}} = \mathbf{R}^{\mathrm{T}}\mathbf{u} \tag{4.5}$$

as the same displacement expressed in the global spinning frame $\bar{x}\bar{y}\bar{z}$, where $\mathbf{R}$ represents the transformation matrix between the two systems of reference. Superscript 'T' denotes a transposition. $\mathbf{R}$ contains the components of the unit vectors defining the

local frame xyz in the spinning global frame $\bar{x}\bar{y}\bar{z}$:

$$\mathbf{R} = \begin{bmatrix} \alpha_{11} & \alpha_{12} & \alpha_{13} \\ \alpha_{21} & \alpha_{22} & \alpha_{23} \\ \alpha_{31} & \alpha_{32} & \alpha_{33} \end{bmatrix} . \tag{4.6}$$

By defining $\mathbf{r}_0$ as the (constant) position vector defining the origin of the xyz frame in the $\bar{x}\bar{y}\bar{z}$ SoR, the position of P after a displacement can be expressed with reference to $\bar{x}\bar{y}\bar{z}$ as

$$\mathbf{r} = \mathbf{r}_0 + \bar{\mathbf{u}} = \mathbf{r}_0 + \mathbf{R}^{\mathrm{T}}\mathbf{u} , \tag{4.7}$$

and by consequence its speed is given by

$$\dot{\mathbf{r}} = \mathbf{R}^{\mathrm{T}}\dot{\mathbf{u}} . \tag{4.8}$$

4.2.1.2 Discretisation of the structure

The vertical-axis wind turbine rotors of interest are skeletal structures, in other words solids mainly composed of long and slender parts (struts, blades, mast). The kinematic hypotheses of the Euler-Bernoulli beam are known to be particularly fit for this type of structure. A method suitable for writing the dynamic EoM representing the vibrations of spinning beams of arbitrary orientation is available in Leung and Fung [226]. The finite-element approach proposed in this article is hence followed, but a caveat must be made: a fundamental assumption of this approach is that beam torsion and bending are mechanically uncoupled. This renders the subsequent model only fit to represent assemblies of slender structures whose sectional centre of gravity corresponds or lies close to the elastic centre (this is the case for the studied Vertiwind rotor components). In the local SoR xyz, the displacements $\mathbf{u}$ of any planar section of a 1D beam such as

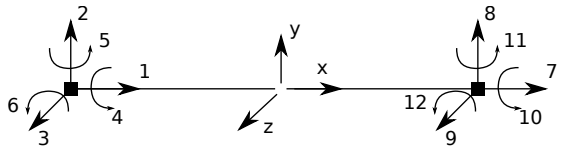

Figure 4.5: Beam element, local system of reference and nodal degrees of freedom.

that displayed in Figure 4.5 are found by interpolation between the coordinates of the e^{th} beam's extremity nodes $\mathbf{q}_e$ (the nodal DoF concerned are indicated in the Figure). The generalised displacement and velocity vectors of the section are hence given by

$$\mathbf{u} = \mathbf{N}\mathbf{q}_e \quad \text{and} \quad \dot{\mathbf{u}} = \mathbf{N}\dot{\mathbf{q}}_e . \tag{4.9}$$

In the above equation matrix $\mathbf{N}$ contains the shape functions which are commonly derived by using the Galerkin method combined with elastic beam theory:

$$\mathbf{N} = \begin{bmatrix} \mathbf{N}_1 & & \\ & \mathbf{N}_2 & \\ & & \mathbf{N}_3 \end{bmatrix}, \tag{4.10}$$

where the numbered terms are the shape function submatrices which (nondimensionally) describe the beam's deformed geometry in its local SoR. The interested reader may also refer to the *Code_Aster* documentation [225, 227]. The Euler-Bernoulli beam tensile and bending shape functions are explicited in Appendix E.

4.2.1.3 Dynamics in the spinning frame

From an energetic point of view, the dynamics of a deformable body can be expressed using the Lagrange equations

$$\frac{\mathrm{d}}{\mathrm{dt}} \frac{\partial T^*}{\partial \dot{\mathbf{u}}} - \frac{\partial T^*}{\partial \mathbf{u}} + \frac{\partial U^*}{\partial \mathbf{u}} = \tilde{\mathbf{f}}\,. \tag{4.11}$$

Here T^* and U^* represent the body's integral kinetic and strain energy, and $\tilde{\mathbf{f}}$ the external generalised force vector, which is set to zero when free vibration is considered. By adopting the hypotheses of the Euler-Bernoulli beam, and by supposing that the structure oscillates about an equilibrium configuration after being pre-tensioned by a steady force (which in the present application is the centrifugal force), T^* and U^* are respectively yielded by

$$T^* = \frac{1}{2} \int \rho_\mathrm{m} A \dot{\mathbf{p}}^\mathrm{T} \dot{\mathbf{p}} \mathrm{d}s\,, \tag{4.12}$$

$$U^* = \frac{1}{2} \int EA \left(\frac{\partial u}{\partial s}\right)^2 \mathrm{d}s + \frac{1}{2} \int EI_z \left(\frac{\partial^2 v}{\partial s^2}\right)^2 \mathrm{d}s + \frac{1}{2} \int EI_y \left(\frac{\partial^2 w}{\partial s^2}\right)^2 \mathrm{d}s + \\ + \frac{1}{2} \int F(s) \left(\frac{\partial v}{\partial s}\right)^2 \mathrm{d}s + \frac{1}{2} \int F(s) \left(\frac{\partial w}{\partial s}\right)^2 \mathrm{d}s\,, \tag{4.13}$$

where the integration occurs along the beam's own longitudinal coordinate s, directed along x. In Equations 4.12 and 4.13 E represents Young's modulus, ρ the material density, A the sectional area, I_y and I_z the sectional second moments of inertia with respect to the section's principal axes, and $F(s)$ the axial force due to pre-tensioning. The contribution of the (uncoupled) torsional mode of the beam is omitted from the above expressions, following the theoretical presentation by Leung and Fung [226]. It is straightforward to recognise the components of the strain energy U^* appearing sequentially in Equation 4.13: the axial elongation term, two bending terms (around

y and z) depending from curvature, and two terms representing the work of the axial pre-tension force in presence of beam deflection.

For the discussed steady rotation of the beam around the Y axis ($\tilde{\omega}_1 \equiv \tilde{\omega}_3 \equiv 0$), Equations 4.3, 4.7, and 4.8 can be used to express $\dot{\mathbf{p}}^{\mathrm{T}}\dot{\mathbf{p}}$ in Equation 4.12. By employing the shape functions as shown in Equation 4.9, the following nodal formulation of kinetic energy for a beam element of length l, cross-sectional area A, and index number e is obtained[2]

$$T_e^* = \frac{1}{2}\dot{\mathbf{q}}_e^{\mathrm{T}}\mathbf{M}_e\dot{\mathbf{q}}_e + \frac{1}{2}\mathbf{q}_e^{\mathrm{T}}\mathbf{K}_{\Omega e}\mathbf{q}_e + T_{0e}^* + \dot{\mathbf{q}}_e^{\mathrm{T}}\mathbf{f}_e + \dot{\mathbf{q}}_e^{\mathrm{T}}\tilde{\mathbf{G}}_e\mathbf{q}_e + \mathbf{f}_{\Omega e}^{\mathrm{T}}\mathbf{q}_e\,, \tag{4.14}$$

where

$$\mathbf{M}_e = \int_0^l \rho_{\mathrm{m}} A\mathbf{m}\mathrm{d}s, \quad \mathbf{K}_{\Omega e} = \int_0^l \rho_{\mathrm{m}} A\mathbf{k}_\Omega \mathrm{d}s, \quad \tilde{\mathbf{G}}_e = \int_0^l \rho_{\mathrm{m}} A\mathbf{g}\mathrm{d}s\,,$$

$$\mathbf{f}_e = \int_0^l \rho_{\mathrm{m}} A\mathbf{N}^{\mathrm{T}}\mathbf{R}\boldsymbol{\Omega}\mathbf{r}_0\mathrm{d}s, \quad \mathbf{f}_{\Omega e} = \int_0^l \rho_{\mathrm{m}} A\mathbf{N}^{\mathrm{T}}[f_{\Omega x}, f_{\Omega y}, f_{\Omega z}]\mathrm{d}s\,,$$

$$T_{0e}^* = \frac{1}{2}\int_0^l \rho_{\mathrm{m}} A\mathbf{r}_0^{\mathrm{T}}\boldsymbol{\Omega}^2\mathbf{r}_0\mathrm{d}s\,,$$

$$\mathbf{m} = \begin{bmatrix} \mathbf{N}_1^{\mathrm{T}}\mathbf{N}_1 & & \\ & \mathbf{N}_2^{\mathrm{T}}\mathbf{N}_2 & \\ & & \mathbf{N}_3^{\mathrm{T}}\mathbf{N}_3 \end{bmatrix}, \quad \mathbf{g} = \Omega\begin{bmatrix} \mathbf{0} & b_1\mathbf{N}_1^{\mathrm{T}}\mathbf{N}_2 & b_2\mathbf{N}_1^{\mathrm{T}}\mathbf{N}_3 \\ & \mathbf{0} & b_3\mathbf{N}_2^{\mathrm{T}}\mathbf{N}_3 \\ & \text{anti-symm.} & \mathbf{0} \end{bmatrix},$$

$$\mathbf{k}_\Omega = \Omega^2\begin{bmatrix} a_{11}\mathbf{N}_1^{\mathrm{T}}\mathbf{N}_1 & a_{12}\mathbf{N}_1^{\mathrm{T}}\mathbf{N}_2 & a_{13}\mathbf{N}_1^{\mathrm{T}}\mathbf{N}_3 \\ & a_{12}\mathbf{N}_1^{\mathrm{T}}\mathbf{N}_2 & a_{23}\mathbf{N}_2^{\mathrm{T}}\mathbf{N}_3 \\ \text{symm.} & & a_{33}\mathbf{N}_3^{\mathrm{T}}\mathbf{N}_3 \end{bmatrix},$$

$$a_{11} = \alpha_{11}^2 + \alpha_{13}^2\,, \quad a_{12} = \alpha_{11}\alpha_{21} + \alpha_{13}\alpha_{23}\,, \quad a_{12} = \alpha_{11}\alpha_{31} + \alpha_{13}\alpha_{33}\,,$$

$$a_{22} = \alpha_{21}^2 + \alpha_{23}^2\,, \quad a_{23} = \alpha_{21}\alpha_{31} + \alpha_{23}\alpha_{33}\,, \quad a_{33} = \alpha_{31}^2 + \alpha_{33}^2\,,$$

$$b_1 = \alpha_{11}\alpha_{23} - \alpha_{13}\alpha_{21}\,, \quad b_2 = \alpha_{11}\alpha_{33} - \alpha_{13}\alpha_{31}\,, \quad b_3 = \alpha_{21}\alpha_{33} - \alpha_{23}\alpha_{31}\,,$$

$$f_{\Omega x} = \Omega^2(x_0\alpha_{11} + z_0\alpha_{13})\,, \quad f_{\Omega y} = \Omega^2(x_0\alpha_{21} + z_0\alpha_{23})\,, \quad f_{\Omega z} = \Omega^2(x_0\alpha_{31} + z_0\alpha_{33})\,.$$

In the above expressions the homogeneous material density is denoted by ρ_{m}. The elementary matrices resulting from the above procedure are reported in Appendix F. It should be noted that the nodal coordinates $\mathbf{q}_e$ are still expressed in the local SoR xyz. They must be re-expressed in a common frame if the system is to be assembled. Here this is chosen as the global spinning frame $\bar{x}\bar{y}\bar{z}$, and the transformation carried out by decomposing $\mathbf{q}_e$ into two translations and two rotation vectors and by using Equation 4.5. Likewise, the vectors produced by the matrix operations need to undergo

[2]The size of the vectors and square matrices defining Equation 4.14 is 12, that reflects the $6 + 6$ nodal displacements of Figure 4.5.

a basis change. Generically speaking, combining these two transformations in presence of a matrix-vector operation leads to writing

$$\mathbf{w} = \mathbf{S}\mathbf{u} = \mathbf{S}\mathbf{R}\bar{\mathbf{u}}\,, \tag{4.15}$$

where $\mathbf{w}$ represents the vector resulting from the operation, and $\mathbf{S}$ a generic 3×3 submatrix. Hence the basis change yields

$$\bar{\mathbf{w}} = \mathbf{R}^{\mathrm{T}}\mathbf{w} = \mathbf{R}^{\mathrm{T}}\mathbf{S}\mathbf{R}\bar{\mathbf{u}} = \bar{\mathbf{S}}\bar{\mathbf{u}}\,, \tag{4.16}$$

where

$$\bar{\mathbf{S}} = \mathbf{R}^{\mathrm{T}}\mathbf{S}\mathbf{R}\,. \tag{4.17}$$

The overbar in the above equations denotes the quantities expressed in the global SoR. The 12×12 beam element matrices are thus transformed by manipulating all 3×3 submatrices according to Equation 4.17. Assembling the element matrices expressed in this form using the classic superposition approach ultimately yields the overall kinetic energy:

$$T^* = \sum_e T_e^* = \frac{1}{2}\dot{\mathbf{q}}_{\mathrm{t}}^{\mathrm{T}}\mathbf{M}\dot{\mathbf{q}}_{\mathrm{t}} + \frac{1}{2}\mathbf{q}_{\mathrm{t}}^{\mathrm{T}}\mathbf{K}_\Omega\mathbf{q}_{\mathrm{t}} + T_0^* + \dot{\mathbf{q}}_{\mathrm{t}}^{\mathrm{T}}\mathbf{f} + \dot{\mathbf{q}}_{\mathrm{t}}^{\mathrm{T}}\tilde{\mathbf{G}}\mathbf{q}_{\mathrm{t}} + \mathbf{f}_\Omega^{\mathrm{T}}\mathbf{q}_{\mathrm{t}}\,. \tag{4.18}$$

Now $\mathbf{q}_{\mathrm{t}}$ contains the aggregate nodal coordinates of the structure in the spinning SoR. It is possible to treat the strain energy of a beam with the same method used above. Through the use of the shape function matrix introduced with Equation 4.9, Equation (4.13) is re-expressed for the generic element e as follows:

$$U_e^* = \frac{1}{2}\mathbf{q}_e^{\mathrm{T}}(\mathbf{K}_{\mathrm{e}e} + \mathbf{K}_{\mathrm{g}e})\mathbf{q}_e\,, \tag{4.19}$$

where

$$\mathbf{K}_{\mathrm{e}e} = \begin{bmatrix} EA\mathbf{K}_a & & \\ & EI_y\mathbf{K}_b & \\ & & EI_z\mathbf{K}_c \end{bmatrix}, \quad \mathbf{K}_{\mathrm{g}e} = \begin{bmatrix} \mathbf{0} & & \\ & \mathbf{K}_{\mathrm{g}b} & \\ & & \mathbf{K}_{\mathrm{g}c} \end{bmatrix},$$

$$\mathbf{K}_a = \int_0^l \mathbf{N}_1'^{\mathrm{T}}\mathbf{N}_1'\mathrm{d}s\,, \quad \mathbf{K}_b = \int_0^l \mathbf{N}_2''^{\mathrm{T}}\mathbf{N}_2''\mathrm{d}s\,, \quad \mathbf{K}_c = \int_0^l \mathbf{N}_3''^{\mathrm{T}}\mathbf{N}_3''\mathrm{d}s\,,$$

$$\mathbf{K}_{\mathrm{g}b} = \int_0^l F(s)\mathbf{N}_2'^{\mathrm{T}}\mathbf{N}_2'\mathrm{d}s\,, \quad \mathbf{K}_{\mathrm{g}c} = \int_0^l F(s)\mathbf{N}_3'^{\mathrm{T}}\mathbf{N}_3'\mathrm{d}s\,.$$

The resulting beam element matrices are reported in Appendix F. In the above expressions the prime symbol stands for a differentiation with respect to the longitudinal coordinate of the beam s, with $s \in [0, l]$. Assembling the element matrices above yields

the overall strain energy:

$$U^* = \sum_e U_e^* = \frac{1}{2}\mathbf{q}_\mathrm{t}^\mathrm{T}(\mathbf{K}_\mathrm{e} + \mathbf{K}_\mathrm{g})\mathbf{q}_\mathrm{t}\,. \tag{4.20}$$

Note that the calculation of the steady-state tensional state of the structure, due to the presence of the distributed centrifugal force, is required for the evaluation of term $\mathbf{K}_\mathrm{g}$. How this is achieved is detailed in Appendix E. By assuming that the structure undergoes small oscillations around the steady-state configuration, we can describe the nodal coordinates of the structure with

$$\mathbf{q}_\mathrm{t} = \mathbf{q}_\mathrm{s} + \mathbf{q}\,, \tag{4.21}$$

where $\mathbf{q}_\mathrm{s}$ represents the global steady-state displacement and $\mathbf{q}$ the global displacement associated to said small vibrations. By using this convention and by posing $\mathbf{G} = 2\tilde{\mathbf{G}}$, the Lagrange Equations 4.11 yield

$$\mathbf{M}\ddot{\mathbf{q}} + \mathbf{G}\dot{\mathbf{q}} + (\mathbf{K}_\mathrm{e} + \mathbf{K}_\mathrm{g} - \mathbf{K}_\Omega)\mathbf{q} = \mathbf{0}\,, \tag{4.22}$$

which represents the law of oscillation about steady state (vibrational equations of motion) when no external forces are applied. Here one can recognise the classic structural mass and stiffness matrices $\mathbf{M}$ and $\mathbf{K}_\mathrm{e}$, which describe a non-rotating elastic structure. Three extra terms, that will be labelled "spinning effects" in the following, appear as a consequence of rotation: the Coriolis matrix $\mathbf{G}$, which is anti-symmetric and represents a conservative planar coupling effect, the symmetric spin-softening matrix $\mathbf{K}_\Omega$, and the symmetric geometric stiffness matrix $\mathbf{K}_\mathrm{g}$. In order to make the system statically determined, a set of boundary conditions must be applied. In the present case, this is implemented by clamping the node which corresponds to the rotor bearing, assuming negligible substructure deformations and a perfectly homogeneous shaft speed at the bearing point – that is, no torsional vibrations are allowed at that location. The six nodal displacements in the rotating frame are therefore identically equal to zero and may be eliminated from the system.
By explicitating the dependence of the spinning effect matrices on Ω, Equation 4.22 may be written as

$$\mathbf{M}\ddot{\mathbf{q}} + \Omega\mathbf{G}^1\dot{\mathbf{q}} + [\mathbf{K}_\mathrm{e} + \Omega^2(\mathbf{K}_\mathrm{g}^1 - \mathbf{K}_\Omega^1)]\mathbf{q} = \mathbf{0}\,, \tag{4.23}$$

where a superscript '1' denotes that the matrix is calculated per unit rotational speed. This form lends to performing parametric studies with respect to rotational speed Ω: all Ω-dependent terms are computed only once for a unit rotational speed (denoted with a superscript '1') in the FE development environment, then a range of values of Ω is

imposed parametrically in the post-treatment phase preceding the modal computation[3]. So long as the structure's interaction with the surrounding fluid is disregarded, and given that appropriate boundary conditions are imposed to make it statically determined, Equation 4.23 suffices to determine the rotor-dynamic behaviour of the structure for small vibrations. This mathematical representation of the rotor as a linear dynamic system enables to describe its motion in modal form as explained next.

4.2.1.4 Modes of a damped linear dynamic system

Equation 4.23 is a second-order differential equation which expresses the linearised EoM of the damped and unexcited dynamic system, that can be generalised as

$$\mathbf{A}\ddot{\mathbf{q}} + \mathbf{B}\dot{\mathbf{q}} + \mathbf{C}\mathbf{q} = \mathbf{0}\,, \tag{4.24}$$

In the most general case, $\mathbf{A}, \mathbf{B}, \mathbf{C} \in \mathbb{C}^{n\times n}$ and $\mathbf{q} \in \mathbb{C}^n$, with n denoting the number of degrees of freedom of the system. If it is assumed that the solution takes the form $\mathbf{q} = \hat{\mathbf{q}}\mathrm{e}^{\lambda t}$, with $\lambda \in \mathbb{C}$, Equation 4.24 can be reformulated as

$$(\lambda^2\mathbf{A} + \lambda\mathbf{B} + \mathbf{C})\hat{\mathbf{q}}\mathrm{e}^{\lambda t} = \mathbf{0}_n\,. \tag{4.25}$$

If the time-dependent term is eliminated, one is left with a quadratic eigenproblem (QEP) whose solution entirely defines the motion of the system under the above assumptions. This consists in finding the $(\lambda, \hat{\mathbf{q}})$ pairings which satisfy

$$(\lambda^2\mathbf{A} + \lambda\mathbf{B} + \mathbf{C})\hat{\mathbf{q}} = \mathbf{0}_n\,,\ \hat{\mathbf{q}} \neq \mathbf{0}_n\,. \tag{4.26}$$

The QEP can be transformed into an equivalent, linear generalised eigenproblem (GEP) of size $2n$:

$$\mathbf{E}\hat{\mathbf{r}} = \lambda\mathbf{F}\hat{\mathbf{r}}\,, \tag{4.27}$$

$$\hat{\mathbf{r}} = \begin{bmatrix} \hat{\mathbf{q}} \\ \lambda\hat{\mathbf{q}} \end{bmatrix}. \tag{4.28}$$

Matrices $\mathbf{E}$ and $\mathbf{F}$ are obtained by assembling the above defined dynamic system matrices with prescribed auxiliary matrices; a range of construction options is available. The details of the implementation of this procedure are given in Appendix G.
Denoting $\mathbf{Q} = \mathbf{F}^{-1}\mathbf{E}$, valid for $\mathbf{F}$ nonsingular, allows to reexpress the GEP in the

[3] After computation in the C++ environment, each matrix is saved to a separate file in sparse format. The Scilab script used for post-treatment loads the matrices, parametrises the problem with respect to rotational speed, assembles the system, and launches the eigen calculation detailed in 4.2.1.4.

Table 4.1: Types of retained eigensolutions and their physical meaning.

Eigenvalue properties	Mode type	Characteristic free motion
$\mathrm{Im}(\lambda) = 0$	Statically undetermined	Unrestrained
$\mathrm{Im}(\lambda) > 0$, $\mathrm{Re}(\lambda) < 0$	Positively damped	Expon. decaying harmonic (valid for $\xi < 1$)
$\mathrm{Im}(\lambda) > 0$, $\mathrm{Re}(\lambda) = 0$	Undamped	Steady harmonic
$\mathrm{Im}(\lambda) > 0$, $\mathrm{Re}(\lambda) > 0$	Negatively damped	Expon. amplifying harmonic

standard form with

$$\mathbf{Q}\hat{\mathbf{r}} = \lambda\hat{\mathbf{r}}\,, \tag{4.29}$$

whose solutions are obtained numerically[4]. These are $(\lambda, \hat{\mathbf{r}})$, the eigenvectors and corresponding eigenvalues of matrix $\mathbf{Q}$. The eigenvalues come in conjugate pairs; it is sufficient, for instance, to discard the eigensolutions with $\mathrm{Im}(\lambda) < 0$ to isolate the desired range of physically meaningful solutions. One can classify system modes as in Table 4.1.

The following quantities can be derived from the eigenvalues for each mode:

1. Damped natural frequency $\omega = \mathrm{Im}(\lambda)$.
2. Undamped natural frequency $\omega^* = \sqrt{\mathrm{Re}(\lambda)^2 + \mathrm{Im}(\lambda)^2}$.
3. Damping ratio $\xi = -\mathrm{Re}(\lambda)/\omega^*$.

These are the ultimate outputs of the modal analysis, along with the modal shapes contained in the eigenvectors $\hat{\mathbf{r}}$. The sign of the damping ratio in particular (see Table 4.1) is the key indicator of a system's dynamic stability. Finally it must be reminded that in the present application the eigenanalysis is set up in the rotating frame; the resulting eigenfrequencies, called relative natural frequencies, differ from those calculated in the inertial SoR, and are traditionally conveyed by a parametric plot with rotor speed in abscissa: the Campbell diagram.

4.2.2 Model verification

Equation 4.23 describes an unexcited rotor-dynamic system. Since all the included force terms are conservative (remember that $\mathbf{G}$ is anti-symmetric), the vibrational modes of the system found by resolving Equation 4.26 are characterised by a nil damping ratio i.e. $\xi \equiv 0$. Parametrising the modal calculation with respect to Ω allows to obtain the rotor's Campbell diagram, which displays the evolution of the rotor's relative natural frequencies (i. e. the natural frequencies ω_i of the system in the spinning SoR) for varying rotational speeds. Two benchmark studies are illustrated

[4]The model exploits the ARPACK (ARnoldi PACKage) library [228], accessible from the Scilab 5.5.0 environment [229]. This library is designed for resolving the eigenproblems of large sparse matrices. Each modal computation is independent, enabling the use of multi-threading.

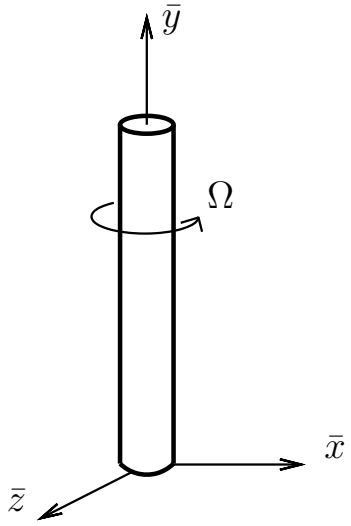

Figure 4.6: Axial beam geometry.

next, where the Campbell diagram of a steadily rotating assembly of beams of circular section is calculated and compared with exact and published results. Both of these structures are treated under the assumption that material and sectional characteristics do not vary over their extension. The cantilever boundary condition is always applied on the node located in O, using the row and column elimination technique. Finally, it should be reported that a broader range of cases featuring the same beams with different orientations in space have been run for the sake of validation, which as expected produced the same outputs as those reported next.

4.2.2.1 Campbell diagram of an axial beam

Figure 4.6 shows a straight, homogeneous beam that spins around its longitudinal axis, which coincides with axis $\bar{y}$. The structure is represented by four equal Euler-Bernoulli beams, whose parameters are given in Table 4.2. The fundamental bending natural frequencies ω^0 of a cylindrical cantilever depend on its geometric and material characteristics: beam length l_b, second order sectional moment with respect to bending

Table 4.2: Axial beam parameters.

Number of elements	4
Overall length l_b [m]	10
Sectional area A [m^2]	$6.252{\cdot}10^{-2}$
Bending inertia $I_y = I_z = I$ [m^4]	$3.095{\cdot}10^{-2}$
Young's modulus E [GPa]	210
Shear modulus G [GPa]	80.8
Material density ρ_m [kg/m^3]	7860

axis $I_y = I_z = I$, Young's modulus E and mass per unit length μ. When the first two bending modes are concerned, beam vibration theory gives:

$$\omega_1^0 \approx \frac{3.5156}{l_\mathrm{b}^2}\sqrt{\frac{EI}{\mu}}\,, \tag{4.30}$$

$$\omega_2^0 \approx \frac{22.036}{l_\mathrm{b}^2}\sqrt{\frac{EI}{\mu}}\,. \tag{4.31}$$

The evolution of the i^{th} natural bending frequency in function of the angular speed Ω follows in this case the linear relationship

$$\begin{aligned} \omega_{i\mathrm{a}}(\Omega) &= \omega_i^0 - \Omega\,, \\ \omega_{i\mathrm{b}}(\Omega) &= \omega_i^0 + \Omega\,. \end{aligned} \tag{4.32}$$

The bending modes of the beam with respect to $\bar{x}$ and $\bar{z}$ coincide when the rotational speed is nil. As soon as $\Omega \neq 0$, two branches appear for each bending mode i, whose frequencies are $\omega_{i\mathrm{a}}(\Omega)$ and $\omega_{i\mathrm{b}}(\Omega)$. These respectively represent the backward and forward whirling modes of a spinning structure, which are well studied in rotordynamics[5]. The resulting Campbell diagram is shown in Figure 4.7, where the whirling frequencies corresponding to the first and second bending modes are obtained using both the analytic solution above and the presented numerical implementation.

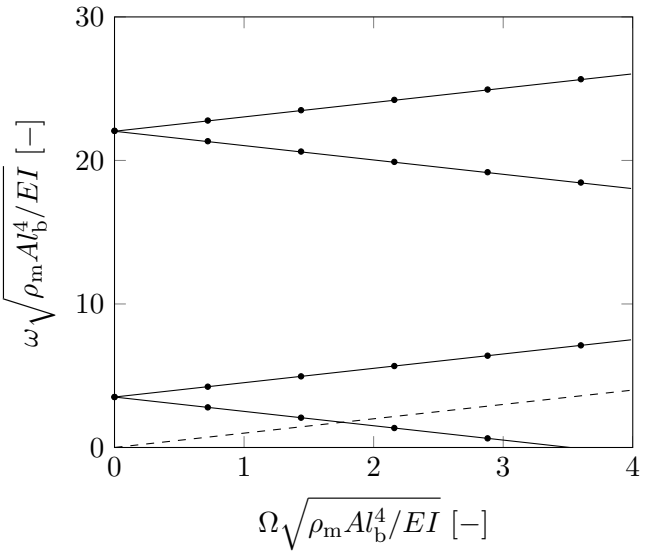

Figure 4.7: Verification of axial beam Campbell diagram. Solid curves represent the analytic solution and dots the results of the presented model. The dotted line represents the synchronous excitation frequency.

[5] A visual example of rotor whirling is available in a video published by NASA [230].

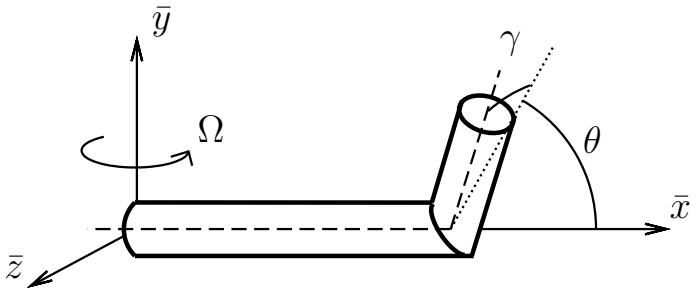

Figure 4.8: Articulated beam geometry. The quoted angles are fixed as $\theta = 30\,^\circ$ and $\gamma = 45\,^\circ$.

An element of interest, aside the agreement of the analytical and numerical solutions in the Figure, is the identification of a critical speed: this is defined as a rotational speed for which excitation (dashed line) meets a whirling mode, and vibration becomes dramatically amplified by resonance if undamped. This criterion is used to study the reliability of rotating structures in their operating range. For a three-bladed wind turbine, for example, synchronous excitation and 3P (blade passage) excitation are of main interest. Continuous operation around any critical speed associated to these sources of forcing is hence avoided, typically using a combination of structural and controller design (see for instance a guideline by Germanischer Lloyd [231]).

4.2.2.2 Campbell diagram of an articulated beam

A cantilevered beam with a broken line shape (Figure 4.8) is studied assuming that it is revolving at constant speed around the $\bar{y}$ axis. The structure is modelled with three equal and homogeneous Euler-Bernoulli beam elements, two of which constitute the straight segment departing from the origin. The parameters defining the system are available in Table 4.3. The beam's Campbell diagram obtained numerically is shown in Figure 4.9 along with a published solution. The plot displays the first three vibrational modes of the spinning structure along with the synchronous excitation line. It is possible

Table 4.3: Articulated beam parameters.

Number of elements	3
Length of segment 1 [m]	1.0
Length of segment 2 [m]	0.5
Overall length l_b [m]	1.5
Sectional area A [m^2]	$4.909{\cdot}10^{-4}$
Bending inertia $I_y = I_z = I$ [m^4]	$1.917{\cdot}10^{-8}$
Young's modulus E [GPa]	200
Shear modulus G [GPa]	80
Material density ρ_m [kg/m^3]	78500

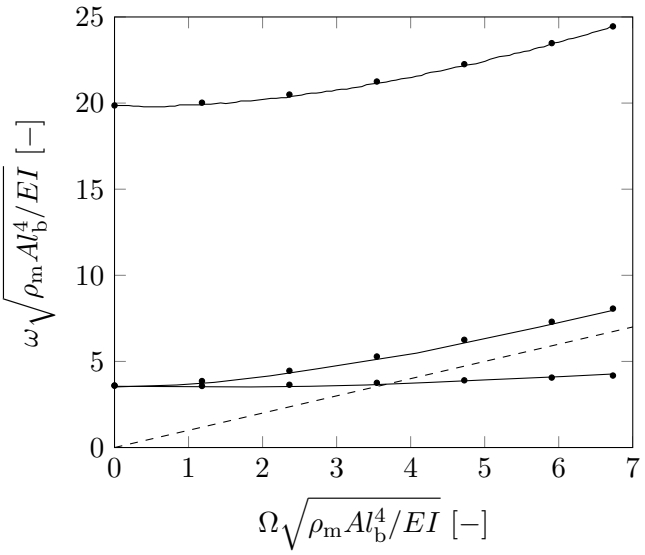

Figure 4.9: Verification of the Campbell diagram of an articulated beam. Solid curves represent the reference solution, which is digitised from Leung and Fung [226], and dots the results of the presented model. The dotted line represents the synchronous excitation frequency.

to observe how natural frequencies shift as a consequence of rotation – in this case upwards because of dominating geometric stiffening – and that the first bending mode evolves once again into forward and backward whirling when the beam spins.

4.2.3 Applications and discussion

A modal rotordynamic analysis of two full-scale Vertiwind-class rotors is organised next based on the representation of Equation 4.23. They are both three-bladed, helical variants of the classic H-type VAWT rotor (Figure 4.10) and feature a diameter of about 50 m. Most notably, the two machines differ in overall height and power output. A 30 m tall configuration, rated at around 600 kW (electrical), is denoted 1H; an onshore prototype with these characteristics has been built and tested in Fos-sur-mer (France) in 2014. The larger configuration, denoted 4H and designed to produce about 2 MW at rated conditions, is about three times taller and represents the baseline design for use on the floating offshore prototype. The geometrical and structural parameters defining these two rotors as assemblies of homogeneous beams are given by the designer in [232] and [233] respectively[6]. The nomenclature adopted in this study to refer to the different rotor components is provided in Figure 4.10.

[6]Confidential documents.

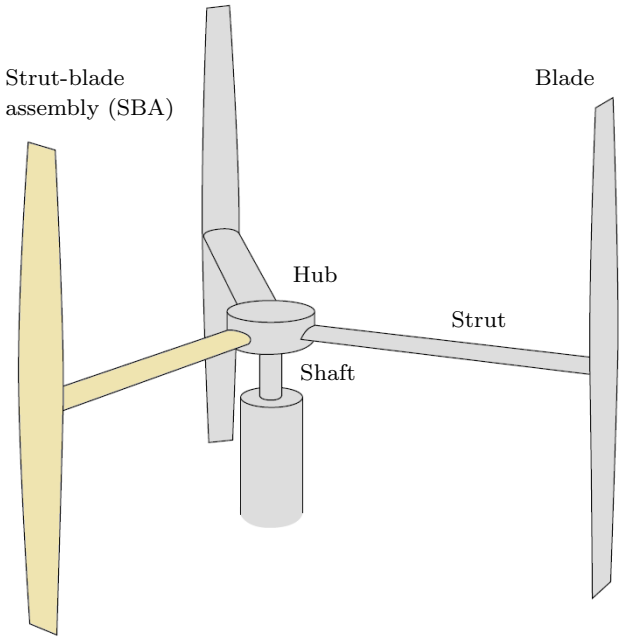

Figure 4.10: Nomenclature of H-type rotor components. Adapted from Ottermo and Bernhoff [234].

4.2.3.1 Analysis of 1H rotor

Figure 4.11 shows a picture of the onshore prototype mounting the 1H rotor which is presently analysed. The rotor architecture is relatively simple as it is formed by three blades supported by one strut each. Since the rotor is of fixed-pitch type, all joints are cantilevered. The forces exerted on the rotor are transferred to the bearing/generator assembly (stator) located at the top of the supporting tower, and then discharged into the foundations with the help of three oblique beams. This arrangement provides a rigid stator-ground coupling. The minimal shaft length used in this configuration also makes the rotor considerably rigid up to the hub, where the struts are attached: the consequence is an effective decoupling of the vibrations of the three strut-blade assemblies (SBAs) in the low-frequency part of the spectrum, which is the most important band from the point of view of rotor structural design. The outputs of the modal analysis directly reflect the above decoupling: rotor modes are grouped in a three-by-three fashion, whilst in each group the eigenvalues are coincident and the eigenvectors are symmetric with respect to the rotational axis.

As it is customary, structural modes are here numbered from the lowest frequency up. The first eight SBA modal shape groups found at zero rotational speed are provided in Figures 4.12 and 4.13. Structural deformations are exaggerated for clear visualisation. As anticipated, the short and rigid shaft is practically unaffected by the low-frequency

Figure 4.11: Full-scale prototype with 1H rotor, Fos-Sur-Mer, France, 2014. After Dodd [235].

modal vibrations. The visualised modes involve simultaneous strut and blade displacements dominated by bending, which is expected for an assembly of slender structures. When a nonzero rotational speed is applied, the apparent force terms in the EoM begin to alter the modal behaviour of the structure. Given an operating envelope (including an overspeed margin) between 0 and 20 rev/min, the normalised Campbell diagram of the 1H rotor is provided in Figure 4.14, where the nondimensional frequency f^* corresponds to the ratio between any dimensional modal frequency and the frequency of the rotor's first mode. The standstill frequencies found are in good agreement with those measured experimentally on the full-scale prototype at least up to the 30^{th} mode (as documented in [204]). As seen in the Figure, only modes 1 to 6 and 40 to 45 exhibit significant dependence from the rotor speed, with a clear bifurcation into a forward and a backward whirl branch. Not reproduced in the Campbell diagram are the synchronous excitation line and its multiples, whose intersections with the modal curves identify the critical rotor speeds.A later time-domain modelling campaign carried out at EDF, where the model was upgraded to include of the incident wind speed and the subsequent unsteady aerodynamic forces, suggests that most vibrational content during operation is associated to modes 1 to 15 [204].

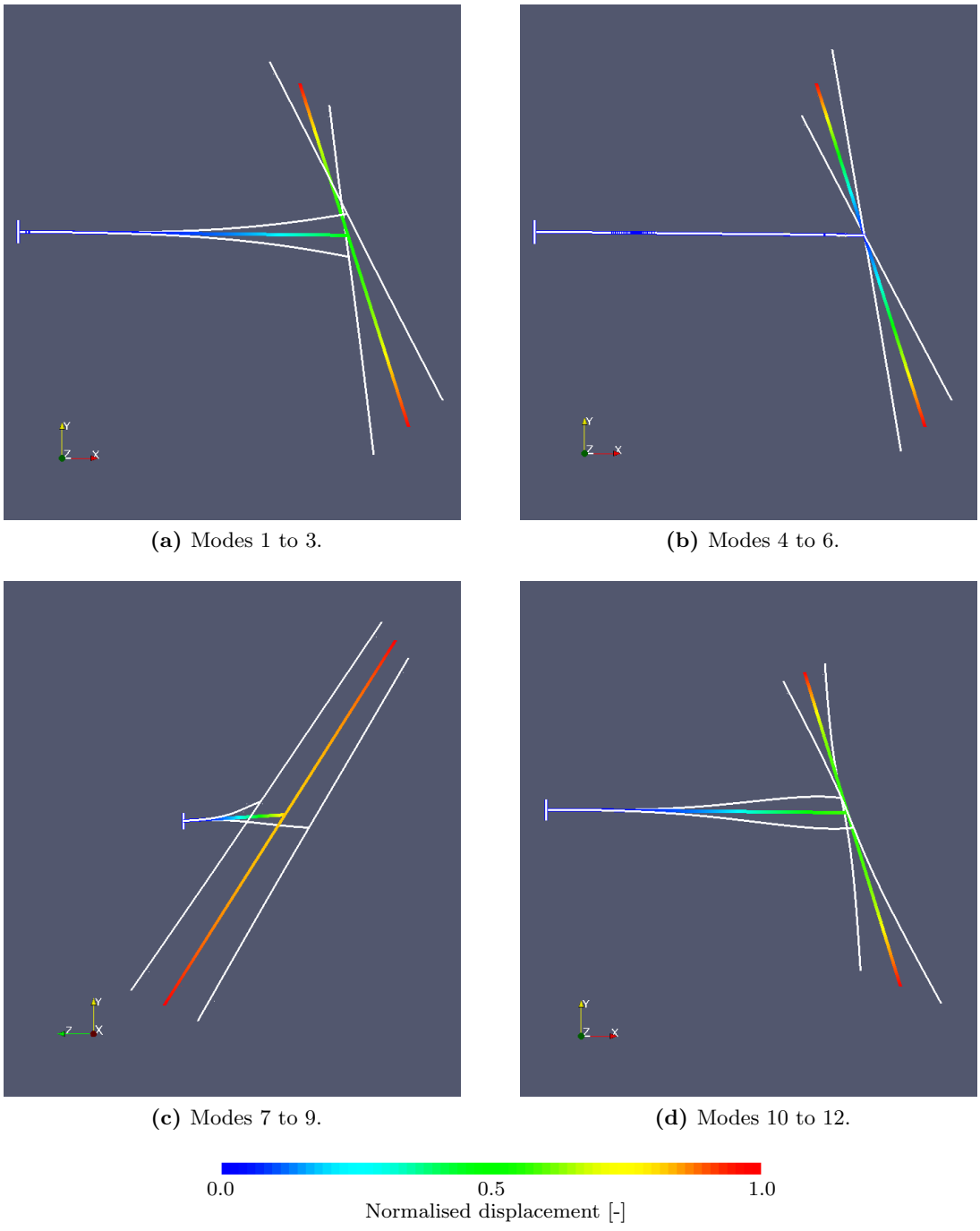

(a) Modes 1 to 3.

(b) Modes 4 to 6.

(c) Modes 7 to 9.

(d) Modes 10 to 12.

Figure 4.12: First 12 modal shapes of 1H rotor at standstill. A single strut-blade assembly is shown.

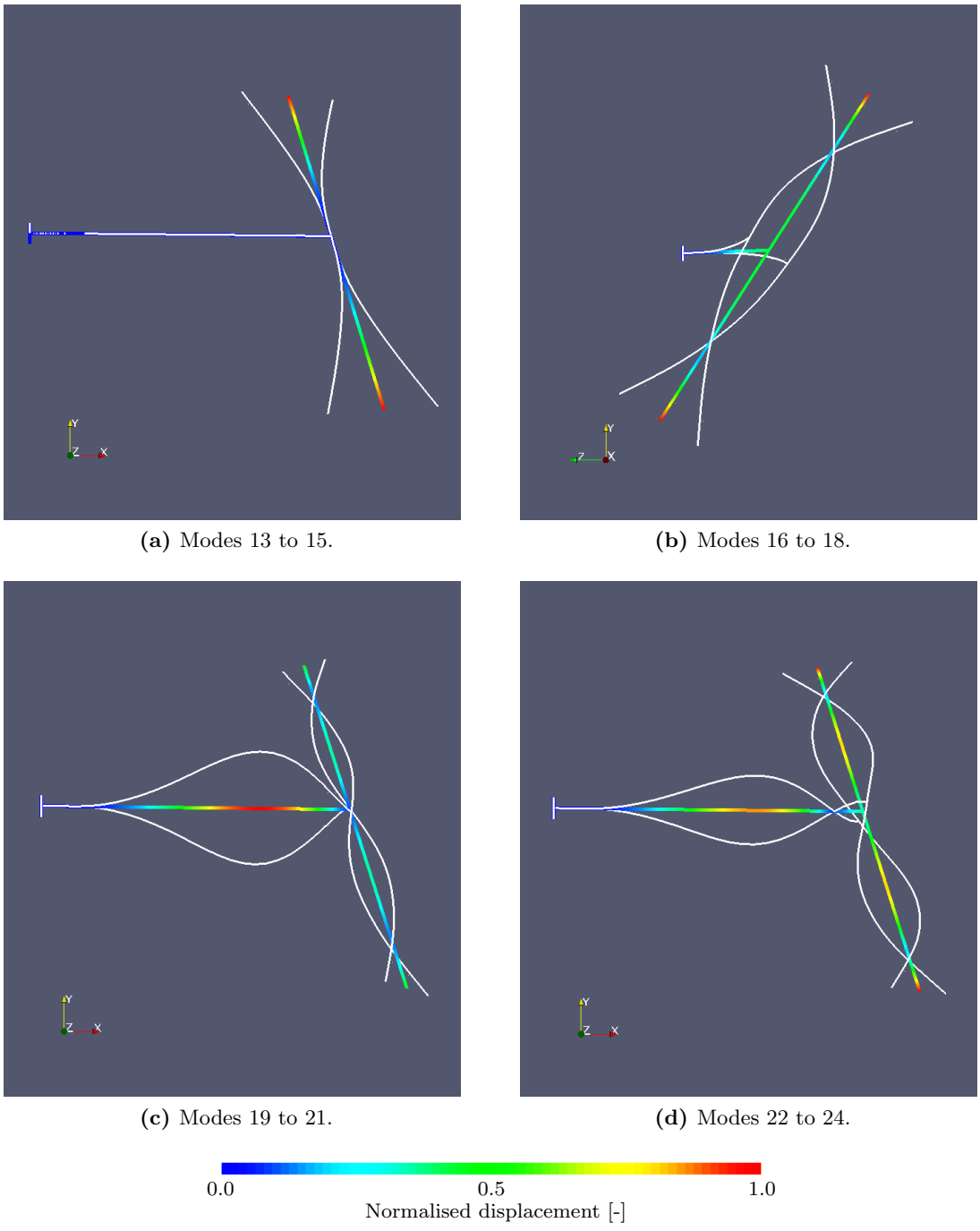

(a) Modes 13 to 15.

(b) Modes 16 to 18.

(c) Modes 19 to 21.

(d) Modes 22 to 24.

Figure 4.13: Second 12 modal shapes of 1H rotor at standstill. A single strut-blade assembly is shown.

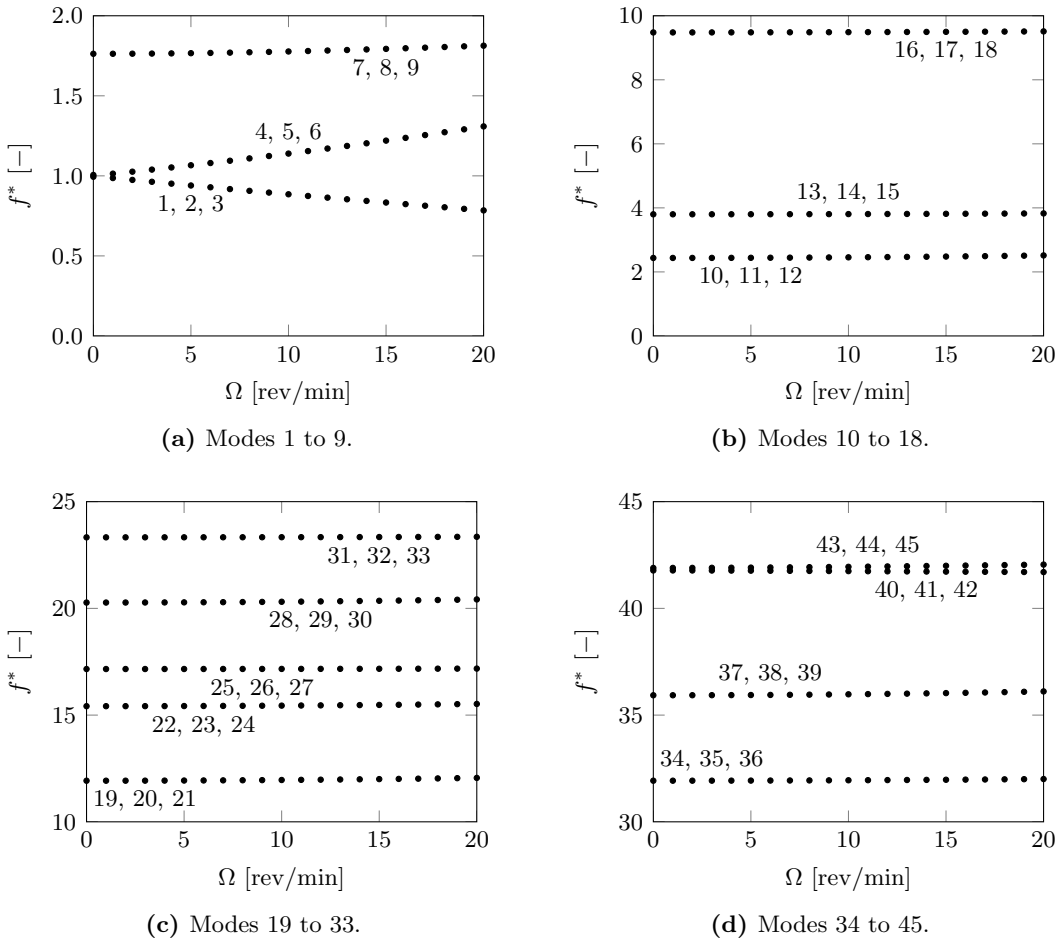

(a) Modes 1 to 9.

(b) Modes 10 to 18.

(c) Modes 19 to 33.

(d) Modes 34 to 45.

Figure 4.14: Campbell diagram of the 1H rotor.

4.2.3.2 Analysis of 4H rotor

The second rotor analysed is one of the basic designs considered in the past. Conceived in 2013, the 2 MW 4H rotor concept has since remained "frozen" to provide a reference configuration for numerical model benchmarking. As the name suggests, its architecture relies on four orders of struts to support the three fixed-pitch helical blades, totalling about 100 m in height. A rendering of the 4H rotor is provided in Figure 4.15.

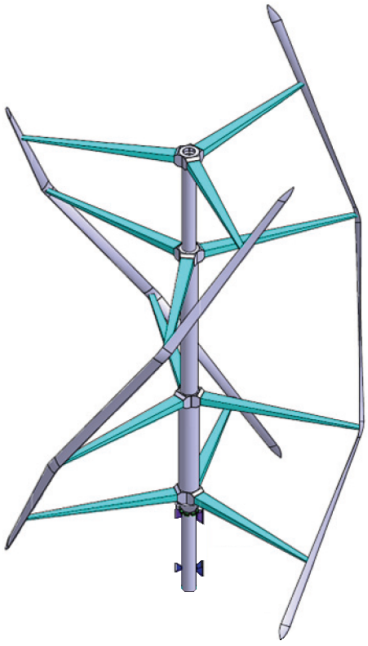

Figure 4.15: Sketch of the 4H rotor, adapted from Cahay et al. [43]. Note that the strut sections are in reality profiled.

Although in the present model the structure is rigidly clamped at the bearing point at the root of the shaft, which is the same boundary condition applied above to the 1H rotor, the shaft itself is long and flexible enough to enable the existence of global low-frequency modes which couple the vibrations of the three SBAs. The rotor's first eight (exaggerated) modal shapes are shown in Figures 4.16 and 4.17. Modes 1 and 2 represent global bending vibrations, for which the upper portion of the shaft undergoes large displacements. Higher-frequency modes, however, describe vibrations which mostly affect the rotor SBAs, with little participation of the shaft.
The evolution of the nondimensional modal frequencies with respect to rotor speed is provided in the Campbell diagram of Figure 4.18. The analysis is once more restricted to an operating envelope of 0 rev/min to 20 rev/min. The 4H rotor exhibits numerous bending modes which evolve into forward and backward whirl branches at relatively low frequencies. The standstill modes and the Campbell diagram found by EDF's industrial partners involved in the rotor dynamics benchmarking programme coincide with the presented results.

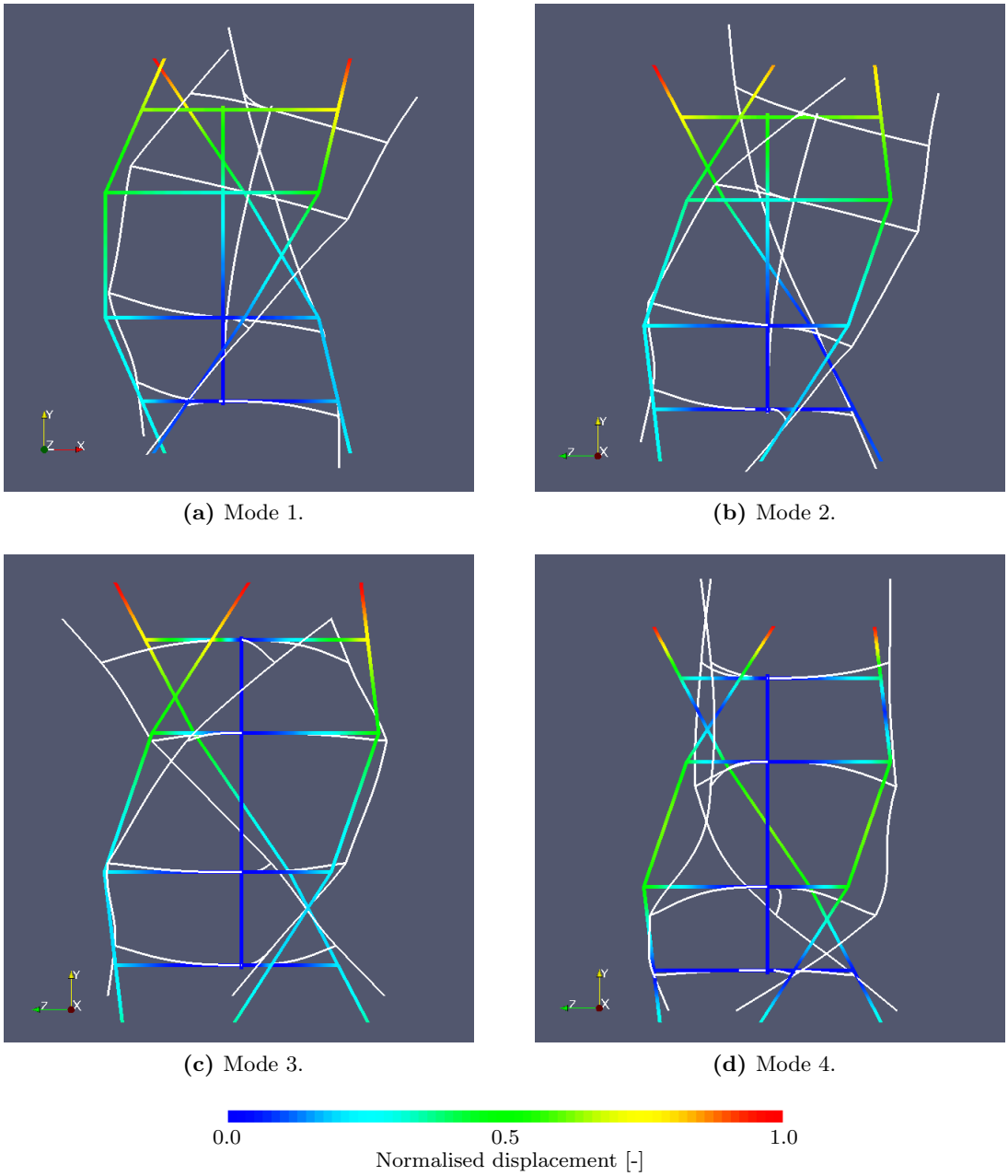

(a) Mode 1.

(b) Mode 2.

(c) Mode 3.

(d) Mode 4.

Figure 4.16: First 4 modal shapes of 4H rotor at standstill.

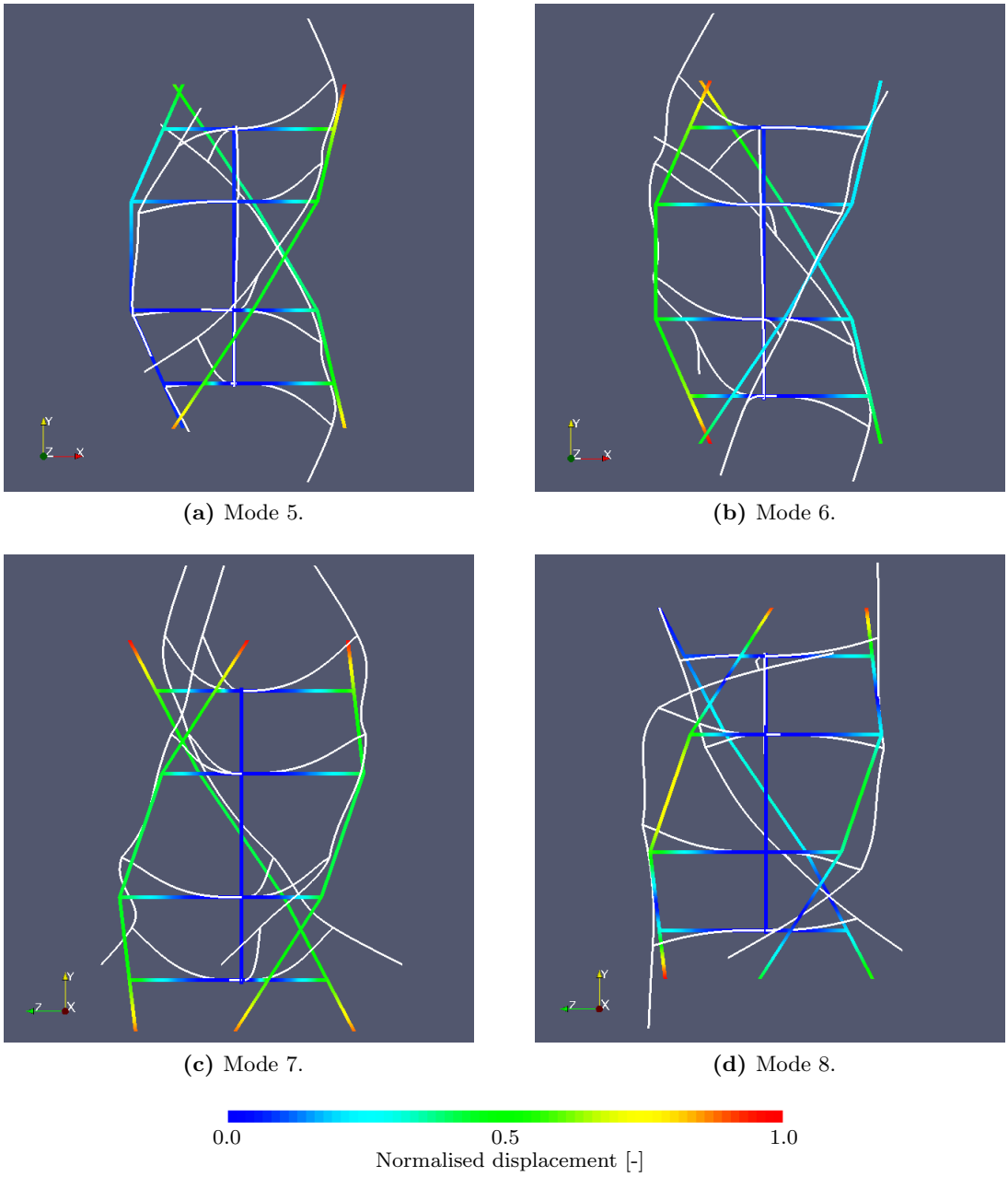

(a) Mode 5.

(b) Mode 6.

(c) Mode 7.

(d) Mode 8.

Figure 4.17: Second 4 modal shapes of 4H rotor at standstill.

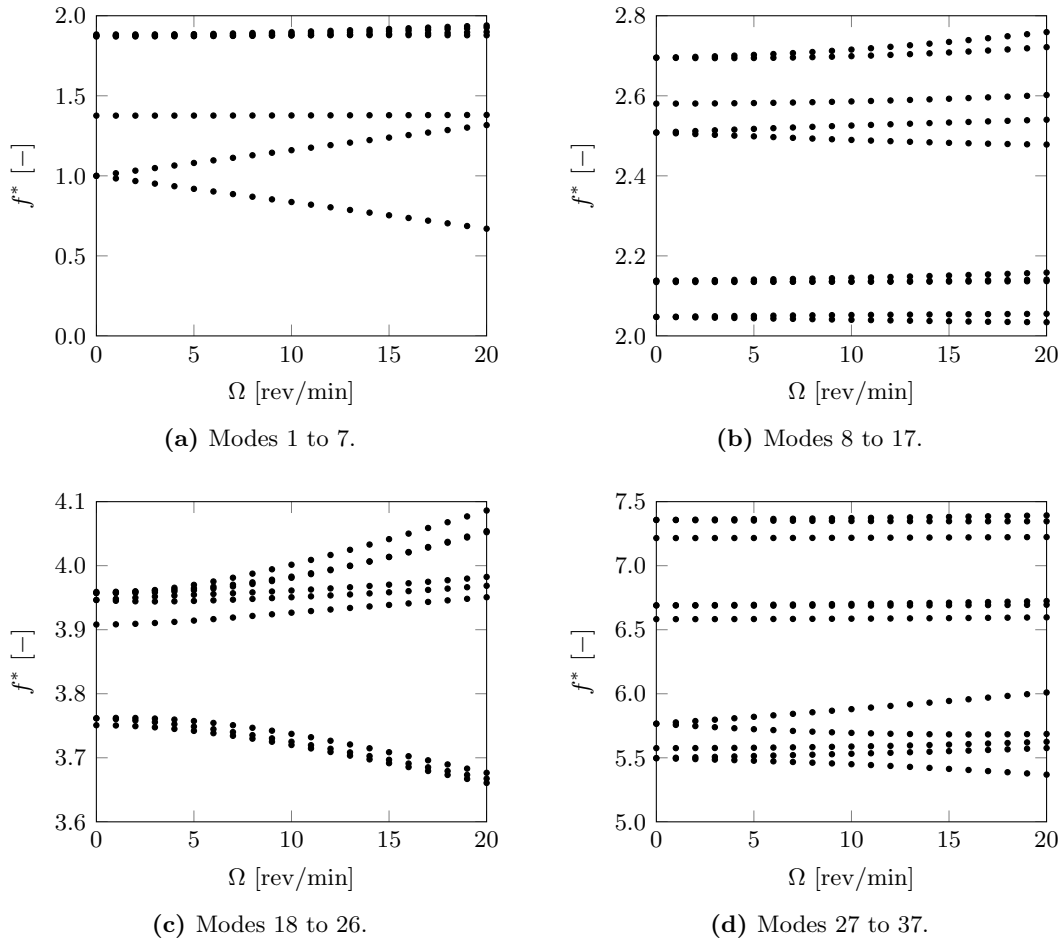

(a) Modes 1 to 7.

(b) Modes 8 to 17.

(c) Modes 18 to 26.

(d) Modes 27 to 37.

Figure 4.18: Campbell diagram of the 4H rotor.

4.3 Aeroelastic analysis of vertical-axis rotors

The goal of the aeroelastic model presented next is to determine the role of aerodynamic interactions in the vibrational behaviour of the rotor. This is realised by augmenting the structural model presented in Section 4.2 with a linearised representation of the aerodynamic forces which interact with the structural vibrations. The fundamental output of interest is the aerodynamic damping affecting the rotor modes: if positive, this phenomenon may significantly reduce the amplitude of resonant motion; if negative, a form of aeroelastic instability may be triggered.
This section presents the methodology used to represent the airflow-structure interaction (4.3.1), a verification of the coupled aeroelastic behaviour of the numerical solver developed (4.3.2), and the results of the full aeroelastic analysis of the two Vertiwind-type rotors introduced in the previous Section (4.3.3).

4.3.1 Methodology

The VAWT rotors object of this analysis operate at speeds between 5 rev/min and about 15 rev/min in normal conditions. By extending the operational envelope to include a 33% overspeed contingency, an upper speed boundary to the rotor-dynamic investigation may be set as 20 rev/min, as done in Section 4.2. Both the considered rotors are characterised by a blade radius r of about 25 m (with a small vertical variability due to the helical construction), and a chord length of $c = 2.5$ m. Disregarding the incident wind speed allows to calculate the Mach and Reynolds numbers for the entirety of the blades with

$$\mathrm{M} = \frac{\Omega r}{\tilde{V}} \quad \text{and} \quad \mathrm{Re} = \frac{\Omega r c}{\nu}\,, \tag{4.33}$$

where the parameters used to define the fluid are specified in Table 4.4 and Ω, the rotor speed, is given in rad/s. The values of Re and M obtained for varying rotational speed are plotted in Figure 4.19. As visible from the Figure, the aerodynamic regimes of the blades are characterised by Reynolds numbers between 10^6 and 10^7 and Mach numbers no larger than 0.15 in all operating conditions. This, combined with the attached flow hypothesis (which is in general valid for streamlined profiles and for small angles of attack) allows to use incompressible, inviscid aerodynamic theory to solve the fluid-structure interaction problem.
Focussing on lift-induced instability due to the interaction of blade vibrations with their

Table 4.4: Air properties at standard sea level, for a temperature of 15 °C.

Density ρ [kg/m^3]	1.229
Kinematic viscosity ν [m^2/s]	$1.408{\cdot}10^{-5}$
Speed of sound $\tilde{V}$ [m/s]	340.3

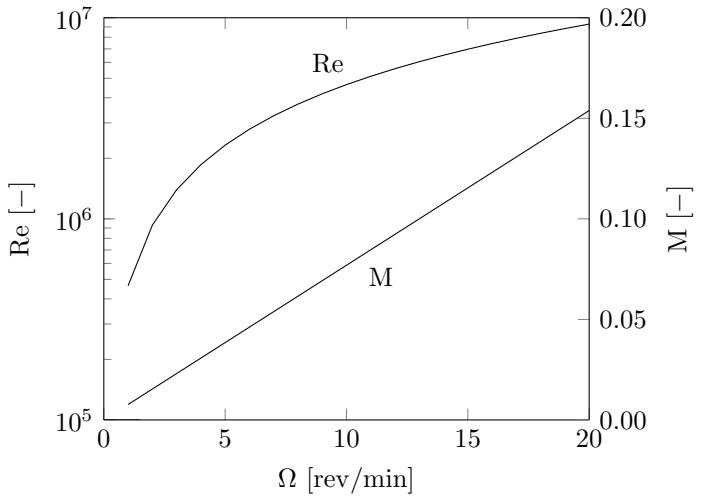

Figure 4.19: Aerodynamic regimes of the Vertiwind turbine blades.

near wake permits – in the current simplified approach – to disregard the wind inflow (see e.g. Lobitz [218]), which in physical terms corresponds to studying a rotor operating in still air. When put in this terms, VAWT blade aerodynamics can be assimilated to those of a wing subjected to a free stream airflow corresponding to the local tangential speed. This assumes that the blade (or profiled strut) encounters calm air throughout the full revolution, and that its airflow is unperturbed by the passage of the preceding blade. Although limiting, these assumptions have proven acceptable in the past when the aeroelastic behaviour of experimental VAWT rotors was successfully predicted by this type of model [206, 222].

The portions of the rotor which provide most aerodynamic loading, namely the blades and the outer parts of the struts, feature airfoil sections of relatively small thickness, which are constant or only slowly varying over the span of the rotor components. These considerations support the adoption of a range of methods founded on thin airfoil theory: for a review of the basics the reader can refer for example to Abbott and Doenhoff [236] or Dimitriadis [237]. The aeroelastic application of this theory, founded on the work of Theodorsen [238], regards the representation of the reactive aerodynamic forces arising when the airfoil oscillates and is typically detailed in aeroelasticity textbooks and training materials [208, 239]. Its most valuable output, namely the aerodynamic operator enabling the representation of aeroelastic coupling for a planar airfoil, are presented in 4.3.1.2 in quasi-steady form and in 4.3.1.3 in their unsteady, harmonic representation. These formulations serve as the building block of the aerodynamic interaction model used in this study. Before presenting their complete formulation, a canonical example of oscillating airfoil is used in 4.3.1.1 to show the fundamental characteristics of an aeroelastic system.

The 3D extension of the 2D airfoil model is detailed in 4.3.1.4, where the final coupled structural-aerodynamic assembly is presented. The fully linear characteristics of the resulting dynamic system and the internalisation of the external aerodynamic forces enables to resolve the vibrational motion of the rotor as a free vibration through the same modal approach used in Section 4.2.

4.3.1.1 The pitch-plunge airfoil

The so-called pitch-plunge airfoil, displayed in Figure 4.20 incorporates all the fundamental components of an aeroelastic system: it couples a compliant structure with an aerodynamic excitation system. Its simplicity and the comprehensive documentation available (for instance it is thoroughly treated by Clark et al. [208] and Stainier [239]) makes it most suitable for demonstrating the principles of aeroelasticity. The in-plane

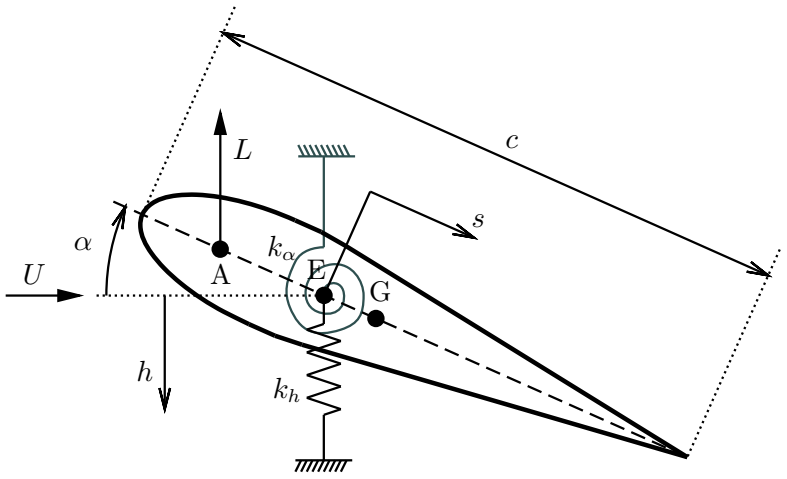

Figure 4.20: Outline of the pitch-plunge airfoil, inspired by Stainier [239].

position of the (symmetric) airfoil is described by two coupled DoF, namely the pitch angle α and the plunge displacement h. In 2D aeroelastic terms plunge refers to the motion of a section in the direction orthogonal to its undisturbed chord, whilst pitch denotes the planar rotation around its elastic centre E. This should not be confused with the notion of global pitch DoF widely used in Parts 2 and 3. The free stream airspeed U is directed along the chord of the airfoil (in equilibrium position), hence inducing an orthogonal lift force L at the centre of lift A when $\alpha \neq 0$.
Assuming a thickness to chord ratio $t_a/c \ll 1$ and treating the material density of the airfoil as a chord-wise varying function $\rho_s(s)$ enables to write (per unit span)

$$m = \int_c \rho_s ds \,, \tag{4.34}$$

$$I = \int_c \rho_s s^2 ds = m r_{\mathrm{g}}^2 \,, \tag{4.35}$$

$$S = \int_c \rho_s s ds \,, \tag{4.36}$$

which represent in turn the mass of the body and its first and second moments of inertia with respect to rotation around the elastic centre. For small values of α, the vertical displacement of a point located on the chord is given by $w = -h - \alpha s$. The kinetic and potential energy T^* and U^* may then be written as

$$T^* = \frac{1}{2} = \int_c \rho_s \dot{w}^2 ds = \frac{1}{2} m \dot{h}^2 + \frac{1}{2} I \dot{\alpha}^2 + S \dot{h} \dot{\alpha} \,, \tag{4.37}$$

$$U^* = \frac{1}{2} k_\alpha \alpha^2 + \frac{1}{2} k_h h^2 \,. \tag{4.38}$$

The use of these two expressions within the Lagrange equation (Equation 4.11) enables once again to write the equations of motion of the pitch-plunge airfoil:

$$\begin{cases} m\ddot{h} + k_h h + S\ddot{\alpha} = -L \\ S\ddot{h} + I\ddot{\alpha} + k_\alpha \alpha = M \end{cases} \,, \tag{4.39}$$

where L denotes the external lift force (note the direction convention) and M the moment of this force along the pitch DoF.

In presence of a constant free stream airspeed U, the angle of attack of the relative airflow on the airfoil is given by

$$\alpha_{\mathrm{r}} \approx \alpha + \frac{\dot{h}}{U} \,, \tag{4.40}$$

which is valid for low-amplitude motion. The effect of the presence of a nonzero speed in the plunge DoF (downwash) is then an alteration of the instantaneous lift force exerted on the airfoil. Using a quasi-steady, linearised formulation of the lift force allows to write (per unit airfoil span)

$$L = qcC_{L\alpha} \left(\alpha + \frac{\dot{h}}{U} \right) = \rho b U^2 C_{L\alpha} \left(\alpha + \frac{\dot{h}}{U} \right) . \tag{4.41}$$

In this expression q represents the stagnation point pressure and equates $0.5\rho U^2$, where ρ is the air density, and $C_{L\alpha} = dC_L/d\alpha$ the slope of the lift coefficient characteristic of the airfoil for $\alpha = 0$. The external pitch moment due to lift may be written as

$$M = ecL = 2ebL \,, \tag{4.42}$$

with $e = -s_{\mathrm{A}}/c$ representing the normalised eccentricity of the centre of lift of the airfoil. The above manipulations enable the internalisation of the external aerodynamic

forces into the dynamic system, that is the expression of the two right-hand side terms of Equation 4.39 in reactive form:

$$\begin{cases} m\ddot{h} + S\ddot{\alpha} + \frac{qcC_{L\alpha}}{U}\dot{h} + k_h h + qcC_{L\alpha}\alpha = 0 \\ S\ddot{h} + I\ddot{\alpha} - \frac{qec^2C_{L\alpha}}{U}\dot{h} + (k_\alpha - qec^2C_{L\alpha})\alpha = 0 \end{cases} . \tag{4.43}$$

The above system of equations can be conveniently vectorised as

$$\underline{\mathbf{M}}\ddot{\mathbf{a}} + \underline{\mathbf{K}}\mathbf{a} + \underline{\mathbf{\Lambda}}(\mathbf{a}) = 0\,, \tag{4.44}$$

where an underline represents in-plane (per unit span) quantities and $\mathbf{a}$ is the pitch and plunge displacement vector, with $a_1 = h$ and $a_2 = \alpha$. The system's mass and stiffness matrices and the aerodynamic operator are defined by

$$\underline{\mathbf{M}} = \begin{bmatrix} m & S \\ S & I \end{bmatrix}, \tag{4.45}$$

$$\underline{\mathbf{K}} = \begin{bmatrix} k_h & 0 \\ 0 & k_\alpha \end{bmatrix}, \tag{4.46}$$

$$\underline{\mathbf{\Lambda}} = qc \begin{bmatrix} \frac{C_{L\alpha}}{U}\frac{d}{dt} & C_{L\alpha} \\ -\frac{ecC_{L\alpha}}{U}\frac{d}{dt} & -ecC_{L\alpha} \end{bmatrix}. \tag{4.47}$$

It is important to notice that pitch and plunge are mechanically coupled via the mass matrix and aerodynamically coupled due to the full structure of $\underline{\mathbf{\Lambda}}$. If the displacement-dependent terms are separated from the velocity-dependent terms, the aerodynamic operator can also be written as

$$\underline{\mathbf{\Lambda}}(\mathbf{a}) = \begin{bmatrix} qc\frac{C_{L\alpha}}{U} & 0 \\ -q\frac{ec^2C_{L\alpha}}{U} & 0 \end{bmatrix}\dot{\mathbf{a}} + \begin{bmatrix} 0 & qcC_{L\alpha} \\ 0 & -qec^2C_{L\alpha} \end{bmatrix}\mathbf{a} = \underline{\mathbf{D}}_{\mathrm{a}}\dot{\mathbf{a}} + \underline{\mathbf{K}}_{\mathrm{a}}\mathbf{a}\,. \tag{4.48}$$

The presence of an airspeed-dependent negative stiffness coefficient in $\underline{\mathbf{K}}_{\mathrm{a}}$ is revealing: one can intuitively understand that as soon as this term reaches the order of magnitude of the corresponding structural stiffness term, the overall restoring capacity of the structure is compromised. For an aeroelastic system this corresponds to a type of static instability called divergence, which will be shown to affect the pitch-plunge airfoil at high airspeeds in 4.3.2. Likewise, the simultaneous presence of positive and negative aerodynamic damping terms within $\underline{\mathbf{D}}_{\mathrm{a}}$ tells a similar story; in case the negative term becomes dominant the onset instability is of dynamic type and is called flutter.
Injecting Equation 4.48 into Equation 4.44 and expliciting U and U^2 in the aerodynamic

operator damping and stiffness matrices finally yields:

$$\underline{\mathbf{M}}\ddot{\mathbf{a}} + U\underline{\mathbf{D}}_{\mathrm{a}}^{1}\dot{\mathbf{a}} + (\underline{\mathbf{K}} + U^2\underline{\mathbf{K}}_{\mathrm{a}}^{1})\mathbf{a} = \mathbf{0}\,, \tag{4.49}$$

where the superscript '1' denotes the matrices calculated per unit airspeed. This is the equation used in 4.3.2 to characterise the stability of a special pitch-plunge airfoil.

4.3.1.2 Full quasi-steady aerodynamics

The aerodynamic system representation used above for the pitch-plunge airfoil is already explicative but does not exhaust the aerodynamic interaction of a 2D foil undergoing small oscillations in pitch and plunge. If the quasi-steady aerodynamic representation is adopted, and hence the memory effect of the wake is ignored, the thin airfoil theory yields, for an incompressible flow, the following lift force components [240]:

1. Added mass type lift force associated to a translational acceleration,

$$L_1 = \rho\pi b^2\ddot{h}\,.$$

2. Added mass type lift force due to a rotational acceleration,

$$L_2 = \rho\pi b^2(b - \tilde{x}_{\mathrm{E}})\ddot{\alpha}\,.$$

3. Convective type lift force associated to rotational speed,

$$L_3 = \rho\pi b^2 U\dot{\alpha}\,.$$

4. Circulatory lift related to pitch,

$$L_4 = \rho b U^2 C_{L\alpha}\alpha\,.$$

5. Downwash circulatory lift,

$$L_5 = \rho b U^2 C_{L\alpha}\frac{\dot{h}}{U}\,.$$

6. Circulatory lift due to virtual camber effect,

$$L_6 = \rho b U^2 C_{L\alpha}\left(\frac{3}{2}b - \tilde{x}_{\mathrm{E}}\right)\frac{\dot{\alpha}}{U}\,.$$

In the above expressions $\tilde{x}$ represents the chord-wise distance from the leading edge such that $s = \tilde{x} - \tilde{x}_{\mathrm{E}}$, where E is the sectional elastic centre. Thin airfoil theory gives $C_{L\alpha} = 2\pi$ and $\tilde{x}_{\mathrm{A}} = c/4$ for the circulatory lift component. Note that when thin airfoil theory is fully reproduced, lift must be interpreted in its broader sense, that is the aerodynamic force directed perpendicularly to the incident airflow (see Figure 4.20 for

its orientation). Lift is here formed by both circulatory and non-circulatory components: the former derive from the pressure differential due to circulation, while the latter represent a reaction to the acceleration impelled on the fluid, which can be direct or convective.
Similarly, the aerodynamic moment exerted on the airfoil with respect to its elastic centre E results from a combination of multiple components:

1. Added mass type moment associated to translational acceleration,

$$M_1 = \rho\pi b^2(\tilde{x}_\mathrm{E} - b)\ddot{h}\,.$$

2. Added mass type moment associated to rotational acceleration,

$$M_2 = -\rho\pi b^2\left[(\tilde{x}_\mathrm{E} - b)^2 + \frac{b^2}{8}\right]\ddot{\alpha}\,.$$

3. Convective type moment associated to rotational speed,

$$M_3 = -\rho\pi b^2 U\,(2b - \tilde{x}_\mathrm{E})\,\dot{\alpha}\,.$$

4. Circulatory lift-induced moment related to pitch,

$$M_4 = 2\rho e b^2 U^2 C_{L\alpha}\alpha\,.$$

5. Moment induced by downwash circulatory lift,

$$M_5 = 2\rho e b^2 U^2 C_{L\alpha}\frac{\dot{h}}{U}\,.$$

6. Moment induced by circulatory lift due to virtual camber effect,

$$M_6 = 2\rho e b^2 U^2 C_{L\alpha}\left(\frac{3}{2}b - \tilde{x}_\mathrm{E}\right)\frac{\dot{\alpha}}{U}\,.$$

Hence the full expressions of the aerodynamic lift force and moment exerted on an oscillating airfoil are

$$L = \sum_{i=1}^{6} L_i \quad \text{and} \quad M = \sum_{i=1}^{6} M_i\,. \tag{4.50}$$

Once again these terms can be moved from the right-hand side of the pitch-plunge airfoil EoM (as they appear in Equation 4.39) to its left-hand side (as in Equation 4.49) through the use of an aerodynamic operator, now taking the full quasi-steady (FQS)

form

$$\underline{\mathbf{\Lambda}}(\mathbf{a}) = \rho\pi b^2 \begin{bmatrix} 1 & b-\tilde{x}_\mathrm{E} \\ b-\tilde{x}_\mathrm{E} & (b-\tilde{x}_\mathrm{E})^2 + \frac{b^2}{8} \end{bmatrix} \ddot{\mathbf{a}} + \\ + \rho b U \begin{bmatrix} C_{L\alpha} & C_{L\alpha}\left(\frac{3}{2}b-\tilde{x}_\mathrm{E}\right)+\pi b \\ -2ebC_{L\alpha} & \pi b\,(2b-\tilde{x}_\mathrm{E}) - 2ebC_{L\alpha}\left(\frac{3}{2}b-\tilde{x}_\mathrm{E}\right) \end{bmatrix} \dot{\mathbf{a}} + \\ + \rho b U^2 \begin{bmatrix} 0 & C_{L\alpha} \\ 0 & -2ebC_{L\alpha} \end{bmatrix} \mathbf{a} = \\ = \underline{\mathbf{M}}_\mathrm{a}\ddot{\mathbf{a}} + \underline{\mathbf{D}}_\mathrm{a}\dot{\mathbf{a}} + \underline{\mathbf{K}}_\mathrm{a}\mathbf{a}\,. \quad (4.51)$$

4.3.1.3 Unsteady harmonic aerodynamics

As thoroughly discussed by Leishman [241] and Paraschivoiu [68], two prevalent sources of aerodynamic unsteadiness are found on a wind turbine rotor. These are the upstream effect of the large-scale wake, which is disregarded in the current study, and the individual blades' vicinity wake, which makes the object of the presented unsteady formulation. The quasi-steady representation of aerodynamic forces on a thin airfoil is accurate for vibrations occurring at $\kappa \ll 1$, where $\kappa = \omega b/U$ is the reduced vibrational frequency. In case the structure undergoes higher-frequency vibrations, the inertia of the circulatory system causes a lag in the establishment of circulation and the associated forces; for a periodic oscillatory state, the reversing of motion before the steady circulatory forces are attained causes a reduction of their amplitude as well as a phase shift. This in turn can have a significant effect on the flutter phenomenon. The classic thin airfoil formulation used by Theodorsen [238] allows to take these effects into account for harmonic oscillations with the introduction of a complex operator $C(\kappa)$ which multiplies the circulatory force terms found in Equation 4.51. While its exact expression is given by Bessel or Hankel functions of the reduced frequency, practical approximations of this operator are available such as [242]:

$$C(\kappa) \approx 1 - \frac{0.165}{1 - \frac{0.0455}{\kappa}\mathrm{i}} - \frac{0.335}{1 - \frac{0.30}{\kappa}\mathrm{i}}\,. \quad (4.52)$$

The values assumed by this function are reproduced in Figure 4.21. The quasi-steady aerodynamic operator hence corresponds to the the nil-frequency case of the unsteady harmonic operator, or $\kappa = 0$. The amplitude of the circulatory forces tends to half its quasi-steady value for high-frequency vibrations, whilst the lag caused by flow unsteadiness is shown to reach a maximum below $\kappa = 0.5$ and gradually rebound. Note that the phase shift of the circulatory force never exceeds one fifth of a right angle. As it will be seen in the following, including the unsteady effects tends to reduce the importance of aerodynamic damping in the system.

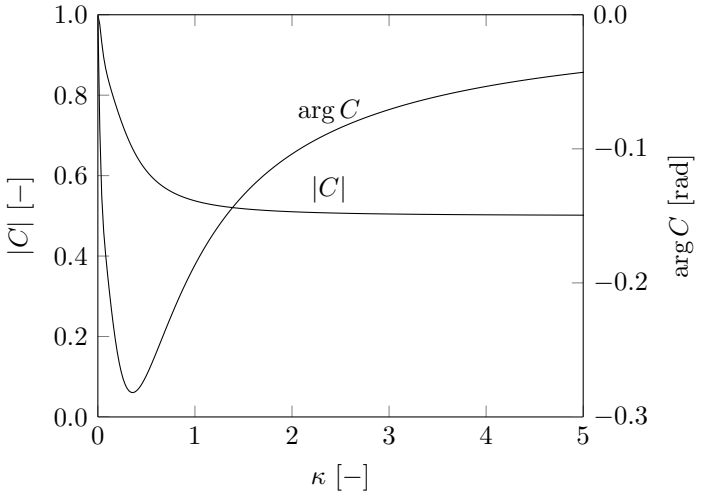

Figure 4.21: Modulus and argument of Theodorsen operator for varying reduced frequency κ.

The unsteady aerodynamic operator of an airfoil section, valid for harmonic oscillations only, is finally written as follows:

$$\begin{aligned}\underline{\mathbf{\Lambda}}(\mathbf{a}) = \rho\pi b^2 &\begin{bmatrix} 1 & b-\tilde{x}_\mathrm{E} \\ b-\tilde{x}_\mathrm{E} & (b-\tilde{x}_\mathrm{E})^2+\frac{b^2}{8} \end{bmatrix} \ddot{\mathbf{a}} + \\ + \rho b U &\begin{bmatrix} C(\kappa)C_{L\alpha} & C(\kappa)C_{L\alpha}\left(\frac{3}{2}b-\tilde{x}_\mathrm{E}\right)+\pi b \\ -2ebC(\kappa)C_{L\alpha} & \pi b\,(2b-\tilde{x}_\mathrm{E}) - 2ebC(\kappa)C_{L\alpha}\left(\frac{3}{2}b-\tilde{x}_\mathrm{E}\right) \end{bmatrix} \dot{\mathbf{a}} + \\ + \rho b U^2 C(\kappa) &\begin{bmatrix} 0 & C_{L\alpha} \\ 0 & -2ebC_{L\alpha} \end{bmatrix} \mathbf{a} = \\ &= \underline{\mathbf{M}}_\mathrm{a}\ddot{\mathbf{a}} + \underline{\mathbf{D}}_\mathrm{a}\dot{\mathbf{a}} + \underline{\mathbf{K}}_\mathrm{a}\mathbf{a}\,. \end{aligned} \quad (4.53)$$

It should be noted that the complex operator $C(\kappa)$ cannot be determined a priori because of its dependence from the vibrational frequency ω, which is an output of the aeroelastic calculation and also varies over the modal spectrum. Past studies have solved this issue by iterating over the reduced frequency at each output point, or by imposing a fixed, representative reduced frequency κ upfront, which is used for the entire spectrum. In this study the modal frequencies obtained from the full quasi-steady aeroelastic resolution (see 4.3.1.2) are used to calculate a representative value of κ for each group of modes and impose it in the unsteady aerodynamic calculation. Since in the presented applications (4.3.3) the modal frequencies are not significantly affected by the upgrade from quasi-steady to unsteady aerodynamics, said approach can justifiably replace iteration over the reduced frequency for the concerned applications.

4.3.1.4 3D aerodynamic element and global dynamics

The preceding sections described the methods used to treat an airfoil subjected to a planar airflow. If 3D flow effects and span-wise sectional changes are disregarded, the aerodynamic interaction of a finite-span portion of a blade may be represented in lump form by extension of the 2D model. The establishment of a local SoR xyz in 3D space as

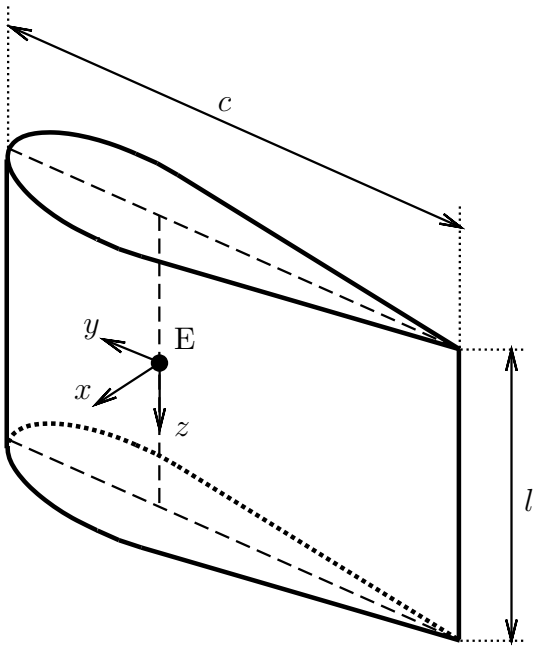

Figure 4.22: Lump aerodynamic element centred on node E.

seen in Figure 4.22, where the airfoil plunge and pitch DoF correspond to a translation in x and a rotation around z respectively, allows to rewrite the aerodynamic operators found in Sections 4.3.1.2 and 4.3.1.3 with respect to the 6 nodal displacements $\mathbf{q}_\mathrm{e}$ using

$$q_{\mathrm{e}1} = a_1 \quad \text{and} \quad q_{\mathrm{e}6} = a_2 \,. \tag{4.54}$$

The coefficients related to these two DoF are assigned accordingly and the remaining are set to zero, yielding a per unit length aerodynamic operator $\underline{\mathbf{\Lambda}}(\mathbf{q}_\mathrm{e})$ of size 6×6. The span dimension l of the aerodynamic element comes into play with

$$\mathbf{\Lambda}_\mathrm{e}(\mathbf{q}_\mathrm{e}) = l\underline{\mathbf{\Lambda}}(\mathbf{q}_\mathrm{e}) \,, \tag{4.55}$$

which represents the operator defining a lump aerodynamic element. The aerodynamic system attached to the profiled segments of the rotor in 3D space is then discretised over the segments' span with a set of elements defined by the above formulation. The local frame of each element is assigned by aligning y with the local tangential speed of the element and imposing that z lies in the plane defined by the span direction and the

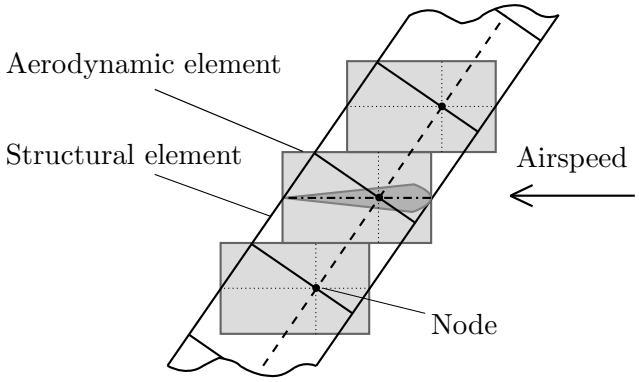

Figure 4.23: Aerodynamic discretisation of a swept rotor blade.

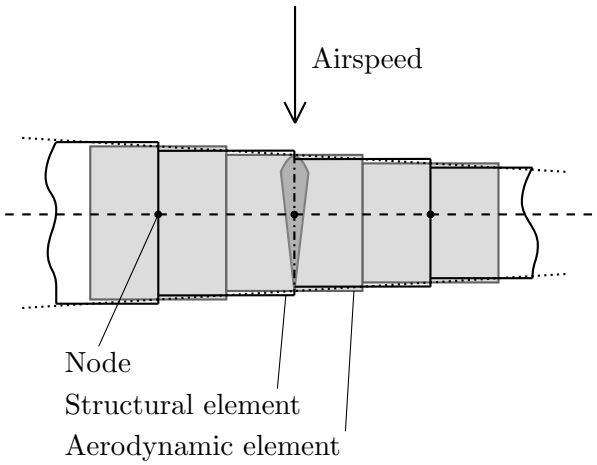

Figure 4.24: Aerodynamic discretisation of a tapered support strut.

tangential speed. The element centre E is located on the neutral fibre of the structure. A visual example of this arrangement is shown in Figures 4.23 and 4.24 for the blade and strut components of a Vertiwind-type rotor. Extending this discretisation method to a Vertiwind-class rotor leads to the setup shown in 4.3.3 (Figures 4.27 and 4.30). The next step is the expression of the element's characterising airspeed U which defines the aerodynamic operator coefficients (Equations 4.51 and 4.53) as a function of the rotor speed Ω, that is

$$U = \Omega r_{\mathrm{e}} \,. \tag{4.56}$$

Here r_{e} represents the distance of the aerodynamic element from the revolving axis. The linear and quadratic dependencies from U observable in Equations 4.51 and 4.53, combined with Equation 4.55, permit to write

$$\mathbf{D}_{\mathrm{ae}} = \Omega \mathbf{D}^1_{\mathrm{ae}} \,, \tag{4.57}$$

$$\mathbf{K}_{\mathrm{ae}} = \Omega^2 \mathbf{K}^1_{\mathrm{ae}} \,, \tag{4.58}$$

where the matrices denoted by a unit superscript adopt a unit rotational speed and the radius of the node r_e to calculate U with Equation 4.56.
Following the transformation of each element's aerodynamic operator into the global spinning frame and the aggregation of the element matrices (see 4.2.1.3), the operator can be incorporated into the overall finite-element system by means of three system-level aerodynamic matrices $\mathbf{M}_a, \mathbf{D}_a, \mathbf{K}_a$ (see Equations 4.51 and 4.53). The offset due to the steady-state displacement due to the presence of the centrifugal force is disregarded by this aerodynamic model; such assumption is valid when the steady-state rotational displacement (i. e. the pitch deformation) of the blade sections is sufficiently small. Combining the global aerodynamic operator with the spinning structural model of Equation 4.22 yields the full aeroelastic description of rotor vibrations:

$$(\mathbf{M} + \mathbf{M}_a)\ddot{\mathbf{q}} + (\mathbf{G} + \mathbf{D}_a)\dot{\mathbf{q}} + (\mathbf{K}_e + \mathbf{K}_g - \mathbf{K}_\Omega + \mathbf{K}_a)\mathbf{q} = \mathbf{0}\,. \tag{4.59}$$

These are the EoM of an aeroelastic, steadily rotating structure expressed in the spinning SoR bound to the rotor's azimuth. As it has been shown with Equation 4.23 for the beam assembly and with Equations 4.57 and 4.58 for the aerodynamic system, it is possible to exploit the dependency of the finite element model's coefficients from Ω to express Equation 4.59 as follows:

$$(\mathbf{M} + \mathbf{M}_a)\ddot{\mathbf{q}} + [\Omega(\mathbf{G}^1 + \mathbf{D}_a^1)]\dot{\mathbf{q}} + [\mathbf{K}_e + \Omega^2(\mathbf{K}_g^1 - \mathbf{K}_\Omega^1 + \mathbf{K}_a^1)]\mathbf{q} = \mathbf{0}\,. \tag{4.60}$$

As seen already with Equation 4.23, all Ω-dependent terms are computed for a unit rotational speed (denoted with a superscript '1'), then a range of revolution speeds is imposed parametrically, hence enabling to parallelise the set of eigenproblems.

4.3.2 Model verification

At this point, having verified the rotordynamic behaviour of the model in 4.2.2 leaves the task of verifying the aerodynamic operator, which is carried out here on the basis of the standard pitch-plunge airfoil problem documented in the aeroelasticity literature.
The aeroelastic system defined in 4.3.1.1 proves useful to test the numerical solver's ability to identify the vibrational modes of a structure together with its aeroalastic stability characteristics. A special (canonical) pitch-plunge airfoil case is defined by the parameters given in Table 4.5, where $b = c/2$. These values are sufficient to determine the ensemble of variables entering Equation 4.49, which is then resolved for its eigenvalues using the numerical model with the procedure explained in 4.2.1.4 for varying free stream airspeed U. Thanks to the limited size of the system of equations, its eigenvalues may also be easily derived by resolving the following equation in a semi-

Table 4.5: Pitch-plunge airfoil parameters.

Normalised CoG coordinate s_G/b [-]	0.05
Normalised radius of gyration $r_\alpha = r_\mathrm{g}/b$ [-]	0.5
Uncoupled plunge-pitch frequency ratio ω_h/ω_α [-]	0.5
System parameter $m/\pi\rho b^2$ [-]	10
Normalised eccentricity of lift centre e [-]	0.2
Slope of airfoil lift characteristic $C_{L\alpha}$ [-]	2π

analytical manner:

$$\begin{vmatrix} k_h + qc\frac{C_{L\alpha}}{U}\lambda + m\lambda^2 & qcC_{L\alpha} + S\lambda^2 \\ -q\frac{ec^2C_{L\alpha}}{U}\lambda + S\lambda^2 & k_\alpha - qec^2C_{L\alpha} + I\lambda^2 \end{vmatrix} = 0\,. \tag{4.61}$$

The resulting normalised damped eigenfrequencies for pitch (1) and plunge (2) are shown in Figure 4.25, where $\bar{\omega}$ is the pitch natural frequency at $U = 0$. The corresponding damping ratios are also plotted. The numerical method developed in this study is shown to be capable of identifying the behaviour of the structure's eigenmodes and their damping ratio for both stable and unstable regimes, systematically reproducing the semi-analytical solution.

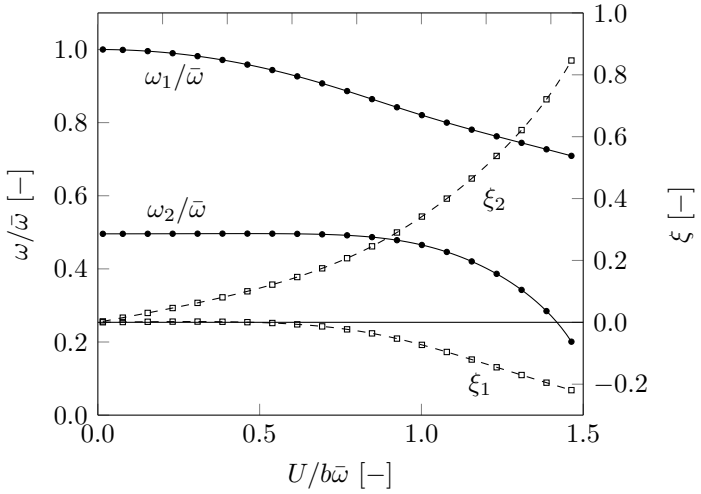

Figure 4.25: Comparison of semi-analytical (lines) and numerical (dots) resolution of the pitch-plunge airfoil vibration modes.

System states can be interpreted as follows: to the extreme left of the Figure, airspeed is nil, and no aerodynamic interaction affects the airfoil's vibrations. The ratio of the plunge and pitch eigenfrequencies is 0.5 as prescribed in Table 4.5, and system damping is nil. As the airspeed increases so does the relative importance of the aerodynamic system. A first consequence consists in the progressive deviation of the eigenfrequencies from the standstill values, caused by the aerodynamic alteration of the effective stiffness.

Secondly, an increasing amount of aerodynamic damping affects the vibrational modes. It is possible to remark that at low reduced airspeeds the behaviour of aerodynamic damping is positive, hence the structure's dynamic stability is improved by the presence of the aerodynamic interaction. This is a typical characteristic of real-world aeroelastic systems.

As soon as the airspeed becomes sufficiently large, two forms of instability appear in Figure 4.25. A tendency toward static aeroelastic instability, introduced in 4.3.1.1, is observable for a reduced airspeed ($U/b\bar{\omega}$) exceeding 1.0: the plunge mode's frequency is progressively reduced as the airspeed increases; the extreme consequence of this process is the loss of system restoring capacity (divergence), which happens when ω approaches 0. In case this occurs in a physical system, the slightest perturbation causes runaway displacement and typically structural failure. Flutter, the other instability observable using the canonical airfoil case, is of dynamic type and is revealed by the negative damping ratio characterising the pitch mode. It appears clear from Figure 4.25 that pitch is affected by flutter at a much lower airspeed than that required to destabilise the system statically (less than 1/3). The modal damping ratios are next reproduced on a semi-logarithmic plot in Figure 4.26 to pinpoint the airspeed at which the flutter instability occurs. The critical airspeed for flutter (or simply, flutter speed) corresponds to a reduced airspeed of about 0.5. It is important to keep in mind that although weakly coupled for $U = 0$, the pitch and plunge DoF become increasingly subjected to aerodynamic coupling at increasing airspeeds, and it is this coupling that permits the onset of flutter. With respect to Figure 4.25, this implies that the further we move toward high airspeeds, the more the two output modes represent a mix of pitch and

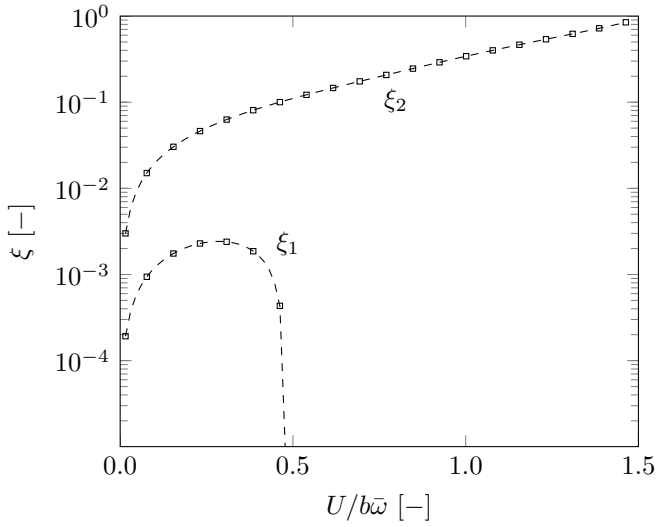

Figure 4.26: Modal damping of pitch-plunge airfoil. Semi-analytical (lines) and numerical (dots) results.

plunge vibrations rather than a single-DoF motion.
What happens if a rotor designer discovers that a similarly behaved blade may encounter or get close to its critical flutter speed over its operating life? A common practical way to increase the flutter speed and remove it from the operating envelope, as suggested among others by Lobitz [220], consists in blade ballasting. Adding a controlled sectional mass allows to displace the chordwise position of G and hence to alter the ratio between the pitch (i.e. torsional) and plunge (i. e. flapwise) eigenfrequencies, which both affect the blade's flutter speed.

4.3.3 Applications and discussion

The vibration modes of the two Vertiwind rotor configurations presented in 4.2.3, denoted 1H and 4H, are next obtained using the integral aeroelastic representation of Equation 4.60. The documents[7] defining the properties of the rotor structure and of its aerodynamic profiling have been provided by an industrial partner [232, 233].

4.3.3.1 Analysis of 1H rotor

A rendering of the aeroelastic model implemented to study the 1H rotor is shown in Figure 4.27. Both the full quasi-steady and the unsteady formulations of the aerodynamic

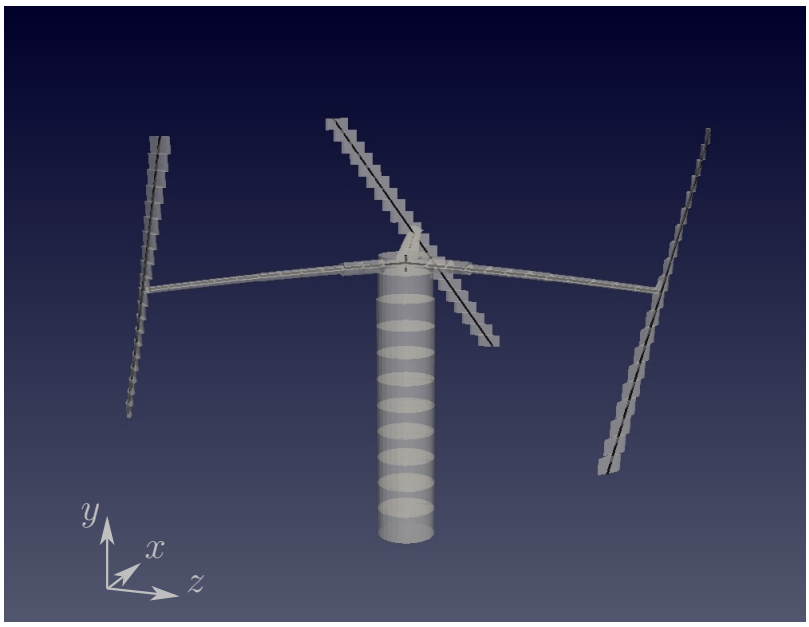

Figure 4.27: Rendering of finite-element beams (black lines) and lump aerodynamic elements (grey profiled volumes) of the 1H rotor. After Relun and Antonutti [204].

[7] Confidential.

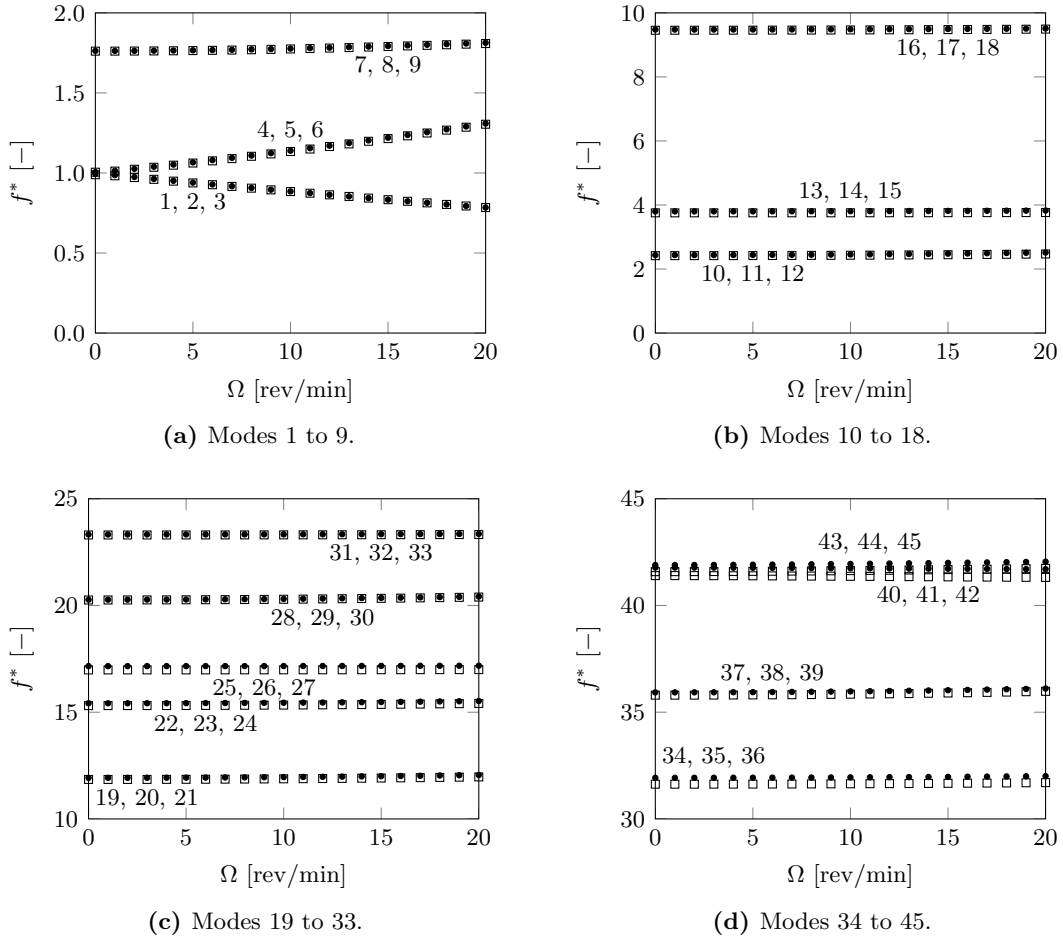

(a) Modes 1 to 9.

(b) Modes 10 to 18.

(c) Modes 19 to 33.

(d) Modes 34 to 45.

Figure 4.28: Aeroelastic Campbell diagram of the 1H rotor (squares). Dots reproduce the classic Campbell diagram already shown in Figure 4.14.

operator are used, giving raise to significantly different predictions of modal damping, as it will be shown below. Since these two options lead to calculating approximately the same modal frequencies, a single set of aeroelastic frequencies is reproduced nondimensionally in the Campbell diagram of Figure 4.28. The classic Campbell diagram already shown in Figure 4.14 is also plotted for comparison. There is no significant difference between the classic and the aeroelastic Campbell frequencies for low-frequency modes. On the contrary, several higher modes exhibit a moderate aeroelastic effect on frequency, in all cases tending to reduce it. These are the vibrations characterised by a relatively large flapwise content. The results of Figure 4.28 may be used to justify the validity of the classic rotordynamic approach of Section 4.2, which disregards all fluid-structure interaction, for the prediction of the structure's eigenfrequencies.

The fundamental added value of the aeroelastic formulation consists in the estimate of the aerodynamic damping ratio of the output modes, which is shown in Figure 4.29. A significant amount of aerodynamic damping affects most low-frequency vibration

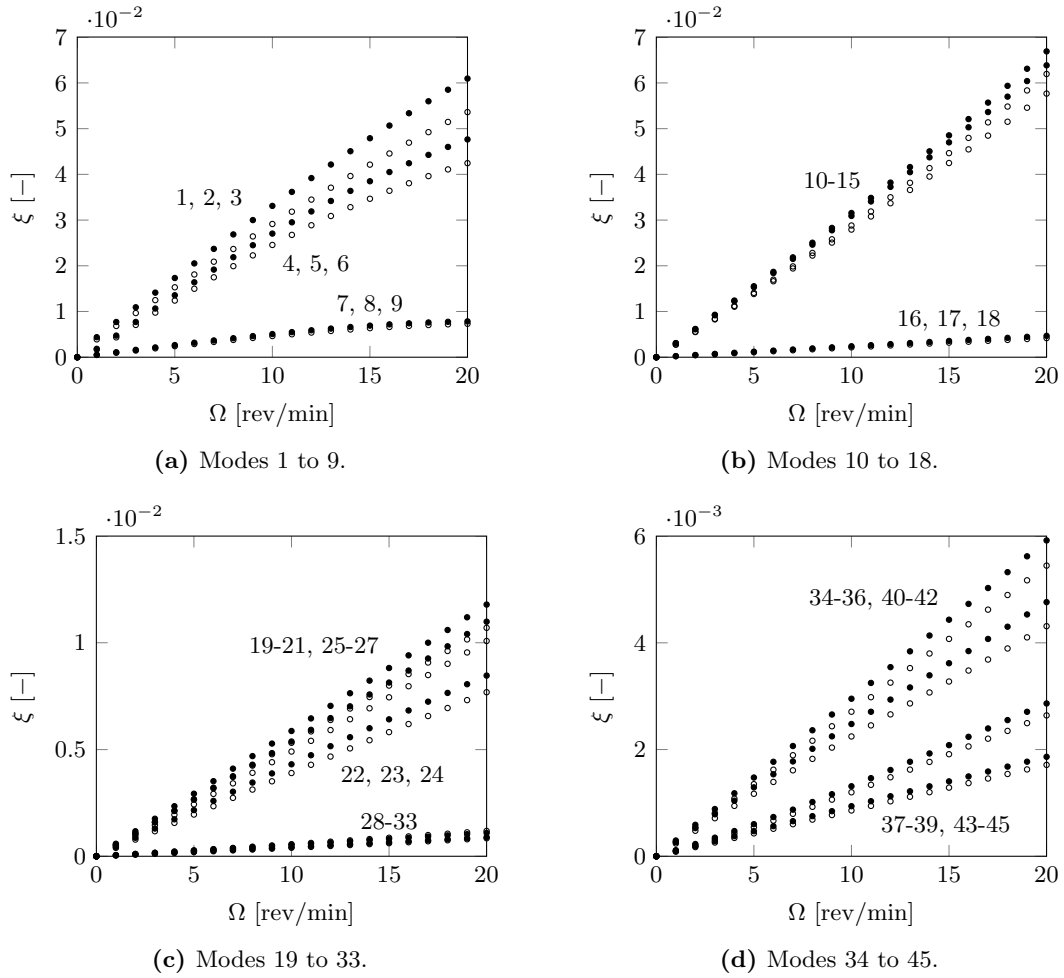

(a) Modes 1 to 9.

(b) Modes 10 to 18.

(c) Modes 19 to 33.

(d) Modes 34 to 45.

Figure 4.29: Modal damping plot of 1H rotor using quasi-steady (full dots) and unsteady (empty dots) aerodynamics.

modes, which increases almost linearly with the revolution speed for the studied range, up to levels of 4% to 6%. Higher modes and in general modes dominated by edgewise vibration tend to be less affected, exhibiting damping ratios of around or less than a percent point. The plots also reveal that the use of unsteady aerodynamic theory reduces the damping-generating capacity of the aerodynamic system compared to the quasi-steady implementation, up to about 15%. This is essentially due to the simultaneous phase shift and magnitude reduction of the aerodynamic forces which affect harmonically vibrating airfoils (see Figure 4.21).

4.3.3.2 Analysis of 4H rotor

Figure 4.30 provides a visualisation of the aeroelastic model representing the 4H rotor. The aeroelastic Campbell diagram obtained for this rotor is shown in Figure 4.31 along with the classic Campbell diagram already reproduced in Figure 4.18. As seen in the previous case study, the lower eigenfrequencies are not significantly affected by aerodynamic interaction, whilst the contrary is true in the higher portion of the modal spectrum. Once again, the main effect observed is a downward frequency shift associated to the aerodynamic added mass. In the 4H rotor case this shift is more important and represents up to 5% of the value found in the classic Campbell diagram (modes 18–26 provide a good example of this). Figure 4.31 also shows the impact of the stiffness component of the aerodynamic operator on modal frequencies, which is reflected in the alteration of the eigenfrequency curve slope. Shown in Figure 4.32 are the damping

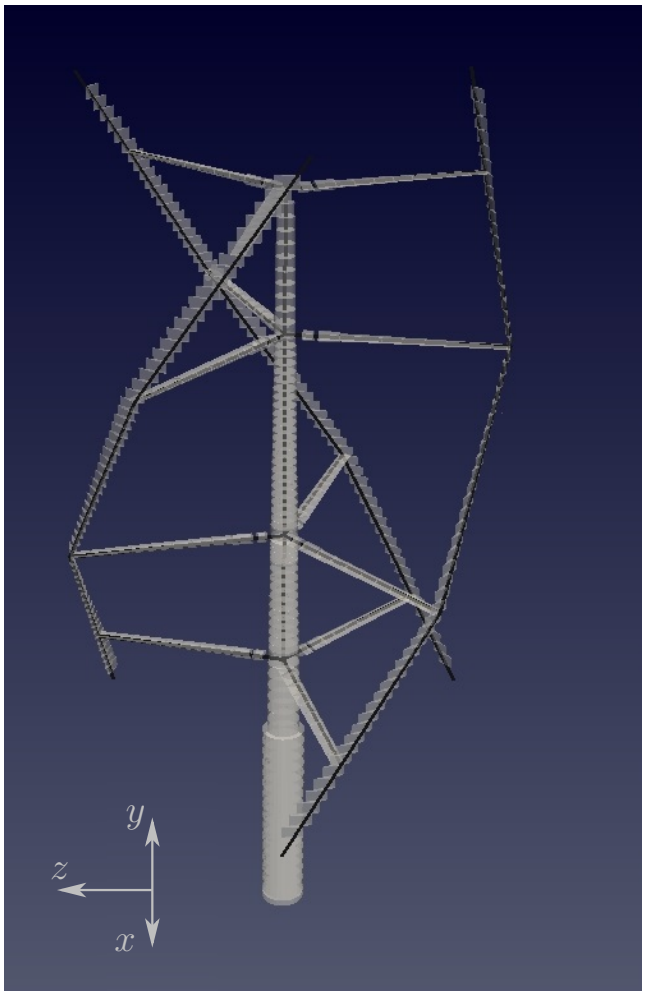

Figure 4.30: Rendering of finite-element beams (black lines) and lump aerodynamic elements (grey profiled volumes) of the 4H rotor. After Relun and Antonutti [204].

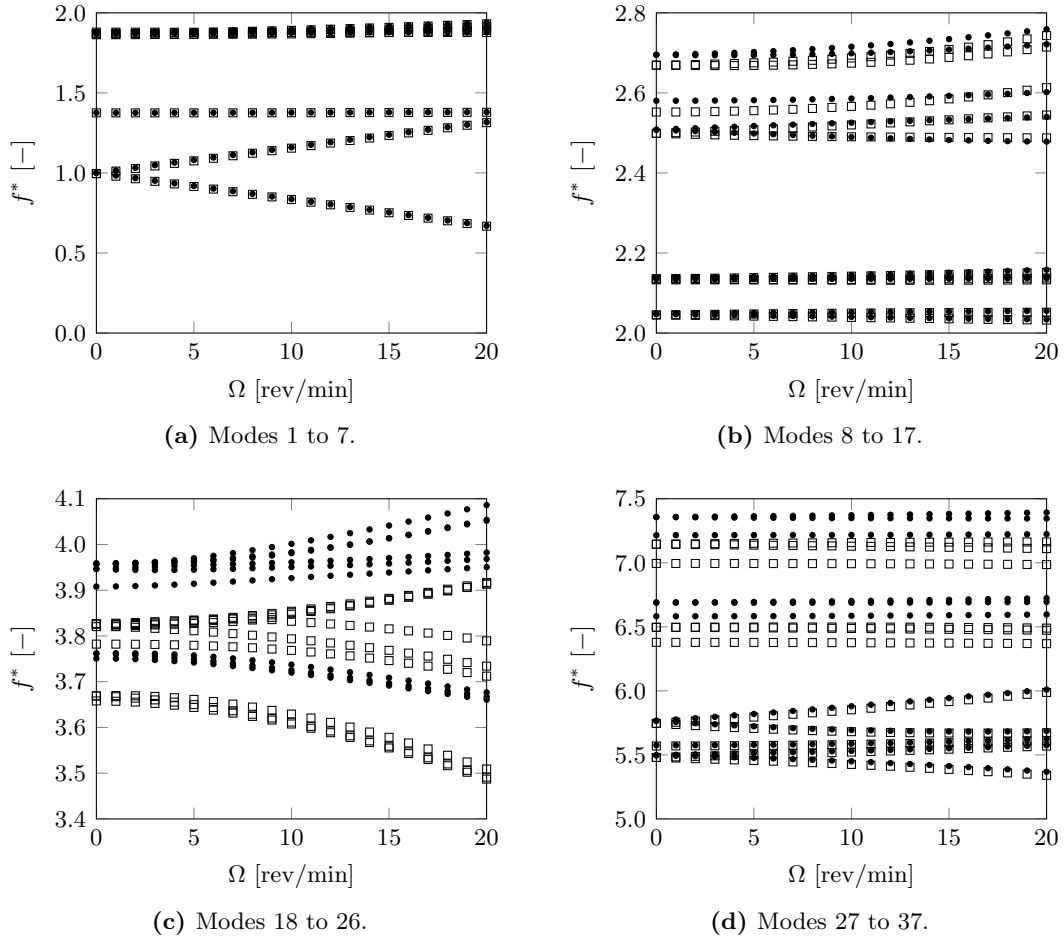

(a) Modes 1 to 7.

(b) Modes 8 to 17.

(c) Modes 18 to 26.

(d) Modes 27 to 37.

Figure 4.31: Aeroelastic Campbell diagram of the 4H rotor (squares). Dots reproduce the classic Campbell diagram already shown in Figure 4.18.

ratios corresponding to the same modes.

Similarly to what was found for the 1H rotor, numerous modes are significantly stabilised by aerodynamic damping, which increases in a quasi-linear fashion with the rotor speed. Depending on the mode type, damping varies between around 1% and 12% at 20 rev/min. The latter order of magnitude in particular characterises the (blade vibration) modes ranging from 18 to 26, where accounting for aerodynamic damping may provide a significant extension of blade fatigue life. Once again, the use of the unsteady aerodynamic model exposes the moderate overestimation of aerodynamic damping provided by the quasi-steady option, which is in the order of 10%–15%.

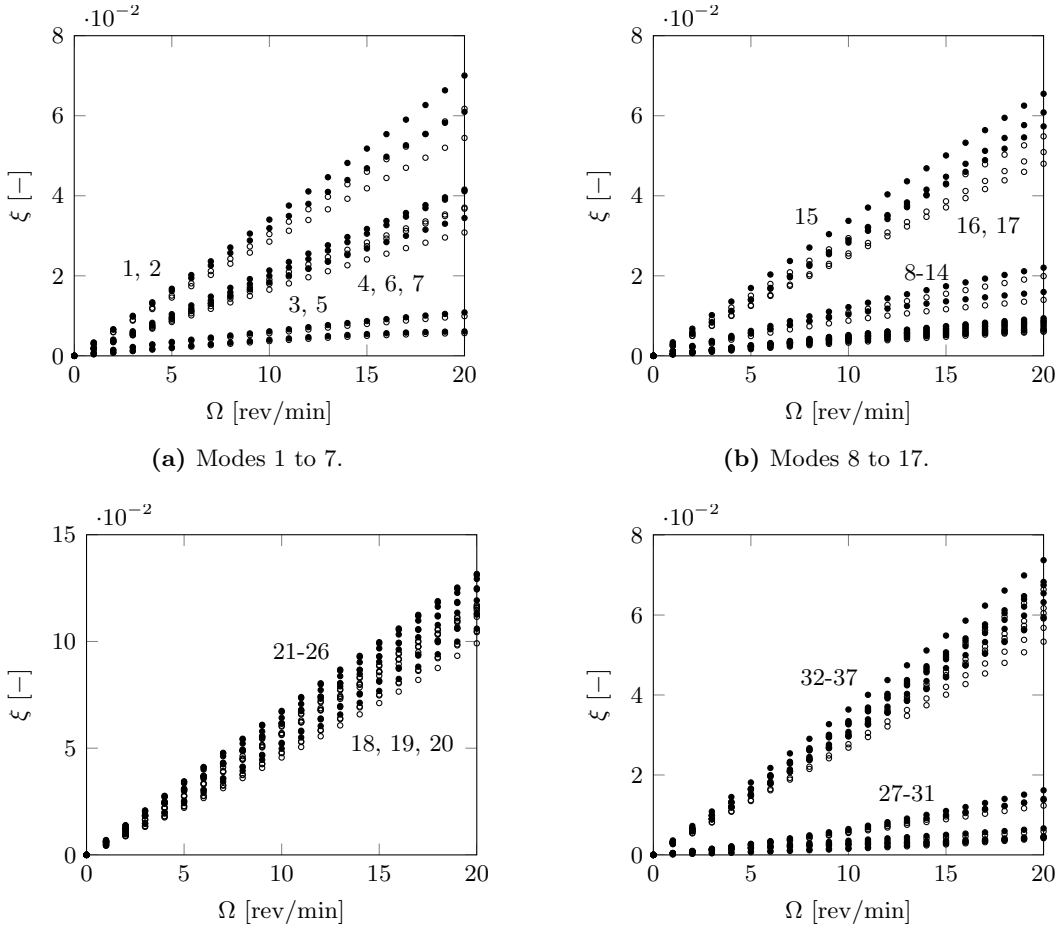

(a) Modes 1 to 7.

(b) Modes 8 to 17.

(c) Modes 18 to 26.

(d) Modes 27 to 37.

Figure 4.32: Modal damping plot of 4H rotor using quasi-steady (full dots) and unsteady (empty dots) aerodynamics.

4.4 Conclusion

Using the present numerical model, EDF R&D has acquired the ability to qualify the aeroelastic behaviour of proposed floating VAWT rotor concepts, helping to reduce project risk and to understand the key parameters at play in the structural design of the aerogenerator. An example of this capability is available in the report by Relun and Antonutti [204]. This Part has detailed the finite-element model implemented and used to carry out frequency-domain aeroelastic analysis of VAWT rotors, as well as its application to two industrial concepts of interest. The entirety of the calculation chain has been set up, from the implementation of the spinning beam element and lump aerodynamic operator methodologies into an existing in-house finite-element environment to the organisation of the post-treatment stage where the system's vibration modes are resolved.

Choosing a corrotating frame for the description of the structure's vibrations has allowed to describe the structural dynamics under the classic small-displacement assumption, thereby avoiding the explicit treatment of the displacements associated to rotor revolution. In the absence of fluid-structure interaction (Section 4.2), identifying the structure's eigenmodes provides the classic Campbell diagram which is commonly used for the detection of critical rotor speeds, where the vibrational and excitation frequencies coincide. Two Vertiwind-type rotors have been analysed with this method, leading to the results discussed in 4.2.3.

After the basic characterisation of the rotor modes, the structural model has been augmented with the aerodynamic interaction model presented in Section 4.3, leading to a coupled, linearised aeroelastic representation of rotor mechanics. This formulation simplifies and internalises the aerodynamic forces into the left-hand side of the equations of motion, enabling an integrated modal representation of the system. Hence, the same two Vertiwind rotor concepts have been analysed in 4.3.3, leading to the following findings:

- Classic modal analysis, which excludes aerodynamics, suffices for the prediction of the lower rotor eigenfrequencies, while tends to overestimate them in the upper part of the spectrum.
- Static aeroelastic instability, which is revealed by a dropping aeroelastic eigenfrequency, is not detected for the two rotors in the studied speed range. No signs of its onset are present at high revolution speed.
- Dynamic aeroelastic instability (flutter), which is revealed by dropping aerodynamic damping of the concerned mode, is not detected for the two rotors in the studied speed range. No signs of its onset are present at high revolution speed.
- A significant amount of aerodynamic damping affects rotor vibrations, often providing an extra 5%–10% on top of the (presently disregarded) structural damping,

which typically amounts to a few points percent on wind turbine structures.

- The use of quasi-steady aerodynamic theory causes an overprediction of modal aerodynamic damping in the order of 15% compared to the unsteady representation.

Both rotor designs have been verified against the onset of aerodynamic instability in the selected operating and overspeed range, and the stabilising contribution of aerodynamic interaction is quantified, potentially enabling to feed this information back into structural design to reduce conservatism. However, as it is further discussed below, the present simplification of the aerodynamic process prompts the future adoption of more complex time-domain methods for a more reliable assessment of aeroelastic stability, possibly including nonlinear phenomena such as stall flutter.

Not treated in this study is the aerodynamic nonstationarity introduced by the free-stream wind velocity in real operating conditions, and the subsequent operation of the blade profiles at large and varying angles of attack. As seen in Part 2, MW-scale VAWTs tend to operate at relatively low tip-speed ratios, where large angles and stall are common. Hence the interest in further developing the model to permit a more in-depth aeroelastic analysis, enabling to challenge the structural design of the rotor from other standpoints such as fatigue life. This aspect has been later addressed by EDF R&D with the merger of the present rotordynamic model with the double-multiple streamtube aerodynamic solver detailed in 2.2.3, to form a time-domain aeroelastic resolution module denoted MuBoWT[8] [204]. The turbulent content of the incident wind and the rotor wake linked to precedent blade passages, as well as 3D flow effects, are also at the origin of additional aerodynamic nonstationarities which are not considered here.

[8]Multi-body Wind Turbine. Using the multi-body theory, this software insures the coherence among the descriptions of the two subdomains, rotor and platform, in the rotating (bound) and global frame respectively.

Part 5

Conclusions and Further Work

A significant number of industrial actors worldwide is engaging in the development of floating wind power, in order to overcome the bathymetric limitations of bottom-fixed offshore wind. With utility-scale prototype demonstration well underway, floating wind technology requires further de-risking, cost optimisation, and standardisation – in one word: industrialisation – to unlock large-scale investment in the coming years. A key requirement for this is the availability of robust simulation tools right from the pre-design stage: these are at the focus of the presented work.

Global coupled dynamics. The system-level mechanical analysis of FWT structures brings together the domains of aerodynamics and offshore hydromechanics. The outcome is an aero-hydromechanical problem which often exhibits strong couplings and is today an active subject of research. The rigid-body mechanics of FWTs are studied in Part 2, where a multi-physical engineering-level simulator developed by EDF R&D is employed to characterise a number of coupling effects for the first time.
A relatively compliant (i.e. inclination-prone) semi-submersible FWT concept is studied in 2.3.2 with respect to the changes of its dynamic response in waves when subjected to the aerogenerator's operating forces, revealing the presence of significant aero-hydrodynamic coupling due to the vertical excursion of the columns. The related close-up investigation has been the object of a journal publication [158]. The platform's large motion control appendices (heave plates) are hence shown to represent an important hub of such hydrodynamic sensitivity (2.3.1), which gives birth to different response knock-ons depending on the direction of wind relative to the waves – an aspect investigated in another journal article [160]. To the Author's knowledge, a surge-pitch aerodynamic coupling mechanism which significantly affects pitch response in the suppression band typical of multi-column semi-submersible platforms is also described in detail for the first time. It is largely the work performed in these areas that has produced new knowledge with respect to the state of the art of floating wind turbine mechanics, which may prove useful in the definition of future design practices.
Existing basin test results are used in 2.3.4 for a validation of the methods used in the above studies, broadly confirming their accuracy and allowing methodologi-

cal improvements which will be incorporated in the VALEF2 project[1] reports. The benchmark still suggests possible limitations in the current hydrodynamic modelling approach, especially regarding the quantification of the vertical added mass for a structure of the kind studied (multi-column floater equipped with heave plates and multiple interconnecting braces).

A novel application of coupled aero-hydromechanical simulation, presented in 2.3.3 and published as part of conference proceedings [159], is the characterisation of the aerodynamic damping of global pitch motion experienced by a large floating VAWT for a range of operating conditions, where for the first time the patterns found shed light on the causal mechanisms determining its pseudo-linear behaviour. In the treated case study, such form of damping is capable of providing 2%–5% of the critical damping for the uncoupled pitch motion, which translates into a significant potential for resonant response reduction when the FWT is subjected to wave excitation. This understanding may be used to introduce a feedback in turbine and controller design, aimed at achieving a mitigation of resonant response by aerodynamic means.

Mooring hydromechanics. The detail study of the mooring mechanics of a floating offshore system demands fully nonlinear, large-displacement dynamic simulation when it comes to representing the highly dynamic and highly compliant arrangements typically found in the floating wind context[2]. Leveraging on the availability of a thoroughly verified structural analysis tool, *Code_Aster* of EDF R&D, Part 3 develops a novel set-up strategy which enables the uncoupled and – currently within certain limits – coupled dynamic simulation of offshore mooring systems with this unspecialised software, which is shown effective for the study of catenary arrangements. Both these options are now part of the EDF arsenal for the mechanical analysis of FWT arrangements as documented in Peyrard and Antonutti [161].

Using a 1D finite-element formulation of structural kinematics, Section 3.3 describes how the hydromechanical properties of a mooring chain are transferred to the simulator (presiding a correct representation of the hydrostatic, hydrodynamic, and weight forces simultaneously) as well as the initialisation of the hydromechanical problem, where the equilibrium catenary state of the system is reached from an unstable, statically ill-conditioned control configuration.

Static analyses of catenary mooring lines and systems are used in 3.4 for an initial verification of the presented methodology. Then, existing small-scale experiments are used in Section 3.5 for the validation of its dynamic functionality. The concerned measurements are the dynamic response and fairlead tensions of a FWT model, moored at an equivalent depth of 200 m by a three-leg catenary system and subjected to

[1] A collaborative R&D project by *France Energies Marines* for the development, verification, and validation of floating wind turbine design methodologies involving industrial and academic bodies [77].

[2] The five MW-scale FWT prototypes installed to date use this arrangement.

wave excitation. It is demonstrated that with the proposed methodology *Code_Aster* is capable of predicting both the fairlead tensions and the platform motions under regular waves (coupled approach), as well as the tension spectra under irregular wave excitation (motion-driven simulation). Among the observed tension response characteristics, the simulations notably reproduce the high-frequency spectral content likely associated to the excitation of the mooring lines' eigenmodes.

Rotor aeromechanics. VAWTs of new conception are currently being proposed for floating use, with an apparent R&D revival of this turbine type at the MW scale since the abandonment of the prototyping programmes of the 1980s. Although marginal for proven HAWT rotors, the aeroelastic stability question addressed in Part 4 is of vital importance in the verification of the operational reliability of large-scale vertical-axis concepts.

In Section 4.2 a mechanical rotordynamic model based on the finite-element beam theory is deployed using the rotor's own spinning frame as a reference, allowing to produce the Campbell diagram of two rotor concepts of interest and hence identify the evolution of their structural modes as a function of the rotational speed. This has helped EDF to verify the methodology used by its industrial partners to demonstrate the structural reliability of these designs [204].

The same model augmented with a linearised aerodynamic operator, internalising the aerodynamic interaction forces in a simplified reactive form, is used in Section 4.3 to verify the same rotor designs against the onset of aeroelastic instabilities, with particular attention to self-excited (flutter) states. An estimate of the beneficial aerodynamic damping found in the operating speed range (up to 10% depending on the modes) is a byproduct of this analysis, potentially allowing to establish a feedback in the design cycle aimed at reducing the conservatism in the sizing of the structure.

Bringing it all together. Using the presented tool set, EDF R&D is now able to produce robust knowledge about the mechanical behaviour of the FWT arrangements proposed by technology developers, and with relatively short notice. Both global dynamics and the structural reliability of critical subsystems may be scrutinised. The analyses of multi-physical phenomena carried out also shed light on mechanisms which may support the provision of design feedbacks from the part of EDF: while on one hand potential dimensioning benefits are unlocked by the quantification and the controlled use of aerodynamic damping, on the other unforeseen failure modes may now be detected thanks to the knowledge of the coupling effects identified.

The presented numerical tools do not live in isolation, as linkages of different nature are already exploited in the present work, while others have been created in the course of further work carried out by EDF R&D. As it is shown in Part 3, the coupled moorings-floater simulations already enable to evaluate the retroaction of the mooring system dynamics on the global motion response. Conversely, the mooring simulation of Part 3

may be driven by the motion history obtained with the FWT aero-hydromechanical simulation of Part 2, neglecting the dynamic mooring force feedback. Using an azimuth-updated basis conversion and an iterative, time-domain mechanical solver, EDF has also been able to link the small-deformation description of rotor mechanics of Part 4 to the global simulator CALHYPSO (Part 2), which has permitted to study the modes of deformable rotors when mounted atop a floating platform (not treated here). Similarly, the full bidirectional coupling of the finite-element dynamic representation of the mooring system to the multi-physical FWT simulation environment is envisaged in the near future, leading to the integrated time-domain simulation prospects explored in Section 5.1.

5.1 Recommendations

This section accommodates a set of recommendations for the further development of EDF R&D's design tools as well as a broader overview of the challenges lying ahead.

5.1.1 EDF perspective

At the time of writing, the numerical models and methodologies presented have already helped with the assessment of competing FWT designs and modelling strategies in the context of the industrial projects of the EDF Group. Whereas these tools are being developed well beyond what has been described in this manuscript, significant areas of future work may be identified to assist the engineering and commercial units in their perspective needs.
Restricting the perimeter to computationally efficient simulations for pre-design, verification, and concept evaluation, further work may be organised around the integration of different functions within CALHYPSO.

Aerodynamics. The aero-servo-elastic tool chain is now in place for the analysis of VAWTs, including an option for the input of turbulent wind; the development of HAWT compatibility may also be of interest, although the aerodynamic (BEMT) calculation routines would need overhauling. Coupling with well-proven open-source software such as NREL's AeroDyn module could be envisaged as an efficient alternative. The relationship between rotor control and the mechanical response of the FWT is an aspect of particular interest, given the present tendency to propose active control for motion mitigation. For both rotor architectures, the implementation of wake-resolving aerodynamic theories such as the potential-flow vortex method could enable a more accurate assessment of the coupled dynamic behaviour of the aerogenerator, albeit at a compromised computational cost.

Platform hydrodynamics. The integration of 2nd order wave forces is already underway in CALHYPSO, following the latest developments of the underlying hydrodynamic solver NEMOH. Improvement margins may reside in the potential-flow representation of sharp appendices, where a hybrid empirical method may be implemented to correct any detected added-mass deficit. Concerning slender member hydrodynamics, the inclusion of the diffracted and radiated wave fields in the calculation of fluid kinematics may be sought to improve the accuracy of the Morison routine in the proximity of large hull sections. Also, runtime adaptive coefficient calibration may be used to improve accuracy in irregular waves. Improvements are also possible in the representation of the intersections of the slender elements with the free surface and with other portions of the hull. The geometric nonlinearity exhibited by FWTs undergoing large-angle operation may be addressed with the systematic use of look-up tables for the calculation of the hydrostatic and potential hydrodynamic forces, thereby generalising the methodology presented in Part 2. Finally, implementing multi-directional wave excitation would permit the representation of fully realistic sea states.

Structural dynamics. The deformability of platform structures and the excitation of platform and tower modes by high-frequency harmonics (e.g. the sum-frequency wave forces) suggest that a hydroelastic representation of FWT mechanics may be highly valuable in the early engineering stage. The finite-element or multi-body theories can be used to model the elastic processes, provided that the interface between the potential-flow hydrodynamic solver and the structural solver be reorganised using the dynamic pressure field in lieu of the aggregated hydrodynamic data base tensors. A successful implementation of hydroelastic simulation should permit the description of nonlinear coupled processes such as springing, which is known to affect the vertical modes of TLPs.

Mooring dynamics. Further validation of the moorings model may extend to semi-taut and taut arrangements, possibly incorporating different segment types typical of offshore moorings (ropes, 6 DoF buoys, etc.). The integration of dynamic mooring simulation within CALHYPSO may prove particularly helpful in the mechanical assessment of tensioned FWT configurations, whose system modes tend to be excited by high-frequency wave loads. As soon as a detailed fatigue assessment of the mooring lines will be sought, accurate prediction of the loading states of catenary moorings will likely demand the implementation of complex line-soil interaction processes such as tangential friction and uplift-repenetration resistance. Finally, nonlinear material behaviour laws should be adopted in the future to accommodate the mechanics of fibre rope segments, which are frequently proposed as part of mooring systems for floating wind.

In the longer term, numerical studies of increasing detail will become necessary to orientate design practices and to mitigate the technological risk associated to vital

and/or less proven FWT components, as well as to highly dynamic transients.
Higher-order computational hydrodynamics, based on the resolution of nonlinear potential or viscous flow in the time domain, may be used to improve the accuracy of dynamic simulations, possibly in coupling with platform flexibility. Parametric modelling campaigns may use models of this class to create a data base for the calibration of engineering-level tools, for instance for the description of heave plate hydrodynamics. Targeted shock and transient studies regarding fluid-structure interaction may also be of particular interest in assessing concentrated, occasional structural damage. Breaking wave impact, slamming, and the subsequent ringing are examples in this sense.
Model improvements on the mechanical side will be required to study structure durability, where special focus may be placed on the fatigue life of the tower-base cradle and of welded platform joints. The ageing of cost-saving materials such as reinforced concrete in the offshore environment should also be investigated. Regarding the turbine rotor, the implementation of composite material behaviour may be envisaged to qualify novel component constructions. Component-specific mechanical models may be extended in the future to cover complex parts such as the umbilical cable and the drive train.
On the aerodynamic side, viscous computational fluid dynamics may be employed for a more accurate description of the aerodynamic loading on the superstructures, and perhaps to investigate the complex interaction of an oscillating rotor with its own wake. Innovative rotor concepts will require accurate aero-servo-elastic investigation to single out their possible failure modes.
Finally, robust methods will be needed to identify the dimensioning load cases and their likelihood based on the statistical analysis of met-ocean data and the knowledge of the dynamic behaviour of the system on a case-by-case basis, in order to organise the numerical simulations efficiently. This may underpin the adoption of reliability-driven methodologies such as response-based design, allowing EDF to further leverage on its modelling capability to challenge the technological solutions proposed. Valuable further work could also be sought in the extension of the utility's modelling capabilities to special and abnormal operating states of a FWT (towing, installation, control or grid fault, mooring failure, hull damage, etc.) in order to anticipate the spectrum of questions posed by the industrialisation of floating wind technology.

5.1.2 Further work

So far, floating wind turbine design has been largely based on the unharmonised combination of the historical know-hows of wind turbine engineering and ocean engineering. As the industry matures, the need for more integrated approaches is increasingly recognised. This translates into the need to deploy new design workflows based on a range of simulation tools of different complexity, applied to a truly representative set of dimensioning conditions. The following challenges can be anticipated:

- In presence of unlimited computing resources, the ideal coupled simulation would include high-fidelity representations of all the involved processes: along with flow-resolving aerodynamics and hydrodynamics, physically accurate structural and drive-train models should be present. Unfortunately, in most applications the allowable computational cost is subjected to limitations. Significant efforts will be then required to establish the best modelling choices (coupled vs uncoupled, time-domain vs frequency-domain, etc.) for each design task.
- In the above context, an overarching problem is the simulation length required to contain the statistical uncertainty inherent to offshore dynamic simulations, caused by the stochastic nature of the met-ocean loads. Due to low-frequency excitation and response, the minimum duration of a simulation in stationary conditions is typically in the order of a few hours. The applicability of high-end, computationally intensive modelling strategies (such as wake-resolving aerodynamics, standard in wind turbine design) is hence restricted and intelligent approximations must be established alongside. In particular, lightweight coupled simulation approaches will be highly valuable for tasks such as pre-design optimisation and reliability-based design, which demand large amounts of load cases to be computed.
- At the opposite end of model complexity, the establishment of robust high-fidelity methods can benefit early design through targeted uses, for instance for the calibration of simpler models. High-end tools may also permit to optimise the system's components at later stages. For instance, nonlinear and/or viscous CFD may be used surgically to reduce design uncertainty in presence of specific dimensioning issues.
- The drive-train is a design-governing component bringing in static and dynamic constraints. Its detailed mechanical simulation is however very demanding in terms of time step resolution; a direct coupling with stochastically excited system-level simulations may be impractical. Cascading procedures using weakly coupled, complementary approaches may be required to acquire a proper understanding of drive-train reliability whilst keeping the computational cost at bay. This may ultimately allow to optimise the system by removing unnecessary conservatism and/or reduce reliability uncertainty.

- Transient abnormal operating states are loosely defined by the existing design standards, and have only been investigated until recently. Due to their frequent occurrence, they can constitute an important source of damage and require to be predicted by adequate coupled modelling. Transients may entail broad-band excitation and set off critical response states (a basic example is the sudden loss of rotor thrust causing a surge swing-back from the offset position). Also, the selection of a suitable fault set will depend on the technology utilised, hence demanding adaptation following future innovation. An example using forthcoming technology is the occurrence of a turret swivel failure in a single-point moored turbine.
- Similar considerations may be drawn for extreme met-ocean events of short duration, such as rapid swings in the wind direction or freak waves. These often challenge the applicability of the available modelling approaches.
- Persistent abnormal states, such as the flooding of a hull compartment or the loss of a mooring line, are today poorly documented and should be made object of systematic analysis. Developing efficient ways to model these occurrences and combine them with the discretised met-ocean parameter space (and possibly with the structural reliability space) in a statistically representative fashion will require considerable work.
- Coupled physical modelling of floating wind systems has proven very challenging so far, as satisfying the Froude and Reynolds number similitudes simultaneously is desirable but impractical. Numerical simulation is currently being summoned for the development of hybrid software-in-the-loop procedures in an attempt to overcome this limitation.

These efforts should be aimed at relating mechanical simulations to the design criteria in a consistent way, potentially leading to the generation of new standards truly fit for the specificities of this novel application. Over time the best practices will eventually emerge, enabling engineers to better answer the industry's interrogatives concerning the operability and survivability of floating offshore wind turbines.

Appendix A

Nomenclature

A.1 Symbols in Part 2

$\bigtriangledown$	Hull volume
α	Angle of attack
β	Stokes parameter
γ	JONSWAP spectrum peak enhancement factor
ζ	Damping ratio
θ	Angle of wave incidence
ϑ	Leeward inclination angle
λ	Wavelength
ν	Kinematic viscosity
ρ_{a}	Air density
ρ_{w}	Water density
σ_x	Axial turbulence intensity
τ	Convolution time
ϕ	Random phase
ω	Angular frequency
ω_{e}	Excitation frequency
ω_{n}	Natural frequency
Δ	Platform displacement
Φ	Phase of excitation harmonic
Ψ	Amplitude of excitation harmonic
Ω	Rotor revolution speed
a	Upstream axial induction factor
a_{r}	Heave added mass coefficient
a'	Downstream axial induction factor
$\tilde{a}$	Wave amplitude

b_r	Heave radiation damping coefficient
c	Nondimensional coefficient (multiple are defined)
d	Upper surface draft of a plate or disc
d_p	Mean plate draft
f_h	Heave force per unit wave amplitude
g	Gravitational acceleration
k	Wave number
l	Length of a cylinder
m	Mass
p	Pressure
q	Column radius
r	Disc or plate radius
r_i	Response transfer function of the i^th degree of freedom
s	Plate submergence
$\tilde{s}$	Longitudinal streamtube coordinate
t	Time
t_p	Plate thickness
u	Motion-induced velocity
v	Flow velocity
$\bar{x}$	Coordinate of mean horizontal position
$\bar{y}$	Coordinate of mean horizontal position
A	Sectional area
A_w	Waterplane area
C_L	Lift coefficient
D	Cylinder diameter
F	Force magnitude
H	Incident wave height
I	Central moment of inertia
I_r	Axial inertia of a rotor
J	Transported moment of inertia
KC	Keulegan-Carpenter number
Q_r	Rotor torque
R	Rotor radius
Re	Reynolds number
S	Cross-sectional area

T	Wave period
T_{2P}	Period of 2P excitation
T_c	Length of convolution window
T_p	Pitch natural period
T_r	Rotor thrust
U	Flow speed
U_m	Maximum flow speed
V	Wind speed at actuator surface
$\mathbf{\Gamma}$	Rotational speed vector
$\mathbf{f}$	Generalised force vector
$\mathbf{i}$	Unit vector
$\mathbf{q}$	Gyroscopic moment vector
$\mathbf{x}$	Position vector
$\mathbf{A}$	Added mass coefficient tensor
$\mathbf{B}$	Radiation damping coefficient tensor
$\mathbf{K}$	Stiffness tensor
$\tilde{\mathbf{K}}$	Convolution kernel
$\mathbf{M}$	Mass tensor

A.2 Symbols in Part 3

$\bigtriangledown$	Line segment volume
α	HHT algorithm parameter
$\check{\alpha}$	Rayleigh damping coefficient
β	Newmark algorithm parameter
$\check{\beta}$	Rayleigh damping coefficient
γ	Newmark algorithm parameter
$\hat{\gamma}$	JONSWAP spectrum peak enhancement factor
δ	Horizontal displacement
ϵ	Strain
κ	Physical axial stiffness
κ_{c}	Axial stiffness of a CABLE element
λ	Wavelength
ξ	Normalised axial coordinate
ρ_{c}	Material density of a CABLE element
ρ_{m}	Physical material density
ρ_{w}	Water density
ϱ	Mass per unit length
σ	Contact stress
ω	Wave frequency
Ω	System state
c	Nondimensional coefficient (multiple are defined)
d	Contact clearance
f	Frequency
f_{A}	Buoyancy force
f_{W}	Weight force
g	Gravitational acceleration
g'	Corrected gravitational acceleration (1)
g''	Corrected gravitational acceleration (2)
h	Height of fairlead over the seabed
l	Length of finite element
l_{c}	Length of CABLE element
m_{a}	Added mass
r	Horizontal distance between anchor and fairlead
s	Mooring line scope

$\tilde{s}$	Longitudinal coordinate
t	Time
A	Sectional area
A_c	Sectional area of a CABLE element
D	Cylinder diameter
E	Physical Young's modulus
E_c	Numerical Young's modulus for tension
E_c^-	Numerical Young's modulus for compression
F	Drag force
F_x	Horizontal force on floater
F^h	Horizontal fairlead force
H	Water depth
H_s	Significant wave height
H_w	Wave height
I	Sectional moment of inertia
L	Length of mooring line
T	Line tension
T_p	Peak period
T_w	Wave period
T_F	Fairlead tension
$\mathbf{g}$	Generalised internal force vector
$\mathbf{i}$	Unit vector
$\mathbf{j}$	Unit vector
$\mathbf{k}$	Unit vector
$\mathbf{q}_\mathrm{e}$	Element displacement vector
$\mathbf{q}_\mathrm{n}$	Nodal displacement vector
$\mathbf{q}^\mathrm{P}$	Reaction force vector at point P
$\mathbf{u}$	Position vector
$\tilde{\mathbf{u}}$	Displacement vector
$\mathbf{v}$	Absolute flow velocity vector
$\mathbf{w}$	Relative flow velocity vector
$\mathbf{A}$	Punctual added mass coefficient tensor
$\mathbf{B}$	Punctual radiation damping coefficient tensor
$\check{\mathbf{C}}$	Damping tensor of mooring lines
$\mathbf{E}$	Error tensor

$\mathbf{K}$	Punctual stiffness tensor
$\check{\mathbf{K}}$	Stiffness tensor of mooring lines
$\mathbf{L}$	Shape function matrix
$\mathbf{M}$	Punctual mass tensor
$\check{\mathbf{M}}$	Mass tensor of mooring lines

A.3 Symbols in Part 4

α	Airfoil pitch degree of freedom
α_{ij}	Component of transformation matrix
α_{r}	Airfoil angle of attack
γ	Geometric angle
θ	Geometric angle
κ	Reduced frequency
λ	Complex eigenvalue
μ	Mass per unit length
ν	Kinematic viscosity
ξ	Damping ratio
ρ	Air density
ρ_{m}	Material density
ρ_s	Chord-wise material density of an airfoil
ω	Natural frequency
$\tilde{\omega}$	Rotational speed component
Ω	Rotor revolution speed
b	Half chord length
c	Chord length
e	Normalised eccentricity of lift centre
f^*	Normalised modal frequency
h	Airfoil plunge degree of freedom
k	Stiffness coefficient
l	Finite element length
l_{b}	Beam length
m	Airfoil mass
q	Stagnation point pressure
r	Blade radius
r_α	Normalised radius of gyration
r_{e}	Aerodynamic element radius
r_{g}	Radius of gyration
s	Longitudinal coordinate (along beam axis or airfoil chord)
t	Time
t_{a}	Airfoil thickness
w	Transverse displacement of airfoil chord

$\tilde{x}_{\mathrm{E}}$	Distance of elastic centre from the leading edge
A	Cross-sectional area
C	Theodorsen operator
C_L	Lift coefficient
$C_{L\alpha}$	Initial slope of lift coefficient curve
E	Young's modulus
F	Pre-tension force
G	Shear modulus
I	Second sectional moment of inertia
L	Lift force
M	Moment of lift force
M	Mach number
Re	Reynolds number
S	First sectional moment of inertia
T^*	Kinetic energy
U	Airspeed
U^*	Strain energy
$\tilde{V}$	Speed of sound
$\mathbf{a}$	Airfoil pitch and plunge displacement vector
$\tilde{\mathbf{f}}$	External force vector
$\mathbf{p}$	Position vector in the inertial frame
$\mathbf{q}$	Displacement vector in the rotating frame
$\mathbf{q}_e$	Nodal coordinates of beam element e in the local frame
$\mathbf{q}_{\mathrm{s}}$	Steady-state displacement vector in the rotating frame
$\mathbf{q}_{\mathrm{t}}$	Nodal coordinates in the rotating frame
$\hat{\mathbf{q}}$	System eigenvector
$\mathbf{r}$	Position vector in the rotating frame
$\hat{\mathbf{r}}$	System eigenvector
$\mathbf{u}$	Displacement vector in the local frame
$\bar{\mathbf{u}}$	Displacement vector in the rotating frame
$\mathbf{\Lambda}$	Aerodynamic operator
$\underline{\mathbf{\Lambda}}$	Per unit span aerodynamic operator
$\mathbf{\Omega}$	Spinning matrix
$\mathbf{A}$	Inertia tensor of a dynamic system
$\mathbf{B}$	Damping tensor of a dynamic system

$\mathbf{C}$	Stiffness tensor of a dynamic system
$\mathbf{D}_\mathrm{a}$	Aerodynamic damping tensor
$\underline{\mathbf{D}}_\mathrm{a}$	Per unit span aerodynamic damping tensor
$\mathbf{E}$	Quadratic eigenproblem partial tensor
$\mathbf{F}$	Quadratic eigenproblem partial tensor
$\mathbf{G}$	Coriolis tensor
$\mathbf{K}$	Stiffness tensor
$\mathbf{K}_\Omega$	Spin-softening tensor
$\mathbf{K}_\mathrm{a}$	Aerodynamic stiffness tensor
$\mathbf{K}_\mathrm{e}$	Elastic stiffness tensor
$\mathbf{K}_\mathrm{g}$	Geometric stiffness tensor
$\underline{\mathbf{K}}$	Per unit span stiffness tensor
$\underline{\mathbf{K}}_\mathrm{a}$	Per unit span aerodynamic stiffness tensor
$\mathbf{M}$	Mass tensor
$\mathbf{M}_\mathrm{a}$	Aerodynamic added mass tensor
$\underline{\mathbf{M}}$	Per unit span mass tensor
$\underline{\mathbf{M}}_\mathrm{a}$	Per unit span aerodynamic added mass tensor
$\mathbf{N}$	Shape function matrix
$\mathbf{Q}$	Quadratic eigenproblem tensor
$\mathbf{R}$	Rotation (transformation) matrix

Appendix B

The Newmark Integration Scheme

Here is presented the Newmark implicit time integration scheme used to discretise Equations 2.1 and D.8 in the time domain. Given a set of system parameters $\mathbf{v}$, which are supposed known at time t, the Newmark scheme enables to develop the system's kinematic state after a finite increment of time, Δt, with [199]

$$\mathbf{v}(t+\Delta t) \approx \mathbf{v}(t) + \Delta t\, \dot{\mathbf{v}}(t) + \frac{\Delta t^2}{2}\left[(1-2\beta)\ddot{\mathbf{v}}(t) + 2\beta\ddot{\mathbf{v}}(t+\Delta t)\right], \tag{B.1}$$

$$\dot{\mathbf{v}}(t+\Delta t) \approx \dot{\mathbf{v}}(t) + \Delta t\left[(1-\gamma)\ddot{\mathbf{v}}(t) + \gamma\ddot{\mathbf{v}}(t+\Delta t)\right], \tag{B.2}$$

which is the so-called A-form, expressing the parameters (displacements) and their first time derivative (speed) with respect to their second derivative (acceleration). The square-bracketed terms can be seen as weighted averages of $\ddot{\mathbf{v}}(t)$ and $\ddot{\mathbf{v}}(t+\Delta t)$, where the weights are dictated by the selection of the Newmark parameters β and γ. Expliciting $\ddot{\mathbf{v}}(t+\Delta t)$ in B.1 yields

$$\ddot{\mathbf{v}}(t+\Delta t) \approx \frac{1}{\beta\Delta t^2}\left[\mathbf{v}(t+\Delta t) - \mathbf{v}(t)\right] - \frac{1}{\beta\Delta t}\dot{\mathbf{v}}(t) + \frac{2\beta-1}{2\beta}\ddot{\mathbf{v}}(t)\,, \tag{B.3}$$

which, when injected in B.2, provides

$$\dot{\mathbf{v}}(t+\Delta t) \approx \frac{\gamma}{\beta\Delta t}\left[\mathbf{v}(t+\Delta t) - \mathbf{v}(t)\right] + \frac{\beta-\gamma}{\beta}\dot{\mathbf{v}}(t) + \frac{(2\beta-\gamma)\Delta t}{2\beta}\ddot{\mathbf{v}}(t)\,. \tag{B.4}$$

Equations B.3 and B.4 represent the Newmark prediction in D-form, that expresses the speed and acceleration with respect to the system's displacement.

Appendix C

Quasi-linearity of Aerodynamic Damping

As pointed out in 2.3.3.3, the nearly constant value of the aggregate aerodynamic damping ratio ζ characterising the free pitch oscillations of a floating VAWT in a given operating condition is a manifestation of the damping force linearity. In the model all aerodynamic forces acting on the blades are computed with the lift and drag formulation; although both of these quantities are a quadratic function of the airspeed, they become essentially linear with respect to its perturbations as explained next.
The magnitude of the drag force exerted on an object in presence of an unperturbed, constant airflow of speed U can be written in the following general form, assumed that the object oscillates with instantaneous velocity $\dot{x}$ in the same direction as U:

$$D = \frac{1}{2}\rho A C_D \left(U - \dot{x}\right)^2 = \frac{1}{2}\rho A C_D \left(U^2 + \dot{x}^2 - 2U\dot{x}\right) . \tag{C.1}$$

It is hence possible to express the instantaneous damping coefficient of motion in the x direction from Equation C.1 with

$$-\frac{\partial D}{\partial \dot{x}} = \rho A C_D \left(U - \dot{x}\right) \approx \rho A C_D U . \tag{C.2}$$

It can be calculated that at most rotor stations the local velocity $\dot{x}$ induced by pitch oscillations (at the natural period T_p, with an amplitude of a few degrees) is at least one order of magnitude smaller than U, given that U is in the order of 10 m/s. This justifies the approximation in Equation C.2. It is found that the dominant component of the drag-induced damping coefficient is $\dot{x}$-independent, implying linearity of drag damping for large enough values of $U/\dot{x}$.
At the dead upwind blade passage (Figure C.1), within the region where large part of the aerodynamic forcing is generally produced, the quasi-steady lift force arising on a blade element oscillating with instantaneous speed $\dot{x}$ in the direction of the incident

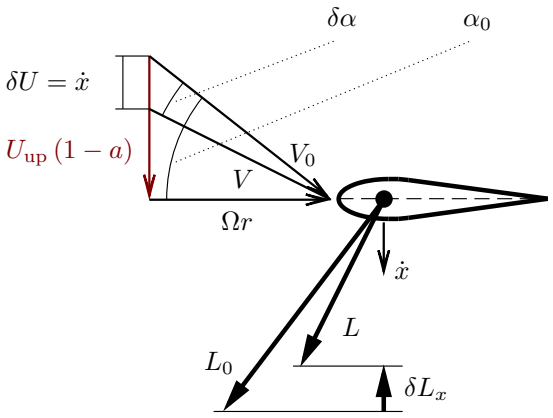

Figure C.1: Snapshot of lift-induced damping mechanism at the upwind blade passage.

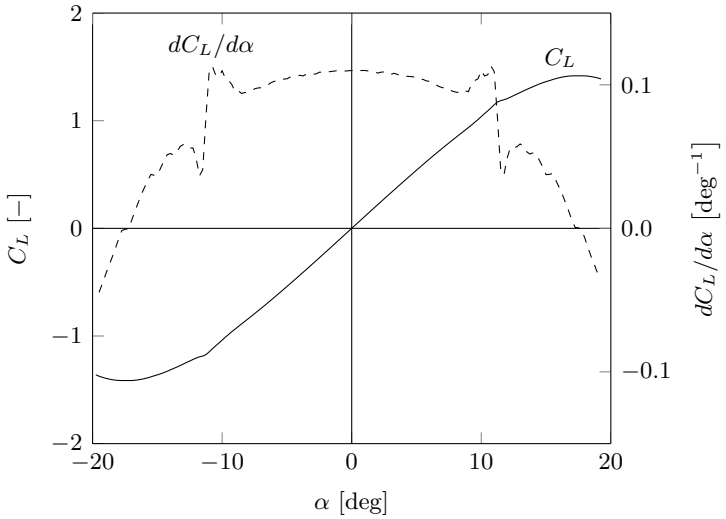

Figure C.2: Lift coefficient characteristic of a NACA 0018 airfoil at high Reynolds as computed by XFOIL [243], with its first derivative.

wind can be written as

$$L = \frac{1}{2}\rho A \left.\frac{dC_L}{d\alpha}\right|_{\alpha=0} \arctan\left[\frac{U_{\mathrm{up}}\,(1-a)-\dot{x}}{\Omega r}\right]\left\{\left[U_{\mathrm{up}}\,(1-a)-\dot{x}\right]^2+\Omega^2 r^2\right\}, \tag{C.3}$$

where a is the local axial induction factor and r the blade element radius. A linear $C_L\,(\alpha)$ relationship is assumed; in practice, as shown in Figure C.2, for a NACA 0018 profile this approximation is accurate for $\alpha \in [-10, 10]\,\mathrm{deg}$. By considering that this limitation translates into $\left[U_{\mathrm{up}}\,(1-a)-\dot{x}\right]/\Omega r \lessapprox 0.2$, and by introducing the small angle approximation, the lift force can be re-expressed with

$$L \approx \frac{1}{2}\rho A \left.\frac{dC_L}{d\alpha}\right|_{\alpha=0} \left[U_{\mathrm{up}}\,(1-a)-\dot{x}\right]\Omega r\,. \tag{C.4}$$

Assuming $L_x \approx L$, where L_x is the component of the lift force that is aligned with the airfoil oscillation, which holds for small angles of attack, allows to write an approximated expression of the instantaneous lift-induced damping coefficient in the x direction:

$$-\frac{\partial L_x}{\partial \dot{x}} \approx \frac{1}{2}\rho A \left.\frac{dC_L}{d\alpha}\right|_{\alpha=0} \Omega r\,. \tag{C.5}$$

It can be noted that the above coefficient is proportional to the rotor speed. Another way to look at this mechanism is focussing on the δL_x lift component generated by the airspeed perturbation shown in Figure C.1: in the absence of blade oscillations, the combination of the relative airspeed components due to the element's tangential speed Ωr and to the transverse wind speed $U_{\text{up}}\,(1-a)$ forms the local incident airspeed vector V_0. An oscillation-induced velocity perturbation, $\dot{x}$, causes it to be redefined as V, a vector with different magnitude and, most importantly, different angle of attack over the profile, $\alpha = \alpha_0 - \delta\alpha$. This causes a change in lift force which gives rise to an extra component δL_x that is opposed to $\dot{x}$ for small angles of attack.
The key information emerging from the damping coefficient examples of Equations C.2 and C.5 is that i) lift and drag forces apply approximately linear damping in the x direction at the upwind (and downwind) blade passage and ii) the drag-induced damping coefficient is proportional to U whilst the lift-induced coefficient is proportional to Ω.

Appendix D

Nonlinear Solvers in Code_Aster

Two nonlinear solver routines available in *Code_Aster* are used in the present study to find the static and dynamic equilibrium configurations of mooring systems, which are respectively denoted static and dynamic solver. The present Appendix provides some insights on their working principles in the mooring simulation context: 1D elements undergoing large displacements in presence of contact and follower loads.

D.1 Nonlinear static solver

The static equilibrium configuration of a structure with nonlinear behaviour can be computed within *Code_Aster* using an iterative routine [244]. A pseudo-time discretisation can be used to parametrise the problem, and most notably to compute equilibrium states which are far removed from the input configuration by gradually incrementing the load.

Problem formulation

By imposing static equilibrium and a set of classic bilateral boundary conditions, the nonlinear quasi-static problem can be written in the global frame as [245]:

$$\begin{cases} \mathbf{g}(\mathbf{u},t) + \mathbf{B}^{\mathrm{T}}\boldsymbol{\lambda} = \mathbf{f}(t) \\ \mathbf{B}\mathbf{u} = \mathbf{h}(t) \end{cases} , \tag{D.1}$$

where $\mathbf{g}$ and $\mathbf{f}$ denote the generalised internal and external force vectors. Note that in linear mechanics one has $\mathbf{g}(\mathbf{u},t) = \mathbf{K}\mathbf{u}$, with $\mathbf{K}$ representing the stiffness matrix of the system. Vector $\mathbf{u}$ contains the displacements (expressed as an increment from the latest reference configuration in case UL is used). The linear operator $\mathbf{B}$ is the boundary condition matrix, $\mathbf{h}$ contains the Dirichlet boundary condition functions, and $\boldsymbol{\lambda}$ the associated Lagrange multipliers (in physical terms, $\mathbf{B}^{\mathrm{T}}\boldsymbol{\lambda}$ represents the opposite of the nodal reaction forces). The problem unknowns are $(\mathbf{u}, \boldsymbol{\lambda})$ and the system is parametrised through the use of the pseudo-time variable t.

When the unilateral contact conditions presented in 3.2.3 are introduced, the quasi-static problem becomes constrained and is written in the form [199]:

$$\begin{cases} \mathbf{g}(\mathbf{u},t) + \mathbf{B}^{\mathrm{T}}\boldsymbol{\lambda} + \mathbf{A}^{\mathrm{T}}\boldsymbol{\mu} = \mathbf{f}(t) \\ \mathbf{B}\mathbf{u} = \mathbf{h}(t) \\ \mathbf{A}\mathbf{u} \leq \mathbf{d} \\ (\mathbf{A}\mathbf{u} - \mathbf{d}) \odot \boldsymbol{\mu} = \mathbf{0} \\ \boldsymbol{\mu} \geq \mathbf{0} \end{cases} . \tag{D.2}$$

In the above expression $\odot$ denotes component-wise multiplication. The additional terms define the Hertz-Signorini-Moreau contact laws via $\mathbf{A}$, the unilateral condition matrix, and the contact distance vector $\mathbf{d}$. Now the unknowns have become $(\mathbf{u}, \boldsymbol{\lambda}, \boldsymbol{\mu}) = \mathbf{v}$, where $\boldsymbol{\lambda}$ and $\boldsymbol{\mu}$ are called the KKT (Karush-Kuhn-Tucker) multipliers.

Pseudo-time discretisation and resolution

By using a notation of the type $\mathbf{x}(\mathbf{u}, t_i) = \mathbf{x}_i$, writing System D.2 at t_i yields

$$\begin{cases} \mathbf{g}_i + \mathbf{B}^{\mathrm{T}}\boldsymbol{\lambda} + \mathbf{A}^{\mathrm{T}}\boldsymbol{\mu} = \mathbf{f}_i \\ \mathbf{B}\mathbf{u} = \mathbf{h}_i \\ \mathbf{A}\mathbf{u} \leq \mathbf{d} \\ (\mathbf{A}\mathbf{u} - \mathbf{d}) \odot \boldsymbol{\mu} = \mathbf{0} \\ \boldsymbol{\mu} \geq \mathbf{0} \end{cases} . \tag{D.3}$$

Resolving the system corresponds to finding the root of the residual expressed by

$$\mathbf{r}_i(\mathbf{v}, t_i) = \begin{bmatrix} \mathbf{g}_i + \mathbf{B}^{\mathrm{T}}\boldsymbol{\lambda} + \mathbf{A}^{\mathrm{T}}\boldsymbol{\mu} - \mathbf{f}_i \\ \mathbf{B}\mathbf{u} - \mathbf{h}_i \\ (\mathbf{A}\mathbf{u} - \mathbf{d}) \odot \boldsymbol{\mu} \end{bmatrix} \tag{D.4}$$

under the given constraints. The root of the residual is typically found iteratively using an algorithm of the Newton family. Among the options available in *Code_Aster*, the classic Newton-Raphson method is retained to remain consistent with the UL approach[1]. Given that the state Ω_{i-1} of the system at the previous pseudo-time instant, t_{i-1}, is known and set as the zero-displacement reference, the present goal of this algorithm is finding a new deformed state Ω_i which zeroes the residual for the loading and boundary conditions found at t_i. This is achieved by constructing a sequence of vectors $\mathbf{v}^n$ which converge toward the sought root when applied to the continuously

[1] Quasi-Newton methods do not recompute the tangent matrix at the intra-step iterations.

actualised geometry. At each Newton-Raphson iteration n, the system's tangent matrix (the Jacobian of the residual) is calculated using the previous iteration's configuration as

$$\mathbf{J}_i^{n-1} = \frac{\partial \mathbf{r}_i^{n-1}}{\partial \mathbf{v}}\,, \tag{D.5}$$

and used to predict the unknowns with

$$\mathbf{v}^n = -(\mathbf{J}_i^{n-1})^{-1}\mathbf{r}_i^{n-1}\,. \tag{D.6}$$

Note that the UL approach prescribes that the new reference geometry found by applying $\mathbf{v}^n$ be used as the new zero-displacement geometry for the next Newton-Raphson iteration. This, in combination with the carryover of the internal variables, defines the new reference state Ω_i^n, and by consequence the internal force vector $\mathbf{g}_i^n$. More detailed information about the mathematical procedures used in *Code_Aster* to update the system state in presence of large displacements and rotations is available in Fléjou [246].

The above procedure is repeated until convergence as shown in Figure D.1, that is when the norm of the residual falls below an arbitrary threshold. Here it is chosen to use the default relative residual criterion, which is defined with

$$r_i^n = \frac{\|\mathbf{r}_i^n\|_\infty}{\|\mathbf{f}_i - \mathbf{B}^{\mathrm{T}}\boldsymbol{\lambda}_i^n - \mathbf{A}^{\mathrm{T}}\boldsymbol{\mu}\|_\infty} \leq \eta\,, \tag{D.7}$$

where $\|\ \|_\infty$ represents the maximum norm and η the relative precision (which assumes a default value of 10^{-6}). Once Inequation D.7 is satisfied at the end of the Newton-Raphson iteration, *Code_Aster* stores the converged equilibrium state for pseudo-time t_i, Ω_i, and moves on to the computing the next. (I omitted the "Euler" prediction phase!)

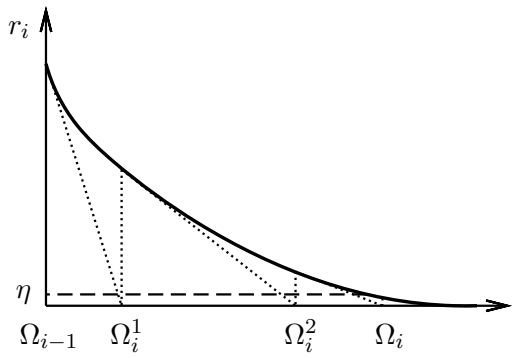

Figure D.1: Newton-Raphson algorithm iterations within a pseudo-time step i.

D.2 Nonlinear dynamic solver

Nonlinear structure dynamics can be explicitly represented in *Code_Aster* in the time domain [247] using a function closely related to the quasi-static solver described in D.1. Its underlying formulation is detailed next.

Problem formulation

Given the unknowns $\mathbf{v} = (\mathbf{u}, \boldsymbol{\lambda}, \boldsymbol{\mu})$, the dynamic equilibrium problem consists in finding a parameter evolution $\mathbf{v}(t)$ which satisfies [199]

$$\begin{cases} \mathbf{w}(\mathbf{u}, \dot{\mathbf{u}}, \ddot{\mathbf{u}}) + \mathbf{g}(\mathbf{u}, \dot{\mathbf{u}}, t) + \mathbf{C}\dot{\mathbf{u}} + \mathbf{B}^{\mathrm{T}}\boldsymbol{\lambda} + \mathbf{A}^{\mathrm{T}}\boldsymbol{\mu} = \mathbf{f}(\mathbf{u}, \dot{\mathbf{u}}, t) \\ \mathbf{B}\mathbf{u} = \mathbf{h}(t) \\ \mathbf{A}\mathbf{u} \leq \mathbf{d} \\ (\mathbf{A}\mathbf{u} - \mathbf{d}) \odot \boldsymbol{\mu} = \mathbf{0} \\ \boldsymbol{\mu} \geq \mathbf{0} \end{cases}, \tag{D.8}$$

where the same nomenclature of System D.2 is adopted. The introduction of dependencies from the first and second time derivatives of the displacement vector define the set of Equations D.8 as a system of second-order differential equations. Compared to the static equilibrium case, new terms contribute in the definition of equilibrium, namely $\mathbf{w}$, the inertial force vector, and the linear damping force vector $\mathbf{C}\dot{\mathbf{u}}$. Note that $\mathbf{w}$ depends from displacement and speed, and not only from acceleration, in case finite rotations are considered; in fact one may decompose it with

$$\mathbf{w}(\mathbf{u}, \dot{\mathbf{u}}, \ddot{\mathbf{u}}) = \mathbf{M}\ddot{\mathbf{u}} + \mathbf{w}^{\mathrm{LR}}(\mathbf{u}, \dot{\mathbf{u}}, \ddot{\mathbf{u}}) \,, \tag{D.9}$$

with $\mathbf{M}$ representing the system mass matrix and $\mathbf{w}^{\mathrm{LR}}$ a large rotations correction term. Additionally, it should be remarked that dynamic mooring simulations require the inclusion of hydrodynamic loads in the RHS term, which are of the follower type[2] and cause its dependency from $\mathbf{u}$ and $\dot{\mathbf{u}}$.

[2] A follower load depends from the structure's displacement.

Time discretisation and resolution

Assuming that the state of the system is known at $t = t_{i-1}$, the equilibrium at i is to be found after a finite increase in time Δt such as $t_i = t_{i-1} + \Delta t$. By using a notation of the type $\mathbf{x}(\mathbf{u}, t_i) = \mathbf{x}_i$, and considering Equation D.9, writing System D.8 at t_i gives

$$\begin{cases} \mathbf{M}\ddot{\mathbf{u}} + \mathbf{w}_i^{\mathrm{LR}} + \mathbf{g}_i + \mathbf{C}\dot{\mathbf{u}} + \mathbf{B}^{\mathrm{T}}\boldsymbol{\lambda} + \mathbf{A}^{\mathrm{T}}\boldsymbol{\mu} = \mathbf{f}_i \\ \mathbf{B}\mathbf{u} = \mathbf{h}_i \\ \mathbf{A}\mathbf{u} \leq \mathbf{d} \\ (\mathbf{A}\mathbf{u} - \mathbf{d}) \odot \boldsymbol{\mu} = \mathbf{0} \\ \boldsymbol{\mu} \geq \mathbf{0} \end{cases} . \tag{D.10}$$

The D-form Newmark equations (see Appendix B) intervene at this point to express the acceleration and speed which have been explicited in Equation D.10 in terms of the unknown displacement vector $\mathbf{u} = \mathbf{u}(t_i)$ and the known variables from the last time stamp. The terms in $\mathbf{u}_{i-1} = \mathbf{u}(t_{i-1})$, $\dot{\mathbf{u}}_{i-1}$, and $\ddot{\mathbf{u}}_{i-1}$ are then moved to the right-hand side of the equilibrium formulation of Equation D.10:

$$\begin{cases} \hat{\mathbf{K}}\mathbf{u} + \mathbf{w}_i^{\mathrm{LR}} + \mathbf{g}_i + \mathbf{B}^{\mathrm{T}}\boldsymbol{\lambda} + \mathbf{A}^{\mathrm{T}}\boldsymbol{\mu} = \hat{\mathbf{f}}_i \\ \mathbf{B}\mathbf{u} = \mathbf{h}_i \\ \mathbf{A}\mathbf{u} \leq \mathbf{d} \\ (\mathbf{A}\mathbf{u} - \mathbf{d}) \odot \boldsymbol{\mu} = \mathbf{0} \\ \boldsymbol{\mu} \geq \mathbf{0} \end{cases} , \tag{D.11}$$

where

$$\hat{\mathbf{K}} = \frac{1}{\beta \Delta t^2}\mathbf{M} + \frac{\gamma}{\beta \Delta t}\mathbf{C} , \tag{D.12}$$

$$\hat{\mathbf{f}}_i = \mathbf{f}_i + \frac{1}{\beta \Delta t^2}\mathbf{M}\left[\mathbf{u}_{i-1} + \Delta t\, \dot{\mathbf{u}}_{i-1} + \Delta t^2 \left(\frac{1-2\beta}{2}\right) \ddot{\mathbf{u}}_{i-1}\right] + \\ + \frac{1}{\beta \Delta t}\mathbf{C}\left[\gamma \mathbf{u}_{i-1} + \Delta t(\gamma - \beta)\dot{\mathbf{u}}_{i-1} + \Delta t^2 \left(\frac{\gamma - 2\beta}{2}\right) \ddot{\mathbf{u}}_{i-1}\right] . \tag{D.13}$$

The system of Equations D.11 is nonlinear because of the presence of terms $\mathbf{w}_i^{\mathrm{LR}}$, $\mathbf{g}_i$, and $\mathbf{f}_i$. From here, it is possible to resolve it iteratively for each time step: a Newton-Raphson root-finding algorithm is hence used, which is equivalent to what presented in D.1. Further details about the implementation of the above in *Code_Aster* are available in documentation by Greffet [199].

Appendix E

Calculation of Centrifugal Loading on a Beam

The matrices enabling the representation of apparent and centrifugal force effects within a structure in a corrotating frame are calculated in Part 4 for a beam element. This is organised upon the assumption that the rotor undergoes small steady-state structural deformations under the action of centrifugal loads. In this case it is possible to calculate the terms of the elementary Coriolis and Softening matrices $\mathbf{G}_{\mathrm{e}}$ and $\mathbf{K}_{\Omega\mathrm{e}}$ a priori, that is before centrifugal loading is applied to the structure. These terms incorporate dependencies from the mass and geometry characteristics of the beams, as well as from the element's orientation in space.

It is more complex to evaluate the terms of the geometric stiffness elementary matrix of a beam, $\mathbf{K}_{\mathrm{ge}}$, because of their dependency from the steady-state axial force arising inside the beam under centrifugal loading, $F(s)$. For a generic hyperstatic frame, this force depends in turn on the deformed state of the whole structure, even under a small displacement assumption, thus requiring the resolution of the static elastic problem. The associated implementation can be broken down into four steps:

a) Calculation of the distributed centrifugal loading for each beam and its repartition on the beam nodes.
b) Assembly of the elementary nodal forces into a global centrifugal loading vector expressed in the global frame.
c) Resolution of the static elastic problem with the application of the above force system.
d) Recovery of the internal axial force for each element, for use in the calculation of $\mathbf{K}_{\mathrm{ge}}$ with Equation 4.19.

Whilst the functions fit for carrying out steps b) and c) were readily available in the existing FE environment, steps a) and d) required fresh implementation. The procedure developed for step a) is detailed next, whilst a description of the computations required by step d) is provided in Leung and Fung [226]. Note that for a structure undergoing linear elastic deformations, the outputs of this procedure are proportional to the rotational speed squared.

Equivalent centrifugal loads on a beam element

The notation defining the local beam SoR, xyz, and the global corrotating frame, $\bar{x}\bar{y}\bar{z}$, is adopted here consistently with Part 4. The latter is assumed to be revolving at constant speed around the Y axis of the global inertial frame, that is coincident with $\bar{y}$. The per unit length centrifugal force acting on a generic beam section of centre P can be written in $\bar{x}\bar{y}\bar{z}$ as:

$$\mathbf{f}^{\mathrm{P}} = \rho A \boldsymbol{\Omega}^2 \mathbf{v}^{\mathrm{P}} \,, \tag{E.1}$$

where ρ denotes material density and A the sectional area, two parameters which are assumed to be homogeneous along the element. Here $\boldsymbol{\Omega}$ represents the spinning matrix as defined in Part 4 and $\mathbf{v}^{\mathrm{P}}$ the position vector of P in $\bar{x}\bar{y}\bar{z}$. This force is exerted radially, as visible in Figure E.1, showing a beam of arbitrary orientation in 3D space. In the figure r represents the spin radius, that is the point's distance from the spinning axis, and f the magnitude of the per unit length centrifugal force as defined in Equation E.1. A simplification is here adopted in writing the distributed load in function of the position along the beam span, allowing a linearisation of the components of the per unit length force vector: the orientation of $\mathbf{f}^{\mathrm{P}}$ is assumed coincident with that of $\mathbf{f}^{\mathrm{C}}$, which is the force exerted on the beam's centre C. This representation is shown in Figure E.2. The force magnitudes correspond to those of Figure E.1. Equation E.1 may then be rewritten as

$$\begin{aligned} \mathbf{f}^{\mathrm{P}} &\simeq \rho A \mathbf{s}^{\mathrm{C}} \frac{|\mathbf{s}^{\mathrm{P}}|}{|\mathbf{s}^{\mathrm{C}}|} \,, \\ \mathbf{s}^{\mathrm{P}} &= \boldsymbol{\Lambda}^2 \mathbf{v}^{\mathrm{P}} \,, \\ \mathbf{s}^{\mathrm{C}} &= \boldsymbol{\Lambda}^2 \mathbf{v}^{\mathrm{C}} \,. \end{aligned} \tag{E.2}$$

Note that $|\mathbf{s}^{\mathrm{P}}| = \Omega^2 r^{\mathrm{P}}$, $|\mathbf{s}^{\mathrm{C}}| = \Omega^2 r^{\mathrm{C}}$, where Ω is the scalar value of the rotational speed. It is clear that the approximation's accuracy deteriorates for beams spanning tangentially featuring a large length-to-radius ratio.

For a beam of length l, this simplification allows to write the vector force acting on the

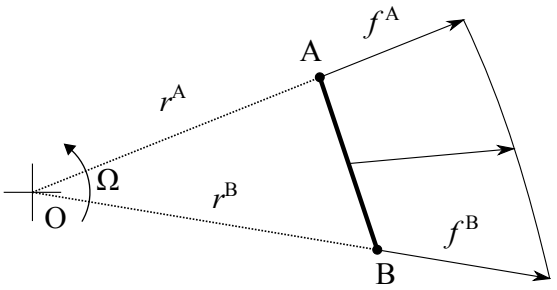

Figure E.1: Projected view of centrifugal forces acting on beam in 3D space. The spinning axis is orthogonal to the drawing plane.

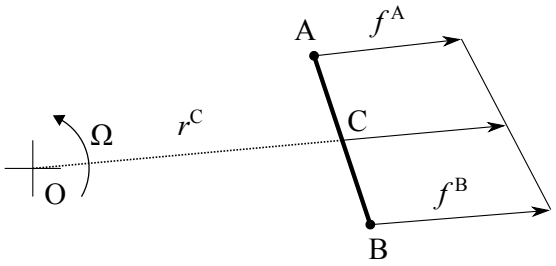

Figure E.2: Projected view of approximated centrifugal forces acting on beam in 3D space. The spinning axis is orthogonal to the drawing plane.

beam in the global SoR as

$$\mathbf{f}(\xi) = \begin{bmatrix} \xi\ \left(f_1^{\mathrm{B}} - f_1^{\mathrm{A}}\right) + f_1^{\mathrm{A}} \\ \xi\ \left(f_2^{\mathrm{B}} - f_2^{\mathrm{A}}\right) + f_2^{\mathrm{A}} \\ \xi\ \left(f_3^{\mathrm{B}} - f_3^{\mathrm{A}}\right) + f_3^{\mathrm{A}} \end{bmatrix}, \tag{E.3}$$

where $\xi = \frac{x}{l}$, $\xi = 0$ at node A and $\xi = 1$ at node B, $\xi \in [0, 1]$. The subscript index indicates the vector's components in the global corrotating frame, as in $\mathbf{f}^{\mathrm{A}} = \begin{pmatrix} f_1^{\mathrm{A}} & f_2^{\mathrm{A}} & f_3^{\mathrm{A}} \end{pmatrix}^{\mathrm{T}}$.
In order to express these loads in the beam's local system of reference, the corresponding basis change matrix $\mathbf{R}$ is required. This is defined using the unit vectors identifying the beam's local frame in the global frame, as done with Equation 4.6. The transformation permitting to express $\tilde{\mathbf{f}}$, the centrifugal force in the local frame, is hence written for any point P as

$$\tilde{\mathbf{f}}^{\mathrm{P}} = \mathbf{R}\mathbf{f}^{\mathrm{P}}. \tag{E.4}$$

By formulating Equation E.4 at node points A and B through Equation E.2, we obtain $\tilde{\mathbf{f}}^{\mathrm{A}}$ and $\tilde{\mathbf{f}}^{\mathrm{B}}$, the elements necessary to express the local centrifugal force in function of ξ:

$$\tilde{\mathbf{f}}(\xi) = \mathbf{R}\mathbf{f}(\xi) = \begin{bmatrix} \xi\ \left(\tilde{f}_1^{\mathrm{B}} - \tilde{f}_1^{\mathrm{A}}\right) + \tilde{f}_1^{\mathrm{A}} \\ \xi\ \left(\tilde{f}_2^{\mathrm{B}} - \tilde{f}_2^{\mathrm{A}}\right) + \tilde{f}_2^{\mathrm{A}} \\ \xi\ \left(\tilde{f}_3^{\mathrm{B}} - \tilde{f}_3^{\mathrm{A}}\right) + \tilde{f}_3^{\mathrm{A}} \end{bmatrix}. \tag{E.5}$$

Following the assumptions of Leung and Fung [226] (uncoupled torsion), the nodal degrees of freedom affected by the distributed centrifugal load $\tilde{\mathbf{f}}(\xi)$ reduce to 10 from a total of 12. By assuming the Euler-Bernoulli beam shape functions for tension and

bending

$$\mathbf{N} = \begin{bmatrix} 1-\xi & 0 & 0 \\ \xi & 0 & 0 \\ 0 & 2\,\xi^3 - 3\,\xi^2 + 1 & 0 \\ 0 & \xi\,\left(\xi^2 - 2\,\xi + 1\right)\,l & 0 \\ 0 & 3\,\xi^2 - 2\,\xi^3 & 0 \\ 0 & \left(\xi^3 - \xi^2\right)\,l & 0 \\ 0 & 0 & 2\,\xi^3 - 3\,\xi^2 + 1 \\ 0 & 0 & -\xi\,\left(\xi^2 - 2\,\xi + 1\right)\,l \\ 0 & 0 & 3\,\xi^2 - 2\,\xi^3 \\ 0 & 0 & \left(\xi^2 - \xi^3\right)\,l \end{bmatrix}, \tag{E.6}$$

the equivalent load applied at the nodes (i.e. the generalised external forces applied in A and B doing the same work as the distributed load on the beam) is expressed by components in xyz using Equations E.5 and E.6, as follows:

$$\tilde{\mathbf{g}} = l\int_0^1 \mathbf{N}\tilde{\mathbf{f}}(\xi)d\xi = \begin{bmatrix} \frac{\left(\tilde{f}_1^{\mathrm{B}}+2\,\tilde{f}_1^{\mathrm{A}}\right)l}{6} \\ \frac{\left(2\,\tilde{f}_1^{\mathrm{B}}+\tilde{f}_1^{\mathrm{A}}\right)l}{6} \\ \frac{\left(3\,\tilde{f}_2^{\mathrm{B}}+7\,\tilde{f}_2^{\mathrm{A}}\right)l}{20} \\ \frac{\left(2\,\tilde{f}_2^{\mathrm{B}}+3\,\tilde{f}_2^{\mathrm{A}}\right)l^2}{60} \\ \frac{\left(7\,\tilde{f}_2^{\mathrm{B}}+3\,\tilde{f}_2^{\mathrm{A}}\right)l}{20} \\ -\frac{\left(3\,\tilde{f}_2^{\mathrm{B}}+2\,\tilde{f}_2^{\mathrm{A}}\right)l^2}{60} \\ \frac{\left(3\,\tilde{f}_3^{\mathrm{B}}+7\,\tilde{f}_3^{\mathrm{A}}\right)l}{20} \\ -\frac{\left(2\,\tilde{f}_3^{\mathrm{B}}+3\,\tilde{f}_3^{\mathrm{A}}\right)l^2}{60} \\ \frac{\left(7\,\tilde{f}_3^{\mathrm{B}}+3\,\tilde{f}_3^{\mathrm{A}}\right)l}{20} \\ \frac{\left(3\,\tilde{f}_3^{\mathrm{B}}+2\,\tilde{f}_3^{\mathrm{A}}\right)l^2}{60} \end{bmatrix}. \tag{E.7}$$

By denoting the equivalent forces to be applied on nodes A and B respectively $\tilde{\mathbf{p}}^{\mathrm{A}}$ and $\tilde{\mathbf{p}}^{\mathrm{B}}$, and the equivalent moments $\tilde{\mathbf{m}}^{\mathrm{A}}$ and $\tilde{\mathbf{m}}^{\mathrm{B}}$, we can then reconstruct these vectors

from the components found by solving Equation E.7 with:

$$\begin{aligned}
\tilde{\mathbf{p}}^{\mathrm{A}} &= \begin{bmatrix} \tilde{\mathbf{g}}(1) & \tilde{\mathbf{g}}(3) & \tilde{\mathbf{g}}(7) \end{bmatrix}^{\mathrm{T}}, \\
\tilde{\mathbf{p}}^{\mathrm{B}} &= \begin{bmatrix} \tilde{\mathbf{g}}(2) & \tilde{\mathbf{g}}(5) & \tilde{\mathbf{g}}(9) \end{bmatrix}^{\mathrm{T}}, \\
\tilde{\mathbf{m}}^{\mathrm{A}} &= \begin{bmatrix} 0 & \tilde{\mathbf{g}}(8) & \tilde{\mathbf{g}}(4) \end{bmatrix}^{\mathrm{T}}, \\
\tilde{\mathbf{m}}^{\mathrm{B}} &= \begin{bmatrix} 0 & \tilde{\mathbf{g}}(10) & \tilde{\mathbf{g}}(6) \end{bmatrix}^{\mathrm{T}}.
\end{aligned} \tag{E.8}$$

The vectors above require to be re-expressed in the global spinning SoR in order to be applied as external forces within the global FE environment. This is done once again by using matrix $\mathbf{R}$, yielding

$$\begin{aligned}
\mathbf{p}^{\mathrm{A}} &= \mathbf{R}^{\mathrm{T}} \tilde{\mathbf{p}}^{\mathrm{A}}, \\
\mathbf{p}^{\mathrm{B}} &= \mathbf{R}^{\mathrm{T}} \tilde{\mathbf{p}}^{\mathrm{B}}, \\
\mathbf{m}^{\mathrm{A}} &= \mathbf{R}^{\mathrm{T}} \tilde{\mathbf{m}}^{\mathrm{A}}, \\
\mathbf{m}^{\mathrm{B}} &= \mathbf{R}^{\mathrm{T}} \tilde{\mathbf{m}}^{\mathrm{B}}.
\end{aligned} \tag{E.9}$$

From this point, standard FE functions can be utilised to assemble the nodal forces acting on all beams to form the rotor's global centrifugal loading vector. The resolution of the elastic deformation problem ultimately yields the internal tensile state of the structure, which is used as an input for Equation 4.19.

Appendix F

Spinning Beam Matrices

The present Appendix reports the tensors deriving from the application of the Lagrange Equations to a spinning mechanical beam following the procedure of 4.2.1.3, which is in turn adopted from Leung and Fung [226].

F.1 Elastic rigidity matrix

$$\mathbf{K}_{ee} = \frac{1}{l}\begin{bmatrix}
EA & 0 & 0 & 0 & 0 & 0 & -EA & 0 & 0 & 0 & 0 & 0 \\
 & 12EI_z/l^2 & 0 & 0 & 0 & 6EI_z/l & 0 & -12EI_z/l^2 & 0 & 0 & 0 & 6EI_z/l \\
 & & 12EI_y/l^2 & 0 & -6EI_y/l & 0 & 0 & 0 & -12EI_y/l^2 & 0 & -6EI_y/l & 0 \\
 & & & GJ_x & 0 & 0 & 0 & 0 & 0 & -GJ_x & 0 & 0 \\
 & & & & 4EI_y & 0 & 0 & 0 & 6EI_y/l & 0 & 2EI_y & 0 \\
 & & & & & 4EI_z & 0 & -6EI_z/l & 0 & 0 & 0 & 2EI_z \\
 & & & & & & EA & 0 & 0 & 0 & 0 & 0 \\
 & & & & & & & 12EI_z/l^2 & 0 & 0 & 0 & -6EI_z/l \\
 & & & & & & & & 12EI_y/l^2 & 0 & 6EI_y/l & 0 \\
 & & & & & & & & & GJ_x & 0 & 0 \\
 & & & & & & & & & & 4EI_y & 0 \\
 & & & & & & & & & & & 4EI_z
\end{bmatrix}.$$

F.2 Mass matrix

$$
\mathbf{M}_e = \rho_m l
\begin{bmatrix}
A/3 & 0 & 0 & 0 & 0 & 0 & A/6 & 0 & 0 & 0 & 0 & 0 \\
 & 13A/35 & 0 & 0 & 0 & 11Al/210 & 0 & 9A/70 & 0 & 0 & 0 & -13Al/420 \\
 & & 13A/35 & 0 & -11Al/210 & 0 & 0 & 0 & 9A/70 & 0 & 13Al/420 & 0 \\
 & & & J_x/3 & 0 & 0 & 0 & 0 & 0 & J_x/6 & 0 & 0 \\
 & & & & Al^2/105 & 0 & 0 & 0 & -13Al/420 & 0 & -Al^2/140 & 0 \\
 & & & & & Al^2/105 & 0 & 13Al/420 & 0 & 0 & 0 & -Al^2/140 \\
 & & & & & & A/3 & 0 & 0 & 0 & 0 & 0 \\
 & & & & & & & 13A/35 & 0 & 0 & 0 & -11Al/210 \\
 & & & & & & & & 13A/35 & 0 & 11Al/210 & 0 \\
 & & & & & & & & & J_x/3 & 0 & 0 \\
 & & & & & & & & & & Al^2/105 & 0 \\
 & & & & & & & & & & & Al^2/105
\end{bmatrix}
\quad \text{sym}
$$

F.3 Coriolis matrix

$\tilde{\mathbf{G}}_e = (\rho_{\mathrm{m}} Al/420)\omega_2$

$$\begin{bmatrix}
0 & 147b_1 & 147b_2 & 0 & -21lb_2 & 21lb_1 & 0 & 63b_1 & 63b_2 & 0 & 14lb_2 & -14lb_1 \\
 & 0 & 156b_3 & 0 & -22lb_3 & 0 & -63b_1 & 0 & 54b_3 & 0 & 13lb_3 & 0 \\
 & & 0 & 0 & 0 & -22lb_3 & -63b_2 & -5b_3 & 0 & 0 & 0 & 13lb_3 \\
 & & & 0 & 0 & 0 & 0 & 0 & 0 & 0 & 0 & 0 \\
 & & & & 0 & 4l^2b_3 & 14lb_2 & 13lb_3 & 0 & 0 & 0 & -3l^2b_3 \\
 & & & & & 0 & -14lb_1 & 0 & 13lb_3 & 0 & 3l^2b_3 & 0 \\
 & & & & & & 0 & 147b_1 & 147b_2 & 0 & 21lb_2 & -21lb_1 \\
 & & & & & & & 0 & 156b_3 & 0 & 22lb_3 & 0 \\
 & & & & \text{antisymmetric} & & & & 0 & 0 & 0 & 22lb_3 \\
 & & & & & & & & & 0 & 0 & 0 \\
 & & & & & & & & & & 0 & 4l^2b_3 \\
 & & & & & & & & & & & 0
\end{bmatrix}.$$

F.4 Spin-softening matrix

$$
\mathbf{K}_{\Omega e} = (\rho_{\mathrm{m}} A l/420)\omega_2^2
\begin{bmatrix}
140a_{11} & 147a_{12} & 147a_{13} & 0 & -21la_{13} & 21la_{12} & 70a_{11} & 63a_{12} & 63a_{13} & 0 & 14a_{13} & -14la_{12} \\
 & 156a_{12} & 156a_{23} & 0 & -22la_{23} & 22la_{22} & 63a_{12} & 54a_{22} & 54a_{23} & 0 & 13a_{23} & -13la_{22} \\
 & & 156a_{33} & 0 & -22la_{33} & 22la_{23} & 63a_{13} & 54a_{23} & 54a_{33} & 0 & 13a_{33} & -13la_{23} \\
 & & & 0 & 0 & 0 & 0 & 0 & 0 & 0 & 0 & 0 \\
 & & & & 4l^2a_{13} & -4l^2a_{23} & -14la_{13} & -13la_{33} & -13la_{23} & 0 & -3l^2a_{33} & 3l^2a_{23} \\
 & & & & & 4l^2a_{22} & 14la_{12} & 13la_{22} & 13la_{23} & 0 & 3l^2a_{23} & -3l^2a_{22} \\
 & & & & & & 140a_{11} & 147a_{12} & 147a_{13} & 0 & 21la_{13} & -21la_{12} \\
 & & & & & & & 156a_{22} & 156a_{23} & 0 & 22la_{23} & -22la_{22} \\
 & & & & & \text{sym} & & & 156a_{33} & 0 & 22la_{33} & -22la_{23} \\
 & & & & & & & & & 0 & 0 & 0 \\
 & & & & & & & & & & 4l^2a_{33} & -4l^2a_{23} \\
 & & & & & & & & & & & 4l^2a_{22}
\end{bmatrix}.
$$

F.5 Geometric stiffness matrix

$$
\mathbf{K}_{\mathrm{ge}} = \frac{F_1}{30l}
\begin{bmatrix}
0 & & & & & 0 & & & & & & \\
 & 36 & & & 3l & & -36 & & & & 3l & \\
 & & 36 & -3l & & & & -36 & & -3l & & \\
 & & & 0 & & & & & 0 & & & \\
 & & & & 4l^2 & & & 3l & & -l^2 & & \\
 & & & & & 4l^2 & -3l & & & & -l^2 & \\
 & & & & & & 0 & & & & & \\
 & & & & & & & 36 & & & -3l & \\
 & & & & \mathrm{sym} & & & & 36 & & 3l & \\
 & & & & & & & & & 0 & & \\
 & & & & & & & & & & 4l^2 & \\
 & & & & & & & & & & & 4l^2
\end{bmatrix}
$$

$$
- \frac{a}{60}
\begin{bmatrix}
0 & & & & & 0 & & & & & & \\
 & 36 & & & 6l & & -36 & & & & 0 & \\
 & & 36 & -6l & & & & -36 & & 0 & & \\
 & & & 0 & & & & & 0 & & & \\
 & & & & 2l^2 & & & 0 & & -l^2 & & \\
 & & & & & 2l^2 & 0 & & & & -l^2 & \\
 & & & & & & 0 & & & & & \\
 & & & & & & & 36 & & & 0 & \\
 & & & & \mathrm{sym} & & & & 36 & 0 & & \\
 & & & & & & & & & 0 & & \\
 & & & & & & & & & & 6l^2 & \\
 & & & & & & & & & & & 6l^2
\end{bmatrix}
$$

$$
- \frac{bl}{420}
\begin{bmatrix}
0 & & & & & 0 & & & & & & \\
 & 72 & & & 15l & & -72 & & & & 6l & \\
 & & 72 & -15l & & & & -72 & & 6l & & \\
 & & & 0 & & & & & 0 & & & \\
 & & & & 4l^2 & & & 15l & & -3l^2 & & \\
 & & & & & 4l^2 & -15l & & & & -3l^2 & \\
 & & & & & & 0 & & & & & \\
 & & & & & & & 72 & & & -6l & \\
 & & & & \mathrm{sym} & & & & 72 & -6l & & \\
 & & & & & & & & & 0 & & \\
 & & & & & & & & & & 18l^2 & \\
 & & & & & & & & & & & 18l^2
\end{bmatrix}.
$$

In the above $a = \rho_{\mathrm{m}} A \omega_2^2 (\alpha_{11} \overline{x}_0 + \alpha_{13} \overline{z}_0)$ and $b = \rho_{\mathrm{m}} A \omega_2^2 (\alpha_{11}^2 + \alpha_{13}^2)$. The quantities $\overline{x}_0$ and $\overline{z}_0$ refer to the position of a reference end-node (arbitrarily chosen) of the beam element in the spinning frame and F_1 to the tensile force at the extremity after the application of pre-loading.

Appendix G

Linearisation of Quadratic Eigenvalue Problems

The eigenvalue problem of a damped linear system of size n assumes the quadratic form (quadratic eigenproblem or QEP)

$$(\lambda^2\mathbf{A} + \lambda\mathbf{B} + \mathbf{C})\hat{\mathbf{q}} = \mathbf{0}\,, \tag{G.1}$$

where in the general case all quantities are complex. It can be noted that in an undamped system, where $\mathbf{B} \equiv \mathbf{0}$, a variable substitution $\kappa = \lambda^2$ can be made, and the problem order is reduced to 1:

$$(\kappa\mathbf{A} + \mathbf{C})\hat{\mathbf{q}} = \mathbf{0}\,. \tag{G.2}$$

In order to resolve the QEP of Equation G.1, it is possible to assemble an equivalent linearised generalised eigenproblem of order $2n$ [248]:

$$\mathbf{E}\hat{\mathbf{r}} = \lambda\mathbf{F}\hat{\mathbf{r}}\,, \tag{G.3}$$

$$\hat{\mathbf{r}} = \begin{bmatrix} \hat{\mathbf{q}} \\ \lambda\hat{\mathbf{q}} \end{bmatrix}. \tag{G.4}$$

If $\mathbf{F}$ is nonsingular, defining $\mathbf{Q} = \mathbf{F}^{-1}\mathbf{E}$, allows to write the problem in standard form:

$$\mathbf{Q}\hat{\mathbf{r}} = \lambda\hat{\mathbf{r}}\,. \tag{G.5}$$

The solutions of Equation G.3 $(\lambda, \hat{\mathbf{r}})$ are the eigenvectors and eigenvalues of matrix $\mathbf{Q}$. There are multiple options for assembling terms $\mathbf{E}$ and $\mathbf{F}$. The rotor aeroelasticity application requires the problem to be formulated for unstructured matrices, because of the presence of nonsymmetric matrix addends representing the aerodynamic system.

Two general forms, known as L1 and L2, are available [248]:

$$\text{L1: } \mathbf{E} = \begin{bmatrix} \mathbf{0}_{n\times n} & \mathbf{N} \\ -\mathbf{C} & -\mathbf{B} \end{bmatrix}, \ \mathbf{F} = \begin{bmatrix} \mathbf{N} & \mathbf{0}_{n\times n} \\ \mathbf{0}_{n\times n} & \mathbf{A} \end{bmatrix}, \tag{G.6}$$

$$\text{L2: } \mathbf{E} = \begin{bmatrix} -\mathbf{C} & \mathbf{0}_{n\times n} \\ \mathbf{0}_{n\times n} & \mathbf{N} \end{bmatrix}, \ \mathbf{F} = \begin{bmatrix} \mathbf{B} & \mathbf{A} \\ \mathbf{N} & \mathbf{0}_{n\times n} \end{bmatrix}, \tag{G.7}$$

where $\mathbf{N}$ is an auxiliary matrix defined with

$$\mathbf{N} = \alpha\mathbf{I}, \ \alpha = \frac{1}{3n}(\|\mathbf{A}\| + \|\mathbf{B}\| + \|\mathbf{C}\|)\,. \tag{G.8}$$

The use of the re-equilibration factor α facilitates the numerical resolution of the eigenvalue problem [249]. It is customary to choose between L1 and L2 depending on the relative singularity of matrices $\mathbf{A}$ and $\mathbf{C}$: if the two-norm condition number of $\mathbf{A}$ is smaller than that of $\mathbf{C}$ (which characterises all applications in this study), then the recommended formulation is L1 , otherwise it is appropriate to use L2 [249].

Appendix H

Published Work

The following publications describe part of the doctoral work presented in this manuscript:

- R. Antonutti, C. Peyrard, L. Johanning, A. Incecik, and D. Ingram, "The effects of wind-induced inclination on the dynamics of semi-submersible floating wind turbines in the time domain", *Renewable Energy*. Forthcoming.
- R. Antonutti, C. Peyrard, L. Johanning, A. Incecik, and D. Ingram, "An investigation of the effects of wind-induced inclination on floating wind turbine dynamics: heave plate excursion", *Ocean Engineering*, vol. 91, pp. 208–217, 2014.
- R. Antonutti, N. Relun, and C. Peyrard, "Aerodynamic damping effect on the motions of a vertical-axis floating wind turbine", in *Proc. 14th Journées de l'Hydrodynamique*, (Val-de-Reuil, France), 2014.

Appendix I

Authorship

All of the applied studies presented can be attributed to the Author, including the verification and validation cases. Conversely, the Author's contribution to the numerical models described in the methodological sections is limited to the following:

Part 2: Methodological and code contributions to the time-domain simulator CAL-HYPSO. Amenable to the Author are improvements in the representation of the inertial wave forces on slender hull elements and the entirety of the aerodynamic and gyroscopic excitation functions described in 2.2.2 and 2.2.4. Developed in the course of this project are also the case-specific methodologies described in 2.3.2.1 and 2.3.4.3.

Part 3: The entire model set-up strategy for *Code_Aster* detailed in 3.3 represents an original contribution.

Part 4: Among the outputs of this project are the implementation of rotating beam theory (4.2.1.3) and of the aerodynamic operator (4.3.1) within an existing in-house development environment of EDF R&D. Of the Author is also the implementation of the resolution chain of the quadratic eigenproblem, using the form presented in 4.2.1.4.

The type and relative amount of effort dedicated to the different Parts of this work are qualitatively indicated in Table I.1.

Table I.1: Research effort expressed over the engineering doctorate.

Part	Methodology development	Code implementation	Validation	Applied studies
2	••	•	•	••
3	••		••	
4	•	••	•	•

References

[1] "Better growth, better climate: The new climate economy report," 2014. The Global Commission on the Economy and Climate.

[2] "World energy outlook - Executive summary," 2014. International Energy Agency.

[3] "2015 world energy issues monitor," 2015. World Energy Council.

[4] J. Rockström, W. Steffen, K. Noone, s. Persson, F. S. Chapin, E. F. Lambin, T. M. Lenton, M. Scheffer, C. Folke, H. J. Schellnhuber, B. Nykvist, C. A. de Wit, T. Hughes, S. van der Leeuw, H. Rodhe, S. Sörlin, P. K. Snyder, R. Costanza, U. Svedin, M. Falkenmark, L. Karlberg, R. W. Corell, V. J. Fabry, J. Hansen, B. Walker, D. Liverman, K. Richardson, P. Crutzen, and J. A. Foley, "A safe operating space for humanity," *Nature*, vol. 461, no. 7263, pp. 472–475, 2009.

[5] "CO2 emissions from fuel combustion - Highlights," tech. rep., International Energy Agency, 2014.

[6] "Comparing the cost of low-carbon technologies: What is the cheapest option?," Tech. Rep. 037/03-A-2014/En, Prognos AG for Agora Energiewende, Berlin, 2014.

[7] A. Burtin and V. Silva, "Technical and economic analysis of the European electricity system with 60% RES," tech. rep., EDF R&D, 2015.

[8] "The European offshore wind industry - Key trends and statistics 2014," 2015. European Wind Energy Association.

[9] "Renewable energy country attractiveness index - September 2015," 2015. Ernst & Young Global Limited.

[10] P. Higgins and A. Foley, "The evolution of offshore wind power in the United Kingdom," *Renewable and Sustainable Energy Reviews*, vol. 37, pp. 599–612, 2014.

[11] A. Smith, T. Stehly, and W. Musial, "2014-2015 offshore wind technologies market report," Tech. Rep. NREL/TP-5000-64283, National Renewable Energy Laboratory, 2015.

[12] "Offshore wind in Europe," 2015. Ernst & Young Global Limited.

[13] "UK offshore wind: Opportunities for trade and investment," 2014. The Crown Estate.

[14] "Appraisal of the offshore wind industry in Japan," 2014. Carbon Trust.

[15] "Deep water - The next step for offshore wind energy," 2013. European Wind Energy Association.

[16] D. Roddier, C. Cermelli, A. Aubault, and A. Weinstein, "WindFloat: A floating foundation for offshore wind turbines," *Journal of Renewable and Sustainable Energy*, vol. 2, no. 3, 2010.

[17] J. Bard, "HiPRWind: High-power, high-reliability wind technology," 2011. Presented at the SET-Plan Conference 2011.

[18] M. Monnier, "Eolien en mer | France Energie Eolienne," Jan. 2015. Online: http://fee.asso.fr/politique-de-leolien/eolien-en-mer/.

[19] "Floating offshore wind foundations: industry consortia and projects in the United States, Europe and Japan," tech. rep., Main(e) International Consulting LLC, 2013.

[20] W. Musial and B. Ram, "Large-scale offshore wind power in the United States: assessment of opportunities and barriers," Tech. Rep. NREL/TP-500-40745, National Renewable Energy Laboratory, 2010.

[21] R. James and M. Costa Ros, "Floating offshore wind: market and technology review," 2015. Carbon Trust.

[22] H. Stiesdal, "Hywind: The world's first floating MW-scale wind turbine," *Wind Directions*, pp. 52–53, Dec. 2009.

[23] "The wind from the future - Fukushima floating offshore wind farm demonstration project," *Hitachi Review*, vol. 63, no. 3, pp. 12–17, 2014.

[24] "Fukushima offshore wind consortium," Oct. 2015. Online: http://www.fukushima-forward.jp/english/index.html.

[25] "Cost reduction monitoring framework summary report," 2015. Offshore Renewable Energy Catapult.

[26] A. Henderson and D. Witcher, "Floating offshore wind energy - A review of the current status and an assessment of the prospects," *Wind Engineering*, vol. 34, no. 1, pp. 1–16, 2010.

[27] "Chronicle: das GICON-SOF schwimmendes offshorefundament," Oct. 2015. Online: http://www.gicon-sof.de/en/sof-chronik.html.

[28] "Ideol, French specialist of floating wind," Oct. 2015. Online: http://ideol-offshore.com/en.

[29] "INFLOW - Industrialization setup of a floating offshore wind turbine," Oct. 2015. Online: http://www.inflow-fp7.eu/.

[30] "Plan d'action national en faveur des énergies renouvelables - Période 2009-2020," 2009. Ministère de l'écologie, de l'énergie, du développement durable et de la mer.

[31] "ADEME AAP - Fermes pilotes éoliennes flottantes," Oct. 2015. Online: https://appelsaprojets.ademe.fr/aap/AAP_EolFlo2015-98.

[32] R. Antonutti and J. Spelling, "Floating offshore wind technology: concepts, players, costs and markets," Tech. Rep. UKC-R-2015-020, EDF R&D, 2015.

[33] A. Myhr, C. Bjerkseter, A. Agotnes, and T. A. Nygaard, "Levelised cost of energy for offshore floating wind turbines in a life cycle perspective," *Renewable Energy*, vol. 66, pp. 714–728, 2014.

[34] A. R. Henderson, D. Witcher, and C. A. Morgan, "Floating support structures enabling new markets for offshore wind energy," in *Proc. European Wind Energy Conference*, (Marseille, France), 2009.

[35] "Wind turbines - Part 3: Design requirements for offshore wind turbines," Tech. Rep. IEC 61400-3:2009, International Electrotechnical Commission, 2009.

[36] T. J. Larsen and T. D. Hanson, "A method to avoid negative damped low frequent tower vibrations for a floating, pitch controlled wind turbine," *Journal of Physics: Conference Series*, vol. 75, no. 1, 2007.

[37] S. Christiansen, T. Bak, and T. Knudsen, "Damping wind and wave loads on a floating wind turbine," *Energies*, vol. 6, no. 8, pp. 4097–4116, 2013.

[38] F. Savenije, J. Peeringa, F. Hujis, and E.-J. de Ridder, "Control development for floating wind," 2013. Poster at the EWEA Offshore 2013 Conference.

[39] H. J. Sutherland, D. E. Berg, and T. D. Ashwill, "A retrospective of VAWT technology," Tech. Rep. SAND2012-0304, Sandia National Laboratories, 2012.

[40] K. Wang, M. O. L. Hansen, and T. Moan, "Model improvements for evaluating the effect of tower tilting on the aerodynamics of a vertical axis wind turbine," *Wind Energy*, vol. 18, no. 1, pp. 91–110, 2013.

[41] P. Jamieson, *Innovation in Wind Turbine Design*. Chichester, UK: John Wiley & Sons, 2011.

[42] K. Boorsma, "Power and loads for wind turbines in yawed conditions - Analysis of field measurements and aerodynamic predictions," Tech. Rep. ECN-E–12-047, Energy research Centre of the Netherlands, 2012.

[43] M. Cahay, E. Luquiau, C. Smadja, and F. Silvert, "Use of a vertical wind turbine in an offshore floating wind farm," in *Proc. Offshore Technology Conference 2011*, (Houston, TX, USA), 2011.

[44] M. Borg, M. Collu, and F. P. Brennan, "Offshore floating vertical axis wind turbines: advantages, disadvantages, and dynamics modelling state of the art," in *Proc. RINA Marine & Offshore Renewable Energy International Conference*, (London, UK), pp. 33–46, RINA, 2012.

[45] M. F. Barone and J. A. Paquette, "Vertical-axis wind turbines revisited: a Sandia perspective," 2012. Presented at the 2012 Wind Turbine Blade Workshop, Sandia National Laboratories.

[46] H. Akimoto, K. Tanaka, J.-C. Park, and S.-m. Jeong, "Preliminary study of the floating axis wind turbine," in *Proc. OCEANS 2012*, (Yeosu, Korea), 2012.

[47] "Design of floating wind turbine structures," Tech. Rep. DNV-OS-J103, Det Norske Veritas, 2013.

[48] E. te Brake, "DNV GL continues drive for risk and cost reduction in global wind industry via three new joint industry initiatives," Oct. 2015. Online: https://www.dnvgl.com/news/dnv-gl-continues-drive-for-risk-and-cost-reduction-in-global-wind-industry-via-three-new-joint-industry-initiatives-18343.

[49] C.-H. Lee, "WAMIT Theory Manual," Tech. Rep. 95-2, MIT Department of Ocean Engineering, Cambridge, MA, USA, 1995.

[50] "Aqwa Theory Manual," tech. rep., ANSYS Inc., Canonsburg, PA, USA, 2013.

[51] ECN, "LHEEA - Nemoh," June 2014. Online: http://lheea.ec-nantes.fr/doku.php/emo/nemoh/start.

[52] J. M. Jonkman, "FAST | NWTC information portal," 2015. Online: https://nwtc.nrel.gov/FAST.

[53] Principia, "Deeplines : Global analysis of risers, moorings and flow-lines," 2015. Online: http://www.principia.fr/expertise-fields-software-products-deeplines-126.html.

[54] M. Philippe, A. Comborieu, C. Peyrard, F. Robaux, G. Delhommeau, and A. Babarit, "Introducing Second Order Low Frequency Loads in the Open-Source Boundary Element Method Code Nemoh," in *Proc. 11th European Wave and Tidal Energy Conference*, (Nantes, France), 2015.

[55] E. Dombre, *Modélisation non-linéaire des interactions vague-structure appliquée à des flotteurs d'éoliennes off-shore*. PhD thesis, Université Paris-Est, Paris, France, 2015.

[56] A. J. Dunbar, B. A. Craven, and E. G. Paterson, "Development and validation of a tightly coupled CFD/6-DOF solver for simulating floating offshore wind turbine platforms," *Ocean Engineering*, vol. 110, pp. 98–105, 2015.

[57] G. R. Tomasicchio, E. Armenio, F. D'Alessandro, N. Fonseca, S. A. Mavrakos, V. Penchev, H. Schuttrumpf, S. Voutsinas, J. Kirkegaard, and P. M. Jensen, "Design of a 3d physical and numerical experiment on floating off-shore wind turbines," *Coastal Engineering Proceedings*, vol. 1, no. 33, p. 67, 2012.

[58] M. D. Masciola, "Instructional and theory guide to the Mooring Analysis Program - MAP version 0.87.06a–mdm," tech. rep., 2013.

[59] Z. Lin, *A hydrodynamic analysis of deep-water moorings*. PhD thesis, University of Strathclyde, Glasgow, Scotland, UK, 2015.

[60] "Code Aster: analysis of structures and thermomechanics for studies & research," 2014. EDF R&D.

[61] "OrcaFlex manual version 9.7a," tech. rep., Orcina Ltd., 2013.

[62] MARIN, "aNySIM documantation - Mooring," tech. rep., 2011.

[63] T. Utsunomiya, H. Matsukuma, S. Minoura, K. Ko, H. Hamamura, O. Kobayashi, I. Sato, Y. Nomoto, and K. Yasui, "At sea experiment of a hybrid spar for floating offshore wind turbine using 1/10-scale model," *Journal of Offshore Mechanics and Arctic Engineering*, vol. 135, no. 3, 2013.

[64] H. Glauert, "Airplane propellers," *Aerodynamic theory*, vol. 4, pp. 169–360, 1935.

[65] M. Karimirad, "Modeling aspects of a floating wind turbine for coupled wave–wind-induced dynamic analyses," *Renewable Energy*, vol. 53, pp. 299–305, 2013.

[66] M. Collu, M. Borg, A. Shires, F. N. Rizzo, and E. Lupi, "FloVAWT: Further progresses on the development of a coupled model of dynamics for floating offshore VAWTs," in *Proc. 33rd International Conference on Ocean, Offshore and Arctic Engineering*, (San Francisco, CA, USA), 2014.

[67] K. Wang, T. Moan, C. Luan, and M. O. L. Hansen, "Comparative study of a FVAWT and a FHAWT with a semi-submersible floater," in *Proc. 24th International Ocean and Polar Engineering Conference*, (Busan, Korea), 2014.

[68] I. Paraschivoiu, *Wind Turbine Design: With Emphasis on Darrieus Concept*. Montréal, Canada: Polytechnic International Press, 2002.

[69] Y. Liu, Q. Xiao, A. Incecik, and D. Wan, "Investigation of the effects of the platform motion on the aerodynamics of a floating offshore wind turbine," in *Proc. 9th International Workshop on Ship and Marine Hydrodynamics*, (Glasgow, UK), 2015.

[70] C. Liu and C. Hu, "CFD Simulation of a Floating Wind Turbine Platform in Rough Sea Conditions," in *Proc. 24th International Ocean and Polar Engineering Conference*, International Society of Offshore and Polar Engineers, 2014.

[71] M. Borg and M. Collu, "Offshore floating vertical axis wind turbines, dynamics modelling state of the art. Part III: Hydrodynamics and coupled modelling approaches," *Renewable and Sustainable Energy Reviews*, vol. 46, pp. 296–310, 2015.

[72] "Guide for building and classing floating offshore wind turbine installations," tech. rep., American Bureau of Shipping, 2013.

[73] L. Sethuraman and V. Venugopal, "Hydrodynamic response of a stepped-spar floating wind turbine: Numerical modelling and tank testing," *Renewable Energy*, vol. 52, pp. 160–174, 2013.

[74] L. Sethuraman, V. Venugopal, and M. Mueller, "Drive-train configurations for Floating wind turbines," in *Proc. 8th International Conference and Exhibition on Ecological Vehicles and Renewable Energies*, (Monte Carlo, Monaco), pp. 1–7, 2013.

[75] L. Sethuraman, V. Venugopal, A. Zavvos, and M. Mueller, "Structural integrity of a direct-drive generator for a floating wind turbine," *Renewable Energy*, vol. 63, pp. 597–616, 2014.

[76] L. Sethuraman, Y. Xing, Z. Gao, V. Venugopal, M. Mueller, and T. Moan, "A 5 MW direct-drive generator for floating spar-buoy wind turbine: Development and analysis of a fully coupled mechanical model," *Proceedings of the Institution of Mechanical Engineers, Part A: Journal of Power and Energy*, pp. 1–24, 2014.

[77] "Projets R&D - France Energies Marines," Oct. 2015. Online: http://en.france-energies-marines.org/R-D/Projets-R-D.

[78] C. Peyrard and N. Relun, "Eolien offshore: Vertiwind FOWT motions estimation using a coupled aero-hydro-mooring approach," Tech. Rep. H-P74-2013-03903-FR, EDF R&D, 2013.

[79] J. M. Jonkman, "Dynamics modeling and loads analysis of an offshore floating wind turbine," Tech. Rep. NREL/TP-500-41958, National Renewable Energy Laboratory, 2007.

[80] DTU Wind Energy, "Welcome to HAWC2," 2015. Online: http://www.hawc2.dk/.

[81] F. Hujis, "Concept design verification of a semi-submersible floating wind turbine using coupled simulations," 2014. Presented at the EERA DeepWind 2014 Conference, Trondheim, Norway.

[82] W. de Boom, "Floating supports for offshore wind: Small structures – big challenges," 2011. Presented at the 30th International Conference on Ocean, Offshore and Arctic Engineering, Rotterdam, The Netherlands.

[83] Bulder, van Hees, Henderson, Huijsmans, Pierik, Snijders, Wijnants, and Wolf, "Study to feasibility of and boundary conditions for floating offshore wind turbines," tech. rep., 2002.

[84] A. J. Coulling, A. J. Goupee, A. N. Robertson, J. M. Jonkman, and H. J. Dagher, "Validation of a FAST semi-submersible floating wind turbine numerical model with DeepCwind test data," *Journal of Renewable and Sustainable Energy*, vol. 5, no. 2, 2013.

[85] M. Masciola, A. Robertson, J. Jonkman, A. Coulling, and A. Goupee, "Assessment of the importance of mooring dynamics on the global response of the DeepCwind floating semisubmersible offshore wind turbine," in *Proc. 23rd International Offshore and Polar Engineering Conference*, (Anchorage, AK, USA), 2013.

[86] M. Philippe, A. Courbois, A. Babarit, F. Bonnefoy, J.-M. Rousset, and P. Ferrant, "Comparison of simulation and tank test results of a semi-submersible floating wind turbine under wind and wave loads," in *Proc. 32nd International Conference on Ocean, Offshore and Arctic Engineering*, (Nantes, France), 2013.

[87] C. A. Cermelli and D. G. Roddier, "Experimental and numerical investigation of the stabilizing effects of a water-entrapment plate on a deepwater minimal floating platform," in *Proc. 24th International Conference on Offshore Mechanics and Arctic Engineering*, (Halkidiki, Greece), 2005.

[88] H. Cozijn, R. Uittenbogaard, and E. ter Brake, "Heave, roll and pitch damping of a deepwater CALM buoy with a skirt," in *Proc. 15th Offshore and Polar Engineering Conference*, (Seoul, Korea), 2005.

[89] A. Aubault, C. A. Cermelli, and D. G. Roddier, "Structural design of a semi-submersible platform with water-entrapment plates based on a time-domain hydrodynamic algorithm coupled with finite elements," in *Proc. 16th International Offshore and Polar Engineering Conference*, (San Francisco, CA, USA), 2006.

[90] "Products - WindFloat," Aug. 2015. Online: http://www.principlepowerinc.com/products/windfloat.html.

[91] L. Tao and S. Cai, "Heave motion suppression of a spar with a heave plate," *Ocean Engineering*, vol. 31, no. 5, pp. 669–692, 2004.

[92] C. Lopez-Pavon and A. Souto-Iglesias, "Hydrodynamic coefficients and pressure loads on heave plates for semi-submersible floating offshore wind turbines: A comparative analysis using large scale models," *Renewable Energy*, vol. 81, pp. 864–881, 2015.

[93] H. Kojima, T. Ijima, and A. Yoshida, "Decomposition and interception of long waves by a submerged horizontal plate," in *Proc. 22nd Conference on Coastal Engineering*, (Delft, The Netherlands), pp. 1228–1241, 1990.

[94] X. Yu, M. Isobe, and A. Watanabe, "Wave breaking over submerged horizontal plate," *Journal of Waterway, Port, Coastal, and Ocean Engineering*, vol. 121, no. 2, pp. 105–113, 1995.

[95] Y. Zhao, J. Yang, and Y. He, "Preliminary design of a multi-column TLP foundation for a 5-MW offshore wind turbine," *Energies*, vol. 5, no. 12, pp. 3874–3891, 2012.

[96] C. P. Butterfield, W. Musial, J. Jonkman, P. Sclavounos, and L. Wayman, "Engineering challenges for floating offshore wind turbines," in *Proc. Offshore Wind International Conference and Exhibition*, (Copenhagen, Denmark), 2005.

[97] J. Sweetman, "Floating offshore wind turbines: conceptual assessment of highly compliant platforms using theory, design and simulation," Feb. 2015. Online: http://grantome.com/grant/NSF/CBET-1133682.

[98] H. Akimoto, K. Tanaka, and K. Uzawa, "Floating axis wind turbines for offshore power generation - a conceptual study," *Environmental Research Letters*, vol. 6, no. 4, 2011.

[99] H. Akimoto, K. Tanaka, and Y. Hara, "Gyroscopic effects on the dynamics of floating axis wind turbine," in *Proc. Grand Renewable Energy Conference*, (Tokyo, Japan), 2014.

[100] F. Hujis, J. Mikx, F. Savenije, and E.-J. de Ridder, "Integrated design of floater, mooring and control system for a semi-submersible floating wind turbine," tech. rep., 2013.

[101] F. Huijs, R. de Bruijn, and F. Savenije, "Concept design verification of a semi-submersible floating wind turbine using coupled simulations," *Energy Procedia*, vol. 53, pp. 2–12, 2014.

[102] M. Le Boulluec, J. Ohana, A. Martin, and A. Houmard, "Tank testing of a new concept of floating offshore wind turbine," in *Proc. 32nd International Conference on Ocean, Offshore and Arctic Engineering*, (Nantes, France), 2013.

[103] L. Wang and B. Sweetman, "Simulation of large-amplitude motion of floating wind turbines using conservation of momentum," *Ocean Engineering*, vol. 42, pp. 155–164, 2012.

[104] B. Sweetman and L. Wang, "Floating offshore wind turbine dynamics: large-angle motions in euler-space," *Journal of Offshore Mechanics and Arctic Engineering*, vol. 134, no. 3, 2012.

[105] L. Wang, *Multibody dynamics using conservation of momentum with application to compliant offshore floating wind turbines*. PhD thesis, Texas A&M University, College Station, TX, USA, 2012.

[106] L. Wang and B. Sweetman, "Multibody dynamics of floating wind turbines with large-amplitude motion," *Applied Ocean Research*, vol. 43, pp. 1–10, 2013.

[107] A. Courbois, *Etude expérimentale du comportement dynamique d'une éolienne offshore flottante soumise à l'action conjuguée de la houle et du vent*. PhD thesis, Ecole Centrale de Nantes, Nantes, France, 2013.

[108] J. M. Jonkman, S. Butterfield, W. Musial, and G. Scott, "Definition of a 5 MW reference wind turbine for offshore system development," Tech. Rep. NREL/TP-500-38060, National Renewable Energy Laboratory, 2009.

[109] J. M. Jonkman, "Influence of control on the pitch damping of a floating wind turbine," Tech. Rep. NREL/CP-500-42589, National Renewable Energy Laboratory, 2008.

[110] M. Borg, K. Wang, M. Collu, and T. Moan, "A comparison of two coupled models of dynamics for offshore floating vertical axis wind turbines," in *Proc. 33rd International Conference on Ocean, Offshore and Arctic Engineering*, (San Francisco, CA, USA), 2014.

[111] K. Wang, T. Moan, and M. O. L. Hansen, "A method for modeling of floating vertical axis wind turbine," in *Proc. 32nd International Conference on Ocean, Offshore and Arctic Engineering*, (Nantes, France), 2013.

[112] M. Borg and M. Collu, "Frequency-domain characteristics of aerodynamic loads of offshore floating vertical axis wind turbines," *Applied Energy*, vol. 155, pp. 629–636, 2015.

[113] K. O. Merz, "A method for analysis of VAWT aerodynamic loads under turbulent wind and platform motion," *Energy Procedia*, vol. 24, pp. 44–51, 2012.

[114] "NWTC • Rigid Wind Turbine with Harmonic Motions," Aug. 2015. Online: https://wind.nrel.gov/forum/wind/viewtopic.php?f=4&t=831.

[115] N. Relun, "Vertical axis wind turbine aero-dynamic models with emphasis on Nénuphar Wind concept," Tech. Rep. H-R22-2013-03014-EN, EDF R&D, 2013.

[116] R. E. Gormont, "A mathematical model of unsteady aerodynamics and radial flow for application to helicopter rotors," Tech. Rep. AD-767 240, Boeing Vertol Compagny, 1973.

[117] D. E. Berg, "Improved double-multiple streamtube model for the Darrieus-type vertical axis wind turbine," in *Proc. 6th Biennial Wind Energy Conference*, vol. 1, (Minneapolis, MN, USA), pp. 231–238, American Solar Energy Society, 1983.

[118] S. Mertens, G. van Kuik, and G. van Bussel, "Performance of an H-Darrieus in the skewed flow on a roof," *Journal of Solar Energy Engineering*, vol. 125, no. 4, pp. 433–440, 2003.

[119] C. Ferreira, G. van Kuik, and G. van Bussel, "An analytical method to predict the variation in performance of an H-Darrieus in skewed flow and its experimental validation," in *Proc. European Wind Energy Conference*, (Athens, Greece), 2006.

[120] C. Ferreira, K. Dixon, C. Hofemann, G. van Kuik, and G. van Bussel, "The VAWT in skew: stereo-PIV and vortex modeling," in *47th AIAA Aerospace Sciences Meeting*, (Orlando, FL, USA), pp. 5–8, 2009.

[121] M. O. L. Hansen, J. N. Sørensen, S. Voutsinas, N. Sørensen, and H. A. Madsen, "State of the art in wind turbine aerodynamics and aeroelasticity," *Progress in Aerospace Sciences*, vol. 42, no. 4, pp. 285–330, 2006.

[122] P. G. Migliore, W. P. Wolfe, and J. B. Fanucci, "Flow curvature effects on Darrieus turbine blade aerodynamics," *Journal of Energy*, vol. 4, no. 2, pp. 49–55, 1980.

[123] M. Borg, A. Shires, and M. Collu, "Offshore floating vertical axis wind turbines, dynamics modelling state of the art. part I: Aerodynamics," *Renewable and Sustainable Energy Reviews*, vol. 39, pp. 1214–1225, 2014.

[124] M. Islam, D. S. K. Ting, and A. Fartaj, "Aerodynamic models for Darrieus-type straight-bladed vertical axis wind turbines," *Renewable and Sustainable Energy Reviews*, vol. 12, no. 4, pp. 1087–1109, 2008.

[125] C. Ferreira, *The near wake of the VAWT*. PhD thesis, TU Delft, Delft, the Netherlands, 2009.

[126] M. Philippe, A. Babarit, and P. Ferrant, "Modes of response of an offshore wind turbine with directional wind and waves," *Renewable Energy*, vol. 49, pp. 151–155, 2013.

[127] P. Blusseau and M. H. Patel, "Gyroscopic effects on a large vertical axis wind turbine mounted on a floating structure," *Renewable Energy*, vol. 46, pp. 31–42, 2012.

[128] H. Fujiwara, T. Tsubogo, and Y. Nihei, "Gyro effect of rotating blades on the floating wind turbine platform in waves," in *Proc. 21st Offshore and Polar Engineering Conference*, (Maui, HI, USA), 2011.

[129] T. Sarpkaya and M. Isaacson, *Mechanics of Wave Forces on Offshore Structures*. New York, USA: Van Nostrand Reinhold Co., 1981.

[130] G. Delhommeau, *Les problèmes de diffraction-radiation et de résistance de vagues: étude théorique et résolution numérique par la méthode des singularités*. PhD thesis, Ecole Nationale Supérieure de Mécanique de Nantes, Nantes, France, 1987.

[131] G. Delhommeau, "Seakeeping codes Aquadyn and Aquaplus," in *Proc. 19th WEGEMT School - Numerical Simulation of Hydrodynamics: Ships and Offshore Structures*, (Nantes, France), 1993.

[132] "Aquaplus: Notice d'utilisation," tech. rep., Ecole Centrale de Nantes, 1999.

[133] W. E. Cummins, "The impulse response function and ship motions," Tech. Rep. Report 1661, David Taylor Model Basin, 1962.

[134] T. Ogilvie, "Recent progress towards the understanding and prediction of ship motions," in *Proc. 6th Symposium on Naval Hydrodynamics*, (Washington D.C., USA), 1964.

[135] J. R. Morison, M. D. O'Brien, J. W. Johnson, and S. A. Schaaf, "The force exerted by surface waves on piles," *Transactions of the Society of Petroleum Engineers of AIME*, vol. 189, pp. 149–154, 1950.

[136] B. Molin, *Hydrodynamique des Structures Offshore*. Paris, France: Editions Technip, 2002.

[137] A. Robertson, J. Jonkman, M. Masciola, and H. Song, "Definition of the semisubmersible floating system for Phase II of OC4," Tech. Rep. NREL/TP-5000-60601, National Renewable Energy Laboratory, 2014.

[138] J. M. J. Journée and W. W. Massie, *Offshore Hydromechanics*. Delft, The Netherlands: TU Delft, 2000.

[139] M. Lake, H. He, A. W. Troesch, M. Perlin, and K. P. Thiagarajan, "Hydrodynamic coefficient estimation for TLP and spar structures," *Journal of Offshore Mechanics and Arctic Engineering*, vol. 122, no. 2, p. 118, 2000.

[140] K. P. Thiagarajan, I. Datta, A. Z. Ran, L. Tao, and J. E. Halkyard, "Influence of heave plate geometry on the heave response of classic spars," in *Proc. 21st International Conference on Offshore Mechanics and Arctic Engineering*, (Oslo, Norway), p. 621–627, 2002.

[141] L. Tao, B. Molin, Y. M. Scolan, and K. Thiagarajan, "Spacing effects on hydrodynamics of heave plates on offshore structures," *Journal of Fluids and Structures*, vol. 23, no. 8, pp. 1119–1136, 2007.

[142] X. Yu, "Functional performance of a submerged and essentially horizontal plate for offshore wave control: a review," *Coastal Engineering Journal*, vol. 44, no. 02, p. 127–147, 2002.

[143] M. McIver, "Diffraction of water waves by a moored, horizontal, flat plate," *Journal of Engineering Mathematics*, vol. 19, no. 4, p. 297–319, 1985.

[144] Y. H. Zheng, P. F. Liu, Y. M. Shen, B. J. Wu, and S. W. Sheng, "On the radiation and diffraction of linear water waves by an infinitely long rectangular structure submerged in oblique seas," *Ocean Engineering*, vol. 34, no. 3–4, pp. 436–450, 2007.

[145] H. Kojima, A. Yoshida, and T. Nakamura, "Linear and nonlinear wave forces exerted on a submerged horizontal plate," *Coastal Engineering*, vol. 1, no. 24, pp. 1312–1326, 1994.

[146] R. Porter, "Linearised water wave problems involving submerged horizontal plates," *Applied Ocean Research*, vol. 50, pp. 91–109, 2015.

[147] T. Vada, "A numerical solution of the second-order wave-diffraction problem for a submerged cylinder of arbitrary shape," *Journal of Fluid Mechanics*, vol. 174, pp. 23–37, 1987.

[148] P. A. Martin and L. Farina, "Radiation of water waves by a heaving submerged horizontal disc," *Journal of Fluid Mechanics*, vol. 337, pp. 365–379, 1997.

[149] N. F. Parsons and P. A. Martin, "Trapping of water waves by submerged plates using hypersingular integral equations," *Journal of Fluid Mechanics*, vol. 284, pp. 359–375, 1995.

[150] C. M. Linton and D. V. Evans, "Trapped modes above a submerged horizontal plate," *The Quarterly Journal of Mechanics and Applied Mathematics*, vol. 44, no. 3, pp. 487–506, 1991.

[151] X. Yu and Z. Dong, "Direct computation of wave motion around submerged plates," in *Proc. 29th International Association for Hydro-Environment Engineering and Research*, (Beijing, China), 2001.

[152] H. Lamb, *Hydrodynamics*. New York, USA: Dover Publications, 6th ed., 1945.

[153] M. Philippe, *Couplages aéro-hydrodynamiques pour l'étude de la tenue à la mer des éoliennes offshore flottantes*. PhD thesis, Ecole Centrale de Nantes, Nantes, France, 2012.

[154] J. G. Maciel, "The WindFloat project," 2012. Presentation at the Conference Atlantic Forum 2012, Brest, France.

[155] M. Somerville, "GE 3.6 MW offshore wind turbine - 3d Warehouse," June 2014. Online: https://3dwarehouse.sketchup.com/user.html?id=01415162189190518286144 01.

[156] M. Philippe, A. Babarit, and P. Ferrant, "Aero-hydro-elastic simulation of a semi-submersible floating wind turbine," *Journal of Offshore Mechanics and Arctic Engineering*, vol. 136, no. 2, 2014.

[157] L. Vita, *Offshore floating vertical axis wind turbines with rotating platform*. PhD thesis, Risø DTU, Roskilde, Denmark, 2011.

[158] R. Antonutti, C. Peyrard, L. Johanning, A. Incecik, and D. Ingram, "An investigation of the effects of wind-induced inclination on floating wind turbine dynamics: heave plate excursion," *Ocean Engineering*, vol. 91, pp. 208–217, 2014.

[159] R. Antonutti, N. Relun, and C. Peyrard, "Aerodynamic damping effect on the motions of a vertical-axis floating wind turbine," in *Proc. 14th Journées de l'Hydrodynamique*, (Val-de-Reuil, France), 2014.

[160] R. Antonutti, C. Peyrard, L. Johanning, A. Incecik, and D. Ingram, "The effects of wind-induced inclination on the dynamics of semi-submersible floating wind turbines in the time domain," *Renewable Energy*. Forthcoming.

[161] C. Peyrard and R. Antonutti, "Offshore wind: mooring lines modelling and validation on the OC4 platform," Tech. Rep. H-P74-2015-05740-FR, EDF R&D, 2015.

[162] S. Chakrabarti, *Handbook of Offshore Engineering*, vol. 2. Oxford, UK: Elsevier, 2005.

[163] "Anchor manual 2010," 2010. Vryhof Anchors.

[164] O. M. Faltinsen, *Sea Loads on Ships and Offshore Structures*. Cambridge, UK: Cambridge University Press, 1990.

[165] L. Johanning, G. H. Smith, and J. Wolfram, "Measurements of static and dynamic mooring line damping and their importance for floating WEC devices," *Ocean Engineering*, vol. 34, no. 14-15, pp. 1918–1934, 2007.

[166] S. A. Mavrakos, V. J. Papazoglou, M. S. Triantafyllou, and J. Hatjigeorgiou, "Deep water mooring dynamics," *Marine Structures*, vol. 9, no. 2, pp. 181–209, 1996.

[167] D. Matha, U. Fechter, and M. Kühn, "Non-linear multi-body mooring system model for floating offshore wind turbines," in *Proc. OFFSHORE2011*, (Amsterdam, The Netherlands), 2011.

[168] M. Masciola, J. Jonkman, and A. Robertson, "Extending the capabilities of the Mooring Analysis Program: A survey of dynamic mooring line theories for integration into FAST," in *Proc. 33rd International Conference on Ocean, Offshore and Arctic Engineering*, (San Francisco, CA, USA), 2014.

[169] S. H. Jeon, Y. U. Cho, M. W. Seo, J. R. Cho, and W. B. Jeong, "Dynamic response of floating substructure of spar-type offshore wind turbine with catenary mooring cables," *Ocean Engineering*, vol. 72, pp. 356–364, 2013.

[170] B. S. Kallesoe, U. S. Paulsen, A. Kohler, and C. H. Hansen, "Aero-hydro-elastic response of a floating platform supporting several wind turbines," in *Proc. 49th AIAA Aerospace Sciences Meeting*, (Orlando, FL, USA), 2011.

[171] H. C. Kim, H. K. Jang, M. H. Kim, and Y. H. Bee, "Coupled dynamic analysis of a MUFOWT with transient broken-blade incident," in *Proc. 25th International Offshore and Polar Engineering Conference*, (Kona, HI, USA), 2015.

[172] Z. Cheng, K. Wang, Z. Gao, and T. Moan, "Dynamic modelling and analysis of three floating wind turbine concepts with vertical axis rotor," in *Proc. 25th International Offshore and Polar Engineering Conference*, (Kona, HI, USA), 2015.

[173] E. E. Bachynski, M. Etemaddar, M. I. Kvittem, C. Luan, and T. Moan, "Dynamic analysis of floating wind turbines during pitch actuator fault, grid loss, and shutdown," *Energy Procedia*, vol. 35, pp. 210–222, 2013.

[174] R. Zhang, Y. Tang, J. Hu, S. Ruan, and C. Chen, "Dynamic response in frequency and time domains of a floating foundation for offshore wind turbines," *Ocean Engineering*, vol. 60, pp. 115–123, 2013.

[175] M. Hall, B. Buckham, C. Crawford, and R. S. Nicoll, "The importance of mooring line model fidelity in floating wind turbine simulations," in *Proc. OCEANS*, (Waikoloa, HI, USA), 2011.

[176] Y. H. Bae and M. H. Kim, "Rotor-floater-tether coupled dynamics including second-order sum–frequency wave loads for a mono-column-TLP-type FOWT (floating offshore wind turbine)," *Ocean Engineering*, vol. 61, pp. 109–122, 2013.

[177] J. Jonkman, T. Larsen, A. Hansen, T. Nygaard, K. Maus, M. Karimirad, Z. Gao, T. Moan, I. Fylling, J. Nichols, M. Kohlmeier, J. Pascual Vergara, D. Merino, W. Shi, and H. Park, "Offshore Code Comparison Collaboration within IEA Wind task 23: Phase IV results regarding floating wind turbine modeling," in *Proc. European Wind Energy Conference*, (Warsaw, Poland), 2010.

[178] M. Muskulus, "Designing the next generation of computational codes for wind-turbine simulations," in *Proc. 21st International Offshore and Polar Engineering Conference*, vol. 318, (Maui, HI, USA), 2011.

[179] "Doc:Code-Aster - CAELinuxWiki," July 2015. Online: http://caelinux.org/wiki/index.php/Doc:Code-Aster.

[180] D. A. Thakore, *Finite Element Analysis Using Open Source Software*. Brisbane, Australia: Moonish Enterprises, 2nd ed., 2014.

[181] D. A. Thakore, *Intermediate Finite Element Analysis Using Open Source Software*. Brisbane, Australia: Moonish Enterprises, 1st ed., 2014.

[182] B. Koo, A. Goupee, K. Lambrakos, and H.-J. Lim, "Model test data correlations with fully coupled hull/mooring analysis for a floating wind turbine on a semi-submersible platform," in *33rd International Conference on Ocean, Offshore and Arctic Engineering*, (San Francisco, CA, USA), 2014.

[183] M. Hall and A. Goupee, "Validation of a lumped-mass mooring line model with DeepCwind semisubmersible model test data," *Ocean Engineering*, vol. 104, pp. 590–603, 2015.

[184] J.-L. Fléjou, "Modélisation des câbles," 2014. Code_Aster documentation R3.08.02.

[185] T. de Soza, "Poutres multi-fibres en grands déplacements," 2014. Code_Aster documentation R3.08.09.

[186] K.-J. Bathe and S. Bolourchi, "Large displacement analysis of three-dimensional beam structures," *International Journal for Numerical Methods in Engineering*, vol. 14, no. 7, pp. 961–986, 1979.

[187] Y.-B. Yang and W. McGuire, "Joint rotation and geometric nonlinear analysis," *Journal of Structural Engineering*, vol. 112, no. 4, pp. 879–905, 1986.

[188] M. Randolph and P. Quiggin, "Non-linear hysteretic seabed model for catenary pipeline contact," in *28th International Conference on Ocean, Offshore and Arctic Engineering*, (Honolulu, HI, USA), pp. 145–154, 2009.

[189] T. de Soza, "Opérateur DEFI_CONTACT," 2015. Code_Aster documentation U4.44.11.

[190] V. Yastrebov, *Computational contact mechanics: geometry, detection and numerical techniques*. PhD thesis, Mines ParisTech, Paris, France, 2011.

[191] E. W. Weisstein, "Kuhn-Tucker Theorem," July 2015. Online: http://mathworld.wolfram.com/Kuhn-TuckerTheorem.html.

[192] M. Abbas, "Formulation discrète du contact-frottement," 2015. Code_Aster documentation R5.03.50.

[193] R. L. Webster, "On the static analysis of structures with strong geometric nonlinearity," *Computers & Structures*, vol. 11, no. 1–2, pp. 137–145, 1980.

[194] J.-L. Fléjou, "Éléments "exacts" de poutres (droites et courbes)," 2015. Code_-Aster documentation R3.08.01.

[195] H. Ormberg and K. Larsen, "Coupled analysis of floater motion and mooring dynamics for a turret-moored ship," *Applied Ocean Research*, vol. 20, no. 1, pp. 55–67, 1998.

[196] "Position mooring," Tech. Rep. DNV-OS-E301, Det Norske Veritas, 2013.

[197] J.-L. Fléjou, "Modélisations DIS_T et DIS_TR," 2013. Code_Aster documentation U3.11.02.

[198] H. M. Hilber, T. J. R. Hughes, and R. L. Taylor, "Improved numerical dissipation for time integration algorithms in structural dynamics," *Earthquake Engineering & Structural Dynamics*, vol. 5, no. 3, pp. 283–292, 1977.

[199] N. Greffet, "Algorithme non linéaire dynamique," 2011. Code_Aster documentation R5.05.05.

[200] "Preliminary mooring sizing analysis," Tech. Rep. Basic-TP-01-04-01-CN-1013-Rev01, Technip, 2012.

[201] B. Le Méhauté, *An Introduction to Hydrodynamics and Water Waves*. New York, USA: Springer-Verlag, 1976.

[202] J. F. Wilson, *Dynamics of Offshore Structures*. Hoboken, NJ, USA: John Wiley & Sons, 2003.

[203] L. Roald, J. Jonkman, A. Robertson, and N. Chokani, "The Effect of Second-order Hydrodynamics on Floating Offshore Wind Turbines," *Energy Procedia*, vol. 35, pp. 253–264, 2013.

[204] N. Relun and R. Antonutti, "Calcul mécanique pour expertise de la technologie de l'éolienne flottante à axe vertical Vertiwind," Tech. Rep. H-R22-2014-07308-EN, EDF R&D, 2014.

[205] "Siemens - Wind Turbine Technology - Blades," Oct. 2015. Online: http://www.energy.siemens.com/nl/en/renewable-energy/wind-power/wind-turbine-technology/blades.htm.

[206] D. W. Lobitz and T. D. Ashwill, "Aeroelastic effects in the structural dynamic analysis of vertical axis wind turbines," Tech. Rep. SAND85-0957, Sandia National Laboratories, Albuquerque, 1986.

[207] A. V. Balakrishnan, *Aeroelasticity: The Continuum Theory*. New York, USA: Springer, 2012 edition ed., 2012.

[208] R. Clark, D. Cox, and H. C. J. Curtiss, *A Modern Course in Aeroelasticity*. Boston, USA: Springer, 4 ed., 2004.

[209] D. Dutta and J. K. Bhattacharjee, "Limit cycle oscillations," in *Vibration Problems ICOVP-2007*, Springer Proceedings in Physics, pp. 125–135, Springer Netherlands, 2008.

[210] T. Buhl, H. Markou, M. H. Hansen, K. Thomsen, and F. Rasmussen, "Aeroelastic stability analysis and passive instability suppression," in *European Wind Energy Conference*, (Athens, Greece), 2006.

[211] G. Bir and J. Jonkman, "Aeroelastic instabilities of large offshore and onshore wind turbines," in *Journal of Physics: Conference Series*, vol. 75, 2007.

[212] T. Ashuri, *Beyond classical upscaling: integrated aeroservoelastic design and optimization of large offshore wind turbines*. PhD thesis, TU Delft, Delft, The Netherlands, 2012.

[213] M. H. Hansen, "Aeroelastic instability problems for wind turbines," *Wind Energy*, vol. 10, no. 6, pp. 551–577, 2007.

[214] H. A. Madsen, J. T. Petersen, A. Björck, H. Ganander, D. Winkelaar, A. Brand, A. Bruining, M. Graham, P. Enevoldsen, and S. Øye, "Prediction of dynamic loads and induced vibrations in stall," Tech. Rep. Risø-R-1045(EN), Risø National Laboratory, Denmark, 1998.

[215] K. Thomsen, J. T. Petersen, E. Nim, S. Øye, and B. Petersen, "A method for determination of damping for edgewise blade vibrations," *Wind Energy*, vol. 3, no. 4, pp. 233–246, 2000.

[216] J. G. Holierhoek, "Investigation into the possibility of flap-lag-stall flutter," in *Proc. 45th AIAA Aerospace Sciences Meeting and Exhibit*, (Reno, NV, USA), 2007.

[217] Z. Zhang and S. R. K. Nielsen, "The influence of turbulence on the aero elastic instability of wind turbines," in *Proc. 9th International Conference on Structural Dynamics*, (Porto, Portugal), 2014.

[218] D. W. Lobitz, "Flutter speed predictions for a MW-sized blade," *Wind Energy*, vol. 7, no. 3, pp. 211–224, 2004.

[219] B. C. Owens, D. T. Griffith, B. R. Resor, and J. E. Hurtado, "Impact of modeling approach on flutter predictions for very large wind turbine blade designs," in *Proc. American Helicopter Society: Forum 69*, (Phoenix, AZ, USA), 2013.

[220] D. W. Lobitz, "Parameter sensitivities affecting the flutter speed of a MW-sized blade," *Journal of Solar Energy Engineering*, vol. 127, no. 4, pp. 538–543, 2005.

[221] B. R. Resor, B. C. Owens, and D. T. Griffith, "Aeroelastic instability of very large wind turbine blades," in *Proc. European Wind Energy Conference*, (Copenhagen, Denmark), 2012.

[222] D. Popelka, "Aeroelastic stability analysis of a Darreius wind turbine," Tech. Rep. SAND82-0672, Sandia National Laboratories, Albuquerque, USA, 1982.

[223] B. C. Owens and D. T. Griffith, "Aeroelastic stability investigations for large-scale vertical axis wind turbines," *Journal of Physics: Conference Series*, vol. 524, no. 1, 2014.

[224] M. Raciti Castelli, A. Dal Monte, M. Quaresimin, and E. Benini, "Numerical evaluation of aerodynamic and inertial contributions to Darrieus wind turbine blade deformation," *Renewable Energy*, vol. 51, pp. 101–112, 2013.

[225] M. Abbas, "La méthode des éléments finis isoparamétriques," Tech. Rep. R3.01.00, EDF R&D, 2013.

[226] A. Y. T. Leung and T. C. Fung, "Spinning finite elements," *Journal of Sound and Vibration*, vol. 125, no. 3, pp. 523–537, 1988.

[227] J.-L. Fléjou, "Elements 'exacts' de poutres (droites et courbes)," Tech. Rep. R3.08.01, EDF R&D, 2014.

[228] R. B. Lehoucq, D. C. Sorensen, and C. Yang, "ARPACK user's guide: solution of large scale eigenvalue problems with implicitly restarted arnoldi methods," tech. rep., 1997.

[229] "Scilab: open source software for numerical computation," Oct. 2015. Online: http://www.scilab.org/scilab/about.

[230] "NASA Langley CRGIS: Propeller Whirl Demonstration," Oct. 2015. Online: https://www.youtube.com/watch?v=j6Q5ggtV-y8.

[231] "Guideline for the certification of offshore wind turbines," tech. rep., Germanischer Lloyd, 2012.

[232] R. Drouard, "Beam-elements model for the 1h onshore wind turbine," Tech. Rep. T_TN_MEC_GLO_0040_B_EN, Nénuphar Wind, 2014.

[233] M. Montaland and J. Le Besnerais, "Beam-elements model for the 2 MW onshore wind turbine," Tech. Rep. T_TN_MEC_GLO_0014_G_EN, Nénuphar Wind, 2013.

[234] F. Ottermo and H. Bernhoff, "Resonances and aerodynamic damping of a vertical axis wind turbine," *Wind Engineering*, vol. 36, no. 3, pp. 297–304, 2012.

[235] J. Dodd, "First 2 MW Vertiwind vertical-axis prototype built," May 2015. Online: http://www.windpowermonthly.com/article/1305428/first-2mw-vertiwind-vertical-axis-prototype-built.

[236] I. H. Abbott and A. E. V. Doenhoff, *Theory of Wing Sections, Including a Summary of Airfoil Data*. Mineola, USA: Dover Publications, 1959.

[237] G. Dimitriadis, "Aerodynamics, lecture notes of course AERO0001-1," tech. rep., University of Liege, Aeroelasticity and Experimental Aerodynamics Research Group, 2009.

[238] T. Theodorsen, "General theory of aerodynamic instability and the mechanism of flutter," Tech. Rep. No. 496, NACA, 1935.

[239] L. Stainier, "Aéroélasticité, notes du cours AERO-016," tech. rep., Université de Liège Département Aérospatiale & Mécanique, 2006.

[240] G. Dimitriadis, "Aeroelasticity and experimental aerodynamics, lecture notes of course AERO0032-1," tech. rep., University of Liege, Aeroelasticity and Experimental Aerodynamics Research Group, 2014.

[241] J. G. Leishman, "Challenges in modelling the unsteady aerodynamics of wind turbines," *Wind Energy*, vol. 5, no. 2-3, pp. 85–132, 2002.

[242] T. Burton, D. Sharpe, N. Jenkins, and E. Bossanyi, *Wind Energy Handbook*. Chichester, UK: John Wiley & Sons, 2001.

[243] M. Drela, "XFOIL - Subsonic Airfoil Development System," Sept. 2015. Online: http://web.mit.edu/drela/Public/web/xfoil/.

[244] M. Abbas, "Opérateur STAT_NON_LINE," 2015. Code_Aster documentation U4.51.03.

[245] M. Abbas, "Algorithme non linéaire quasi-statique," 2013. Code_Aster documentation R5.03.01.

[246] J.-L. Fléjou, "Modélisation statique et dynamique des poutres en grandes rotations," 2013. Code_Aster documentation R5.03.40.

[247] M. Abbas, "Opérateur DYNA_NON_LINE," 2015. Code_Aster documentation U4.53.01.

[248] C. Campos, J. E. Román, E. Romero, and A. Tomás, "SLEPc users manual," Tech. Rep. DSIC-II/24/02, Universitat Politècnica de València, 2013.

[249] O. Boiteau, "Résolution du problème modal quadratique (QEP)," 2014. Code_-Aster documentation R5.01.02.